

REPORT DOCUMENTATION PAGE

Form Approved
OMB No. 0704-0188

Public reporting burden for this collection of information is estimated to average 1 hour per response, including the time for reviewing instructions, searching existing data sources, gathering and maintaining the data needed, and completing and reviewing the collection of information. Send comments regarding this burden estimate or any other aspect of this collection of information, including suggestions for reducing this burden, to Washington Headquarters Services, Directorate for Information Operations and Reports, 1215 Jefferson Davis Highway, Suite 1204, Arlington, VA 22202-4302, and to the Office of Management and Budget, Paperwork Reduction Project (0704-0188), Washington, DC 20503.

1. AGENCY USE ONLY (Leave blank)			2. REPORT DATE 31 March 1996		3. REPORT TYPE AND DATES COVERED Final Technical Report 4/1/93 - 3/31/96		
4. TITLE AND SUBTITLE Electro-Mechanical Modeling of the Dynamics of Active Control Systems Based on an Impedance Approach			5. FUNDING NUMBERS AFOSR Grant No. F49620-93-1-0166				
6. AUTHOR(S) Frederic Lalande and Craig A. Rogers			AFOSR TR 96-0410				
7. PERFORMING ORGANIZATION NAME(S) AND ADDRESS(ES) Center for Intelligent Material Systems and Structures Virginia Polytechnic Institute and State University Blacksburg, VA 24061-0261			8. PERFORMING ORGANIZATION REPORT NUMBER				
9. SPONSORING / MONITORING AGENCY NAME(S) AND ADDRESS(ES) Air Force Office of Scientific Research Captain Brian Sanders, Program Manager, Structural Mechanics AFOSR/MA Bolling AFB DC 20332-0410			10. SPONSORING / MONITORING AGENCY REPORT NUMBER N/A 93-1-0166				
11. SUPPLEMENTARY NOTES					12a. DISTRIBUTION / AVAILABILITY STATEMENT <i>Approved for public release, distribution unlimited</i>		12b. DISTRIBUTION CODE 19960806 020
13. ABSTRACT (Maximum 200 words) In this fundamental research program, the focus was to develop an understanding of the physics of actively-controlled material systems, especially the power consumption and energy transfer mechanisms. A new impedance approach was further developed, giving particular attention to applications involving structures with impedance characteristics similar to aircraft structures. This newly developed impedance approach has an advantage over conventional approaches, such as the quasi-static and equivalent thermal-force approaches, in that it includes the dynamic interaction between the structure and the actuator.					14. SUBJECT TERMS impedance modeling, power factor, piezoelectric, vibration control, intelligent materials		15. NUMBER OF PAGES 108
16. PRICE CODE		17. SECURITY CLASSIFICATION OF REPORT U		18. SECURITY CLASSIFICATION OF THIS PAGE U		19. SECURITY CLASSIFICATION OF ABSTRACT U	
20. LIMITATION OF ABSTRACT U							

DISCLAIMER NOTICE



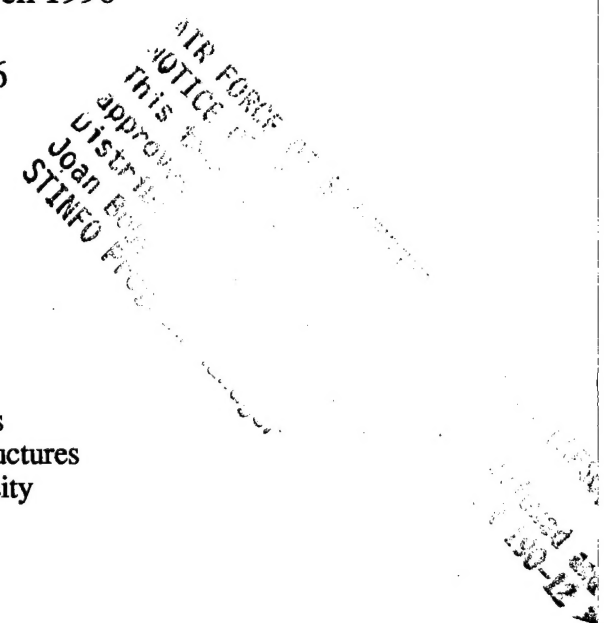
**THIS DOCUMENT IS BEST
QUALITY AVAILABLE. THE
COPY FURNISHED TO DTIC
CONTAINED A SIGNIFICANT
NUMBER OF PAGES WHICH DO
NOT REPRODUCE LEGIBLY.**

Final Technical Report

**Electro-Mechanical Modeling of the Dynamics of Active
Control Systems Based on an Impedance Approach**

For the period: 1 April 1993 - 31 March 1996

Grant No: F49620-93-1-0166



Prepared by: Dr. Frederic Lalande and Prof. Craig A. Rogers
Center for Intelligent Material Systems and Structures
Virginia Polytechnic Institute and State University
Blacksburg, VA 24061-0261
(540) 231-2900
(540) 231-2903 (FAX)

DATA QUALITY IMPACTED 0

Submitted to: Brian Sanders, Program Manager
Air Force Office of Scientific Research
AFOSR/NA
100 Duncan Ave, Suite B115
Bolling AFB, DC 20332-0001

Approved for public release,
distribution unlimited

Research Objectives:

In this fundamental research program, the focus was to develop an understanding of the physics of actively-controlled material systems, especially the power consumption and energy transfer mechanisms. The newly-developed impedance approach, which has a great advantage over conventional approaches, such as the quasi-static and equivalent thermal-force approaches, was further developed with particular attention to structures with impedance characteristics similar to aircraft structures.

Major Technical Achievements:

Impedance methodology for active control systems

The impedance methodology was further refined and extended to plate and shell structures. As for the beam model previously developed, an impedance-based model to predict the dynamic responses of plates and shells subjected to excitation from surface-bonded induced-strain actuators was developed. For the case of plate structures, only the common pure bending loading was modeled. For the case of shell structures, the pure bending, pure extension, and unsymmetrical loading was modeled using the shell governing equations. The plate and shell models were verified experimentally.

Technical details of the work described above can be found in the attached papers, entitled, "An Impedance-Based System Modeling Approach for Induced-Strain Actuator-Driven Structures," and "Impedance-Based Modeling of Actuators Bonded to Shell Structures."

Power consumption and energy transfer mechanisms

A coupled electro-mechanical system model for beam and plate structures was developed to determine the power consumption and actuator energy conversion efficiency. The model has been used to predict the power factor, the power dissipation, and the power requirement of the system. The model has been verified experimentally. This modeling approach has been helpful for understanding the power flow in active structures and can assist in the design of energy efficient actuators and associated control systems.

Technical details of the work described above can be found in the attached paper, entitled, "Power Flow and Consumption in Piezoelectrically-Actuated Structures."

Influence of actuator parameters on the energy efficiency

The actuator power factor, defined as the ratio of the total dissipative mechanical power of a PZT actuator to the supplied electrical power to the PZT actuator, was used to optimize the actuator location and configuration on a complex structure. A comparison between experimental and theoretical power factor results was used to analyze the capabilities and limitations of the actuator power factor algorithm as a tool for determining the optimal configuration and location for a PZT actuator for simple, as well as complex, structural vibration control applications.

Technical details of the work described above can be found in the attached papers, entitled, "Experimental Determination of Optimal Actuator Locations on Complex Structures Based on the Actuator Power Factor," and "Experimental Verification of Optimal Location and Configuration Based on the Power Factor."

Thermal dissipation and thermal stress of induced strain actuators

A simple analytical approach to estimating temperature increase and thermal stress in PZT patch actuators due to dynamic excitation was developed. Case studies have demonstrated that when the PZT actuators operate at system resonance, or with a relatively high electrical field, the heat generation and temperature rise of the PZT is significant and may cause thermal degradation, even damaging the PZT elements.

Technical details of the work described above can be found in the attached paper, entitled, "Heat Generation, Temperature, and Thermal Stress of Structurally-Integrated Piezo-Actuators."

Integration and design of piezoelectric actuators

The design of induced-strain actuators is a comprehensive issue, involving not only the materials and geometry of the actuators, but also the behaviors of the coupled host structures. In particular, the design of the actuators is essentially related to the prediction of induced strain or stress in the actuators. A high stress level in the actuators is useful to excite the host structure but can lead to degradation or fatigue of the actuators. Thus, to include this design issue, the mechanical peak stress was added to the other issues previously addressed (energy efficiency, power requirements, and thermal stresses) in the dynamic modeling.

Technical details of the work described above can be found in the attached paper, entitled, "Integration and Design of Piezoceramic Elements in Intelligent Structures."

Analysis of other types of actuators

The impedance-based approach was extended to other types of actuators, showing that it can be applied to various actuators. First, the dynamic transduction characterization of magnetostrictive actuators was made, including the mechanical dynamics and the electro-magneto-mechanical interaction of the actuator. Second, the impedance approach was applied to dynamic modeling of piezoelectric stack actuators. The electro-dynamic behavior of the stack was first modeled in a free configuration and then integrated into a complex structure.

Technical details of the work described above can be found in the attached papers, entitled, "Dynamic Transduction Characterization of Magnetostrictive Actuators," "Electro-Dynamic Transduction Equations for Piezoelectric Stack Actuators," and "Dynamic Output and Structural Response Prediction for Stack Active Members Integrated in Complex Structures."

Impedance methodology for active control systems

Zhou, S.W., Liang, C., and Rogers, C.A., "An Impedance-Based System Modeling Approach for Induced Strain Actuator-Driven Structures," *Journal of Vibration and Acoustics*, Vol. 118, January 1996, pp.

Lalande, F., Chaudhry, Z., and Rogers, C.A., "Impedance-Based Modeling of Actuators Bonded to Shell Structures," *Journal of Intelligent Material Systems and Structures*, Vol. 6, November 1995, pp. 765-775.

A dynamic model of piezoelectric actuator-driven thin plates

Suwei Zhou, Chen Liang and C. A. Rogers

Center for Intelligent Material Systems and Structures
Virginia Polytechnic Institute and State University
Blacksburg, VA 24061-0261

ABSTRACT

This paper presents the theoretical development and the experimental verification of a dynamic model of distributed piezoelectric (PZT) actuators locally coupled with two-dimensional structures. The model includes the dynamic interaction between PZT actuators and their host structures. An analytical solution of the moment (or force) outputs of the PZT patch actuators has been developed based upon the input impedance of the piezoelectric actuator and the mechanical impedance of host structures. A simply-supported thin plate with surface-bonded PZT patches was built and tested so that the ability of the impedance approach to predict the dynamic performance of the actuator and intelligent structures has been verified. When compared with conventional static models or quasi-static models, the impedance modeling method offers insight into the dynamics and electro-mechanical coupling of the integrated PZT/substrate systems and more accurately predicts the actuation of induced strain actuators.

1. INTRODUCTION

Recent research efforts have focused on the use of piezoelectric materials (PZT) as actuators and sensors in intelligent structures to tune the response of the structures since the compact PZT actuator and sensor allows a more flexible design of control systems. A mathematic description of a PZT/substrate adaptive system is desirable and beneficial for performance prediction and parametric optimization of the actuator and sensor. In the modeling of these distributed piezoelectric actuators locally coupled with two-dimensional structures, static strain or stress-based analytical approaches have been used to estimate the induced loading (Dimitriadis et al., 1989; Wang et al., 1990; Crawley et al., 1991; Kim et al., 1991). It is typically assumed in the static models that the piezoelectric actuators do not significantly alter the inertia mass and the stiffness of the host structures. The dynamic interaction between PZT actuators and the structures is thus ignored. The static analysis usually leads to the conclusion that the amplitude of the excitation force of the PZT actuator is frequency independent.

A more realistic and accurate model of an adaptive structure must include the dynamic interaction between actuators and host structures. When a control voltage is applied to the PZT patch along the polarization direction, the dynamic strain is induced on the host structure. The active force is then generated as a result of the mechanical interaction between the actuator and host structure. The dynamic mass loading and stiffening effect of the PZT patch should be considered. This added dynamic effect plays an important role in the actuation on the host structure and may significantly change the mechanical resonant frequencies of the original system. Therefore, a dynamic model which relates the actuator dynamics to the host structure dynamics is desired. Liang et al. (1993a) suggested an impedance model and derived the formulation of the force output of a piezoelectric actuator-driven one-degree-of-freedom spring-mass-damping system. Then, the impedance modeling approach is expanded to one-dimensional structures, such as beams (Liang et al., 1993b) and circular rings (Rossi et al., 1993). For generic two-dimensional structures, the mechanical impedance coupling in different coordinate directions should be included.

and the cross impedance of the host structures has an impact on the actuator dynamics. Therefore, a coupled mechanical impedance model for generic two-dimensional smart structures is required. Such a coupled impedance analysis applicable to thin cylindric structures was performed by Zhou et al. (1993).

This paper will further expand the impedance modeling method to piezoelectric actuator-driven two-dimensional structures. First, a generic impedance analysis will be developed to obtain the dynamic outputs of the PZT actuator based upon the input impedance of the PZT patch and the mechanical impedance of the host structure. Then, an analytical solution for the admittance and impedance of a simply-supported thin plate excited by a pair of moments will be derived. Furthermore, a vibration excitation experiment is conducted on the plate to verify the theoretical model. The comparison of the conventional static approach and the impedance method is also performed to demonstrate the significant difference between these two types of modeling approaches. It should be noted that the current work is focusing on the prediction of the dynamic output behavior of the PZT actuator using a structural impedance analysis. To estimate the power consumption and energy efficiency of the PZT actuator-driven intelligent structures, a coupled electro-mechanical impedance model is needed to include the electrical properties of the PZT actuator. Such a coupled electro-mechanical impedance model for two-dimensional adaptive structures has been developed and the results will be published elsewhere (Zhou et al., 1994).

2. A DYNAMIC MODEL FOR PZT ACTUATORS INTEGRATED WITH 2-D STRUCTURES

Figure 1 illustrates the equivalent dynamic model of a PZT actuator-driven two-dimensional structure. The dynamic performances of the host structure in the x and y directions is represented by the direct impedance Z_{xx} and Z_{yy} , as well as the cross impedance Z_{xy} and Z_{yx} , respectively.

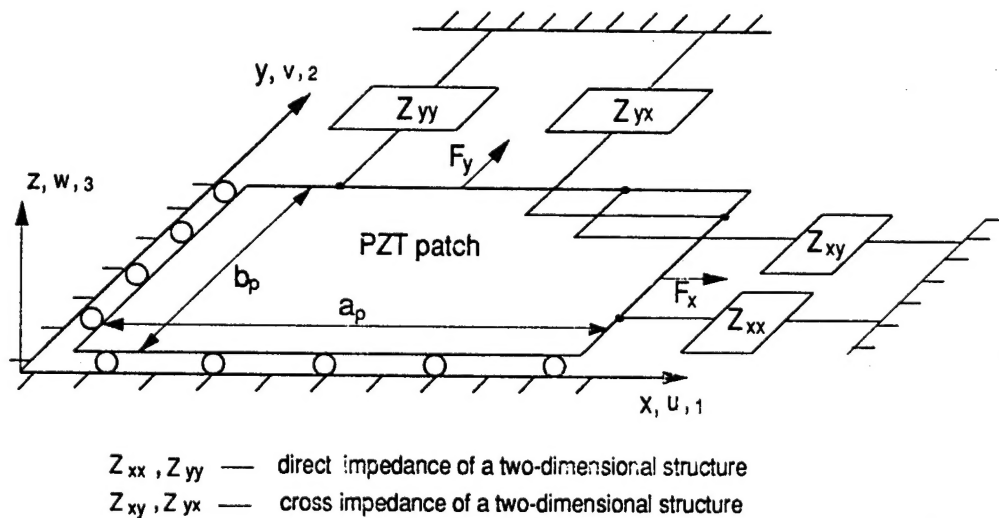


Figure 1: A model of dynamic interaction between a PZT patch actuator and a two-dimensional structure represented by mechanical impedance.

When a voltage is applied to the PZT patch along the polarization direction (3), the dynamic displacement is induced in both the x (u) and y (v) directions. The active force provided by the PZT actuator, F_x and F_y , may be expressed by:

$$\begin{pmatrix} F_x \\ F_y \end{pmatrix} = - \begin{pmatrix} Z_{xx} & Z_{xy} \\ Z_{yx} & Z_{yy} \end{pmatrix} \begin{pmatrix} u \\ v \end{pmatrix}, \quad (1)$$

where the minus sign indicates that the structural reactions are equal and opposite to the output forces of the PZT actuator. u and v are the in-plane velocity response of the PZT actuator. The equation of motion of the PZT actuator may be described by:

$$\rho_p \frac{\partial^2 u}{\partial t^2} = Y_p^{EI} \frac{\partial^2 u}{\partial x^2} \quad (2a)$$

$$\rho_p \frac{\partial^2 v}{\partial t^2} = Y_p^{EJ} \frac{\partial^2 v}{\partial y^2}, \quad (2b)$$

in which the subscript p refers to the parameters of the PZT patch and the subscript II (22) indicates the direction of the piezoelectric material. ρ is the mass density and Y^E is the complex Young's modulus at a constant field:

$$Y^E = Y(1 + j\eta), \quad (3)$$

where η is the structural loss factor, j is the complex number, and Y is the real Young's modulus. The displacement response of the PZT actuator is written as:

$$u = [A \sin(k_{pII}x) + B \cos(k_{pII}x)] e^{j\omega t} \quad (4a)$$

$$v = [C \sin(k_{p22}y) + D \cos(k_{p22}y)] e^{j\omega t}, \quad (4b)$$

where A, B, C and D are unknowns and can be determined by the boundary conditions. Considering the isotropy of the material gives the wave number, $k_{pII(22)}$:

$$k_p = k_{pII} = k_{p22} = \omega \sqrt{\frac{\rho_p}{Y_p^E}}, \quad (5)$$

where ω is the input angular frequency. Applying the displacement boundary condition, $u_{x=0}=0$ and $v_{y=0}=0$ to Eq. (4) leads to $B=D=0$. The displacement response of the PZT actuator is reduced to:

$$u = A \sin(k_p x) e^{j\omega t} \quad (6)$$

$$v = C \sin(k_p y) e^{j\omega t}. \quad (7)$$

The unknowns A and C may be evaluated from the constitutive equation of the PZT patch at $x=a_p$ and $y=b_p$, as shown in Fig. 1:

$$\begin{pmatrix} \epsilon_x \\ \epsilon_y \end{pmatrix} = \begin{pmatrix} \frac{\partial u}{\partial x} \\ \frac{\partial v}{\partial y} \end{pmatrix} = \begin{pmatrix} \frac{1}{Y_p^E b_p t_p} & -\frac{v_p}{Y_p^E a_p t_p} \\ -\frac{v_p}{Y_p^E b_p t_p} & \frac{1}{Y_p^E a_p t_p} \end{pmatrix} \begin{pmatrix} F_x \\ F_y \end{pmatrix} + \begin{pmatrix} d_{31} \\ d_{32} \end{pmatrix} E, \quad (8)$$

where $\epsilon_{x(y)}$ is the dynamic strain. a_p , b_p , and t_p are the length, the width, and the thickness of the PZT patch, respectively. d_{31} and d_{32} are the piezoelectric constants of the PZT material in the 1 and 2 directions. $E=V/t_p$ is the electric field and V is the voltage.

applied voltage. Note that the Poisson's ratio of the PZT material, ν_p , is introduced so that the mechanical coupling of the in-plane motions in the x and y directions of the PZT actuator can be included in the modeling. Substituting Eqs. (1) and (6) into Eq. (7) and taking the algebraic operation to rearrange A and C yields:

$$\begin{pmatrix} k_p \cos(k_p a_p) \left(1 - \frac{\nu_p}{\alpha} \frac{Z_{xy}}{Z_{pxx}} + \frac{Z_{xx}}{Z_{pxx}}\right) & k_p \cos(k_p b_p) \left(\alpha \frac{Z_{yx}}{Z_{pyy}} - \nu_p \frac{Z_{yy}}{Z_{pyy}}\right) \\ k_p \cos(k_p a_p) \left(\frac{1}{\alpha} \frac{Z_{xy}}{Z_{pxx}} - \nu_p \frac{Z_{xx}}{Z_{pxx}}\right) & k_p \cos(k_p b_p) \left(1 - \nu_p \alpha \frac{Z_{yx}}{Z_{pyy}} + \frac{Z_{yy}}{Z_{pyy}}\right) \end{pmatrix} \begin{pmatrix} A \\ C \end{pmatrix} = \begin{pmatrix} d_{31} \\ d_{32} \end{pmatrix} E , \quad (8)$$

where $\alpha = a_p/(b_p)$ is the ratio of the length to the width of the PZT patch. Z_{pxx} and Z_{pyy} are the short-circuit input impedance of the PZT actuator in the x and y directions, defined as:

$$Z_{pxx} = \frac{F_x}{\dot{u}} = -j \frac{K_{px}}{\omega} \frac{k_p a_p}{\tan(k_p a_p)} \quad (9a)$$

$$Z_{pyy} = \frac{F_y}{\dot{v}} = -j \frac{K_{py}}{\omega} \frac{k_p b_p}{\tan(k_p b_p)} , \quad (9b)$$

with the static extension stiffness of the PZT actuator in the x and y directions, K_{px} and K_{py} :

$$K_{px} = \frac{Y_p^E b_p t_p}{a_p} \quad (10a)$$

$$K_{py} = \frac{Y_p^E a_p t_p}{b_p} . \quad (10b)$$

Solving for A and C from Eq. (8), the dynamic force output of the PZT actuator is determined from Eq. (1) with the substitution of the velocity response:

$$\begin{pmatrix} F_x \\ F_y \end{pmatrix} = \begin{pmatrix} \bar{F}_x \\ \bar{F}_y \end{pmatrix} e^{j\omega t} = -j\omega \begin{pmatrix} Z_{xx} & Z_{xy} \\ Z_{yx} & Z_{yy} \end{pmatrix} \begin{pmatrix} A \sin(k_p a_p) \\ C \sin(k_p b_p) \end{pmatrix} e^{j\omega t} . \quad (11)$$

Accordingly, the amplitude of the line moments per unit length created by a pair of the PZT actuators, $\bar{M}_{x(y)}$ (in N·m/m), can be obtained by:

$$\begin{pmatrix} \bar{M}_x \\ \bar{M}_y \end{pmatrix} = (h + t_p) \begin{pmatrix} \bar{F}_x / b_p \\ \bar{F}_y / a_p \end{pmatrix} = -j\omega \frac{h + t_p}{a_p b_p} \begin{pmatrix} a_p Z_{xx} & a_p Z_{xy} \\ b_p Z_{yx} & b_p Z_{yy} \end{pmatrix} \begin{pmatrix} A \sin(k_p a_p) \\ C \sin(k_p b_p) \end{pmatrix} , \quad (12)$$

where h is the thickness of the host structure. The distributed line moments are thus expressed by:

$$M_x = \bar{M}_x [\delta(x - x_1) - \delta(x - x_2)] [h(y - y_1) - h(y - y_2)] e^{j\omega t} \quad (13a)$$

$$M_y = \bar{M}_y [\delta(y - y_1) - \delta(y - y_2)] [h(x - x_1) - h(x - x_2)] e^{j\omega t} , \quad (13b)$$

where $\delta(x)$ and $\delta(y)$ are the Dirac delta functions. $h(x)$ and $h(y)$ are the Heaviside functions. x_1 , x_2 , y_1 and y_2 are the location coordinates of the edge of PZT patches on the plate, as illustrated in Fig. 2. Notice that the coefficients A and C as well as

the mechanical impedance of the host structure in Eq. (12) are functions of frequency. Therefore, the moment outputs of PZT actuator must be frequency dependent.

Thus far, the dynamic forces and moments of the PZT actuator have been obtained based upon the impedance characteristics of the PZT itself and the host structure. This dynamic model is also called the impedance model. The input impedance of the PZT actuator is given by Eq. (9). The mechanical impedance of the host structure depends on the location of the actuation and the geometric configuration, the physical and material properties, and the boundary condition of the structure. As a numerical example, the next section will address how to calculate the admittance of a simply-supported thin plate actuated by the line moments. For complex structures, the structural impedance can be determined from either experiments or finite element analysis.

3. ADMITTANCE ANALYSIS OF A THIN PLATE ACTUATED BY LINE MOMENTS

A geometric representation of a simply-supported thin plate with a pair of PZT actuators is shown in Fig. 2. The PZT patches are assumed to be perfectly bonded on the top and bottom surfaces of the plate. When the PZT actuators are actuated out-of-phase, a pure bending moment excitation is created at the edges of the PZT patches.

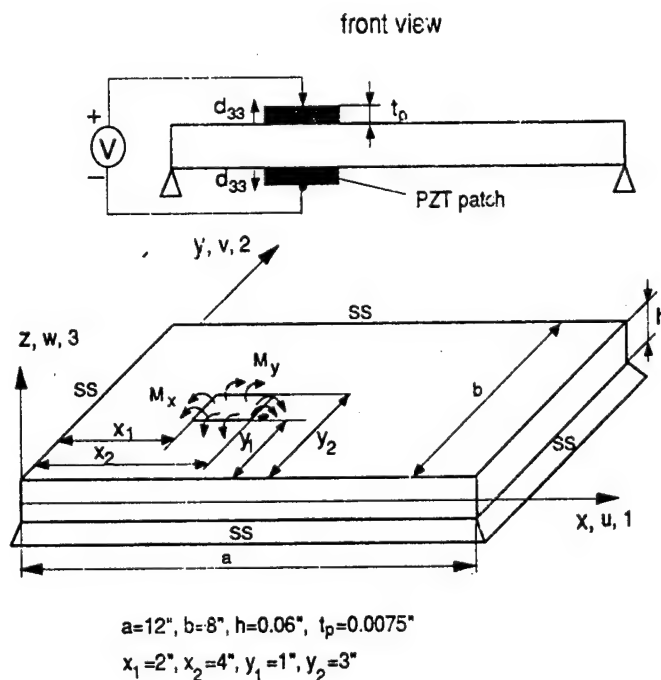


Figure 2: A geometric configuration of a simply-supported (ss) thin plate with surface-bonded PZT actuators.

Under the actuation of M_x and M_y , the total angular velocity response of the plate at the edge of the PZT patch can be written as:

$$\nabla \beta_x = -[(\frac{\partial \dot{w}}{\partial x})_{x=x_1} - (\frac{\partial \dot{w}}{\partial x})_{x=x_2}] = -(H_x M_x + H_y M_y)$$

$$\nabla \beta_y = -[(\frac{\partial \dot{w}}{\partial y})_{yy} - (\frac{\partial \dot{w}}{\partial y})_{yy}] = -(H_{yy}M_x + H_{yx}M_y) , \quad (14b)$$

where H_{xx} and H_{yy} are the direct moment admittances of the plate. H_{xy} and H_{yx} are the cross moment admittances of the plate and indicate mechanical impedance coupling of the host structure in the x and y directions. The moment admittance here is defined as:

$$H_{lk} = \frac{\nabla \beta_k}{M_l} \quad (l, k = x, y) . \quad (15)$$

Using the relation of the force and the moment, $M_{xy} = (h + t_p)F_{xy}$, as well as the geometric relation of $u(v) = (h + t_p) \cdot \nabla \beta_{xy}/2$, as illustrated in Fig. 3, Eq. (14) is rewritten in terms of the force admittance matrix:

$$\begin{pmatrix} F_x \\ F_y \end{pmatrix} = -\frac{2}{(h+t_p)^2} \begin{pmatrix} H_{xx} & H_{yx} \\ H_{xy} & H_{yy} \end{pmatrix}^{-1} \begin{pmatrix} \dot{u} \\ \dot{v} \end{pmatrix} = -\begin{pmatrix} Q_{xx} & Q_{yx} \\ Q_{xy} & Q_{yy} \end{pmatrix}^{-1} \begin{pmatrix} \dot{u} \\ \dot{v} \end{pmatrix} . \quad (16)$$

The coefficient $2/(h+t_p)^2$ in Eq. (16) is developed for transformation of the moment admittance to the in-plane force admittance. The corresponding force impedance matrix is thus determined by:

$$Z = \begin{pmatrix} Z_{xx} & Z_{xy} \\ Z_{yx} & Z_{yy} \end{pmatrix} = \begin{pmatrix} Q_{xx} & Q_{yx} \\ Q_{xy} & Q_{yy} \end{pmatrix} . \quad (17)$$

Under the actuation of distributed moments normal to the surface of the plate, the governing equation for the forced transverse motion of the plate may be written based upon Love's theory and Hamilton principle (Soedel, 1981):

$$L(w) - \rho h \ddot{w} = -\left(\frac{\partial M_x}{\partial x} + \frac{\partial M_y}{\partial y}\right) , \quad (18)$$

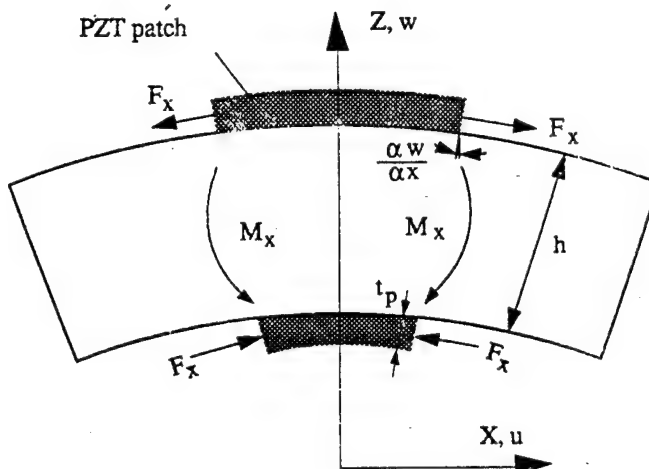
where w is the transverse displacement response of the plate. $L(w)$ is the Love operator, which can be evaluated from the eigenvalue analysis:

$$L(w) = -\rho h \omega_m^2 w , \quad (19)$$

where ω_m is the complex resonant frequency of the plate because the damping factor of the system is introduced through the complex Young's modulus in Eq. (3). The subscript m and n refer to the mode numbers in the x and y directions. The forced response of the plate may be expressed by the modal expansion series solution:

$$w = \sum_{m=1}^{\infty} \sum_{n=1}^{\infty} p_{mn} W_{mn}(x, y) , \quad (20)$$

Figure 3: The geometric deformation of a plate actuated by a pair of moments.



where p_{mn} is the modal participation factor which determines the amount of participation of each mode in the total transverse dynamic response. W_{mn} is the eigenfunction. Substituting Eqs. (19) and (20) into Eq. (18) results in:

$$\sum_{m=1}^{\infty} \sum_{n=1}^{\infty} (\rho h \ddot{p}_{mn} + \rho h \omega_{mn}^2 p_{mn}) W_{mn}(x, y) = \frac{\partial M_x}{\partial x} + \frac{\partial M_y}{\partial y}. \quad (21)$$

For a simply-supported plate, the eigenfunction $W_{mn}(x, y)$ can be described by:

$$W_{mn}(x, y) = \sin \frac{m\pi}{a} x \cos \frac{n\pi}{b} y, \quad (22)$$

where a and b are the length and the width of the plate. Substituting Eq. (22) into Eq. (21) and using the usual modal expansion technique yields:

$$\ddot{p}_{mn} + \omega_{mn}^2 p_{mn} = F_{mn} e^{i\omega t}, \quad (23)$$

where the equivalent forcing function, F_{mn} , is the form of

$$F_{mn} = \frac{1}{\rho h N_{mn}} \int_0^a \int_0^b W_{mn}(x, y) \left(\frac{\partial M_x}{\partial x} + \frac{\partial M_y}{\partial y} \right) dx dy, \quad (24)$$

and

$$N_{mn} = \int_0^a \int_0^b \sin^2 \frac{m\pi x}{a} \cos^2 \frac{n\pi y}{b} dx dy = \frac{ab}{4}. \quad (25)$$

Applying Eqs. (13) and (22) into Eq. (24) yields:

$$F_{mn} = \frac{4}{ab\rho h} \left(\frac{bm}{an} \bar{M}_x + \frac{an}{bm} \bar{M}_y \right) \left(\cos \frac{m\pi}{a} x_2 - \cos \frac{m\pi}{a} x_1 \right) \left(\cos \frac{n\pi}{b} y_1 - \cos \frac{n\pi}{b} y_2 \right).$$

The steady-state solution of the forced vibration of the plate is thus obtained by:

$$w(x, y, t) = \sum_{m=1}^{\infty} \sum_{n=1}^{\infty} \frac{F_{mn} \sin \frac{m\pi}{a} x \sin \frac{n\pi}{b} y e^{i\omega t}}{\omega_{mn}^2 - \omega^2},$$

where x and y are the location coordinates at which the response is picked up. The resonant frequency, ω_{mn} , is determined by the homogenous equation of the transverse motion of the plate:

$$\omega_{mn} = \pi^2 \sqrt{\frac{D}{\rho h}} \left(\left(\frac{m}{a} \right)^2 + \left(\frac{n}{b} \right)^2 \right),$$

where

$$D = \frac{h^3 Y^E}{12(1-\nu^2)}$$

is the flexural stiffness of the plate.

Recalling the definition of the admittance in Eq. (15) and the relation of $Q_{lk} = (h+t_p)^2 H_{lk}/2$ ($l,k=x,y$), the direct force admittance of the plate at the edge of the PZT patch is obtained by:

$$Q_{xx} = \frac{2\pi(h+t_p)^2\omega}{\rho h a^3 b_p} \sum_{m=1}^{\infty} \sum_{n=1}^{\infty} \left(\frac{m^2(\cos \frac{m\pi x_1}{a} - \cos \frac{m\pi x_2}{a})^2 \sin \frac{n\pi(y_1+y_2)}{2b} (\cos \frac{n\pi y_1}{b} - \cos \frac{n\pi y_2}{b})}{n(\omega_{mn}^2 - \omega^2)} \right) e^{jn/2} \quad (30)$$

and

$$Q_{yy} = \frac{2\pi(h+t_p)^2\omega}{\rho h b^3 a_p} \sum_{m=1}^{\infty} \sum_{n=1}^{\infty} \left(\frac{n^2(\cos \frac{m\pi x_1}{a} - \cos \frac{m\pi x_2}{a})^2 \sin \frac{m\pi(x_1+x_2)}{2a} (\cos \frac{n\pi y_1}{b} - \cos \frac{n\pi y_2}{b})^2}{m(\omega_{mn}^2 - \omega^2)} \right) e^{jn/2}. \quad (31)$$

Similarly, the cross admittance is determined by:

$$Q_{xy} = \frac{2\pi(h+t_p)^2\omega}{\rho h a^2 b b_p} \sum_{m=1}^{\infty} \sum_{n=1}^{\infty} \left(\frac{m(\cos \frac{m\pi x_1}{a} - \cos \frac{m\pi x_2}{a})^2 \sin \frac{m\pi(x_1+x_2)}{2a} (\cos \frac{n\pi y_1}{b} - \cos \frac{n\pi y_2}{b})^2}{\omega_{mn}^2 - \omega^2} \right) e^{jn/2} \quad (32)$$

and

$$Q_{yx} = \frac{2\pi(h+t_p)^2\omega}{\rho h a b^2 a_p} \sum_{m=1}^{\infty} \sum_{n=1}^{\infty} \left(\frac{n(\cos \frac{m\pi x_2}{a} - \cos \frac{m\pi x_1}{a})^2 \sin \frac{n\pi(y_1+y_2)}{2b} (\cos \frac{n\pi y_1}{b} - \cos \frac{n\pi y_2}{b})}{(\omega_{mn}^2 - \omega^2)} \right) e^{jn/2}. \quad (33)$$

The thin plate is usually assumed to be a linear system, hence, the cross admittances are equal, that is, $Q_{xy} = Q_{yx}$, which is proved by the numerical calculation.

4. DYNAMIC OUTPUT CHARACTERISTICS OF THE PZT ACTUATOR

In the static models, the amplitude of the moment outputs of the actuator are assumed to be independent of the frequency and the dynamic behavior of the host structure. In addition, the same amplitude of the moment is assumed to be in both the x and y directions even though the mechanical impedance of the structure may be quite different. There are several static models for the actuation of PZT patches on two-dimensional plate structures (Dimitriadis et al., 1989; Wang et al., 1990; Crawley et al., 1991; Kim et al., 1991). One of which was developed from the stress-based pure bending model (Dimitriadis et al., 1989) is used in this paper to compare with the dynamic model.

A simply-supported thin plate is used in the numerical calculation. The thin plate is made of aluminum and the PZT material is G1195. Their geometric parameters are shown in Fig. 2. The basic material properties are listed in Table 1.

Figure 4 demonstrates the difference of moment outputs of the actuator predicted by the dynamic model and the static model. In the dynamic model, the amplitude of the moment varies significantly near the resonant frequencies of the system because of the dynamic interaction between the actuator and the plate. This interaction can be explained by the impedance matching, as shown in Fig. 5. When the input impedance of the PZT actuator approaches to and matches with the structural

impedance of the plate, the moment output of the actuator varies significantly. Therefore, the actuation is greatly strengthened. In the static model, however, the amplitude of the moment output is constant over the whole frequency band as shown in Fig. 4 and the dynamic output of the actuator can not be predicted. In addition, Figure 5 shows that the mechanical impedance of the plate is different in the x and y directions because of the asymmetric geometry of the plate. Therefore, the actuation of the PZT actuator is not equal, i.e., $\bar{M}_x \neq \bar{M}_y$.

Table 1: Material Properties of PZT* and Aluminum

	Young's Modulus (N/m ²)	Mass Density (kg/m ³)	Poisson's Ratio	Piezoelectric Constant (m/volt)	Loss Factor
PZT	6.3×10^{10}	7650	0.3	1.66×10^{-10}	0.001
Aluminum	7.1×10^{10}	2800	0.33	N/A	0.005

*From Piezo System, Inc.

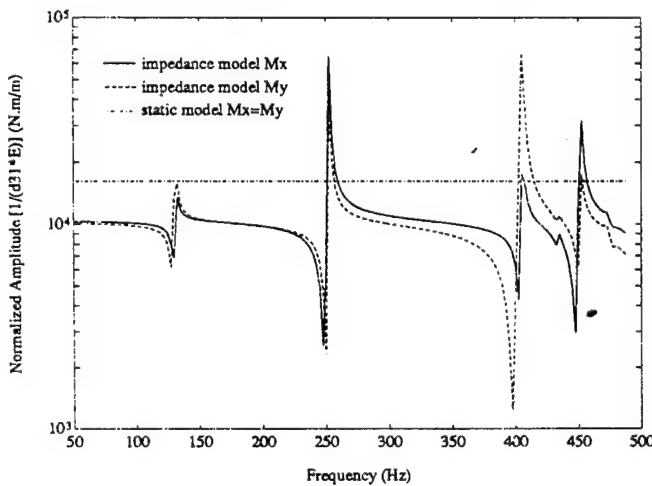


Figure 4: The comparison of the predicted moment outputs of the PZT actuator.

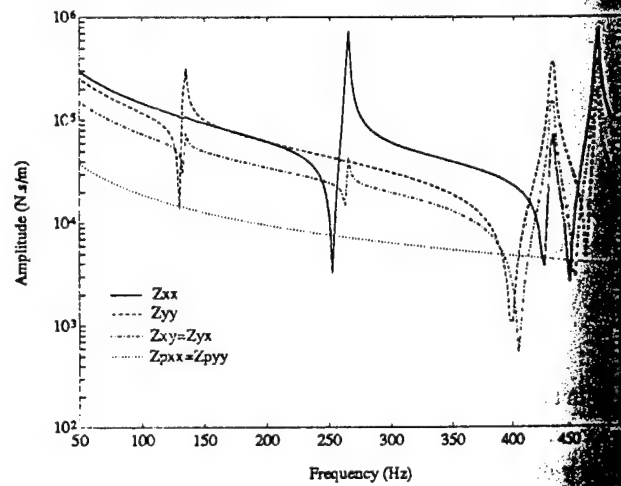


Figure 5: The input impedance of the PZT actuator and mechanical impedance of the host structure.

The parametric study (Zhou et al., 1993) has shown that the moment output depends on the location of the PZT patch due to location dependence of the mechanical impedance of the host structure. Moreover, with increase in the thickness of the actuator, the impedance matching is strengthened and the actuation is thus significantly intensified. When the size of the PZT patch, especially the thickness of the actuator, is much smaller than that of the host structure, the impedance model may result similar to the static model.

To examine the utility and generality of the two-dimensional impedance model, the developed model above is applied to

one-dimensional structures. It is assumed that the mechanical coupling terms of the host structure, i. e., the cross impedance Z_{xy} and Z_{yx} in Eq. (8) is zero and the Poisson effect of the piezoelectric material is also ignored. A decoupling analysis is then obtained. The force output of the PZT actuator predicted by Eq. (11) is reduced to:

$$F_{xy} = -\frac{Z_{xx(y)}}{Z_{pxx(y)} + Z_{xx(y)}} Y_p S_{pxy} d_{31} E , \quad (34)$$

where S_{pxy} is the cross section area of the PZT patch. This result is exactly same as that derived by Liang et al. (1993a). Therefore, the two-dimensional impedance analysis presented in the previous sections is more general and applicable to one-dimensional structures if the motion of the PZT patch is considered in only one direction.

5. EXPERIMENTAL VERIFICATION

A simply-supported thin plate was built and tested to verify the dynamic model. The experimental setup of vibration excitation of the plate is illustrated in Fig. 6. The thin plate in the experiment is made of aluminum and the PZT material is G1195. Their geometric parameters are shown in Fig. 2. The basic material properties are listed in Table 1.

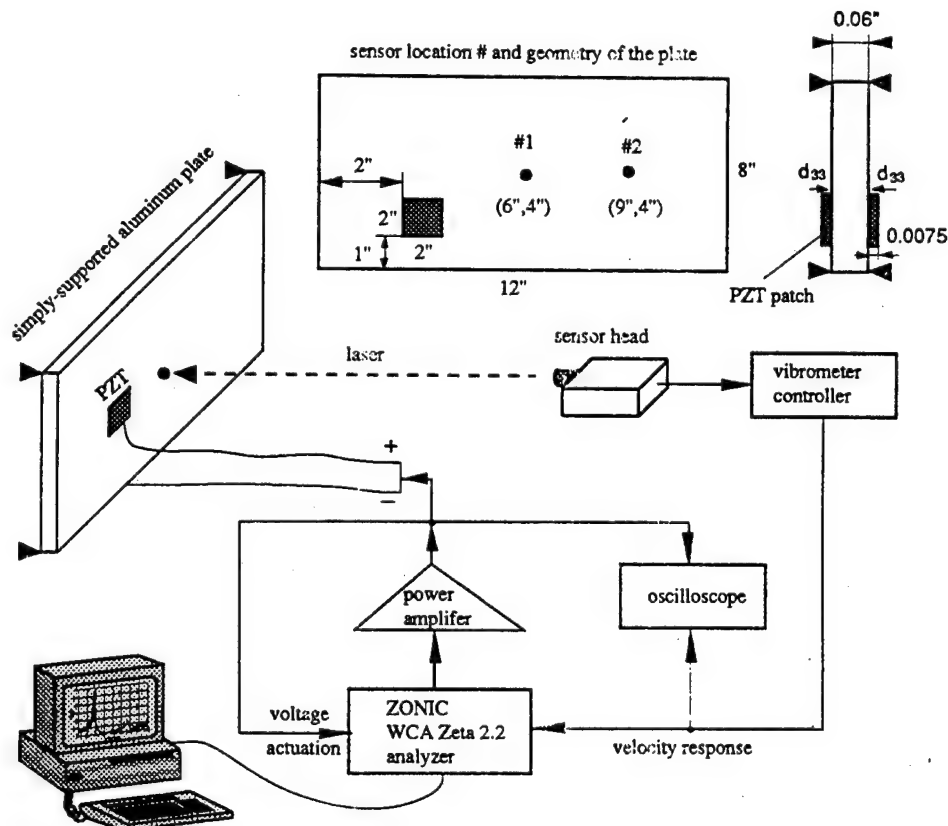


Figure 6: The experimental setup for measuring velocity of the plate integrated with PZT patch actuators.

A pseudo-random signal was used in a burst mode to activate the plate. The transverse velocity response of the plate is accurately measured using a noncontact laser sensor such that the effect of the added mass and stiffening effect of the sensor on the plate has been eliminated. The response is picked up at two different locations: $x=6"$, $y=4"$, and $x=9"$, $y=4"$, as shown in Fig. 6. The coherence of the actuation voltage and the velocity response is used to examine the accuracy of the excited modes.

Figure 7 illustrates the measured and predicted frequency response function of the plate at the sensor location #1. Two important results have been observed:

First, the theoretical prediction based upon the impedance analysis (dash line) agrees well with the experimental data (solid line). The static model (dashed-dotted line), however, misrepresents the velocity response of the plate and is not able to predict the 2nd (2,1) mode and the 3rd mode (1,2). The reason is that the sensor location #1 is on the nodal lines of these two modes and, assuming a constant moment input in the static model, misses these two modes. As a matter of fact, the input moment is a function of frequency and is maximized at the resonant frequencies of the integrated system. The 2nd and 3rd modes are thus excited.

Second, Figure 7 clearly demonstrates that the dynamic performance of the original system is altered due to the added PZT patches. The resonant frequency of the original plate is shifted to high values. The maximum frequency shift happens to be at 4th mode (1,3) and the resonant frequency increases about 100 Hz within the frequency band less than 1000 Hz. At the same time, the amplitude of the system response decreases. This can be explained by the observation that the PZT patches bonded on the surface of the plate stiffen the structure and add parasitic mass in the original system. In general, the stiffening effectiveness will increase the resonant frequencies of the structure while the added mass has the opposite influence. However, the stiffening effect may have the greater impact on the dynamic characteristics of the plate than the added mass. Consequently, the resonant frequencies of the integrated system are shifted to the higher value. The intensity of the variation of the frequencies depends on the extent of the impedance mismatch between PZT and the plate. In static model, the dynamic behavior of the plate is assumed to be unchanged, hence the phenomena of resonant frequency shift can't be observed in the experiment.

When the sensor location is moved from the location #1 to the location #2, the same phenomena as shown in Fig. 7 happens. This time, the sensor location #2 is placed on the nodal line of only 3rd mode (1,2). Thus, the static model picks up the 2nd mode but misses the 3rd mode, as shown in Fig. 8. The resonant frequency shift and the dynamic response variations of the original system caused by the bonded PZT actuators still exist. However, these dynamic performance variations are not predicted by the static model.

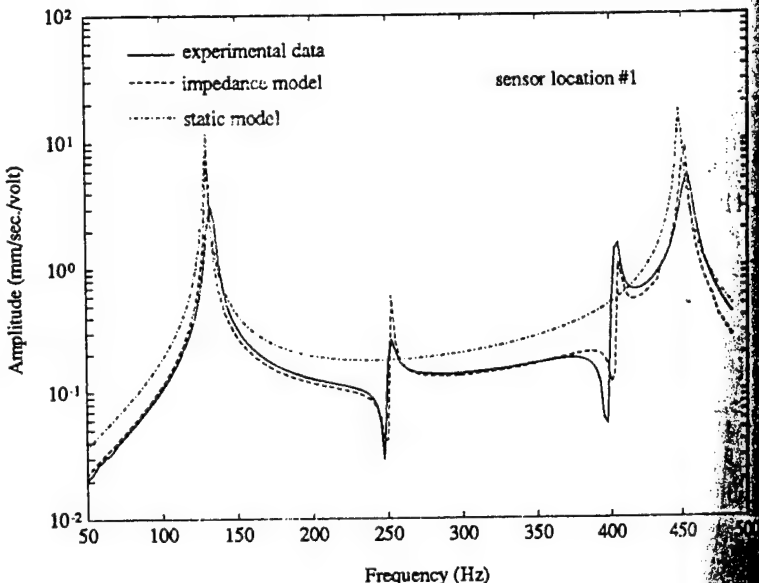


Figure 7: The predicted and measured velocity response of the plate.

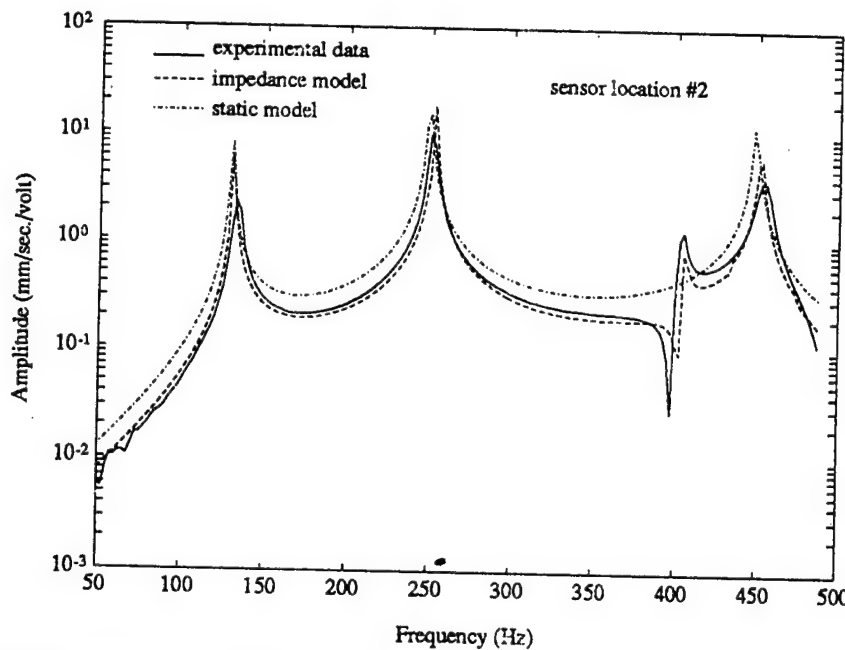


Figure 8: The predicted and measured velocity response of the plate at the sensor location #2.

6. SUMMARY

- A dynamic model for the actuation of two-dimensional structures has been developed using the mechanical impedance analysis. The impedance modeling approach has clearly demonstrated its advantage over conventional static models and its potential in the design and the application of PZT actuators. It reveals the dynamic essence of the actuation of the PZT actuators and offers more accurate prediction.
- The experiment has verified the accuracy of the impedance model to predict the dynamic outputs (forces or moments) of the induced strain actuators and the vibration response of the adaptive structures.
- The dynamic performance of the adaptive structures may be strongly affected by the stiffening effect of the distributed piezoelectric actuators.

7. ACKNOWLEDGEMENT

The authors gratefully acknowledge the support of the Air Force Office of Scientific Research of this work under Grant AFOSR Grant NO. F49620-93-1-0166; Dr. Jim Chang Program Manager.

8. REFERENCE

Crawley, Edward F. and K. B. Lazarus, "Induced Strain Actuation of Isotropic and Anisotropic Plates", AIAA Journal, VOL. 29, NO. 6, pp. 944-951, 1991.

Dimitriadis, E. K., C. R. Fuller and C. A. Rogers, "Piezoelectric Actuators for Distributed Noise and Vibration Excitation of Thin Plates", ASME Failure Prevention and Reliability, DE-Vol. 16, pp. 223-233, 1989.

Kim, S. J. and J. D. Jones, "Optimal Design of Piezoactuators for Active Noise and Vibration Control", AIAA Journal, Vol. 29, NO. 12, pp2047-2053, 1991.

Leissa, Arthur W., 1973, Vibration of Shells, NASA, pp. 31-157.

Liang, C., F. P. Sun and C. A. Rogers, "Dynamic Output Characteristics of Piezoceramic Actuators", Smart Structures and Materials '93, SPIE, Albuquerque, NM, 1993a.

Liang, C., F. P. Sun and C. A. Rogers, "An Impedance Method for Dynamic Analysis of Active Material Systems", 34th SDM Conference, La Jolla, CA, 1993b.

Piezo System, In., Piezoelectric Motor/Actuator Kit Manual, 1991.

Rossi, Anna, C. Liang and C. A. Rogers, "Coupled Electric-Mechanical Analysis of a Piezoceramic Actuator Driven System An Application to a Circular Ring", 34th SDM Conference, La Jolla, CA, 1993.

Soedel, W., 1981, Vibrations of shells and Plates, Marcel Dekker Inc., New York, pp. 199-228, and pp. 248-260.

Wang, B. T. and C. A. Rogers, 1990, "Laminate Plate Theory for Spatially Distributed Induced Strain Actuators", Fifth Japan U. S. Conference on Composite Materials, Tama City, Japan.

Zhou, Suwei, C. Liang and C. A. Rogers, "Impedance Modeling of Two-Dimensional Piezoelectric Actuators Bonded on a Cylinder", Proceedings of the Adaptive Structures and Material Systems, ASME Winter Annual Meeting, New Orleans, LA, pp247-256, 1993.

Zhou, Suwei, C. Liang and C. A. Rogers, "An Electro-Mechanical Impedance Analysis to Predict Power Consumption of Piezoelectric Actuators Integrated with Thin Plates", accepted by AIAA/ASME/ASCE/AHS/ASC 35th SDM and Adaptive Structures '94, Hilton Head, SC, 1994.

Impedance-Based Modeling of Actuators Bonded to Shell Structures

F. LALANDE, Z. CHAUDHRY AND C. A. ROGERS*

Center for Intelligent Material Systems and Structures

Virginia Polytechnic Institute and State University

Blacksburg, Virginia 24061-0261

ABSTRACT: When discrete piezoelectric actuator patches bonded on structures are used for active shape, vibration, and acoustic control, the desired deformation field in the structure is obtained through the application of localized line forces and moments generated by expanding or contracting bonded piezoelectric actuators. An impedance-based model to predict the dynamic response of cylindrical shells subjected to excitation from surface-bonded induced strain actuators is presented. The essence of the impedance approach is to match the actuator impedance with the structural impedance at the ends of the actuators, which will retain the dynamic characteristics of the actuators. A detailed derivation of the actuator and structural impedance is included. It is found that the actuator's output dynamic force in the axial and tangential direction are not equal. Various case studies of a cylindrical thin shell are performed to illustrate the capabilities of the developed impedance model. Out-of-phase actuation is shown to be the most efficient in exciting the lower order bending modes of shell structures. The paper is concluded with a finite element analysis verification of the derived impedance model.

INTRODUCTION

In any mechanical system with moving parts, special attention must be given to reducing vibrations and accompanying noise. If the system cannot be balanced or is subjected to random vibrations, passive or active control of the structure can be considered to reduce vibrations. One way to perform active control is to use shaker type actuators, but this involves many moving parts external to the base structure. By fully integrating the vibration control components within the base structure, self equilibrium of the complete system is insured and simplifies the overall design of the mechanical system. Piezoelectric (PZT), and other induced strain actuators are one type of actuators which can be easily integrated in the structure. When PZT patches are bonded or embedded in the structure, they apply forces or moments which are concentrated at the edges of the actuator. Using those forces and moments on the structure, the vibrations can be reduced by modifying the apparent structural impedance.

The piezoelectric actuators are often used in pairs, bonded on opposite sides of the structure. By controlling the voltage applied on each actuator it is possible to drive the actuators in-phase (both actuators expanding or contracting together), which creates an extensional deformation of the middle surface or out-of-phase (one actuator expands while the other contracts), which creates bending deformation of the middle surface. In between these two extreme cases,

unequal voltage application will create a combination of bending and extension. An actuator bonded only on one side of the structure is the most common case of unsymmetric actuation. Out-of-phase and in-phase actuation will have a different impact on the vibrational response of the structure, out-of-phase actuation being more suitable for exciting the structural bending modes and in-phase being more suitable extensional modes (Lalande et al., 1995a).

A number of theoretical models have been proposed for out-of-phase actuation of beams (Crawley and de Luis, 1987; Crawley and Anderson, 1990; Wang and Rogers, 1991; Dimitriadis et al., 1989) and plates (Crawley and Lazarus, 1989; Crawley et al., 1988). Other models based on the layered shell theory have also been proposed (Tzou and Gadre, 1989; Jia and Rogers, 1990). For shells actuated with discrete actuator patches, plate models were adapted to shells (Sonti and Jones, 1991; Lester and Lefebvre, 1991) and other models directly based on the shell governing equations (Sonti and Jones, 1993; Larson and Vinson, 1993; Lalande et al., 1994a). In all of these models, the actuator output force is computed from static considerations (i.e., local actuator/structural geometric and material properties) and, for vibrational control, the static fixed amplitude actuator forces are simply applied over the whole frequency range of interest.

Impedance models based on the dynamic properties of the actuators and the structure have also been proposed. The essence of the impedance approach is to match the actuator impedance to the structural impedance along the edges of the actuators. Impedance models for out-of-phase actuation

*Author to whom correspondence should be addressed.

have been derived for beams (Liang et al., 1993), plates (Zhou et al., 1994), rings (Rossi et al., 1993; Lalande et al., 1994b), and shells (Zhou et al., 1993). An impedance model for in-phase actuation of rings has also been proposed (Lalande et al., 1994c).

Even though unsymmetrical actuation can be represented with simple linear superposition of in-phase and out-of-phase actuation (Lalande et al., 1994c), no model for such unsymmetrical actuation has been presented yet. In this paper, an impedance-based model of two-dimensional shells subjected to in-phase, out-of-phase, and unsymmetrical actuation is proposed.

IMPEDANCE MODEL DERIVATION

An impedance-based model for a simply supported thin cylindrical shell excited with piezoelectric actuator(s) is derived (Figure 1). The impedance model is derived in four major steps: (1) calculation of the structural impedance at the edges of the actuators using the shell governing equations and the appropriate boundary conditions; (2) calculation of the actuator impedance; (3) calculation of the actuator output force based on the structural and actuator impedances interaction; and (4) application of frequency-dependent the actuator output forces to the shell governing equations previously used to obtain the shell response.

The assumptions used in the following derivation are a perfect bonding of the actuators to the structure, a constant stress distribution through the thickness of the actuators, and a thin shell. Based on these assumptions, the linear Love-Kirchoff shell theory is used. In view of the mechanics through which the forces from the actuator are transferred to the sub-structure, the actuator patches are replaced by discrete line forces and moments along the edges of the footprint of the actuators (Crawley and de Luis, 1987).

The pair of piezoelectric actuators can be excited independently if the substructure is not used as a ground and electrical insulation between the actuators and the structure is introduced (Figure 2). This type of bonding allows the pair of actuators to be excited in-phase, out-of-phase, one actuator alone, or unsymmetrically.

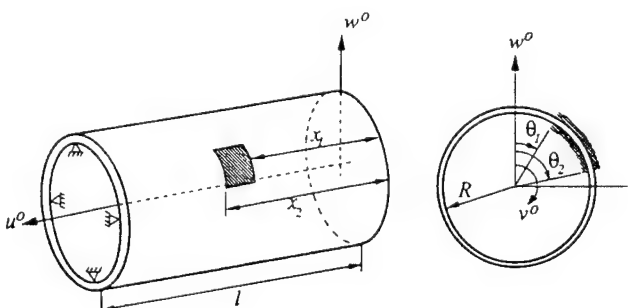


Figure 1. Simply supported thin shell with surface bonded actuators.

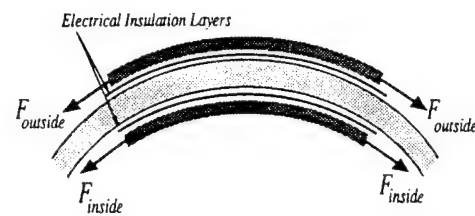


Figure 2. Unsymmetric actuation created by electrically insulating the actuators from the structure.

The superposition of the in-phase and out-of-phase actuation structural responses will be used to predict the response due to unsymmetrical actuation. It was shown in Lalande et al. (1994c) that any unsymmetrical actuation can be expressed as a linear combination of pure in-phase actuation and pure out-of-phase actuation. The appropriate weighting factors for in-phase (ξ^i) and out-of-phase (ξ^o), which are based on the free induced strains (Λ) applied on each actuators, are:

$$\xi^i = \frac{\Lambda_{\text{inside}} + \Lambda_{\text{outside}}}{2\Lambda_{\max}} \quad (1a)$$

$$\xi^o = \frac{-\Lambda_{\text{inside}} + \Lambda_{\text{outside}}}{2\Lambda_{\max}} \quad (1b)$$

where Λ_{\max} is the largest of the inside or outside actuator free induced strain. Based on this definition, the free induced strain ratios ξ^i and ξ^o will vary from $-1/2$ to 1 , $\xi^o = 1$ being pure out-of-phase and $\xi^i = 1$ being pure in-phase. The ξ ratios are dependent only on the free induced strain, assuming identical actuators are bonded on both sides of the shell. For cases where the actuators do not have the same thicknesses, the equation derivation becomes more complicated due to different actuator impedances. However, a simple superposition of the structural response to actuators bonded on the inside and on the outside of the shell can still be used to predict the dynamic response using this method.

Determination of the Structural Impedance

The dynamic response of structures can be described through its impedance or admittance. The structural admittance, which is simply the inverse of the impedance, and is defined based on the velocity response of the cylinder at the edges of the piezoelectric actuator, both in the x and the θ directions. Making use of linear superposition, the admittance definition [Equation (2)] has been separated into two parts: pure in-phase actuation admittance and pure out-of-phase actuation admittance. H_{xx} and $H_{\theta\theta}$ are the direct admittances which directly couple the forces in the x and θ directions, while $H_{x\theta}$ and $H_{\theta x}$ are the cross admittances which couple the input forces in the x and θ directions to the response in the θ and x directions, respectively. In the case of one-dimensional structures, the coupling disappears and the

admittance definition simplifies to a single term instead of the 2×2 matrix involved for two dimensional structures.

$$\begin{aligned} & \left(2\dot{u}^o|_{Inphase} - \frac{(t_s + t_a)^2}{2} \frac{\partial \dot{w}^o}{\partial x} \Big|_{Outphase} \right) \Big|_{x=x_2} \\ & - \left(2\dot{u}^o|_{Inphase} - \frac{(t_s + t_a)^2}{2} \frac{\partial \dot{w}^o}{\partial x} \Big|_{Outphase} \right) \Big|_{x=x_1} \\ & = -(H_{xx}F_x + H_{\theta\theta}F_\theta) \end{aligned} \quad (2a)$$

$$\begin{aligned} & \left(2\dot{v}^o|_{Inphase} - \frac{(t_s + t_a)^2}{2} \frac{\partial \dot{w}^o}{\partial R\partial\theta} \Big|_{Outphase} \right) \Big|_{\theta=\theta_2} \\ & - \left(2\dot{v}^o|_{Inphase} - \frac{(t_s + t_a)^2}{2} \frac{\partial \dot{w}^o}{\partial R\partial\theta} \Big|_{Outphase} \right) \Big|_{\theta=\theta_1} \\ & = -(H_{x\theta}F_x + H_{\theta\theta}F_\theta) \end{aligned} \quad (2b)$$

where u^o , v^o and w^o are the axial, tangential, and radial midplane displacements, respectively. t is the thickness and subscripts a and s stand for actuator and shell, respectively, and R is the radius of the shell. F_x and F_θ are the actuator output forces in the x and θ directions. In Equation (2), the minus sign on the right hand side is necessary to indicate that the actuator output forces are equal and opposite to the structural reactions.

The first step of the impedance approach is to calculate the structural impedance of the cylinder, which will be dependent on the actuator's location, the boundary conditions, and the physical properties of the shell. The structural impedance calculations will be based on the modal expansion method. This method is numerically efficient and accurate when the natural modes are available, which is the case for a simply supported shell. The Rayleigh-Ritz method can be used for more complex shell boundary conditions. Using the thin shell theory of a circular cylinder, the equations of motion including the actuator induced forces and moments are (Soedel, 1981):

$$L_1(u^o, v^o, w^o) - \varrho_s t_s \ddot{u}^o = \frac{\partial n_x}{\partial x} \quad (3a)$$

$$L_2(u^o, v^o, w^o) - \varrho_s t_s \ddot{v}^o = \frac{\partial n_\theta}{\partial R\partial\theta} + \frac{\partial m_\theta}{R^2\partial\theta^2} \quad (3b)$$

$$L_3(u^o, v^o, w^o) - \varrho_s t_s \ddot{w}^o = -\frac{n_\theta}{R} + \frac{\partial^2 m_x}{\partial x^2} + \frac{\partial^2 m_\theta}{R^2\partial\theta^2} \quad (3c)$$

where the induced uniform tangential and axial forces can be written using Heaviside functions:

$$n_x = N_x[H(x - x_1) - H(x - x_2)][H(\theta - \theta_1) - H(\theta - \theta_2)] \quad (4a)$$

$$n_\theta = N_\theta[H(x - x_1) - H(x - x_2)][H(\theta - \theta_1) - H(\theta - \theta_2)] \quad (4b)$$

with an in-phase force magnitude of:

$$N_x = 2F_x\xi^i \quad (5a)$$

$$N_\theta = 2F_\theta\xi^i \quad (5b)$$

and where the induced uniform tangential and axial moments can also be written using Heaviside functions:

$$m_x = M_x[H(x - x_1) - H(x - x_2)][H(\theta - \theta_1) - H(\theta - \theta_2)] \quad (6a)$$

$$m_\theta = M_\theta[H(x - x_1) - H(x - x_2)][H(\theta - \theta_1) - H(\theta - \theta_2)] \quad (6b)$$

with an out-of-phase moment magnitude of:

$$M_x = (t_a + t_s)F_x\xi^o \quad (7a)$$

$$M_\theta = (t_a + t_s)F_\theta\xi^o \quad (7b)$$

In the solution of the structural impedance, the actuators forces are transferred to the midplane of the structure, and the actuators are removed from the structure. It is noted that, at this stage, the actuator output forces F_x and F_θ are still unknown. For a general unsymmetric actuation, the shell will be subjected both to in-plane forces [Equations (4-5)] and out-of-plane moments [Equations (6-7)] on the edges of the actuators (Figure 3).

Using the modal expansion method, the forced response of the shell is expressed with the following series (Soedel, 1981):

$$u_i(x, \theta, t) = \sum_k p_k U_{ik}(x, \theta) e^{i\omega t} \quad (8)$$

where p_k is the modal participation factor. For a simply supported cylindrical shell, the axial, tangential, and radial dis-

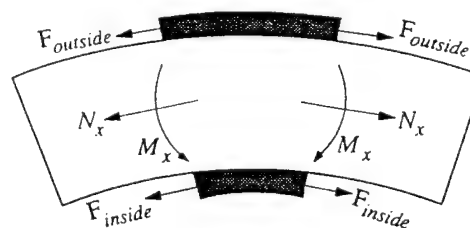


Figure 3. Transfer of the actuator's forces to the shell midplane.

placements are assumed to be under harmonic loading and may be expressed as:

$$U_{ik} = U_{mnp} = A_{mnp} \cos \alpha x \sin n\theta \quad (9a)$$

$$U_{2k} = V_{mnp} = B_{mnp} \sin \alpha x \sin n\theta \quad (9b)$$

$$U_{3k} = W_{mnp} = C_{mnp} \sin \alpha x \cos n\theta \quad (9c)$$

where $\alpha = m\pi/l$. The subscript p refers to the bending, torsional and extensional modes. Based on the eigenvalue analysis of the system, the Love operators $L_i(u^o, v^o, w^o)$ are obtained, as well as the natural frequencies ω_{mnp} and the displacement ratios A_{mnp}/C_{mnp} and B_{mnp}/C_{mnp} (Soedel, 1981).

$$L_i(u^o, v^o, w^o) = -\rho_s t_s \omega_k^2 U_{ik} \quad (10)$$

Substituting Equation (10) in Equation (3), the modal expansion method yields:

$$\ddot{p}_k + \omega_k^2 p_k = F_k e^{i\omega t} \quad (11)$$

with the forcing function F_k :

$$F_k = F_{mnp} = \frac{1}{\rho_s t_s N_{mnp}} \int_0^{2\pi} \int_0^l \left[\left(\frac{\partial n_x}{\partial x} \right) U_{mnp} \right. \\ \left. + \left(\frac{\partial n_\theta}{R \partial \theta} + \frac{\partial m_\theta}{R^2 \partial \theta} \right) V_{mnp} \right. \\ \left. + \left(-\frac{n_\theta}{R} + \frac{\partial^2 m_x}{\partial x^2} + \frac{\partial^2 m_\theta}{R^2 \partial \theta^2} \right) W_{mnp} \right] R d\theta dx \quad (12)$$

where

$$N_{mnp} = C_{mnp}^2 N_{mnp}^* = \int_0^{2\pi} \int_0^l [U_{mnp}^2 + V_{mnp}^2 + W_{mnp}^2] R d\theta dx \quad (13)$$

Solving Equation (11), the modal participation factor is

$$p_k = \frac{F_k}{\omega_k^2 - \omega^2} \quad (14)$$

At this point, the forced response of the shell under steady state excitation is determined as:

$$u^o(x, \theta, t) = \sum_{p=1}^3 \sum_{m=1} \sum_{n=1} \times \{ \vartheta A_{mnp}/C_{mnp} (S_\theta \cos n\theta - C_\theta \sin n\theta) \cos \alpha x \} e^{i\omega t} \quad (15a)$$

$$v^o(x, \theta, t) = \sum_{p=1}^3 \sum_{m=1} \sum_{n=1}$$

$$\times \{ \vartheta B_{mnp}/C_{mnp} (S_\theta \sin n\theta + C_\theta \cos n\theta) \sin \alpha x \} e^{i\omega t} \quad (15b)$$

$$w^o(x, \theta, t) = \sum_{p=1}^3 \sum_{m=1} \sum_{n=1}$$

$$\times \{ \vartheta [S_\theta \cos n\theta - C_\theta \sin n\theta] \sin \alpha x \} e^{i\omega t} \quad (15c)$$

where

$$\vartheta = \frac{R}{\rho_s t_s N_{mnp}^* (\omega_{mnp}^2 - \omega^2)} \left[-\frac{A_{mnp}}{C_{mnp}} (N_x) + \frac{B_{mnp}}{C_{mnp}} \right. \\ \left. \times \left(\frac{N_\theta}{R\alpha} + \frac{M_\theta}{R^2\alpha} \right) + \left(\frac{N_\theta}{R\alpha n} + \frac{M_x\alpha}{n} + \frac{M_\theta n}{R^2\alpha} \right) \right] \quad (16a)$$

$$S_\theta = \sin n\theta_1 - \sin n\theta_2 \quad (16b)$$

$$C_\theta = \cos n\theta_1 - \cos n\theta_2 \quad (16c)$$

Based on the admittance definition [Equation (2)], the direct structural admittances are:

$$H_{xx} = \frac{1}{R_a} \sum_{p=1}^3 \sum_{m=1} \sum_{n=1} \left\{ \left(\frac{\chi_{in}(A_{mnp}/C_{mnp})^2}{n} + \frac{\chi_{out}\alpha^2}{n} \right) \right. \\ \left. \times (S_\theta \cos n\theta_o - C_\theta \sin n\theta_o) C_x \right\} \quad (17a)$$

$$H_{\theta\theta} = \frac{1}{l_a} \sum_{p=1}^3 \sum_{m=1} \sum_{n=1} \left\{ \left(\frac{-\chi_{in}(1 + nB_{mnp}/C_{mnp})(B_{mnp}/C_{mnp})}{R\alpha n} \right. \right. \\ \left. \left. + \frac{\chi_{out}n(n + B_{mnp}/C_{mnp})}{R^3\alpha} \right) (S_\theta^2 + C_\theta^2) \sin \alpha x_o \right\} \quad (17b)$$

and the cross admittances are:

$$H_{\theta x} = \frac{1}{l_a} \sum_{p=1}^3 \sum_{m=1} \sum_{n=1} \left\{ \left(\frac{-\chi_{in}(1 + n)(A_{mnp}/C_{mnp})(B_{mnp}/C_{mnp})}{R\alpha n} \right. \right. \\ \left. \left. + \frac{\chi_{out}(n + B_{mnp}/C_{mnp})}{R^2} \right) (S_\theta \cos n\theta_o - C_\theta \sin n\theta_o) C_x \right\} \quad (18a)$$

20

$$H_{x\theta} = \frac{1}{R_a} \sum_{p=1}^3 \sum_{m=1}^M \sum_{n=1}^N \left\{ \left(\frac{\chi_{in}(A_{mnp}/C_{mnp})(B_{mnp}/C_{mnp})}{n} + \frac{\chi_{out}\alpha}{R} \right) \times (S_\theta^2 + C_\theta^2) \sin \alpha x_o \right\} \quad (18b)$$

where

$$\chi_{in} = -\frac{Ri\omega}{\rho_s t_s} \frac{2\xi^i}{N_{mnp}^*(\omega_{mnp}^2 - \omega^2)} \quad (19a)$$

$$\chi_{out} = -\frac{Ri\omega}{\rho_s t_s} \frac{(t_s + t_a)^2 \xi^o}{2N_{mnp}^*(\omega_{mnp}^2 - \omega^2)} C_x \quad (19b)$$

$$C_x = \cos \alpha x_1 - \cos \alpha x_2 \quad (19c)$$

and (x_o, θ_o) are the coordinates of the actuator center. $t_a = x_2 - x_1$ and $R_a = R(\theta_2 - \theta_1)$ are the actuator dimensions in the axial and tangential directions. Finally, the structural impedance along the actuator edges is obtained by inverting the admittance matrix:

$$\begin{bmatrix} Z_{xx} & Z_{x\theta} \\ Z_{\theta x} & Z_{\theta\theta} \end{bmatrix} = \begin{bmatrix} H_{xx} & H_{x\theta} \\ H_{\theta x} & H_{\theta\theta} \end{bmatrix}^{-1} \quad (20)$$

Determination of the Actuator Impedance

With the structural admittance now determined, the next step in the impedance approach is to calculate the actuator impedance and match it to the structural impedance. Making use of the isotropy of the actuator in the 1-1 and 2-2 plane and assuming a thin shell, the Love's equations of motion of the PZT actuator vibrating in the axial and tangential directions can be expressed as:

$$\rho_a \ddot{u}^o = Y_a^E \frac{\partial \epsilon_x}{\partial x} \quad (21a)$$

$$\rho_a \ddot{v}^o = Y_a^E \frac{\partial \epsilon_\theta}{R \partial \theta} \quad (21b)$$

where ρ_a is the PZT density and Y_a^E is the PZT complex Young's modulus at zero electrical field. The complex Young's modulus is used to include the piezoelectric material's damping.

Under thin shell assumption, the piezoelectric patch is thin with a large radius of curvature. If the actuator patch is small enough, the actuators can be assumed to be flat and the strain-displacement relations for flat structures can be used. This assumption allows us to decouple the radial displacement of the shell from the dynamics of the piezoelectric actuators, i.e.,

$$\begin{Bmatrix} \epsilon_x \\ \epsilon_\theta \end{Bmatrix} = \begin{Bmatrix} \frac{\partial u^o}{\partial x} \\ \frac{\partial v^o}{R \partial \theta} \end{Bmatrix} \quad (22)$$

Thus, the equations of motion in the axial and tangential directions for the PZT actuator are:

$$\rho_a \ddot{u}^o = Y_a^E \frac{\partial^2 u^o}{\partial x^2} \quad (23a)$$

$$\rho_a \ddot{v}^o = Y_a^E \frac{\partial^2 v^o}{R^2 \partial \theta^2} \quad (23b)$$

Assuming harmonic excitation by separating the displacements into time and spatial domains, the solution of the equations of motion will give the axial and tangential response of the actuator:

$$u^o(x, t) = [A \sin(kx) + B \cos(kx)] e^{i\omega t} \quad (24a)$$

$$v^o(\theta, t) = [C \sin(kR\theta) + D \cos(kR\theta)] e^{i\omega t} \quad (24b)$$

where ω is the input angular velocity and k is the wave number, which is given by:

$$k^2 = \omega^2 \frac{\rho_a}{Y_a^E} \quad (25)$$

The short-circuit direct input impedances of the piezoelectric actuators in the axial and tangential directions are respectively defined as:

$$Z_{ax} = \frac{Y_a^E t_a k R_a}{i\omega \tan(kl_a)} \quad (26a)$$

$$Z_{a\theta} = \frac{Y_a^E t_a k l_a}{i\omega \tan(kR_a)} \quad (26b)$$

and the short-circuit cross input impedances are:

$$Z_{ax\theta} = \frac{Y_a^E t_a k l_a}{i\omega \tan(kl_a)} \quad (27a)$$

$$Z_{a\theta x} = \frac{Y_a^E t_a k R_a}{i\omega \tan(kR_a)} \quad (27b)$$

Finally, the constitutive equations of the piezoelectric actuator:

$$\begin{Bmatrix} \epsilon_x \\ \epsilon_\theta \end{Bmatrix} = \begin{Bmatrix} \frac{\partial u^o}{\partial x} \\ \frac{\partial v^o}{R \partial \theta} \end{Bmatrix} = \begin{Bmatrix} \frac{1}{Y_a^E t_a R_a} & \frac{-\nu_a}{Y_a^E t_a l_a} \\ \frac{-\nu_a}{Y_a^E t_a R_a} & \frac{1}{Y_a^E t_a l_a} \end{Bmatrix} \begin{Bmatrix} F_x \\ F_\theta \end{Bmatrix} + \begin{Bmatrix} d_{31} \\ d_{32} \end{Bmatrix} E \quad (28)$$

where d_{3i} are the piezoelectric constants of the PZT actuators, E is the electrical field and ν_a is the actuator's Poisson's ratio.

Structural/Actuator Dynamic Interaction

With the structural and actuator impedances now determined, the third step in the impedance modeling is to consider the structural/actuator dynamic interaction (Figure 4). The interaction between the actuator is taken into account by the equilibrium and compatibility equations, which state the equilibrium of the forces between the actuator and the structure at the actuator edges. Applying the displacement boundary conditions ($u_{x=0} = 0, v_{\theta=0} = 0$) (Zhou et al., 1993) to Equation (28), B and D are found to be zero. The remaining unknowns A and C will be determined using the constitutive equations of the piezoelectric actuator [Equation (28)] at $x = l_a$ and $\theta = \theta_a$:

$$\begin{bmatrix} k \cos(kl_a) \left(1 - \nu_a \frac{Z_{x\theta}}{Z_{ax\theta}} + \frac{Z_{xx}}{Z_{axx}} \right) & k \cos(kl_a) \left(\frac{Z_{x\theta}}{Z_{ax\theta}} - \nu_a \frac{Z_{xx}}{Z_{axx}} \right) \\ k \cos(kR_a) \left(\frac{Z_{\theta z}}{Z_{a\theta z}} - \nu_a \frac{Z_{\theta\theta}}{Z_{a\theta\theta}} \right) & k \cos(kR_a) \left(1 - \nu_a \frac{Z_{\theta z}}{Z_{a\theta z}} + \frac{Z_{\theta\theta}}{Z_{a\theta\theta}} \right) \end{bmatrix} \begin{Bmatrix} A \\ C \end{Bmatrix} = \begin{Bmatrix} d_{31} \\ d_{32} \end{Bmatrix} E \quad (29)$$

Based on the impedance definition, the dynamic actuator forces output per unit length are:

$$F_x = -\frac{i\omega}{R_a} (A \sin(kl_a) Z_{xx} + C \sin(kR_a) Z_{x\theta}) e^{i\omega t} \quad (30a)$$

$$F_\theta = -\frac{i\omega}{l_a} (A \sin(kl_a) Z_{x\theta} + C \sin(kR_a) Z_{\theta\theta}) e^{i\omega t} \quad (30b)$$

Thus, the dynamic actuator force output has been calculated based on the structural impedance.

Shell Response Calculations

Using the dynamic actuator force output, the shell response can be calculated based on the shell governing equations developed above. The axial, tangential and radial displacements are given in Equation (15).

THEORETICAL RESULTS

The derived impedance model that was presented in Figure 1 will be applied to the thin cylinder, with dimensions and properties given in Table 1. The dimensions were chosen such that the shell is thin and the actuators are small enough not to increase the structural stiffness substantially. The shell is made of aluminum and G1195 piezoelectric actuator patches are used. Various case studies are presented, with a particular attention to pure out-of-phase and to pure in-phase actuation. For comparison purposes, all ac-

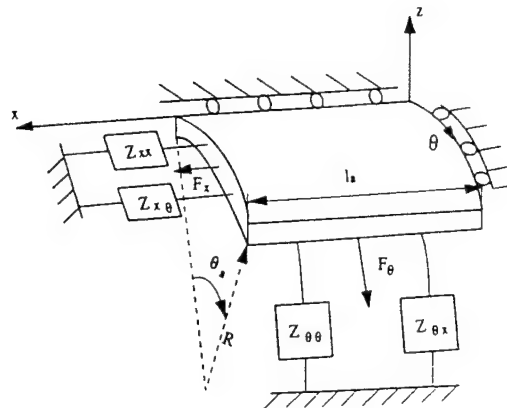


Figure 4. Dynamic interaction between the piezoelectric patch and the shell structure represented by mechanical impedance.

tutors are always excited with a free induced strain (Λ) of $\pm 1000 \mu\text{strain}$.

The structural admittance for in-phase actuation is shown in Figure 5. The four peaks corresponds to the first four natural frequencies of the shell, as expected. The reader's attention should be drawn to the cross admittances $H_{x\theta}$ and $H_{\theta x}$. In most cases, one can expect the cross admittances to be equal. However, it can be easily seen that the cross admittances are different both in shape and magnitude, having different antiresonant frequencies. This difference is due to the admittance definition that was used in Equation (2). In that equation, the admittance definition was based only on F_x and F_θ . However, if a special attention is given to the third equilibrium equation [Equation (3c)], one will notice the presence of the induced uniform tangential force n_θ . It was previously discussed that this loading term n_θ can be viewed as an external transverse pressure load, necessary to maintain the self equilibrium of the shell when actuated in-phase (Chaudhry et al., 1994). If viewed as such, the admittance definition is not only dependent on the forces F_x and F_θ , but also on the radial pressure term $-(n_\theta/R)$. Based on this observation, the admittance for pure in-phase actuation can be defined as a 3×3 matrix:

Table 1. Material and geometric properties of the PZT actuator and the aluminum shell.

	Aluminum Shell	PZT Actuator
Young's modulus, Pa	69×10^9	63×10^9
Density, kg/m ³	2700	7650
Poisson's ratio	0.3	0.3
Loss factor	0.006	0.001
Piezo coefficient d_{32} , m/V	N/A	-166×10^{-12}
Applied electric field, V/m	N/A	8.20×10^6
Length/radius, cm	10.65	10°
Width, cm	34	2
Thickness, mm	1.1	0.24

22

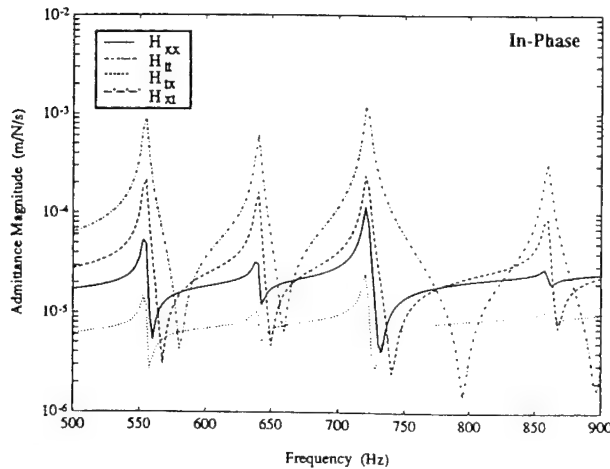


Figure 5. Structural admittance for in-phase actuation. Cross admittances are not equal when two dimensional admittance definition is used.

$$(2\dot{u}^o|_{Inphase})|_{x=x_2} - (2\dot{u}^o|_{Inphase})|_{x=x_1} = -[H_{xx}F_x + H_{\theta\theta}F_\theta + H_{rr}F_\theta^*] \quad (31a)$$

$$(2\dot{v}^o|_{Inphase})|_{\theta=\theta_2} - (2\dot{v}^o|_{Inphase})|_{\theta=\theta_1} = -[H_{x\theta}F_x + H_{\theta\theta}F_\theta + H_{r\theta}F_\theta^*] \quad (31b)$$

$$2 \int_{\theta_1}^{\theta_2} \dot{w} d\theta = -[H_{xx}F_x + H_{\theta\theta}F_\theta + H_{rr}F_\theta^*] \quad (31c)$$

where F_θ^* is the term resulting from radial pressure term. Using this definition, the cross admittances will all be exactly equal, as shown in Figure 6. However, for the purpose of the impedance modeling, it is necessary to lump the radial pressure term F_θ^* with the tangential force F_θ in the admittance definition. This is attributed to the close dependency between the two loads involving F_θ .

The structural admittance for out-of-phase actuation is shown in Figure 7. Once again, the cross admittances $H_{x\theta}$ and $H_{\theta x}$ are not exactly equal. This time, the difference is due to the transverse shear resultant that is included in the governing equations (Lalande et al., 1994b). If the shear stress resultant is omitted in the second governing equation, the cross admittances will become equal since the admittances will now have only one dependency on M_θ . For both in-phase and out-of-phase actuation, an increased shell radius will reduce the differences between the cross admittances; and for plates, the cross admittances will be exactly equal. Admittance graphs are not presented for unsymmetric voltages applied to the PZT actuators, since they will be a simple linear combination of the in-phase and out-of-phase admittances.

The in-plane forces created by the in-phase actuation of the piezoelectric patches are shown in Figure 8. In the im-

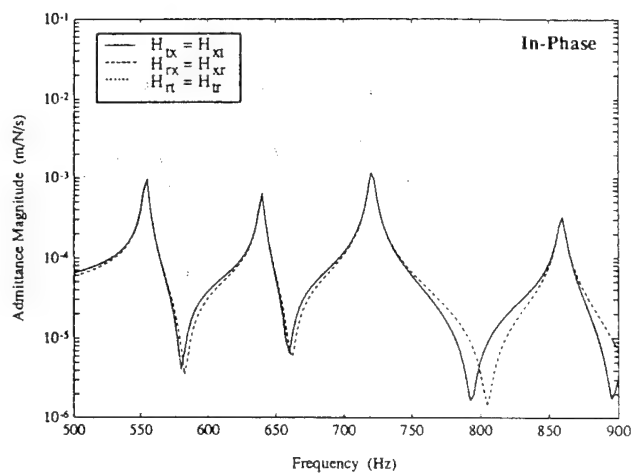


Figure 6. Structural cross admittances for in-phase actuation are equal when three dimensional admittance definition is used.

pedance technique, the force calculations are based on both the actuator and the structural impedances. In Figure 5, the direct admittance in the axial direction is different from the direct admittance in the tangential direction. Thus, if the admittances are different, the dynamic forces produced by the actuators should also be different in the axial and tangential directions. This can be observed in Figure 8. The dashed line is a static model previously developed (Wang and Rogers, 1991) agrees well with the impedance model for the force in the x direction only. However, when this static model or other static models are used, there is no distinction between the two directions and the actuator forces are thus mistakenly assumed to be equal. At the natural frequencies of the structure, the tangential equivalent force developed is larger than the axial equivalent force. This behavior is a simple characteristic of the system, the structural tangential admittance being smaller than the direct axial admittance.

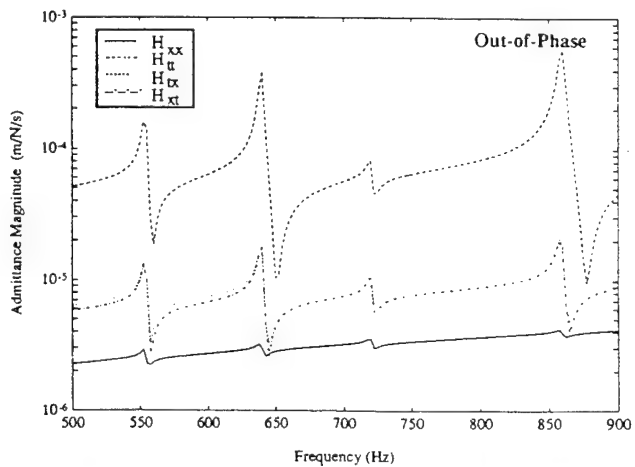


Figure 7. Structural admittance for out-of-phase actuation. Slight difference in the cross admittances due to the transverse shear stress included in the equations.

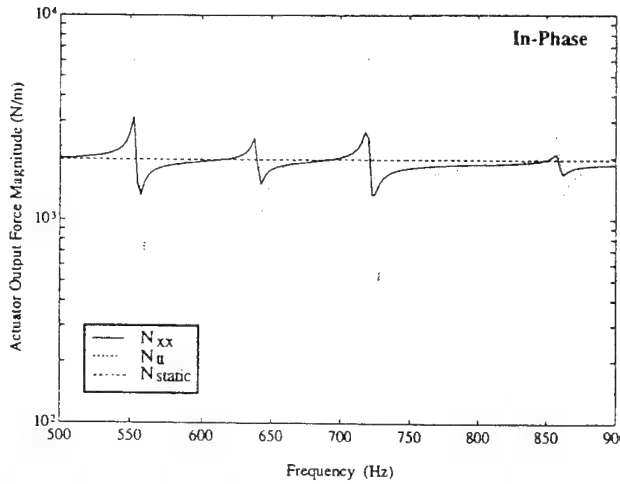


Figure 8. Dynamic equivalent forces produced by pure in-phase actuation on the structure are not equal in the axial and tangential directions.

The next figure (Figure 9) shows the dynamic equivalent moments produced by pure out-of-phase actuation. The conclusions are similar to those of in-phase actuation, and produced moments of different magnitude in the axial and tangential directions.

The radial displacement response to in-phase and out-of-phase dynamic actuation of the shell at ($x = 0.09, \theta = 90^\circ$) is presented in Figure 10. For comparison purposes, the shell response using static modeling (Wang and Rogers, 1991) is also presented. The most remarkable characteristic of Figure 10 is the greater authority of out-of-phase actuation when compared to in-phase actuation. The displacements produced by out-of-phase actuation are an order of magnitude larger than the displacements obtained from in-phase actuation. This behavior is predictable based on the admittances plots (Figures 5 and 6), since the shell has greater tangential impedance. Thin shells are more sensitive

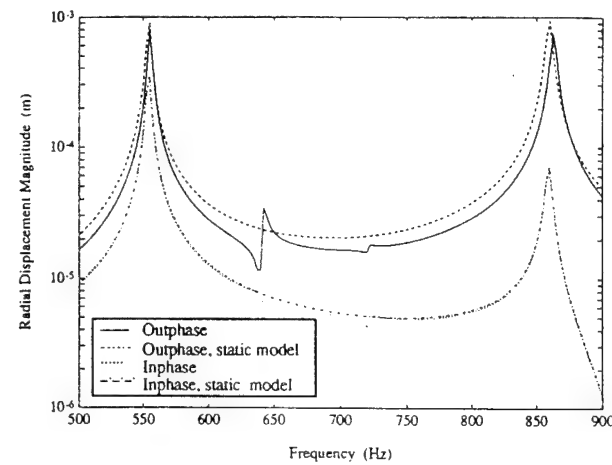


Figure 10. The comparison of the structural response between in-phase and out-of-phase actuation shows greater authority for out-of-phase actuation at ($x = 0.09, \theta = 90^\circ$).

to transverse loading (out-of-phase actuation) than to in-plane loading (in-phase actuation). The transverse natural modes are directly excited when out-of-phase actuation is used, while they are only excited through the in-plane/out-of-plane coupling property of shells when in-phase actuation is used. The resonant frequencies of the shell based on the impedance model are shifted to the right when compared to the resonant frequencies based on the static model. This behavior is due to the increased stiffness of the actuators on the host structure which is included in the impedance model, as opposed to the static model where the actuator stiffness is not included.

In Figure 11, the shell response to a single actuator bonded on the inside and on the outside of the shell at ($x = 0.09, \theta = 90^\circ$) is shown. Even though the shell is thin, the shell response is different. The finite element analysis that will be presented in the next section verifies this shell re-

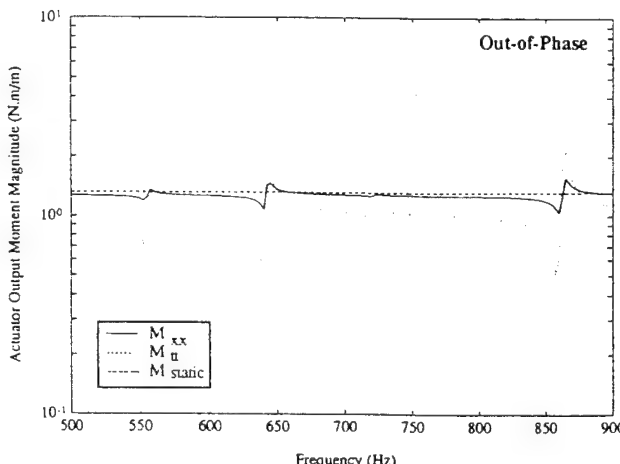


Figure 9. Dynamic equivalent moments produced by pure out-of-phase actuation on the structure are not equal in the axial and tangential directions.

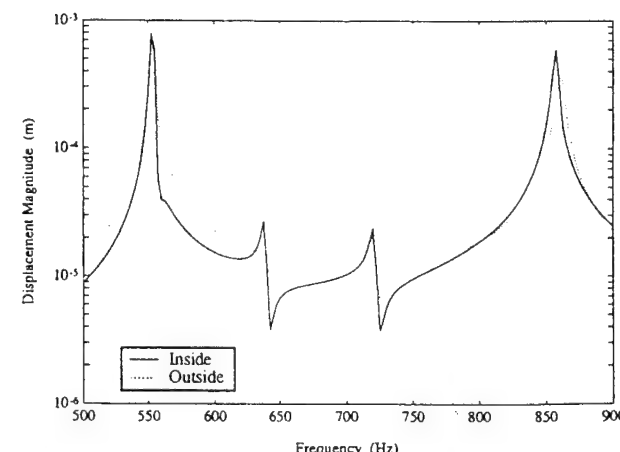


Figure 11. Even for thin shells, the structural response to single side actuation (inside and outside patches) is not equal at ($x = 0.09, \theta = 90^\circ$).

sponse, as well as the linear combination of pure in-phase and out-of-phase actuation [Equation (1)] concept to model unsymmetrical actuation. Thus, special considerations should be taken when single sided actuation is used.

A number of other cases were simulated using the impedance model, but only the most relevant information obtained from them will be discussed. Firstly, the stiffness of the actuator has an important impact on the behavior of the system. A thicker actuator will produce higher forces on the host structure, but it will also be more difficult to model the shell response due to the increased non-uniformity of the host structure. Changing the type of actuation material also changes the stiffness of the actuator, e.g., PVDF has a smaller Young's modulus than piezoceramic material, and thus will have a lesser authority on the structure. The size of the actuator patches bonded on the structure also needs to be considered when designing such structures. Another design parameter is the location of the actuator patch on the structure: the mechanical impedance of the structure is dependent on the actuator location and will thus affect the dynamic forces produced by the actuators. At a particular location, the actuator patches will be efficient in exciting some resonant frequencies, while another location will be more efficient at exciting other resonant frequencies. Many cases using different shell and actuator dimensions were considered and all showed better authority when out-of-phase actuation is used.

FINITE ELEMENT VERIFICATION

To verify the derived impedance model, a finite element analysis of the case study presented in the previous section was carried out. Making use of symmetry, the finite element model consists of only one quarter of the shell, and uses thin shell elements. The actuator patches are also modeled with thin shell elements, and are connected to the shell structure with rigid elements. The finite element analysis will only

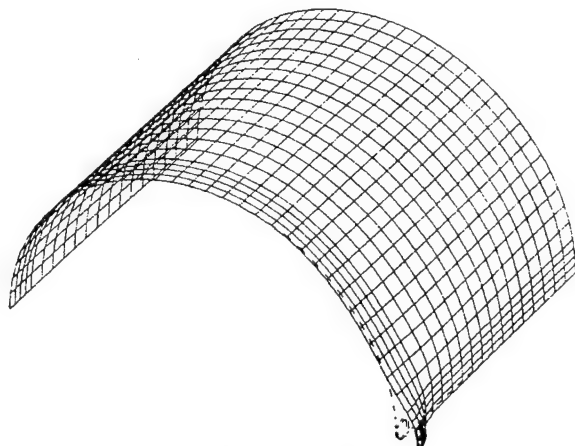


Figure 12. Structural response to static in-phase actuation based on finite element analysis.

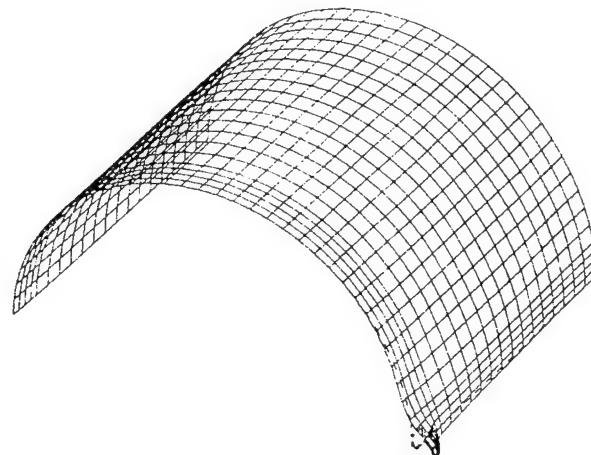


Figure 13. Structural response to static out-of-phase actuation based on finite element analysis.

consider static actuation and will be compared to the impedance model with an excitation frequency of 5 Hz, which is well below the first natural frequency of the shell. This model does not make any assumption on the actuator stiffness or mass. Three different types of loading on the finite element model were considered. Firstly, thermal contraction and/or expansion of the actuators is used to simulate in-phase or out-of-phase actuation. The deformed shapes of the shell under such actuation are presented in Figures 12 and 13.

The second loading type use line forces and moments, and uniform pressures applied on the elements modeling the shell structure leaving the actuators elements in the model to include their stiffness. The magnitudes of the forces and moments are based on the actuators free expansion and are given by (Chaudhry et al., 1994):

$$N_A = 2 \frac{Y_a^E t_a}{1 - \nu} d_{32} E \quad (32a)$$

$$M_A = (t_s + t_a) \frac{Y_a^E t_a}{1 - \nu} d_{32} E \quad (32b)$$

The displacements obtained by this second model matches almost exactly the displacements from the thermal loading case, and is thus the appropriate way to apply the loading when the actuators are left on the structure. Finally, the third type of loading also use line forces and moments and uniform pressures applied on the elements modeling the shell structure, but the actuator elements are removed from the model, leaving a uniform structural stiffness. However, for this case the magnitudes of the forces and moments are based on the continuity of the strains at the interface of the shell and the actuators, which is often referred to as the Euler-Bernoulli model, and are given by (Chaudhry et al., 1994):

$$N_{eq} = \frac{Y_s t_s}{1 - \nu} \frac{2}{2 + \psi} d_{32} E \quad (33a)$$

25

$$M_{eq} = (t_s + t_a) \frac{Y_s t_s}{1 - \nu} \frac{1}{6 + \psi + \frac{12}{T} + \frac{8}{T^2}} d_{32} E \quad (33b)$$

where T is the thickness ratio t_s/t_a . The deformed shape based on this loading is the same as the two previous cases, but differs in magnitude. This magnitude difference comes from the assumptions made in the derivation of the equivalent forces and moments applied to the shell. In the equation derivation, the boundary conditions are assumed to be free. When shells are considered, the structure is a closed body and does not have free boundary conditions, since stresses will be present in the whole shell. The same phenomena occurs for simpler structures such as beams (Chaudhry and Rogers, 1993). When the beam is simply supported, the boundary conditions will be free and the equivalent loading based on the Euler-Bernoulli method will give accurate results. If the boundary conditions are changed to clamped, the assumed stress free boundary condition in the equation derivation is no longer valid and will produce errors in the magnitude of the structural displacements. In Figures 14 and 15, the displacements of the shell at $x = 0.09$ based on the two loading types are presented. It can be easily seen from the displacements that the deformed shape is similar, but differs in the magnitude.

The final step in this paper is to directly compare the impedance model at 5 Hz with the static finite element model. For both in-phase and out-of-phase actuation, the radial displacements based on the impedance model match the finite element results in shape, but not in magnitude (Figures 14 and 15). In the impedance modeling, the actuator stiffness is included in the calculations of the actuator forces output. At that point of the modeling, no assumptions have been made either on the mass or the stiffness of the actuators. When the displacements are calculated using the dynamic actuator forces, the displacement equations [Equation (15)] are based

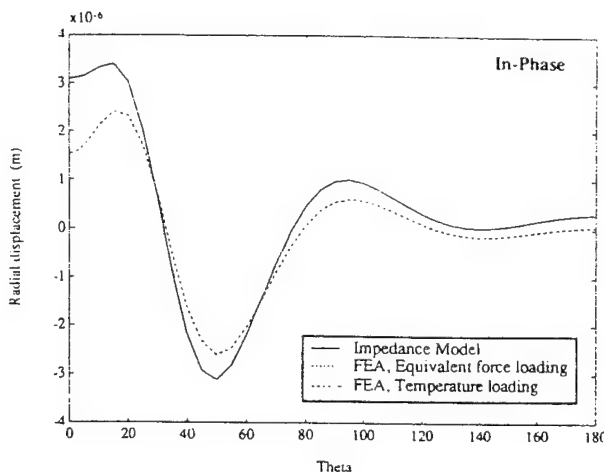


Figure 14. Comparison of the displacements of the static finite element model and the impedance model at 5 Hz for in-phase actuation at $x = 0.09$.

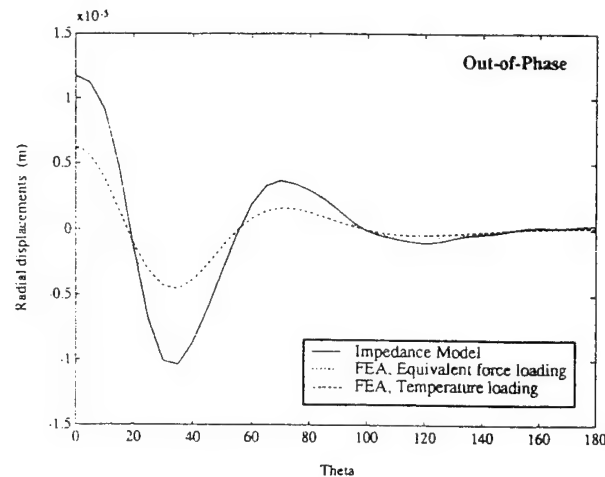


Figure 15. Comparison of the displacements of the static finite element model and the impedance model at 5 Hz for out-of-phase actuation at $x = 0.09$.

on a uniform shell stiffness, not including the increased mass or stiffness due to the actuators. Neglecting the actuator stiffness will reduce the stiffness of the integrated system, and thus produce larger impedance model displacements seen in the last two figures. The discrepancies between the impedance model and the finite element analysis will reduce with decreasing actuator size and thickness.

CONCLUSIONS

In this paper, an impedance-based model to predict the dynamic response of cylindrical shells subjected to excitation from surface-bonded induced strain actuators was presented. The strength of the impedance model over the conventional static approach is the inclusion of the dynamic interaction between the induced strain actuators and the host structure. In its derivation, the impedance model includes the actuator mass and stiffness for a more accurate representation of the actual system. The impedance model also considers the different shell stiffnesses in the axial and tangential directions. Doing so, it was found that the actuators' dynamic forces in the axial and tangential direction are not equal and are frequency dependent. However, in the shell response calculations the actuator mass and stiffness are neglected to simplify the shell governing equations, and thus will over-predict the displacements. Out-of-phase actuation is shown to be more efficient than in-phase actuation in exciting the lower order bending modes of shell structures. The impedance-based model for low frequencies was validated by a static finite element analysis.

ACKNOWLEDGEMENTS

The authors would like to acknowledge the funding support of the Air Force Office of Scientific Research, Grant

AFOSR #F49620-93-1-0166, Dr. Walter F. Jones, program manager.

REFERENCES

- Chaudhry, Z., F. Lalande and C. A. Rogers. 1994. "Modeling of Induced Strain Actuator Patches", *Proceedings, SPIE Conference on Smart Structures and Materials*, Orlando, FL, Vol. 2190, SPIE Publishing, Bellingham, WA, pp. 563-570.
- Chaudhry, Z. and C. A. Rogers. 1993. "Performance and Optimization of Induced Strain Actuated Structures Under the Action of External Loads", *Proceedings, AIAA/ASME/ASCE/AHS/ASC 34th Structures, Structural Dynamics and Materials Conference*, La Jolla, CA, AIAA Publishing, Washington, D.C., pp. 3475-3484.
- Crawley, E. F. and E. H. Anderson. 1990. "Detailed Models of Piezoceramic Actuation of Beams", *Journal of Intell. Mater. Syst. and Struct.*, 1(1):4-25.
- Crawley, E. F. and J. de Luis. 1987. "Use of Piezoelectric Actuators as Elements of Intelligent Structures", *AIAA Journal*, 25(10):1373-1385.
- Crawley, E. F. and K. B. Lazarus. 1989. "Induced Strain Actuation of Isotropic and Anisotropic Plate", *AIAA Journal*, 29(6):944-951.
- Crawley, E. F., J. de Luis, N. W. Hagood and E. H. Anderson. 1988. "Development of Piezoelectric Technology for Applications in Control of Intelligent Structures", *Proceedings, The American Control Conference*, Atlanta, GA, June 1988, pp. 1890-1896.
- Dimitriadis, E. K., C. R. Fuller and C. A. Rogers. 1989. "Piezoelectric Actuators for Distributed Vibration Excitation of Thin Plates", *Journal of Vibration and Acoustics*, 111:100-107.
- Jia, J. and C. A. Rogers. 1990. "Formulation of a Laminated Shell Theory Incorporating Embedded Distributed Actuators", *Journal of Mechanical Design*, 112:596-604.
- Lalande, F., Z. Chaudhry and C. A. Rogers. 1994a. "Modeling Considerations for In-Phase Actuation of Actuators Bonded to Shell Structures", *Proceedings, AIAA/ASME/ASCE/AHS/ASC 35th Structures, Structural Dynamics and Materials Conference, Adaptive Structures Forum*, Hilton Head, SC, AIAA Publishing, Washington, DC, pp. 429-437.
- Lalande, F., Z. Chaudhry and C. A. Rogers. 1994b. "Comparison of Different Impedance-Based Models for Out-of-Phase Actuation of Actuators Bonded on Ring Structures", *Proceedings, Second International Conference on Intelligent Materials*, Williamsburg, VA, Technomic Publishing Company, Inc., Lancaster, PA, pp. 771-782.
- Lalande, F., Z. Chaudhry and C. A. Rogers. 1994c. "Impedance Modeling of In-Phase Actuation of Actuators Bonded on Ring Structures", *Proceedings, ASME Winter Annual Meeting, Adaptive Structures Forum*, Chicago, IL, AD-Vol. 45, ASME Technical Publishing, New York, NY, pp. 193-200.
- Lalande, F., Z. Chaudhry and C. A. Rogers. 1995. "Comparison of In-Phase and Out-of-Phase Induced Strain Actuation of Shells: An Experimental Verification", *Proceedings, AIAA/ASME/ASCE/AHS/ASC 36th Structures, Structural Dynamics and Materials Conference, Adaptive Structures Forum*, New Orleans, LA, AIAA Publishing, Washington, DC, in press.
- Larson, P. H. and J. R. Vinson. 1993. "The Use of Piezoelectric Materials in Curved Beams and Rings", *Proceedings, ASME Winter Annual Meeting Adaptive Structures Symposium*, New Orleans, LA, AD-Vol. 35, ASME Technical Publishing, New York, NY, pp. 277-286.
- Lester, H. C. and S. Lefebvre. 1991. "Piezoelectric Actuator Models for Active Vibration Control of Cylinders", *Proceedings, Recent Advances in Active Noise and Vibration Control*, Blacksburg, VA, Technomic Publishing Company, Inc., Lancaster, PA, 3:3-26.
- Liang, C., F. P. Sun and C. A. Rogers. 1993. "An Impedance Method for Dynamic Analysis of Active Material Systems", *Proceedings, AIAA/ASME/ASCE/AHS/ASC 34th Structures, Structural Dynamics and Materials Conference*, La Jolla, CA, AIAA Publishing, Washington, DC, pp. 3587-3599.
- Rossi, A., C. Liang and C. A. Rogers. 1993. "Impedance Modeling of Piezoelectric Actuator-Driven Systems: An Application to Cylindrical Ring Structures", *Proceedings, AIAA/ASME/ASCE/AHS/ASC 34th Structures, Structural Dynamics and Materials Conference*, La Jolla, CA, AIAA Publishing, Washington, DC, pp. 3618-3624.
- Soedel, W. 1981. *Vibrations of Plates and Shells*. New York: Marcel and Decker Inc.
- Sonti, V. R. and J. D. Jones. 1991. "Active Vibration Control of Thin Cylindrical Shells Using Piezoelectric Actuators", *Proceedings, Recent Advances in Active Noise and Vibration Control*, Blacksburg, VA, Technomic Publishing Company, Inc., Lancaster, PA, pp. 27-38.
- Sonti, V. R. and J. D. Jones. 1993. "Curved Piezo-Actuator Models for Active Vibration Control of Cylindrical Shells", *Proceedings, Meeting of the Acoustical Society of America*, Ottawa, Canada.
- Tzou, H. S. and M. Gadre. 1989. "Theoretical Analysis of a Multi-Layered Thin Shell Coupled with Piezoelectric Shell Actuators for Distributed Vibration Control", *Journal of Sound and Vibrations*, 132(3):433-450.
- Wang, B. T. and C. A. Rogers. 1991. "Modeling of Finite Length Spatially Distributed Induced Strain Actuators for Laminate Beams and Plates", *Journal of Intell. Mater. Syst. and Struct.*, 2(1):38-58.
- Zhou, S., C. Liang and C. A. Rogers. 1993. "Impedance Modeling of Two Dimensional Piezoelectric Actuators Bonded on a Cylinder", *Proceedings, ASME Winter Annual Meeting Adaptive Structures Symposium*, New Orleans, LA, AD-Vol. 35, ASME Technical Publishing, New York, NY, pp. 247-255.
- Zhou, S., C. Liang and C. A. Rogers. 1994. "A Dynamic Model of a Piezoelectric Actuator Driven Thin Plate", *Proceedings, SPIE Conference on Smart Structures and Materials*, Orlando, FL, Vol. 2190, SPIE Publishing, Bellingham, WA, pp. 550-562.

Power consumption and energy transfer mechanisms

Zhou, S.W., and Rogers, C.A., "Power Flow and Consumption in Piezoelectrically Actuated Structures," *AIAA Journal*, Vol. 33, No. 7, July 1995, pp. 1305-1311.

Power Flow and Consumption in Piezoelectrically Actuated Structures

Su-Wei Zhou* and Craig A. Rogers†

Virginia Polytechnic Institute and State University, Blacksburg, Virginia 24061

In a piezoelectric (PZT) actuator-driven adaptive structure, the electromechanical power consumption and power flow of the system are dominated by the complex electromechanical impedance of the system. The entire actuator/substrate system can essentially be represented by a coupled electromechanical system model. This paper presents such a system model to quantitatively determine where the energy goes and how the power is consumed in an active structure. The formulation of a coupled electromechanical admittance for a generic PZT actuator-driven two-dimensional structure was developed. The model was then used to predict the power factor, the power dissipation, and the power requirement of the system. As a numerical example, the modeling approach was applied to a simply supported thin plate excited by a pair of PZT path actuators in pure bending mode. A parametric study was performed to examine the nature and components of electromechanical power flow and consumption in the active structure. An experiment was conducted to directly measure the complex electromechanical admittance of an integrated PZT/plate system to verify the theoretical model.

Nomenclature

<i>a</i>	= length of structure
<i>b</i>	= width of structure
<i>d</i>	= piezoelectric constant
<i>E</i>	= electric field
<i>F</i>	= force output of piezoelectric actuator
<i>H</i>	= mechanical admittance
<i>h</i>	= thickness of structure
<i>I</i>	= current
<i>i</i>	= imaginary part of a complex number
<i>k</i>	= wave number
<i>P</i>	= dissipative power
<i>Q</i>	= reactive power
<i>t</i>	= time
<i>u</i>	= displacement in <i>x</i> direction
<i>V</i>	= voltage
<i>v</i>	= displacement in <i>y</i> direction
<i>S</i>	= Young's modulus
<i>Y</i>	= electromechanical admittance
<i>Z</i>	= mechanical impedance
<i>W</i>	= complex power
δ	= dielectric loss factor
ϵ	= strain
η	= structural loss factor
ν	= Poisson's ratio
ρ	= mass density
σ	= stress
ω	= angular frequency

Superscript

*	= complex parameter
---	---------------------

Subscripts

<i>p</i>	= parameters of piezoelectric actuator
<i>x</i>	= <i>x</i> direction
<i>y</i>	= <i>y</i> direction

0 = magnitude of electrical parameters
1, 2, 3 = piezoelectric material directions

Introduction

PIEZOELECTRIC (PZT) materials have been widely used as actuators and sensors in active structural vibration and acoustic control because of their compact size and good dynamic performance.¹⁻³ A great deal of effort has focused on the analysis and optimization of the mechanical performance of PZT transducers.¹⁻⁸ However, investigations of the power consumption and electrodynamics of PZT actuator-driven adaptive structures have been limited. There appears to be little in the literature on the topic of power relations for active structures. In fact, adaptive structures are complex electromechanical coupling systems in which electrical energy is converted into mechanical energy and vice versa. The ability and efficiency of the energy conversion of the actuators is always of concern in the design and application of active structures, especially for aerospace applications. Large and complex aerospace structures may require a great number of relatively large actuators, which will dictate large, expensive power supplies. Thus, minimizing the power consumption and enhancing the energy conversion efficiency of actuators will result in reductions in the cost and mass of the system, two of the major objectives in designing intelligent structures.⁹ To achieve this, it is highly desirable to explore the nature and components of electromechanical power flow and consumption in active structures.

Liang et al.¹⁰ suggested a coupled electromechanical analysis for a piezoelectric actuator-driven spring-mass-damper system and discussed the concepts of actuator power factor and energy transfer of the system. Lomenzo et al.¹¹ developed a technique to maximize mechanical power transfer from stacked PZT actuators to host structures. Hagood et al.² proposed a dynamic model to include the coupling between the actuator, structure, and electrical network. The model is based on a finite element analysis using the Rayleigh-Ritz energy formulation. However, his work does not discuss electromechanical power relations in active structures, and the actuator force loading is not explicitly expressed as a function of the input impedance of the actuator itself and the mechanical impedance of the host structure. A mechanical impedance model applicable to two-dimensional structures⁷⁻⁸ focused on quantifying the mechanical outputs of PZT actuators; and this model now needs to be extended to include system electrical parameters to analyze electromechanical power flow and consumption in PZT actuator-driven active structures.

Received Feb. 26, 1994; revision received Sept. 19, 1994; accepted for publication Sept. 20, 1994. Copyright © 1995 by the American Institute of Aeronautics and Astronautics, Inc. All rights reserved.

*Ph.D. Research Associate, Mechanical Engineering, Center for Intelligent Material Systems and Structures. Member AIAA.

†Professor and Director, Mechanical Engineering, Center for Intelligent Material Systems and Structures. Member AIAA.

The concept of energy conversion in a PZT actuator-driven system involves a two-step conversion: one is the energy transfer from the support power electronics to the integrated PZT/substrate mechanical system; the other is the energy conversion from the electrical energy of the PZT actuator to the mechanical energy driving the host structure. The focus of this current work is on the analysis of the second-step energy conversion, i.e., the electromechanical power consumption and power flow in PZT actuator-driven active structures. In this paper, the formulation of a coupled electromechanical admittance for generic two-dimensional PZT actuator-driven structures will be derived. The model will be used to analyze the components of the electromechanical power flow, and to determine the power consumption and energy conversion efficiency of an integrated PZT/plate system. A parametric study will examine the effects of different system elements on power dissipation and energy transfer, including the effects of damping and geometric parameters. An experiment on a simply supported thin plate using an impedance analyzer will be conducted so that the theoretical model can be validated.

Coupled Electromechanical System Model

A schematic of a two-dimensional PZT/substrate coupling system is shown in Fig. 1. The PZT element is used as an actuator to excite the host structure. It is assumed that the integrated system is linear, and the host structure is a generic two-dimensional structure. The host structural dynamics are represented by the direct impedance Z_{xx} and Z_{yy} , and the cross impedance Z_{xy} and Z_{yx} , as shown in Fig. 1. When a voltage is applied to the piezoelectric patches along the polarization direction (3), an in-plane strain is induced in the PZT actuator in both the $x(1)$ and $y(2)$ directions. This induced strain applies active forces (F_x and F_y) on the host structure. Thus, only the in-plane motion of the actuator is considered in the following development of formulations. Furthermore, it is assumed that the PZT material is isotropic, which results in $d_{31} = d_{32}$. The in-plane motion of the actuator is similar to an equivalent thermal expansion or contraction occurring in both x and y directions. The equation of motion of the PZT actuator, derived from Newton's law of motion and strain-displacement compatibility, may be

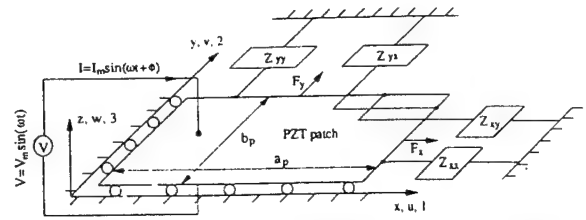


Fig. 1 Coupled electromechanical model of a two-dimensional integrated PZT/substrate system.

Applying the equivalent displacement boundary conditions $u_{x=0} = 0$ and $v_{y=0} = 0$, as shown in Fig. 1, to Eq. (3), the response of the PZT actuator is reduced to

$$u = A \sin(k_p x) e^{j\omega t} \quad (5a)$$

$$v = C \sin(k_p y) e^{j\omega t} \quad (5b)$$

The unknowns A and C may be evaluated from the constitutive equation of the PZT material at $x = a_p$ and $y = b_p$

$$\begin{pmatrix} \varepsilon_x \\ \varepsilon_y \end{pmatrix} = \begin{pmatrix} \frac{\partial u}{\partial x} \\ \frac{\partial v}{\partial y} \end{pmatrix} = \frac{1}{S_p^*} \begin{pmatrix} 1 & -v_p \\ -v_p & 1 \end{pmatrix} \begin{pmatrix} \sigma_x \\ \sigma_y \end{pmatrix} + \begin{pmatrix} d_{31} \\ d_{32} \end{pmatrix} E \quad (6)$$

where d_{31} and d_{32} are the piezoelectric constants of the PZT material in the 1 and 2 directions, respectively. The force outputs of the PZT actuator, F_x and F_y , are equal and opposite to the reactions of the host structure. The induced stress at the edge of the PZT patch $\sigma_{x(y)}$ may be expressed using the mechanical impedance of the host structure

$$\begin{pmatrix} \sigma_x \\ \sigma_y \end{pmatrix} = - \begin{pmatrix} 1/(b_p h_p) & 0 \\ 0 & 1/(a_p h_p) \end{pmatrix} \begin{pmatrix} Z_{xx} & Z_{xy} \\ Z_{yx} & Z_{yy} \end{pmatrix} \begin{pmatrix} \dot{u} \\ \dot{v} \end{pmatrix} \quad (7)$$

Substituting Eqs. (5) and (7) into Eq. (6) and taking the algebraic operation to rearrange A and C yields

$$\begin{bmatrix} k_p C_a \left(1 - v_p \frac{b_p Z_{yx}}{a_p Z_{pxx}} + \frac{Z_{xx}}{Z_{pxx}} \right) & k_p C_b \left(\frac{a_p Z_{xy}}{b_p Z_{pyy}} - v_p \frac{Z_{yy}}{Z_{pyy}} \right) \\ k_p C_a \left(\frac{b_p Z_{xy}}{a_p Z_{pxx}} - v_p \frac{Z_{xx}}{Z_{pxx}} \right) & k_p C_b \left(1 - v_p \frac{a_p Z_{yx}}{b_p Z_{pyy}} + \frac{Z_{yy}}{Z_{pyy}} \right) \end{bmatrix} \begin{pmatrix} A \\ C \end{pmatrix} = \begin{pmatrix} d_{31} \\ d_{32} \end{pmatrix} E \quad (8)$$

expressed by

$$\rho_p \frac{\partial^2 u}{\partial t^2} = S_p^* \frac{\partial^2 u}{\partial x^2} \quad (1a)$$

$$\rho_p \frac{\partial^2 v}{\partial t^2} = S_p^* \frac{\partial^2 v}{\partial y^2} \quad (1b)$$

where S_p^* is the Complex Young's modulus at a zero electrical field

$$S_p^* = S_p(1 + i\eta_p) \quad (2)$$

The sinusoidal time response of the PZT actuator can be solved from Eq. (1),

$$u = [A \sin(k_{p11} x) + B \cos(k_{p11} x)] e^{i\omega t} \quad (3a)$$

$$v = [C \sin(k_{p22} y) + D \cos(k_{p22} y)] e^{i\omega t} \quad (3b)$$

where A , B , C , and D are unknowns and can be determined by the boundary conditions; and the wave number is expressed by

$$k_p = k_{p11} = k_{p22} = \omega \sqrt{\rho_p / S_p^*} \quad (4)$$

where $C_a = \cos(k_p a_p)$ and $C_b = \cos(k_p b_p)$. Z_{pxx} and Z_{pyy} are the input mechanical impedance of the PZT actuator in the x and y directions, defined as

$$Z_{pxx} = \frac{F_x}{\dot{u}} = -i \frac{S_p^* h_p}{\omega} \frac{k_p b_p}{\tan(k_p a_p)} \quad (8a)$$

$$Z_{pyy} = \frac{F_y}{\dot{v}} = -i \frac{S_p^* h_p}{\omega} \frac{k_p a_p}{\tan(k_p b_p)} \quad (8b)$$

Solving the unknowns A and C from Eq. (8) leads to

$$\begin{pmatrix} A \\ C \end{pmatrix} = [M]^{-1} \begin{pmatrix} d_{31} \\ d_{32} \end{pmatrix} E \quad (9)$$

where $[M]$ is the coefficient matrix of A and C in Eq. (8). Substituting Eqs. (5) and (10) into Eq. (7), the dynamic stress output of the PZT actuator is then determined by

$$\begin{pmatrix} \sigma_x \\ \sigma_y \end{pmatrix} = \frac{S_p^* E}{1 - v_p^2} \begin{pmatrix} 1 & v_p \\ v_p & 1 \end{pmatrix} \left[k_p \begin{pmatrix} \cos(k_p x) & 0 \\ 0 & \cos(k_p y) \end{pmatrix} \times [M]^{-1} \begin{pmatrix} d_{31} \\ d_{32} \end{pmatrix} - \begin{pmatrix} d_{31} \\ d_{32} \end{pmatrix} \right] \quad (11)$$

The constitutive equation of the PZT material is again invoked in terms of the electrical displacement field D_3 in the $z(3)$ direction⁶

$$D_3 = \varepsilon_{33}^* E + d_{31}\sigma_x + d_{32}\sigma_y \quad (12)$$

where

$$\varepsilon_{33}^* = \varepsilon_{33}(1 - i\delta_p) \quad (13)$$

is the complex dielectric constant at a constant stress. Substituting Eq. (11) into Eq. (12) and letting $d_{32} = d_{31}$ yields the electrical displacement field

$$D_3 = E \left\{ \varepsilon_{33}^* + \frac{d_{31}^2 S_p^*}{1 - v_p} \left(k_p [\cos(k_p x) \cos(k_p y)] \right. \right. \\ \times [M]^{-1} \left(\begin{matrix} 1 \\ 1 \end{matrix} \right) - 2 \left. \right\} \quad (14)$$

where the applied electric field E can be expressed in terms of the applied voltage V

$$E = \frac{V}{h_p} = \frac{V_0}{h_p} e^{i\omega t} \quad (15)$$

The charge in the PZT patch can be obtained by integrating the displacement in Eq. (14) with respect to x and y

$$q = \int_0^{a_p} \int_0^{b_p} D_3 dx dy \quad (16)$$

The current is thus given by

$$I = I_0 e^{i\omega t} = \dot{q} \\ = i V_0 \omega \frac{a_p b_p}{h_p} \left\{ \varepsilon_{33}^* - \frac{2d_{31}^2 S_p^*}{1 - v_p} + \frac{d_{31}^2 S_p^*}{1 - v_p} \left[\frac{s_1}{a_p} \frac{s_2}{b_p} \right] \right. \\ \times [M]^{-1} \left(\begin{matrix} 1 \\ 1 \end{matrix} \right) \left. \right\} e^{i\omega t} \quad (17)$$

where $s_1 = \sin(k_p a_p)$ and $s_2 = \sin(k_p b_p)$. When the PZT actuator is driven by an active voltage V , the current in the circuit I is related to the driven voltage through the coupled electromechanical admittance, $Y^* = I/V$. Accordingly, rewriting Eq. (17) produces the coupled electromechanical admittance

$$Y^* = i \omega \frac{a_p b_p}{h_p} \left\{ \varepsilon_{33}^* - \frac{2d_{31}^2 S_p^*}{1 - v_p} + \frac{d_{31}^2 S_p^*}{1 - v_p} \right. \\ \times \left[\frac{s_1}{a_p} \frac{s_2}{b_p} \right] [M]^{-1} \left(\begin{matrix} 1 \\ 1 \end{matrix} \right) \left. \right\} \quad (18)$$

It is noted that the admittance Y^* represents the integrated electromechanical characteristics of a piezoelectric actuator-driven system, and it is frequency dependent. The complex admittance Y^* contains all of the parameters concerning the system electrodynamic performance, including mass, stiffness, damping, material and physical properties, electrical parameters, and boundary conditions. Once these parameters are selected, the admittance will be determined. The input structural impedance of the PZT actuator is given by Eq. (9). The mechanical impedance matrix of the host structure in Eq. (7) is determined by

$$Z = \begin{pmatrix} Z_{xx} & Z_{xy} \\ Z_{yx} & Z_{yy} \end{pmatrix} = \begin{pmatrix} H_{xx} & H_{yx} \\ H_{xy} & H_{yy} \end{pmatrix}^{-1} \quad (19)$$

where H_{xx} and H_{yy} are the direct mechanical admittances of the host structure at the edge of the PZT patches, and H_{xy} and H_{yx} are the cross mechanical admittances.

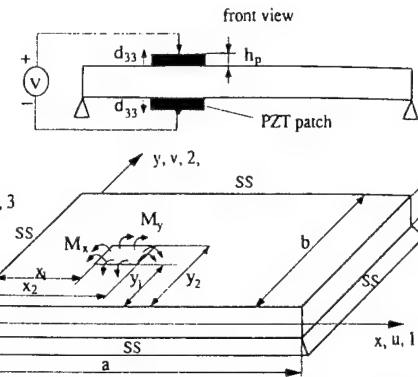


Fig. 2 Geometry of a surface-bonded PZT actuator-driven simply supported (SS) plate.

As an example, we consider a simply supported thin plate, as shown in Fig. 2. Two PZT actuators are assumed perfectly bonded on the top and bottom surfaces. When a voltage is applied to the PZT patches along the polarization direction 3, the PZT actuators can be actuated out-of-phase. This actuation creates two pairs of line bending moments at the boundaries of the PZT patch. Under the actuation of the line moments, an analytical solution of the mechanical admittance matrix of a simply supported plate at the mid point of the edge of the PZT patch was derived by the authors.⁸ results were

$$H_{xx} = i \frac{2\pi(h + h_p)^2 \omega}{\rho h a^3 b_p} \\ \times \sum_{m=1}^{\infty} \sum_{n=1}^{\infty} \left(\frac{m^2 C_x^2 C_y \sin[m\pi(y_1 + y_2)/(2b)]}{n(\omega_{mn}^2 - \omega^2)} \right) \quad (20)$$

$$H_{yy} = i \frac{2\pi(h + h_p)^2 \omega}{\rho h a^3 a_p} \\ \times \sum_{m=1}^{\infty} \sum_{n=1}^{\infty} \left(\frac{n^2 C_x C_y^2 \sin[m\pi(x_1 + x_2)/(2a)]}{m(\omega_{mn}^2 - \omega^2)} \right) \quad (21)$$

$$H_{xy} = H_{yx} = i \frac{2\pi(h + h_p)^2 \omega}{\rho h a^2 b b_p} \\ \times \sum_{m=1}^{\infty} \sum_{n=1}^{\infty} \left(\frac{m C_x C_y^2 \sin[m\pi(x_1 + x_2)/(2a)]}{\omega_{mn}^2 - \omega^2} \right) \quad (22)$$

where $C_x = \cos(m\pi x_1/a) - \cos(m\pi x_2/a)$ and $C_y = \cos(m\pi y_1/b) - \cos(m\pi y_2/b)$. As illustrated in Fig. 2, x_1 , x_2 , y_1 , and y_2 are the location coordinates of the edges of the PZT patches on the plate. The resonant frequency of the plate ω_{mn} can be determined from the homogeneous equation of the transverse motion of the plate; and m and n are the modal indices in the x and y directions, respectively.

It is noted that the structural admittance is a function of driving point location on the structure, and the admittance along the edge of the PZT patch is different. The numerical calculations have shown that the midpoint admittance is a very good approximation of the average admittance along the edge of the path. For simplification and not losing generality, the admittance at the midpoint of the edge of the PZT patch is used to represent the admittance characteristics of the plate, as expressed in Eqs. (20–22).

Once the mechanical admittance (impedance) is obtained, the coupled electromechanical admittance of an integrated PZT/substrate system can be determined from Eq. (18). The electromechanical power consumption and flow of the system can then be predicted, which will be developed later.

So far, the assumption made in the derivation is that the system is linear, and the host structure is a generic two-dimensional structure. The formulation Eq. (18) is a generic solution for coupled admittance of a system and can be applied to general

two-dimensional structures. For complex structures with irregular geometry, Eq. (18) is still applicable, although a close-form solution of the structural impedance is difficult to obtain. In this case, the structural impedance can be determined from either finite element analysis or experiments.

Electromechanical Power Consumption and Power Flow

Since a PZT actuator acts as a plate capacitor, when a voltage $V = V_0 e^{i\omega t}$ is applied to it, the current in the circuit can be expressed by

$$I = I_0 e^{i(\omega t + \phi)} \quad (23)$$

where ϕ is the phase between the current and voltage. The electrical power supplied to the PZT actuator is actually decomposed into two components P and Q . The real (dissipative) power is

$$P = \frac{I_0 V_0}{2} \cos \phi = \frac{V_0^2}{2} \operatorname{Re}(Y^*) \quad (24)$$

where $\cos \phi$ is called the power factor. The reactive power is

$$Q = \frac{I_0 V_0}{2} \sin \phi = \frac{V_0^2}{2} \operatorname{Im}(Y^*) \quad (25)$$

Physically, the real power is the electrical power supplied to the PZT actuator and converted into mechanical power to drive the host structure. The reactive power is the power circulating between the electrical power source and the integrated PZT/structure system. The total power may be expressed as

$$W^* = P + iQ \quad (26)$$

The magnitude of the complex power is defined as the apparent power,

$$W_0 = \sqrt{P^2 + Q^2} = \frac{I_0 V_0}{2} = \frac{V_0^2}{2} Y_0 \quad (27)$$

where Y_0 is the magnitude of the admittance Y^* . The apparent power reflects the power requirement of the system which includes both the dissipative power and the reactive power. The emphasis of the current work is on the analysis of the dissipative power consumption of a PZT actuator-driven structure. When power supplies are considered in the system modeling, the reactive power in the system will exert an important influence on the power requirement. In that case, a large reactive power is usually expected as a high-current demand is required from the power supply. In addition, the dissipative power consumed in the power supply itself should also be considered in the power requirement for the integrated system as a whole. Future work will include the electronics of power supplies in order to determine the overall power requirement.

Substituting Eq. (27) into Eq. (24), the power factor is rewritten as

$$FP = \cos \phi = \frac{\operatorname{Re}(Y^*)}{Y_0} = \frac{P}{W_0} \quad (28)$$

The power factor FP is the ratio of the dissipative power to the apparent power and represents the energy conversion efficiency from electrical power to mechanical power in the integrated PZT/substrate system. It is noted that the dissipative power consumption, the power requirement, and the energy conversion efficiency of the system are strongly related to the coupled electromechanical admittance Y^* .

The dissipative (real) power in an integrated PZT/substrate system includes three parts:

The first is the power dissipated by the structural damping of the host structure, which is related to the structural loss factor η in the complex Young's modulus. This power is proportional to the mechanical vibration power of the host structure. Second is the power consumed by the structural damping of the PZT actuator, which is associated with the mechanical loss factor η_p of the PZT actuator. Third is the power consumption caused by the dielectric loss of the PZT actuator, which is related to the dielectric loss factor δ_p in the complex dielectric constant.

The real power is eventually converted into internal heat in the system, resulting in heat generation and inducing thermal stress in the PZT actuator.¹² The first two parts of the system power consumption just mentioned are directly used in driving the host structure. They may be considered to represent the total mechanical power dissipation in the system. A suggested actuator power factor PF_a is defined as¹⁰

$$PF_a = \frac{\text{dissipative mechanical power}}{\text{apparent power}} = \frac{\operatorname{Re}(Y_a^*)}{|Y_a^*|}, \quad (29)$$

in which Y_a^* is calculated by assuming the dielectric loss factor δ_p to be zero in Eq. (18). Apparently, the difference between the system power factor [Eq. (28)] and the actuator power factor [Eq. (29)] is that the former includes the dielectric power consumption of the PZT actuator in the dissipative power consumption. When the power factor is experimentally determined, the system power factor should be used because the dielectric loss of the PZT actuator is usually not zero in a real system. In this paper, the system power factor is used in the following numerical examples. A comparison between the system power factor and the actuator power factor will also be performed.

Parametric Study and Discussion

A parametric study is conducted in this section to quantitatively examine how the dissipative power is consumed in the system and how much power is required to drive the system. The influence of the thickness and the location of the PZT actuator is also discussed.

A thin plate made of aluminum is used in the numerical example. The size of the plate is $304.8 \times 203.2 \times 1.53$ mm. Two PZT actuators are symmetrically bonded on the plate and located at $x_1 = 50.8$ mm and $y_1 = 25.4$ mm, as shown in Fig. 2. The size of the PZT patch is $50.8 \times 50.8 \times 0.19$ mm. The PZT material is G1195. The basic material properties are listed in Table 1. It is assumed in the numerical case that the magnitude of the voltage applied to the PZT actuator is 20 V.

Figure 3 illustrates the components and distribution of the dissipative (real) power in the frequency domain. The solid line represents the total dissipative power. The dashed line is the power consumption of the mechanically loss of the plate obtained from Eq. (24) by assuming $\delta_p = \eta_p = 0$. The dash-dotted line is the power consumption from the mechanical loss of the PZT actuator, found by setting $\delta_p = \eta = 0$ in Eq. (24). The dotted line is the power consumed by the dielectric loss of the PZT actuator, found by assuming $\eta = \eta_p = 0$ in Eq. (24).

It is clearly seen in Fig. 3 that at the resonant frequencies, the dissipative power is primarily consumed by the structural damping of the plate, whereas at off resonance, it is significantly affected by the dielectric loss of the PZT itself. The mechanical damping of the PZT actuator, however, has a slight influence on the real power consumption because of its small size.

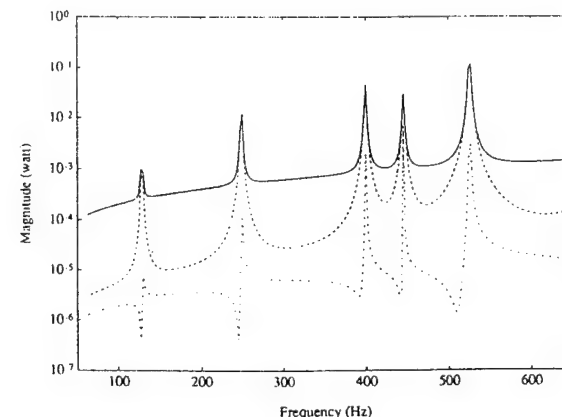


Fig. 3 Dissipative power of an integrated PZT/substrate system: — total dissipative power of PZT/plate system; - - - mechanical power consumption (plate); ······ mechanical power consumption (PZT); dielectric power consumption (PZT).

32

Table 1 Material properties of the PZT and the aluminum

	Young's modulus, N/m ²	Mass density, kg/m ³	Poisson ratio	Piezoelectric constants, m/V	Dielectric constant, F/m	Dielectric loss	Loss factor
PZT	6.3×10^{10}	7650	0.3	-1.66×10^{-10}	1.5×10^{-8}	0.015	0.005
Aluminum	6.9×10^{10}	2700	0.33	N/A	N/A	N/A	0.005

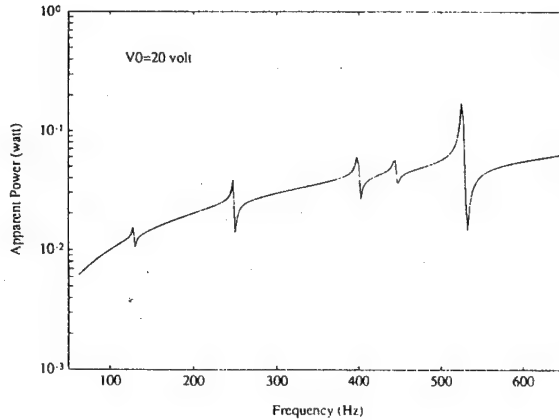


Fig. 4 Apparent power of a PZT/plate system.

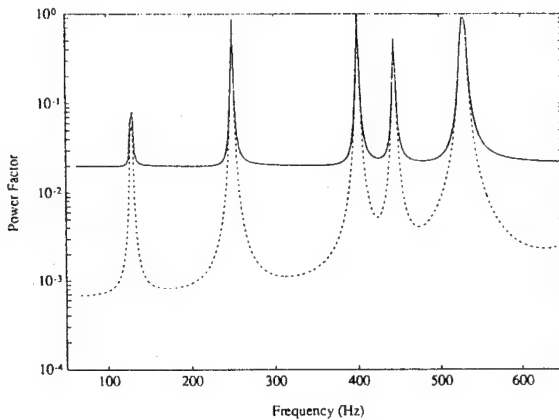


Fig. 5 Comparison of system power factor and actuator power factor: — system power factor; - - - actuator power factor.

Figure 4 shows the characteristics of the apparent power of the system. The peak power appears at the fifth mode in the range of less than 650 Hz, and it can be used to estimate the power requirement of the system in this frequency band. The power consumption significantly goes up when the excitation frequency increases. Once the interesting frequency band is determined, the power requirement of the system can be numerically predicted.

Figure 5 demonstrates the difference of the power factor predicted from Eq. (28) and Eq. (29), respectively. At resonant frequencies, the power factor is maximized because of the minimum resistance to the structural vibration. Both the system power factor and the actuator power factor give the same prediction. At off resonance, however, the actuator power factor is much smaller than the system power factor because the dissipative power is dominated by the dielectric loss behavior of the PZT actuator. Assuming a zero dielectric loss gives a very low-power consumption, resulting in a low-actuator power factor.

When the damping value in the system changes, the basic relations of the power consumption as shown in Fig. 3 are still applicable. Figure 6 illustrates that if the loss factor of the plate increases from 0.001 to 0.005, the dissipative power goes up at resonant frequencies and increases slightly at off resonance. In contrast, Fig. 7 shows that if the dielectric loss factor of the PZT actuator doubles from 0.015

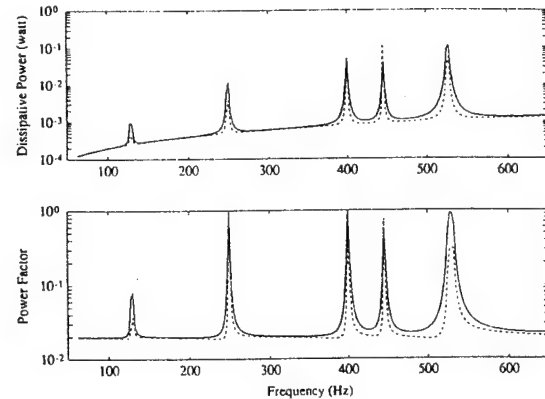


Fig. 6 Influence of the plate loss factor on the dissipative power and power factor of a PZT/plate system: — loss factor of plate: 0.005; - - - loss factor of plate: 0.001.

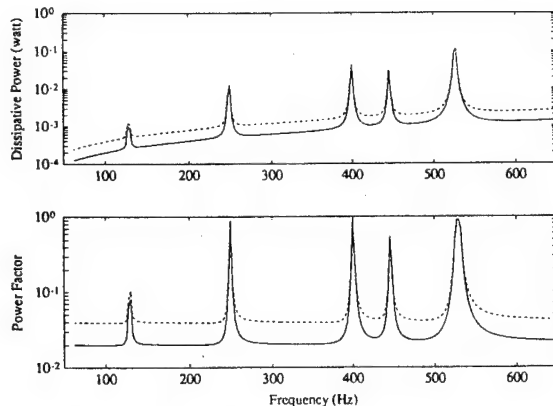


Fig. 7 Influence of the PZT actuator dielectric loss factor on the dissipative power and power factor of a PZT/plate system: — dielectric loss factor of PZT: 0.015; - - - dielectric loss factor of PZT: 0.03.

to 0.03, the dissipative power and the power factor increase by about 50% at off-resonant frequencies and remain the same at the resonant frequencies.

The geometric parameters of the PZT actuator, such as the thickness and the location, have significant influence on the dissipative power and the power factor because the mechanical impedance of the system strongly varies with these geometric parameters.^{7,8} Under the assumption of the constant magnitude of the applied voltage ($v_0 = 20$ V), when the thickness of the PZT patch increases from 0.19 mm to 2×0.19 mm and 4×0.19 mm, the real power consumption decreases on the whole frequency band, as displayed in Fig. 8. The power factor also decreases at off resonance. However, the power factor has a complicated variation at the resonant frequencies. The observation indicates that when the thickness of the PZT actuator varies, the maximum power factor will depend on the individual mode. Another important observation in Fig. 8 is that the resonant frequencies of the system apparently shift to higher values when the thickness of the PZT actuator increases. It can be explained that the added PZT patches stiffen the original plate and shift the resonant frequencies to the high values.

Figure 9 shows that when the location of the PZT actuator on the structure varies, the mechanical impedance changes and so does

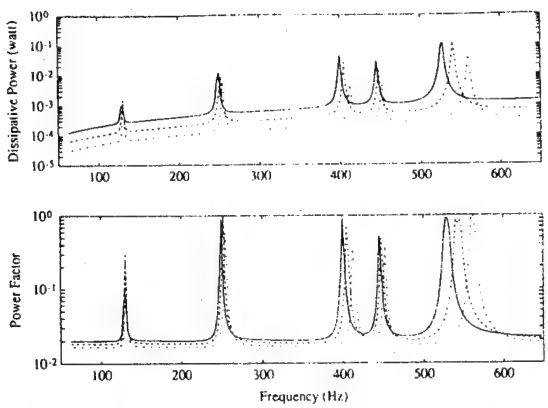


Fig. 8 Influence of the PZT thickness on the dissipative power and power factor of a PZT/plate system: —— $hp = 0.19$ mm; - - - $hp = 0.38$ mm; ····· $hp = 0.76$ mm.

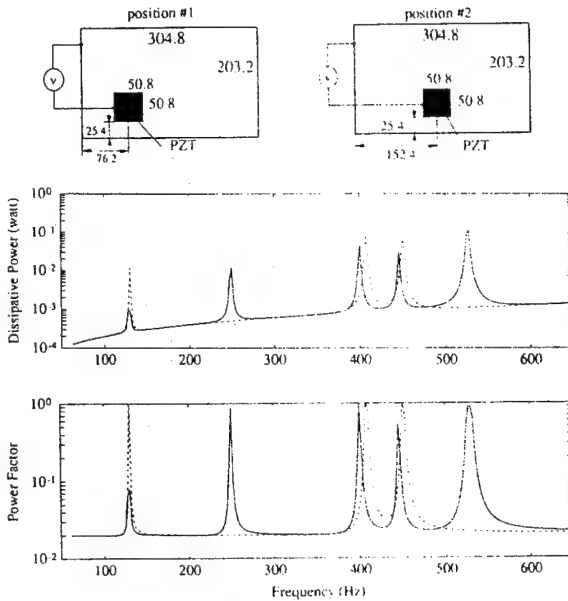


Fig. 9 Influence of the PZT location on the dissipative power and power factor of a PZT/plate system: —— location #1; - - - location #2.

the power consumption of the system. Note that when the center of the PZT actuator locates at the node line position in the x direction (location 2), the corresponding modes, i.e., the second and the fifth modes, are tailored off since little mechanical vibrational energy is supplied to these vibrational modes.

Experimental Verification

A simply supported thin plate integrated with surface-bonded PZT patches was built and tested to validate the coupled electromechanical system model. The size and physical properties of the plate and the PZT material are the same as those used in the numerical calculation in the previous section. An HP 4194A impedance/gain-phase analyzer was used to directly measure the coupled electromechanical admittance of the piezoelectric actuator-driven plate. Then, a comparison between the theoretical model and the experimental results was performed.

Figure 10 illustrates the measured and predicted complex admittance of the system in terms of the real part and the imaginary part, respectively. The corresponding power factor, calculated from the experimental data using Eq. (28), is displayed in Fig. 11. In both figures, the theoretical prediction based on the complex system impedance (dashed line) agrees well with the experimental data (solid line). The coupled electromechanical system model has provided a reasonably accurate prediction of the power consumption and the energy conversion efficiency of the PZT actuator-driven

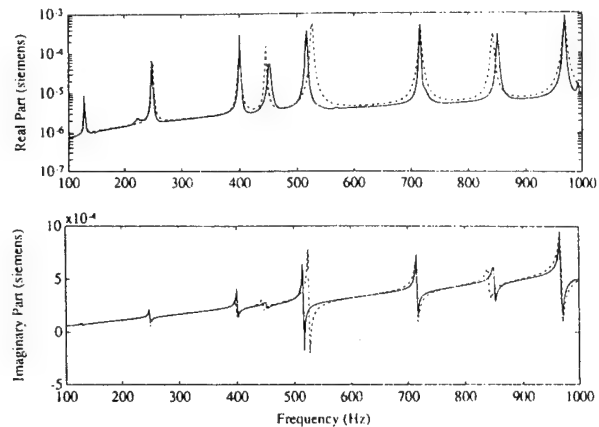


Fig. 10 Measured and predicted complex electromechanical admittance of a PZT/plate system: —— experimental data; - - - coupled impedance model.

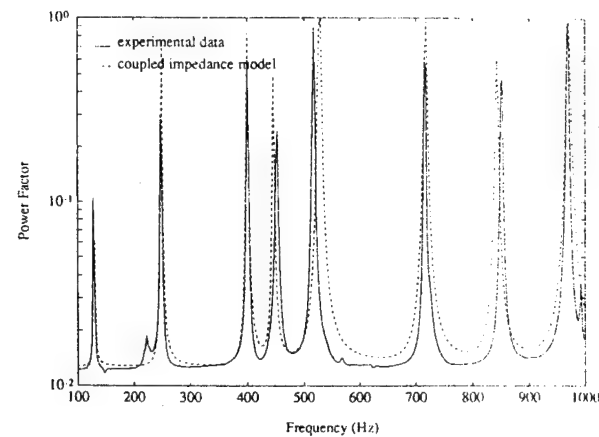


Fig. 11 Measured and predicted power factor of a PZT/plate system.

system. It should be noted that the maximum difference between the theoretical model and the experimental results appears at the fifth mode, i.e., (2, 2) mode. It may be explained that when the geometric center of the PZT actuator locates on the antinode position of the host plate ($x = 76.2$ mm, $y = 50.8$ mm), the excitation of that mode is maximized. The inertial effect caused by the added mass loading of the PZT patch is then intensified. The measured resonant frequency and the response of this mode [the fifth mode (2, 2)] are thus smaller than those predicted by the theoretical model.

Summary

A coupled electromechanical system model for a generic two-dimensional piezoelectric actuator-driven structure has been developed to predict the electromechanical power consumption and power flow. This modeling approach is helpful in understanding where the energy goes and in designing induced strain actuators and energy-efficient intelligent structures.

The coupled electro-mechanical system model has been experimentally verified.

The parametric study has demonstrated that the dissipative power supplied to the PZT actuator is primarily consumed by the mechanical damping of the host structure at resonant frequencies and is dissipated by the dielectric loss of the PZT itself at off resonance.

The thickness and location of the PZT actuator have an impact on the dissipative power consumption and power factor of the integrated system because these geometric parameters may cause significant changes in the mechanical impedance of the system.

Future work on system power consumption will include the electronics of power supplies in order to determine the overall power requirement. Additional work will also focus on power flow relations under closed-loop control.

Acknowledgments

The authors gratefully acknowledge the support of the Air Force Office of Scientific Research under AFOSR Grant F49620-93-1-0166; C. I. Chang, Program Manager.

References

- ¹Dimitriadis, E. K., Fuller, C. R., and Rogers, C. A., "Piezoelectric Actuators for Distributed Noise and Vibration Excitation of Thin Plates," *Proceedings of the 8th Biennial Conference on Failure Prevention and Reliability*, American Society of Mechanical Engineers, Montreal, Canada. DE-Vol. 16, Sept. 1989, pp. 223-233.
- ²Hagood, N. M., Chung, W. H., and von Flotow, A., "Modeling of Piezoelectric Actuator Dynamics for Active Structural Control," *Proceedings of the AIAA/ASME/ASCE/AHS/ASC 31st Structures, Structural Dynamics, and Materials Conference* (Long Beach, CA), AIAA, Washington, DC, 1990, pp. 2242-2256 (AIAA Paper 90-1097).
- ³Wang, B. T., "Active Control of Sound Transmission/Radiation from Elastic Plates Using Multiple Piezoelectric Actuators," Ph.D. Dissertation, Dept. of Mechanical Engineering, Virginia Polytechnic Inst. and State Univ., Blacksburg, VA, June 1991.
- ⁴Crawley, E. F., and Lazarus, K. B., "Induced Strain Actuation of Isotropic and Anisotropic Plates," *AIAA Journal*, Vol. 29, No. 6, 1991, pp. 945-951.
- ⁵Crawley, E. F., and de Luis, J., "Use of Piezoelectric Actuators as Elements of Intelligent Structures," *AIAA Journal*, Vol. 25, No. 10, 1987, pp. 1373-1385.
- ⁶Ikeda, T., *Fundamentals of Piezoelectricity*, Oxford Univ. Press, New York, 1990.
- ⁷Zhou, S. W., Liang, C., and Rogers, C. A., "Impedance Modeling of Two-Dimensional Piezoelectric Actuators Bonded on a Cylinder," *Proceedings of the Adaptive Structures and Material Systems*, American Society of Mechanical Engineers, Winter Annual Meeting, New Orleans, LA, 1993, pp. 247-256.
- ⁸Zhou, S. W., Liang, C., and Rogers, C. A., "A Dynamic Model of Piezoelectric Actuator-Driven Thin Plates," *Proceedings of Smart Structures and Materials*, Society of Photo-Optical Instrumentation Engineers, Orlando, FL, 1994, Vol. 2190, pp. 550-562.
- ⁹Rogers, C. A., "Intelligent Material Systems: The Dawn of a New Materials Age," *Journal of Intelligent Material Systems and Structures*, Vol. 4, No. 1, 1993, pp. 4-12.
- ¹⁰Liang, C., Sun, F. P., and Rogers, C. A., "Coupled Electro-Mechanical Analysis of Piezoelectric Ceramic Actuator-Driven Systems—Determination of the Actuator Power Consumption and System Energy Transfer," *Proceedings of Smart Structures and Materials*, Society of Photo-Optical Instrumentation Engineers, Albuquerque, NM, 1993, pp. 229-235.
- ¹¹Lomenzo, R. A., Sumali, H., and Cudney, H. H., "Maximizing Mechanical Power Transfer from Piezoelectric Stacked Actuators to Structures," *Proceedings of the Adaptive Structures and Material Systems*, American Society of Mechanical Engineers, Winter Annual Meeting, New Orleans, LA, 1993, pp. 229-235.
- ¹²Zhou, S. W., Liang, C., and Rogers, C. A., "Temperature Rise and Thermal Stress of Piezoelectric Elements in Active Structures," *Proceedings of the Adaptive Structures and Material Systems*, American Society of Mechanical Engineers International Mechanical Engineering Congress and Exposition, Chicago, IL, 1994, American Society of Mechanical Engineers, AD-Vol. 45, MD-Vol. 54, pp. 183-191.

Influence of actuator parameters on the energy efficiency

Bhargava, A., Chaudhry, Z., Liang, C., and Rogers, C.A., 1995a, "Experimental Determination of Optimal Actuator Locations on Complex Structures Based on the Actuator Power Factor", *Proceedings, AIAA/ASME/ASCE/AHS/ASC 36th Structures, Structural Dynamics, and Materials Conference, Adaptive Structures Forum*, April 1995, New Orleans, LA, pp. 3515-3523.

Bhargava, A., Chaudhry, Z., Liang, C., and Rogers, C.A., 1995b, "Experimental Verification of Optimal Location and Configuration Based on the Power Factor," *Journal of Intelligent Material Systems and Structures*, Vol. 6, No. 3, pp. 411-418.

EXPERIMENTAL DETERMINATION OF OPTIMAL ACTUATOR LOCATIONS
BASED ON THE ACTUATOR POWER FACTOR **AIAA-95-1138-CP**

Adesh Bhargava*, Zaffir Chaudhry** and Craig A. Rogers***
Virginia Polytechnic Institute and State University
Blacksburg, VA, 24061-0261

Abstract

The actuator power factor, defined as the ratio of the structural dissipative mechanical power to the apparent supplied electrical power, describes the effectiveness of the electromechanical actuator to convert supplied electrical energy to mechanical energy which in-turn produces the desired structural response. If measured experimentally, it can be used to optimize the actuator location for complex structures. This paper describes the actuator location optimization for an aircraft panel type structure with applications in aircraft interior acoustic and structural vibration control. The experimental power factor results for this structure were validated by comparing the maximum power factor in a given region to the specific panel mode shape as generated by a finite-element model. The results showed good correlation between the experimentally measured power factor data and the panel mode shapes. The future implications of this work are towards the design of a power factor meter for a cost as well as a time effective means of actuator location optimization.

I. Background

The concept of actuator power factor is based on the ability of an integrated induced strain actuator such as a piezoelectric (PZT) actuator to transfer supplied electrical energy into structural mechanical energy.⁽²⁾ For a given structure, the location and configuration of an actuator will directly influence the authority of the actuator towards exciting the structure. Therefore by maximizing the average power factor for a given frequency interval, the actuator driving authority can be maximized.

Theoretically the actuator power factor is defined as the ratio of the real part of the PZT actuator electromechanical admittance to the magnitude:

$$P.F. = \frac{\text{Re}(Y)}{|Y|}, \quad (1)$$

where Y, is the PZT actuator electromechanical admittance. The actuator power factor approach has been ana-

lytically as well as experimentally verified for the simple case of a cantilever beam.⁽¹⁾ Experimentally, the power factor was measured using an HP4194A Impedance Analyzer and a removable PZT actuator unit as shown in Fig. 1.

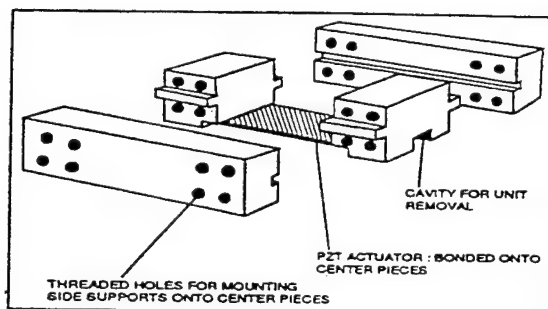


Fig. 1 Removable PZT actuator layout.

The design allows for the relocation of the same PZT actuator to various locations on the structure to obtain a power factor map. The power factor results using this removable unit showed good similarities between the experimental and the analytical results for the simple structure. The same unit was used to excite the complex structure described in this paper.

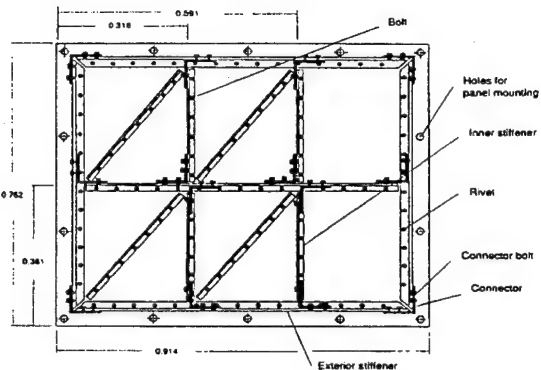
II. Complex Structure Analysis

Since typical low frequency noise within aircraft occurs due to the side-wall panel or structural vibrations,⁽³⁾ a complex structure resembling an aircraft panel was tested for actuator location optimization using the power factor approach.⁽⁴⁾ The panel model shown in Fig. 2 on the next page, has the pertinent dimensions labeled on the figure and is constructed of structural aluminum. The panel skin thickness is 0.0008 m. The stiffeners (L-section beams) for this panel are 0.0254 m beams for the outer stiffeners (vertical and horizontal) and 0.019 beams for the inner stiffeners (vertical, horizontal, and angle). In order to allow for the removal of the inner angle stiffeners for alternate panel structural analysis, the inner stiffeners were attached using 0.0031 m diameter hexagonal bolts.

* Graduate Student

** Research Scientist, Member AIAA, ASME

*** Professor, Member AIAA, ASME



All dimensions in m.

Fig. 2 Aircraft panel geometry.

The material designations for the panel parts described above are shown in Table 1 and 2.

Table 1 Panel parts material designation.

Panel part	Skin	Stiffener	Rivet	Stiffener bolt	Angle connector	Connector bolt
Material	Alum.	Alum.	Alum.	Steel	Steel	Steel

Table 2 Material property designation.

Material	ρ (kg/m^3)	E (N/m^2)	Poisson rat. ν
Aluminum	2800	69×10^9	0.33
Steel	7650	207×10^9	0.29

Holes were also drilled outside the exterior stiffener framework to resemble holes for mounting the panel onto the aircraft structure. The final modification to the panel model was to attach connectors onto the beam frame-work as shown in Fig. 2. This modification further stiffened the complete panel structure. Finally, for the power factor analysis, the panel was hung on a wooden stand and connected by elastic cords for a free-free analysis as shown in Fig. 3.

A finite-element model (f.e.m.) for this aircraft panel model was next constructed in order to have an analytical bases for validating the actuator location optimization results. The final f.e.m. for the aircraft panel is shown in Fig. 4.

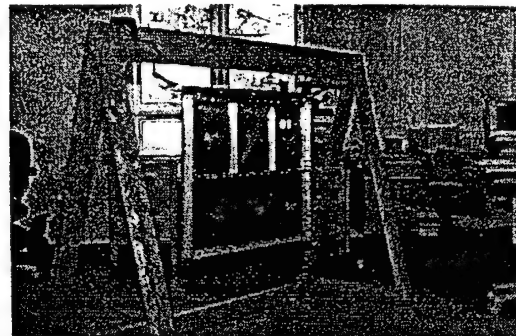


Fig. 3 Aircraft panel test configuration.

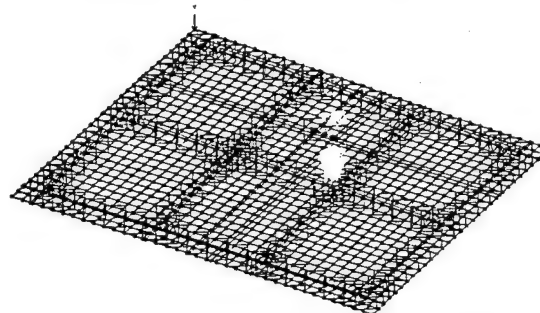


Fig. 4 Aircraft panel finite-element model.

This model consists of approximately 2800 elements and 1700 nodes. The elements for the f.e.m. for the various parts are listed in Table 3.

Table 3 Aircraft panel f.e.m. element designations.

Panel part	Element designation
Skin	Thin shell-linear quadrilateral
Stiffener	Angle beam
Rivet	Rigid connection
Bolt	Rigid connection
L-angle connector	Rigid element
Weights: rivet, bolt, angle connector.	Lumped mass
Weights: Bracket unit blocks	Lumped mass
Bracket unit mounted PZT Actuator	Offset beam

For the mode shape analysis, the Guyan-Reduction Method was used and mode shapes and natural frequencies were obtained using CAEDS. This model had a first natural frequency at 45 Hz and this mode could be reliably excited and measured, as shown in Fig. 5 on the next page, in the frequency response plot using a signal analy-

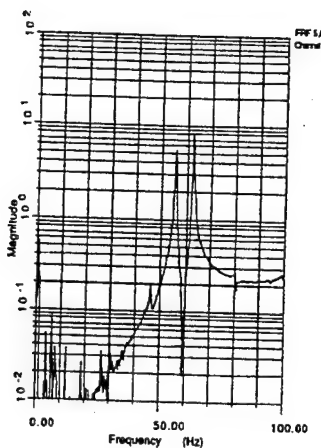


Fig. 5 Plate frequency response.

zer. The frequency response plots for Fig. 5 is for PZT #1 ($l = 0.0500 \text{ m}$, $w = 0.0130 \text{ m}$, $h = 0.0008\text{m}$) excited at 120 V. The frequency response plot shows that the reliably measurable modes for this panel are (45 Hz, 55 Hz, 64 Hz, 80 Hz, and so forth).

Next, in order to validate the plate f.e.m., a mode shape identification of the panel excited by the bracket unit mounted PZT actuator was performed. This was done by placing the PZT actuator in region #3 as shown in Fig. 6.

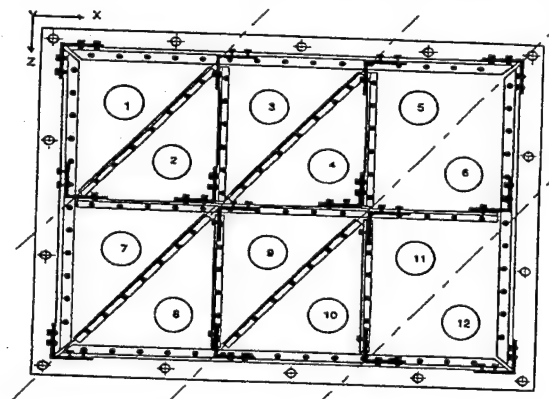


Fig. 6 Aircraft panel region designation.

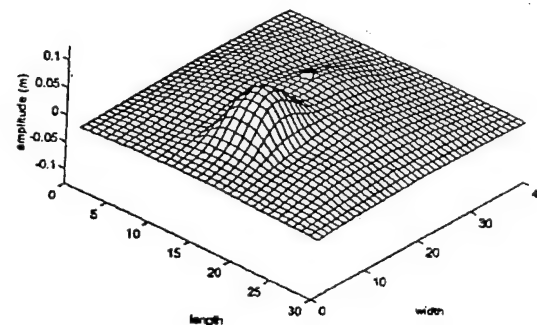
The midpoint locations for the PZT-unit (oriented with the length direction parallel to the x-axis), relative to the coordinate system shown on the top left hand corner of Fig. 6 are shown in Table 4. For Fig. 6 and Table 4, regions 1-12 are labeled and the PZT-unit midpoint coordinates are given for later reference. Since the panel modes at 55 Hz and 64 Hz had the strongest amplitude as shown in Fig. 5, these modes were experimentally measured using a laser scanner. The experimentally measured mode

Table 4 PZT-unit midpoint location on panel structure.

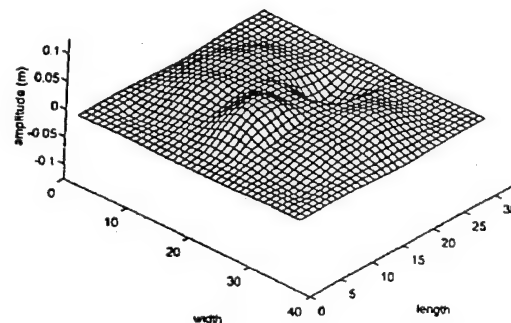
Location #	1	2	3	4	5	6
Coordinate (X, Z) m	0.14, 0.15	0.25, 0.29	0.42, 0.15	0.53, 0.29	0.69, 0.15	0.81, 0.29

Location #	7	8	9	10	11	12
Coordinate (X, Z) m	0.14, 0.47	0.25, 0.61	0.42, 0.47	0.53, 0.61	0.69, 0.47	0.81, 0.61

shapes along with the finite-element mode shapes are shown in Fig. 7.



Experimental (55.4 Hz)



Finite-Element (55.7 Hz)

Fig. 7a Mode shape 55 Hz.

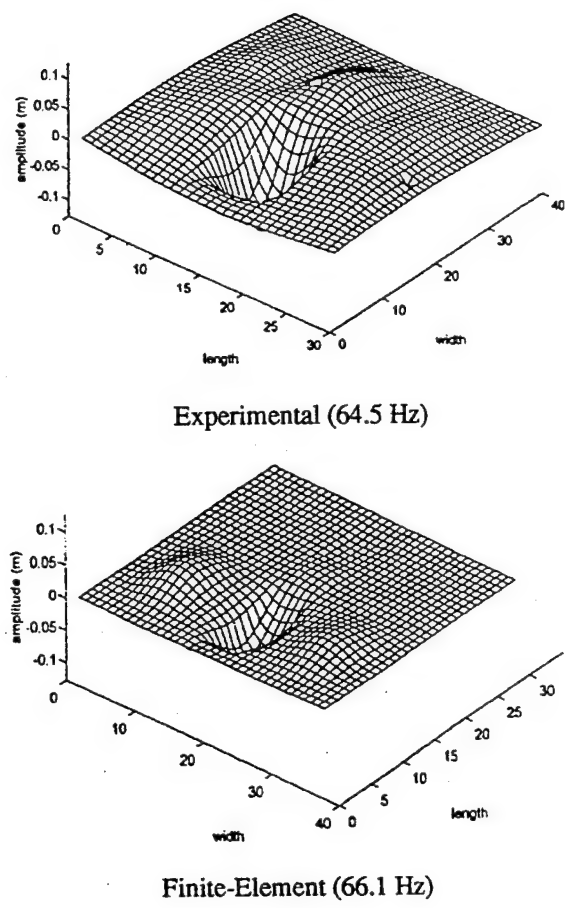


Fig. 7b Mode shape 64 Hz.

Notice that although the panel's structure seems symmetric, it however is not because of the spacing of the inner vertical stiffeners, the alignment of the inner vertical, angle, and horizontal stiffeners, the inner angle stiffener holes, and the addition of the bracket unit mass loading as shown in Fig. 2. Therefore, as displayed in Fig. 7, the mode shapes are not completely symmetric. The comparison between the experimentally measured and the f.e.m. generated mode shapes shows good agreement in terms of the general pattern and the direction of the deflection within the respective panel regions for all the regions except region 3 for 55 Hz. This region partially deflects upward and then downward for the f.e.m. generated mode shape. These and any other deviations between the f.e.m. generated and the experimentally measured mode shapes could be due to the difficulty in implementing the L-angle connectors because of their points of attachment, the weight distribution of the angle connectors and because the holes on the panel were not accounted for. Also, since the 64 Hz and the 55 Hz modes are relatively close together, each one has a significant impact on

the other one's mode shape since a single location excitation as by this bracket-unit can only yield an operational (a combination of other modes) mode shape, whereas the f.e.m. generated mode shape is a pure mode shape. Besides these inaccuracies, the overall mode shape results are satisfactory in terms of the general panel deflection pattern as well as the respective frequency locations for the given modes for validating the f.e.m. under 75 Hz. Above 75 Hz however, the specific panel regions vibrate with more than one type of motion and it becomes more difficult to match the experimentally measured and f.e.m. generated mode shapes. Therefore for the subsequent analysis, mode #2 (55 Hz) and mode #3 (64 Hz) will be used for the power factor analysis for this panel configuration.

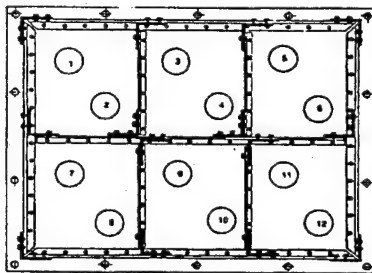
Using the structural mode shapes, the experimentally determined power factor results will be analytically validated by comparing the maximum curvature location with the maximum power factor location. For example, for the f.e.m. generated mode shape for 55 Hz with the PZT unit placed within the center of the rectangular region 3&4 (without any angle stiffeners) shown in Fig. 7, by examining the mode shape it can be seen that the maximum curvature and thus the maximum power factor amplitude should occur in regions 9&10, (see Fig. 6). Notice, without the PZT-unit mass loading, the modes shift up by approximately 2 Hz. Therefore for this panel configuration (without any angle stiffeners), for exciting or controlling the mode at 55 Hz, the optimal PZT actuator location would be in approximately 0.55 m from the top (half way down in regions 9 and 10) as an initial approximation for single frequency power factor maximization. For multiple frequency power factor maximization, the same type of reasoning will be used as well. Finally, in order to truly optimize an actuator location for a limited number of measured points, a simple numerical algorithm will be used. This algorithm will allow for the approximate determination of the power factor contours for the aircraft panel structure. The interpolation between each of the power factor magnitudes will be cubic interpolation. For single frequency or broadband power factor maximization, this algorithm will also allow for the control frequency input, and the output will consist of the approximate location(s) that will provide the maximum power factor for the specified control frequencies.

For the experimental work reported here, the mass loading of the removable PZT unit influences the vibration modes, natural frequencies, and also the power factor. This problem can be eliminated by refining the design of the PZT unit such that it imposes no more constraints on the structure than a surface mounted PZT actuator. Also, for complex full-scale structures, it is believed that the influ-

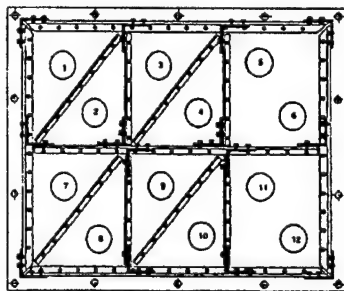
ence of the PZT unit would be minimum and the power factor map would not be contaminated by the mass and stiffness of the removable unit.

III. Complex Structure Results

In order to analyze the power factor technique for actuator location optimization for the panel structure, three different configurations of the structure were analyzed, however, in this paper only two are presented. For these configurations, both single frequency as well as multiple frequency power factor maximization was analyzed. The three tested aircraft panel configurations are shown in Fig. 8.



Config. #1



Config. #2

Fig. 8 Aircraft panel model tested configurations.

The first set-up (Config. #1) consists of only of vertical and horizontal stiffeners. The second set-up (Config. #2) consists of four angle stiffeners to analyze the local and the global effect of adding numerous angle stiffeners. In order to analyze the power factor layout for these panel configurations, the PZT-unit #1 was attached at the twelve locations as shown earlier in Fig. 6 and Table 4. For the experimental measurements, an HP 4192A Impedance Analyzer was used. This impedance analyzer is specifically designed for low frequency impedance measurement (5 Hz - 13 kHz). For the frequency range 40-80 Hz, the maximum error for the admittance measurement

was 3 %. This error was determined by dividing the maximum variation by the average admittance for the experimental readings. For the initial analysis, Config. #1 shown earlier in Fig. 8 was tested.

For single frequency power factor maximization for 55 and 64 Hz the electromechanical admittance was measured at the twelve points shown earlier in Fig. 6. For these two frequencies, the maximum power factor at each of these locations for a interval of ± 2 Hz is shown in Table 5.

Table 5 Power factor; Config. #1

Freq. Hz	Loc 1; %	Loc 2; %	Loc 3; %	Loc 4; %	Loc 5; %	Loc 6; %
55	2.3	2.4	2.7	2.8	2.4	2.3
64	2.2	2.3	2.4	2.3	2.2	2.1

Freq. Hz	Loc 7; %	Loc 8; %	Loc 9; %	Loc 10; %	Loc 11; %	Loc 12; %
55	2.2	2.2	2.8	2.8	2.3	2.3
64	2.4	2.4	2.8	2.8	2.5	2.2

The ± 2 Hz interval was used because typically the power factor peaks rise and fall gradually over a 3-4 Hz interval. The panel mode shape for 55 Hz and 64 Hz are shown in Fig. 7. Based on the power factor measurements for Table 5, the power factor mesh as generated by the numerical interpolation algorithm are shown in Fig. 9 .

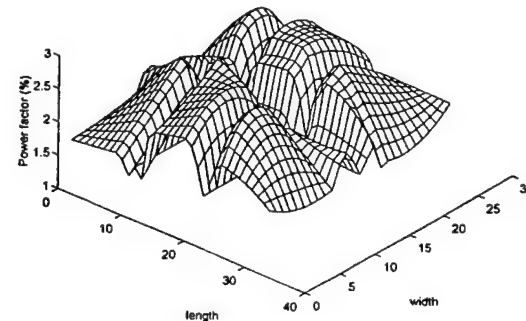


Fig. 9a Power factor mesh; 55 Hz.

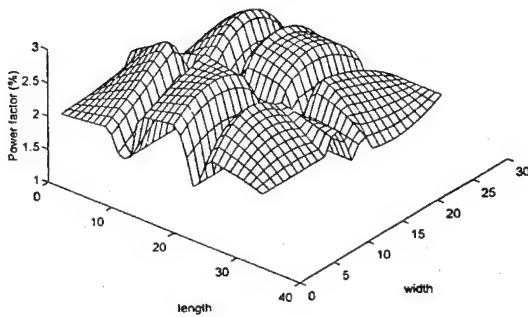


Fig. 9b Power factor mesh; 64 Hz.

The plots for Fig. 9 show that the optimal actuator location at 55 Hz is at $x = 0.38$ m and $z = 0.58$ m with a maximum power factor magnitude of 2.95 % (within regions 9&10). For 64 Hz, the maximum power factor is 2.87 % at $x = 0.42$ m and $z = 0.53$ m (within regions 9&10). Experimentally, the maximum power factor for a 2 % frequency interval at the respective locations for the modes at 55 Hz and 64 Hz is 2.9 % and 2.9 %, respectively. These results show good correlation with the interpolated power factor outputs for Fig. 9. By examining the mode shape for 55 Hz (Fig. 7a), it can be seen regions 9&10 have the maximum curvature and therefore within these regions the power factor is maximum. By using the same analogy for the mode shape for 64 Hz (Fig. 7b), it can be seen that the optimal actuator location for single frequency power factor maximization for this frequency is indeed within regions 9&10. Furthermore, in order to evaluate the accuracy of this interpolation technique, four other arbitrary points were tested. The x and z coordinates of these points were $(x,z) = pt. \#1 (0.23, -0.25)$, $pt. \#2 (0.79, -0.25)$, $pt. \#3 (0.23, -0.59)$, $pt. \#4 (0.79, -0.59)$. The interpolated and the experimentally measured power factor at 55 Hz for these points was; $pt. \#1 (2.25\%, 2.4\%)$, $pt. \#2 (2.55\%, 2.5\%)$, $pt. \#3 (2.14\%, 2.2\%)$, $pt. \#4 (2.46\%, 2.4\%)$. Therefore this interpolation algorithm satisfactorily predicts the power factor between the originally measured locations for Fig. 6.

Next, for multiple frequency power factor maximization, by averaging the power factor over the frequency range of 50 - 70 Hz for Fig. 9a and Fig. 9b, the interpolated power factor at the measured locations is plotted in Fig. 10. The numerical interpolation algorithm for this plot yielded the optimal actuator location for multiple frequency control for Config. #1 over this frequency range (50 - 70 Hz) of $x = 0.41$ and $z = 0.55$ m (within regions

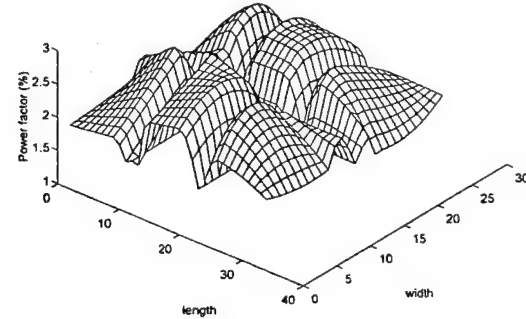


Fig. 10 Multiple-frequency power factor mesh; Config. #1.

9&10). The maximum power factor magnitude at this location is 2.87 %. Experimentally, the maximum average power factor over this frequency interval at the specified location is 2.9 %. Therefore for multiple frequency power factor maximization as well, the interpolation algorithm satisfactorily predicts the optimal actuator location. By examining the two mode shape plots for Fig. 7, it can be seen that on average regions 9&10 have the highest curvature. Therefore the power factor for multiple frequency control in these regions is maximum because the strain energy in these regions is also high. It should also be pointed out that since the error in determining these power factor results is $\pm 3\%$, other locations that generate a power factor as low as 2.8 % would also be adequate.

For this aircraft panel configuration, it can be seen that this PZT actuator configuration is not as efficient at exciting this structure as compared to the cantilever beam analyzed in a previous case.⁽¹⁾ For example, on average the maximum power factor for this panel model for PZT unit #1 is on the order of 3% whereas for the cantilever beam it was on the order of 15-30%. The reason for this difference is that for a given structure the power factor is maximum when the actuator impedance is close to the structural impedance. For this panel, because of the relatively low power factor magnitude, it can be deduced that the actuator and the panel impedance mismatch is much higher than that for the cantilever beam case. Therefore in order to ensure that a PZT actuator is a suitable device for exciting a structure such as this one, for the frequency range of 40-70 Hz, the actuator impedance within this frequency range would also have to be of the same approximate magnitude. It should be noted that for location optimization work it is the relative power factor amplitude which is important and not the actual value. Therefore, as long as the power factor and its variation with

location can be accurately measured, the power factor magnitude is not necessarily important. For an actual vibration suppression problem, however, the goal is to maximize the power factor. This is accomplished by matching the impedance of the actuator to the structural impedance at the location. Several options are available for this: changing the offset distance of the actuator; changing the thickness of the actuator.

In order to analyze the effect of adding angle stiffeners, the case with four angle stiffeners, Config. #2 shown earlier in Fig. 8, was analyzed. For single frequency power factor maximization, first the finite element model with the four angle stiffeners was checked to determine the shift in the natural frequencies. For this configuration, the first three modes shifted to 50 Hz, 73 Hz, and 92 Hz. For this case the modes at 50 Hz and 73 Hz were analyzed. The maximum power factor at 50 Hz and 73 Hz for a interval of ± 2 Hz at the measured locations is shown in Table 6.

Table 6 Power factor; Config. #2.

Freq. Hz	Loc 1: %	Loc 2: %	Loc 3: %	Loc 4: %	Loc 5: %	Loc 6: %
50	2.4	2.6	2.5	2.4	2.8	2.9
73	3.4	3.3	3.7	3.8	4.4	4.5

Freq. Hz	Loc 7: %	Loc 8: %	Loc 9: %	Loc 10: %	Loc 11: %	Loc 12: %
50	2.4	2.4	2.4	2.4	3.0	2.9
73	3.2	3.1	3.5	3.5	4.2	4.4

The f.e.m. generated panel modes for 50 Hz and 73 Hz are shown in Fig. 11.

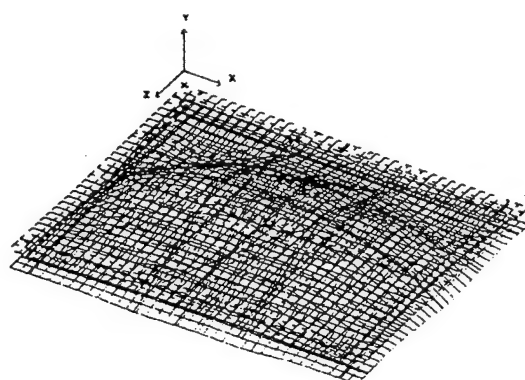


Fig. 11a Mode shape; 50 Hz; Config. #2.

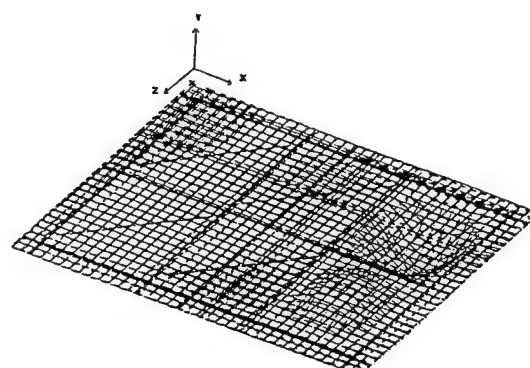


Fig. 11b Mode shape; 73 Hz; Config. #2.

The plots for Fig. 11 show that adding the four angle stiffeners first of all shifted the natural frequencies up by approximately 5 Hz. Secondly, for 50 Hz, the angle stiffeners do not significantly suppress the deflection magnitude in the specific panel regions because this mode is a global mode. For 73 Hz, the angle stiffeners suppress the vibration in regions 1, 2, 3, 4, 7, 8, 9, and 10 because this mode is a local mode. Based on the power factor measurements for Table 7 the power factor contours as generated by the numerical interpolation algorithm are shown in Fig. 12.

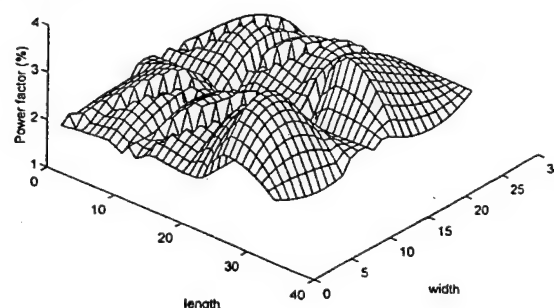


Fig. 12a Power factor mesh; 50 Hz.

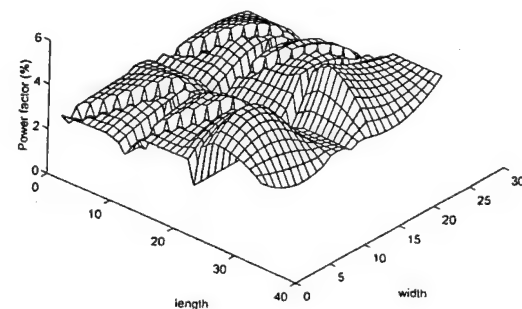


Fig. 12b Power factor mesh; 73 Hz.

The plots for Fig. 12 show that the optimal actuator location for narrow-band power factor maximization for 50 Hz is at $x = 0.71$ m and $z = 0.53$ m with a maximum power factor magnitude of 3.52 % (within regions 11&12). For 73 Hz, the maximum power factor is 4.87 % at $x = 0.79$ m and $z = 0.18$ m (within regions 5&6). Experimentally, the maximum power factor for a $\pm 2\%$ frequency interval at the respective locations for the modes at 50 Hz and 73 Hz is 3.6 % and 4.7 %, respectively.

For multiple frequency power factor maximization, by averaging the power factor over the frequency range of 40 - 80 Hz for Fig. 12a and Fig. 12b, the average interpolated power factor at the measured locations is plotted in Fig. 13.

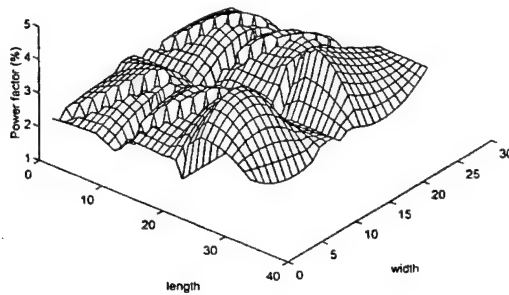


Fig. 13 Multiple-frequency power factor mesh; Config. #2.

The numerical interpolation algorithm for this plot yielded the optimal actuator location for broadband control for Config. #3 over this frequency range (40 - 80 Hz) should be at $x = 0.68$ and $z = 0.66$ m (within regions 11&12). The maximum power factor magnitude at this location is 4.32 %. Experimentally, the maximum average power factor over this frequency interval at the specified location is 4.4 %. Again, by examining the two mode shape plots for Fig. 11, it can be seen that regions 11&12 on average have the highest strain energy. The results for broadband as well as single frequency power factor maximization show good correlation between the experimentally measured and the interpolated optimal actuator locations with the four angle stiffener. It should again be pointed out that since the error in determining these power factor results is 3 %, other locations that generate a power factor as low as 4.2 % would also be adequate.

IV Conclusion

The results for this paper have shown that the power factor technique for optimizing an actuator location or configuration on a complex structure can be used for single-frequency as well as multiple frequency power factor maximization. This technique relies on experimentally obtaining the power factor for a limited number of points on a structure. From this limited information, through interpolation, a power factor contour plot for the complete structure can be obtained. The contour map identifies locations where the power factor is maximum for a given resonant frequency or several resonant frequencies. These locations are points where the maximum amount of supplied electrical energy is converted into mechanical energy and, therefore, the best locations for exciting or conversely cancelling vibrations.

For this paper, the concept was applied to a built-up structure resembling an aircraft panel. To validate the experimentally constructed power factor maps, a finite element model was also constructed. The mode-shapes predicted by the finite element model were verified through correlation with laser-scanner obtained mode-shapes. The best locations predicted by the power factor maps correspond to the points of maximum strain energy and for this structure the points of maximum vibration amplitude.

This technique for actuator location optimization can be used to quickly identify, on a complex structure, the best location(s) for mounting induced strain actuators such as PZTs in aid of vibration or acoustic control. The only hardware required for this procedure is a commercially available impedance analyzer.

Acknowledgements

The authors would like to acknowledge the support of the Air Force Office of Scientific Research, AFOSR Grant No. F49620-93-1-0166, Walter F. Jones and Spencer Wu, Program Managers.

References

1. Bhargava, A., Liang, C., Chaudhry, Z. and Rogers, C., 1994, *Experimental Verification of Optimal Actuator Location and Configuration based on the Actuator Power Factor*, ICIM Conference, pp. 185-197.
2. Liang, C., Sun, F. P. and Rogers, C. A., 1994, *Development of an Actuator Power Factor Meter for Experimental*

tal Determination of the Optimal Actuator Locations on Complex Structures, Proceedings, 1994 North American Conference on Smart Materials and Structures.

3. SenGupta, G., 1977, *Reduction of Cabin Noise and Vibration by Intrinsic Structural Tuning*, AIAA Journal, pp. 545-546.

4. SenGupta, G., 1978, *Reduction of Cabin Noise During Cruise Conditions by Stringer and Frame Damping*, AIAA Journal, pp. 504-508.

Experimental Verification of Optimal Actuator Location and Configuration Based on Actuator Power Factor

ADESH BHARGAVA, ZAFFIR CHAUDHRY, CHEN LIANG AND CRAIG A. ROGERS*

Center for Intelligent Material Systems and Structures, Virginia Polytechnic Institute and State University, Blacksburg, VA 24061-0261

ABSTRACT: The actuator power factor is defined as the ratio of the total dissipative mechanical power of a PZT actuator to the total supplied electrical power to the PZT actuator. If measured experimentally, it can be used to optimize the actuator location and configuration for complex structures. The concept of actuator power factor is based on the ability of an integrated induced strain actuator such as a PZT to transfer supplied electrical energy into structural mechanical energy. For a given structure such as a beam or a plate, the location and configuration of an actuator will directly influence the authority of the actuator towards driving the structure. Presented in this paper are the experimental as well as the theoretical results for the case of a cantilever beam as a proof-of-concept of this technique. The design of a fixture which allows for the relocation of a PZT patch which can be used for both actuation and sensing is presented as well. For the experimental case, the electromechanical PZT admittance was measured by an HP 4194A impedance analyzer for the power factor analysis. The experimental and the theoretical power factor results were subsequently compared and showed good qualitative similarities over the frequency range analyzed. This initial comparison between the experimental and the theoretical power factor results will be used to analyze the capabilities and limitations of the actuator power factor algorithm as a tool for determining the optimal configuration and location for a PZT actuator for simple as well as complex structural vibration control applications.

INTRODUCTION

IN general, the typical procedure used to determine the optimal actuator location and configuration for a given structure is based on the modal domain approach. Compared to the overall power factor approach, the modal domain approach requires the determination of the response characteristics of the complete structure under consideration. For the modal domain approach, the interaction between the actuator and the host structure is assumed to be independent of frequency. Liang, Sun and Rogers (1993a) have shown that the interaction between the actuator and the host structure, which depends on the impedance of the actuator and the structure, is frequency dependent. The actuator power factor approach is based on the coupled electromechanical impedance model for an active material system (Liang, Sun and Rogers, 1994). Compared to the modal domain approach, the analytical power factor algorithm only requires knowledge of the actuator and the host structure properties, and a measurement of the excitation voltage input. For complex structures that can be difficult to model analytically, the actuator power factor can be determined experimentally as well.

The concept of actuator power factor is based on the ability of an integrated induced strain actuator such as a PZT to

transfer supplied electrical energy into structural mechanical energy. The optimal actuator location and configuration for a given structure is the point at which the given structure has the highest strain energy for a given frequency of excitation (Preumont et al., 1991). However since a typical structure is excited for a range of frequencies, the actuator power factor, which is a function of the excitation frequency, varies throughout the given excitation range. Since for a given structure such as a beam or a plate, the location of the actuator will directly influence the actuator authority towards exciting the structure, the actuator placement and configuration is critical to make maximum use of the supplied electrical energy.

In order to determine the effectiveness of the actuator power factor algorithm as a tool for analytically determining the optimal actuator location and configuration for a given structure, the actuator power factor is analytically determined initially for a cantilever beam set-up for a given excitation range. A complete analysis and description for the power factor algorithm for the case of a cantilever beam is included in this paper. The layout of the experimental set-up to verify the analytically determined results by the actuator power factor algorithm is also described. The experimental set-up explanation will consist of a full description of the configuration of the cantilever beam and the bracket-type structure to allow for actuator relocation on the beam. The relocation capability for the PZT actuator allowed by the bracket-type structure for this case was included to allow for the verification of the actuator power factor algorithm for

*Author to whom correspondence should be addressed.

variations in the actuator location or the actuator configuration. The experimental results for the actuator power factor are compared to the analytically predicted results by the actuator power factor algorithm. A three-dimensional plot for the actuator power factor, versus frequency, versus actuator location for the cantilever beam is presented. This type of a plot is presented to demonstrate how the actuator power factor layout can be practically used in a three-dimensional format for optimizing the actuator location and configuration for simple as well as complex structures.

THEORY AND RESULTS

PZT Actuator Power Factor: Cantilever Beam

In theory, the actuator power factor is defined as the ratio of the total dissipative mechanical power of a PZT actuator to the total supplied electrical power to the PZT actuator. This can be expressed as (Liang et al., 1994):

$$\text{P.F.} = \frac{\text{Dissipative Mechanical Power}}{\text{Supplied Electrical Power}} = \frac{\text{Re}(Y)}{|Y|} \quad (1)$$

Here, Y is the electro-mechanical admittance of the PZT actuator. In order to evaluate the power factor algorithm, for the case of a cantilever beam with an offset PZT actuator, an experiment was set up, as shown in Figure 1. The cantilever beam for this case was a steel beam. The following symbols for the cantilever beam are stated for future reference: free length (l_B), width (w_B), thickness (h_B), and mass density (ρ_B). In order to allow for PZT relocation on the beam as necessary, a bracket-type structure, as shown in Figure 2, was designed.

The main function of this bracket structure is to provide a practical means of relocating the PZT on a cantilever beam and to ensure that the PZT will not be damaged during the relocation process. In order to move the PZT as necessary, the side supporters for the bracket structure are simply mounted onto the center pieces, and the complete unit can be removed from or bonded onto the beam as required. The side supports are designed to ensure that the PZT will not be

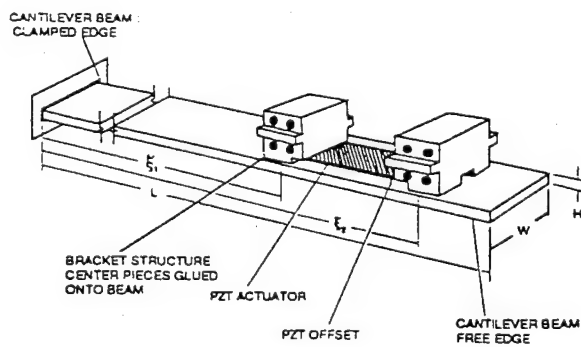


Figure 1. Experimental set-up.

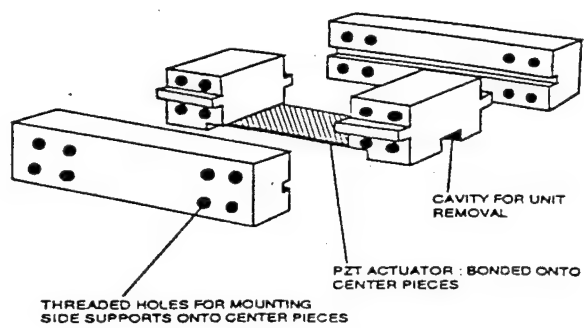


Figure 2. Bracket unit set-up.

damaged while being removed from the cantilever beam. Thus when the complete unit is assembled, a screwdriver can simply be used to pry the unit off without transferring any of the prying force onto the PZT.

With the design of the experimental setup for measuring the actuator power factor complete, the analytical model for the algorithm for the case of a cantilever beam can next be evaluated. In order to analytically evaluate the power factor algorithm, first the coupled electromechanical admittance of the PZT, Y , for Equation (1) is evaluated. The electromechanical admittance for a PZT actuator is given by (Liang et al., 1994):

$$Y = i\omega \frac{w_A l_A}{h_A} \left(\bar{\epsilon}_{33}^T - \frac{Z}{Z_A + Z} d_{32}^2 \bar{Y}_{22}^E \right) \quad (2)$$

Here ω is the excitation frequency, w_A , l_A , h_A are the actuator width, length, and thickness, respectively, $\bar{\epsilon}_{33}^T$ is the complex dielectric constant at zero stress given by $\epsilon_{33}^T(1 - \delta i)$, where δ is the dielectric loss factor, Z_A is the actuator impedance, Z is the structural impedance, d_{32} is the PZT constant, \bar{Y}_{22}^E is the complex PZT modulus at zero electric field defined by $Y_{22}^E(1 + i\eta)$, and η is the mechanical loss factor of the PZT. The short-circuit mechanical impedance of the PZT actuator, Z_A , is given by (Liang et al., 1994):

$$Z_A = - \frac{K_A(1 + \eta i)}{\omega} \frac{kl_A}{\tan(kl_A)} i \quad (3)$$

For this equation, the wave number squared, k^2 , is given by:

$$k^2 = \omega^2 \rho_A / \bar{Y}_{22}^E \quad (4)$$

Here, ρ_A is the PZT actuator mass density. The PZT static stiffness, K_A , is given by:

$$K_A = Y_{22}^E \frac{w_A l_A}{h_A} \quad (5)$$

In order to calculate the structural impedance, Z , the equa-

tion of motion for a beam with an offset strain actuator, as shown earlier in Figure 1, is used:

$$\rho_B \frac{\partial^2 w}{\partial t^2} = -\bar{Y}_B K^2 \frac{\partial^4 w}{\partial x^4} + \frac{p(x,t)}{a} \quad (6)$$

where

$$w(x,t) = \sum W_n \phi_n e^{i\omega t} \quad (7)$$

$$p(x,t) = \sum p_n \phi_n e^{i\omega t} \quad (8)$$

Here K^2 is $h_B^2/12$, ϕ_n is the normalized eigenfunction given by $\phi(\lambda_n x)$, λ_n is the eigenvalue, \bar{Y}_B is the complex Young's modulus for the steel beam, and a is the beam cross-sectional area. For this initial case, the actuator and the bracket structure mass loading is neglected. Next by substituting Equations (7) and (8) into Equation (6), the equation of motion for the beam can be expressed in a matrix format (Liang et al., 1994):

$$\{\bar{Y}_B K^2 [\lambda^4]_{diag} - \omega^2 (\rho_B [I])\}[W] = \frac{1}{a} [p] \quad (9)$$

For this case, the eigenvalue matrix is a diagonal matrix, the $[I]$ matrix is the identity matrix, the $[W]$ matrix is the modal amplitude matrix for the transverse displacement Equation (7), and the $[p]$ matrix is the modal amplitude matrix for the pressure Equation (8). In order to calculate the modal pressure amplitude for Equation (8), the equivalent PZT effect on the cantilever beam first has to be modeled. The general technique for utilizing an actuator for structural excitation is bonding the actuator onto the beam. By doing so, the in-plane forces of the actuator are transferred onto the structure via the bonding material as line moments distributed along the periphery of the actuator, as shown in Figure 3. Offsetting the actuator as done for this case simply eliminates the line moments from the two sides that are not connected to the beam and also increases the actuator force transferred onto the structure (Chaudhry and Rogers, 1993). Note that in this case the offset is not to enhance actuator authority,

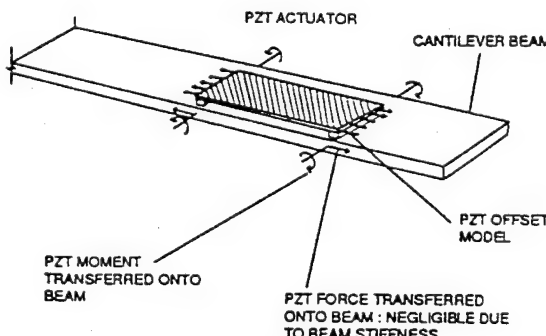


Figure 3. PZT moment model.

but to allow for actuator relocation. Offsetting the actuator and increasing the actuator thickness also yield a proportional increase in the overall structural stiffness. The overall qualitative actuator response characteristics, however, are not significantly changed from the bonded to the offset configuration. This moment distribution onto the beam can be expressed in terms of Heaviside functions as:

$$M(x) = M[H(x - \xi_2) - H(x - \xi_1)] \quad (10)$$

Here ξ_1 and ξ_2 represent the PZT location from the clamped edge of the cantilever beam, also shown in Figure 1. This moment equation can be used to express the pressure function, Equation (8) as:

$$p(x) = \frac{d^2 M(x)}{dx^2} = M[\delta'(x - \xi_2) - \delta'(x - \xi_1)] \quad (11)$$

The modal amplitude for the pressure equation can be determined as:

$$P_m = \frac{\int_0^L p(x) \phi_m(x) dx}{\int_0^L \phi_m^2(x) dx} \quad (12)$$

For a cantilever beam, the eigenfunction is given by (Shames and Dym, 1985):

$$W_n = \cosh(k_n x) - \cos(k_n x) - \frac{\cos(k_n L) + \cosh(k_n L)}{\sin(k_n L) + \sinh(k_n L)} (\sinh(k_n x) - \sin(k_n x)) \quad (13)$$

For the cantilever beam eigenfunction, Equation (13), k_n represents the normalized eigenvalue. The value of k_n for the eigenfunction equation are the zeros of the equation: $\cos(k_n L) - \cosh(k_n L) = -1$, where L is the length of the beam. For $n \geq 5$, the eigenvalues can be approximated by the equation: $k_n \approx (4n + 1)\pi/4$. Since the effect of the PZT actuator can be modeled by a pair of moments at the PZT edges, as shown in Figure 3, the equivalent rotational structural impedance due to a pure bending moment is given by (Liang et al., 1994):

$$Z_R = M/(\dot{\theta}_2 - \dot{\theta}_1) = M/(\theta_2 - \theta_1)i\omega \quad (14)$$

Here, θ_1 and θ_2 correspond to the rotational angles at ξ_1 and ξ_2 , respectively, M is the unit moment, and ω is the excitation frequency. The beam rotations can be calculated by:

$$\theta_1 = \sum_{m=1}^{\infty} W_m \phi'_m |_{x=\xi_1} \quad (15)$$

$$\theta_2 = \sum_{m=1}^{\infty} W_m \phi'_m |_{x=\xi_2} \quad (16)$$

Since the actuator power factor approach is based on the concept of mechanical impedance, the actuator force onto the host structure can be expressed as:

$$F = Z \dot{x} \quad (17)$$

Therefore, the equivalent mechanical impedance Z can be determined as a function of the equivalent structural impedance, Z_R , as:

$$Z = \left[Z_R \left(\frac{h_B}{2} + PZT_{OFFSET} + \frac{h_A}{2} \right) \right] \quad (18)$$

Here, the PZT_{OFFSET} is the distance from the top of the cantilever beam to the bottom of the bonded PZT on the bracket unit, as shown earlier in Figure 1. Therefore by substituting Equations (18) and (14) into Equation (2), the actuator power factor can be determined by Equation (1). This overall procedure can then be used to analytically plot the PZT actuator power factor variation as a function of the excitation frequency. The analytically predicted results for the actuator power factor for the cantilever beam set-up will next be compared to the experimentally measured results for the actuator power factor.

Analytically and Experimentally Determined Actuator Power Factor: Cantilever Beam

In order to compare the analytically predicted results for the actuator power factor to the experimentally measured results, the cantilever beam described earlier was excited at five points. For these five points, two different PZT actuators were used such that the effect of varying the PZT properties could also be evaluated. The properties for the cantilever beam and the two different PZT actuators used for this experiment are listed in Table 1. The PZT electromechanical properties are listed in Table 2. Analytically the ex-

Table 1. Cantilever beam and PZT specifications.

Properties	<i>l</i> (m)	<i>w</i> (m)	<i>h</i> (m)	ρ (kg/m ³)	γ (N/m ²)
Cantilever beam	0.4572	0.0254	0.0064	7850	207e9
PZT #1	0.0380	0.0190	0.0004	7650	62.7e9
PZT #2	0.0500	0.0130	0.0008	7650	62.7e9

Table 2. PZT electromechanical properties.

d_{32} (m/V)	Y_{22}^E (N/m ²)	ϵ_{33}^T (Farads/m)	δ	η
-166×10^{-12}	6.5×10^{10}	1.5×10^{-4}	0.012	0.001

pected natural frequencies for this cantilever beam can be calculated by the equation:

$$\omega_n = k_n^2 \left(\frac{E_B I_B}{Q_B A_B} \right)^{1/2} \quad (19)$$

Here, I_B is the beam moment of inertia, A_B is the beam cross-sectional area. Using this equation, the first four natural frequencies for this beam are shown in Table 3. The expected node locations from the clamped edge of the beam corresponding to the respective natural frequency are listed in Table 4. A PZT location with respect to a node location on a given beam is critical in determining which mode can be excited with maximum efficiency. These node locations, as shown in Table 4, will later be used to analyze a PZT actuator's ability to excite a given mode with respect to the PZT location on the cantilever beam. The PZT placement distances given from the beam clamped edge for the five points at which the experimentally measured and the analytically predicted results are compared are listed in Table 5 for PZT #1 and PZT #2. These points are selected by simply dividing the cantilever beam into five equal sections and measuring ξ_1 and ξ_2 by centralizing the PZT bonded onto the bracket unit within each of these sections. For PZT #1, the offset distance, as shown in Figure 1, is 0.0044 mm; for PZT #2 the offset distance is 0.0036 m.

Before proceeding further, a brief check was made to see whether the two PZT actuators buckle or not in the present configuration during the excitation process. If the PZT actuators do not buckle, the analytical model for the PZT resultant moments will be correct. For an applied sinusoidal voltage to a PZT, the PZT response is sinusoidal as well. However in the offset configuration shown earlier in Figure 3, a PZT can buckle and produce a nonharmonic excitation force. This nonharmonic PZT excitation force output will lead to a nonharmonic structural excitation and thus a false structural response. Therefore, for a PZT in the clamped-clamped configuration, the critical compressive force is defined as:

$$P_{cr.} = \frac{4\pi^2 EI}{l^2} \quad (20)$$

Table 3. Cantilever beam natural frequencies.

ω_{n1} (Hz)	ω_{n2} (Hz)	ω_{n3} (Hz)	ω_{n4} (Hz)
24	149	418	819

Table 4. Cantilever beam node locations.

Nodes (ω_{n1}) (m)	Nodes (ω_{n2}) (m)	Nodes (ω_{n3}) (m)	Nodes (ω_{n4}) (m)
0	0, 0.357	0, 0.229, 0.402	0, 0.165, 0.293, 0.412

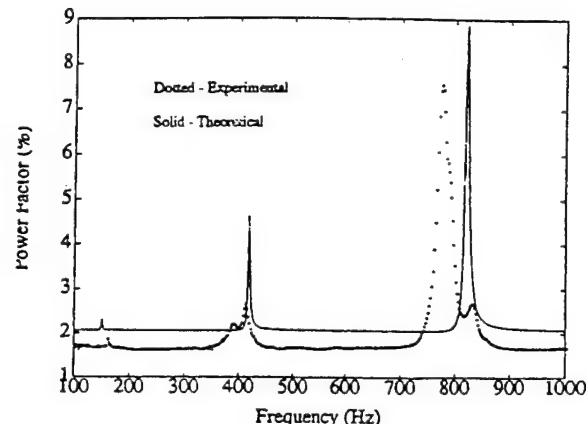
For the PZT actuators used, the modulus of elasticity $E \approx 62.7 \times 10^9 \text{ N/m}^2$, and I is the PZT moment of inertia. Thus for PZT #1, $P_{cr.} \approx 170 \text{ N}$, and for PZT #2, $P_{cr.} \approx 550 \text{ N}$. For the maximum supply voltage of $V_{max} = 1 \text{ V}$, as supplied by the impedance analyzer used for the power factor measurement, the maximum electric field for PZT #1 will be 156 V/m , and for PZT #2 will be 1250 V/m . The maximum compressive force for the perfect constraint case (i.e., blocked) for the PZT can be computed as (Crawley and deLuis, 1993):

$$F_{max} = AE(E_{max})d_{31} \quad (21)$$

Here, A is the PZT cross-sectional area, and $d_{31} = 166 \times 10^{-12} \text{ m/V}$. Thus for PZT #1, $F_{max} \approx 0.012 \text{ N}$, and for PZT #2, $F_{max} \approx 0.135 \text{ N}$. Therefore the compressive forces for PZT #1 or PZT #2 are small enough such that buckling does not occur.

In order to experimentally determine the power factor variation for a cantilever beam, an HP 4194 A impedance analyzer was used to measure the PZT admittance (Y) for an excitation range of 100–1000 Hz. The frequency interval for the measurement was 2.250 Hz (the minimum step allowed by the impedance analyzer). The impedance analyzer outputs a $\pm 1 \text{ V}$ signal throughout the given frequency range. The current is modulated due to the PZT-structure interaction and results in a change in the PZT admittance. The real and the imaginary parts of the admittance can then be used in Equation (1) to determine the actuator power factor.

The power factor variation for pt. #1 for PZT #1 is evaluated for the analytical model and the experimental measurement, and the power factor plot is shown in Figure 4. This plot shows good conformity between the experimental and the theoretical results. It can be seen that at pt. #1, the actuator is much more efficient at exciting the fourth mode of vibration (819 Hz) for the beam, than the second mode (149 Hz) or the third mode (418 Hz). This can be verified by checking the node locations for the respective natural frequencies. Since the node for the second mode is located near 0.357 m and for the third mode is located near

**Figure 4. Actuator power factor: pt. #1 for PZT #1.**

0.402 m, the actuator location between $\xi_1 = 0.389 \text{ m}$ and $\xi_2 = 0.437 \text{ m}$ fails to efficiently excite these two modes. The plot also shows that the magnitudes for the analytically predicted power factor peaks are greater than the magnitudes for the experimentally measured peaks. The beam used for the experimental power factor measurement was slightly "bowed". This lack of uniformity in the beam configuration resulted in variations in the power factor peak magnitudes depending on how the bracket unit was bonded onto the beam (i.e., bonded onto the concave up or concave down side). The frequencies at which the analytically predicted peaks occur are also higher than those for the experimental results. One explanation for this is that for the experimental set-up, the additional mass loading of the bracket structure leads to a decrease in the cantilever beam natural frequency magnitudes. In relation to the cantilever beam, the ratio of the weights of the cantilever beam to the bracket unit without the side supports is (10.4:1 or 583 g: 53 g). For this initial analytical model, the bracket unit mass loading was not taken into account. Also, as explained earlier, the increase in the beam stiffness due to the offset actuator also leads to an increase in the experimental natural frequencies. For large structures, where the ratio of the bracket unit weight to the structural weight and where the effect of the actuator offset on the structural stiffness, can be negligible, the variations between the experimental and the theoretical power factor peaks and natural frequency magnitudes should be greatly reduced. The baseline for the analytically predicted results is also higher than that for the experimental results. This is because of the approximation for the PZT dielectric loss factor, δ , for the analytical model. An increase in δ raises the analytical power factor baseline

Table 5. PZT placement distances ξ_1 and ξ_2 (m).

Locations	Pt. #1 (ξ_1, ξ_2) (m)	Pt. #2 (ξ_1, ξ_2) (m)	Pt. #3 (ξ_1, ξ_2) (m)	Pt. #4 (ξ_1, ξ_2) (m)	Pt. #5 (ξ_1, ξ_2) (m)
PZT #1	0.389, 0.437	0.297, 0.345	0.198, 0.246	0.114, 0.163	0.020, 0.069
PZT #2	0.384, 0.445	0.292, 0.353	0.201, 0.262	0.109, 0.170	0.018, 0.079

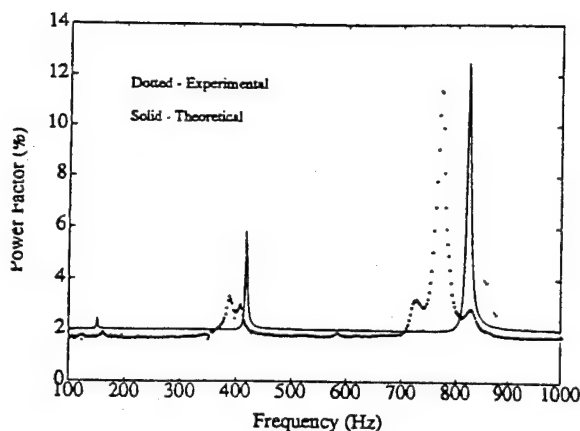


Figure 5. Actuator power factor: pt. #1 for PZT #2.

and a decrease in δ will yield a closer analytical model in terms of the power factor baseline. For the analytical results, the magnitude of the power factor peaks were also strongly dependent on the PZT location on the beam (i.e., ξ_1 , ξ_2). Therefore, since the bracket structure contacted the cantilever beam over an area of approximately $0.02 \times 0.02 \text{ m}^2$, the locations ξ_1 and ξ_2 could only be approximated. Thus the actual moment locations may not be exactly at ξ_1 and ξ_2 , as shown in Figure 1.

The power factor variation for pt. #1 for PZT #2 for the analytical model and the experimental measurement is shown in Figure 5. This plot also is qualitatively similar to the plot for pt. #1 for PZT #1. For this case, even with a significant change in the actuator configuration, the experimental results show good conformity to the theoretical results. As for the case for PZT #1 for these experimental results, the main reason for the decrease in the experimental natural frequency values is the mass loading effect of the bracket unit. Since PZT #2 was longer than PZT #1, a longer bracket unit was also used for this case. The overall dimensions of the center pieces for this case, however, are identical to those used for PZT #1.

The experimentally measured and the analytically predicted actuator power factor plots for PZT #1 for pt. #2, pt. #3, pt. #4, and pt. #5, respectively, are shown in Figure 6. The plots show that as the bracket unit location (i.e., actuator location) is shifted on the beam towards the clamped edge (i.e., from pt. #1 to pt. #5), the actuator's ability to excite a given mode of vibration changes. At pt. #3, which is close to one of the nodes at 0.229 m of the cantilever beam corresponding to the third mode of vibration (418 Hz), the actuator is extremely inefficient at exciting this mode. This trend for pt. #3 as predicted by the power factor algorithm is also demonstrated by the experimental data. The power factor plots for pt. #2, pt. #3, and pt. #4 show reasonably good conformity between the analytical and the experimental results. For pt. #5, analytically, the fourth mode of vibration for the beam (819 Hz) should not occur. However experimentally, this mode does occur. One reason for this

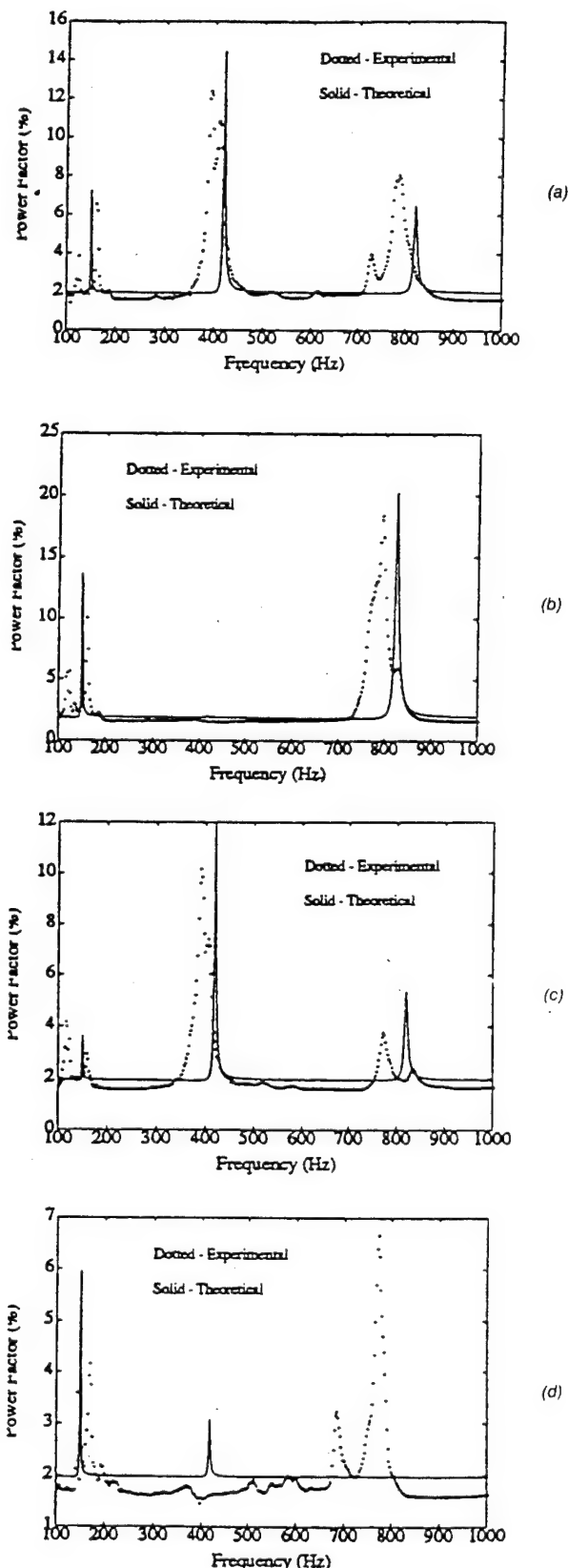


Figure 6. Actuator power factor for PZT #1: (a) pt. #2 for PZT #1, (b) pt. #3 for PZT #1, (c) pt. #4 for PZT #1 and (d) pt. #5 for PZT #1.

occurrence is that, analytically, the bracket unit is located near one of the nodes for the fourth mode (i.e., at 0 m). However, the bracket unit location as seen by the beam for the experimental setup is actually further away from the clamped edge than represented by ξ_1 and ξ_2 for pt. #5. The reason for this effect includes an "imperfect" clamped configuration and a shift towards the free edge of the beam in the node locations due to the addition of the bracket unit mass for the experimental setup. Therefore, if the mass loading effect (weight and location) of the bracket unit were taken into account, this fourth mode perhaps could have been predicted analytically.

The experimentally measured and the analytically predicted actuator power factor plots for PZT #2 for pt. #3, and pt. #5, respectively, are shown in Figure 7. As for the case for PZT #1, the analytical and the experimental power factor results for PZT #2 for pt. #3 shows good correlation. Again as pt. #3 is close to one of the nodes for the cantilever beam (node at 0.229 m corresponding to $\omega_{n3} = 418$ Hz), the actuator is unable to excite this mode efficiently. For pt. #5, the actuator in this case analytically should be unable to excite the fourth mode of vibration (i.e., 819 Hz). However experimentally, this mode is excited for the given actuator

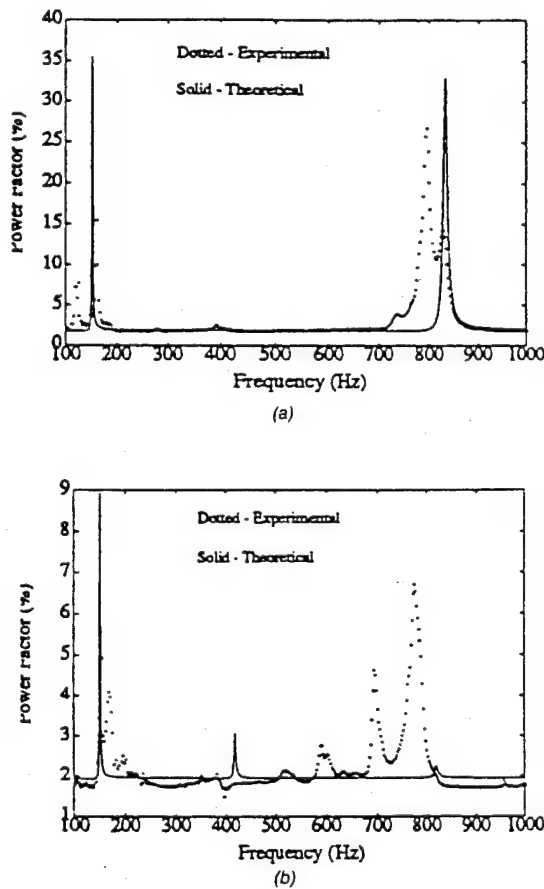


Figure 7. Actuator power factor for PZT #2: (a) pt. #3 for PZT #2 and (b) pt. #5 for PZT #2.

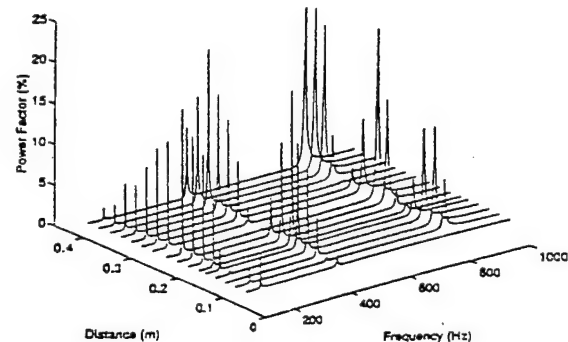


Figure 8. Three-dimensional power factor layout.

location. As in the case for PZT #1, if the bracket unit mass loading effect was taken into account for PZT #2, for pt. #5 this mode perhaps could have been predicted analytically.

Next, the power factor results for PZT #1, as predicted by the actuator power factor algorithm, are plotted in three dimensions, as shown in Figure 8. The distance label on the graph represents the distance measured from the beam clamped edge. This type of a 3-D plot can be very helpful as a practical "tool" for a more complicated structure for evaluating and determining approximately at which location and for which excitation frequency range a given actuator is best suited as the actuator location on the structure is varied.

CONCLUSION

In conclusion, the concept of actuator power factor has thus far proven to be a very helpful tool in determining the optimal actuator location and configuration for a given structure, as demonstrated by the cantilever beam example in this paper. For variations in the actuator location and the actuator configuration, the analytically determined power factor results show good conformity with the experimentally measured results. These results also complement the ability of the bracket-type unit designed for the actuator plate relocation to efficiently excite a structure in a manner qualitatively similar to a bonded actuator. For the future, the actuator power factor algorithm will be evaluated for a larger structure (i.e., plate, cylinder). Again, the relocation capability of the actuator plate as allowed by the bracket unit will similarly be utilized for the case of the more complex structure. These comparisons will lead to a broader understanding as to the capabilities and the limitations of the actuator power factor algorithm as a tool for determining the optimal configuration and location for a PZT actuator for structural vibration control applications.

ACKNOWLEDGEMENTS

The authors wish to acknowledge the support of the Air Force Office of Scientific Research, AFOSR Grant No.

F49620-93-1-0166, Walter F. Jones and Spencer Wu, Program Managers.

REFERENCES

- Blevins, R. D. 1989. *Formulas for Natural Frequency and Mode Shapes*. Van Nostrand Reinhold Company, pp. 119-122.
- Chaudhry, Z. and C. A. Rogers. 1993. "Enhancing Induced Strain Actuator Authority through Discrete Attachment to Structural Elements", *AIAA Journal*, 31(7):1287-1292.
- Crawley, E. F. and J. de Luis. 1986. "Use of Piezoelectric Actuators as Elements of Intelligent Structures", *AIAA/ASME/ASCE/AHS Journals, AIAA Journal*, pp. 1373-1384.
- Liang, C., F. P. Sun and C. A. Rogers. 1993a. "An Impedance Method for Dynamic Analysis of Active Material Systems", *Proceedings, 34th SDM Conference*, pp. 3587-3599.
- Liang, C., F. P. Sun and C. A. Rogers. 1994. "Development of an Actuator Power Factor Meter for Experimental Determination of the Optimal Actuator Locations on Complex Structures", *Proceedings, 1994 North American Conference on Smart Materials and Structures*.
- Meirovitch, L. 1975. *Elements of Vibration Analysis*. McGraw-Hill, Inc., pp. 221-225.
- Preumont, A., J. P. Dufour and C. Malekian. 1991. "Active Damping by a Local Force Feedback with Piezoelectrical Actuators", *Proceedings, 1991 SDM Conference*, pp. 1879-1887.
- Shames, I. H. and C. L. Dym. 1985. *Energy and Finite Element Methods in Structural Mechanics*. Hemisphere Publishing Company, pp. 330-333.

Thermal dissipation and thermal stress of induced strain actuators

Zhou, S.W., and Rogers, C.A., "Heat Generation, Temperature, and Thermal Stress of Structurally Integrated Piezo-Actuators," *Journal of Intelligent Material Systems and Structures*, Vol. 6, May 1995, pp. 372-379.

Heat Generation, Temperature, and Thermal Stress of Structurally Integrated Piezo-Actuators

SU-WEI ZHOU AND CRAIG A. ROGERS*

*Center for Intelligent Material Systems and Structures
Virginia Polytechnic Institute and State University, Blacksburg, VA*

ABSTRACT: While converting electrical energy into mechanical energy to actuate structures, piezoelectric (PZT) elements experience a temperature increase due to internal heat generation caused by their mechanical damping and dielectric loss. In practice, if the actuation is operated at system resonance or with a relatively high electrical field, the heat generation throughout PZT actuators may be significant. The temperature rise of PZT elements may result in the acceleration of material aging, even thermal damage. The situation becomes worse if the actuated host structures are made of thermal-resistant materials, such as polymeric matrix composites and glass. In addition, the temperature distribution in PZT elements induces thermal stress that may increase the overall stress level and reduce the maximum safe stress. However, investigations done to date on these issues have been limited.

This paper presents a simple analytical approach to estimate temperature rise and thermal stress in PZT patch actuators due to dynamic excitation. A one-dimensional heat transfer model is developed for integrated PZT/plate structures. The temperature field of the PZT actuators is analytically found and the corresponding thermal stress is predicted. To determine the internal heat dissipation in PZT actuators, an electro-mechanical impedance model developed by the authors is directly applied. The dissipative power in the systems, consumed by mechanical damping and dielectric loss of the PZT actuators, and structural damping of the host structure, is first determined. The dissipative power is then treated as the equivalent thermal dissipation to create a distributed heat source throughout the PZT actuators and host structures.

In the case studies, the PZT patch elements were used to actuate a simply-supported plate. The impact of the thermal stress on the overall stress level is discussed in the paper. The effects of actuator thickness and material properties on the actuator temperature and the thermal stress level have also been investigated.

INTRODUCTION

PIEZOELECTRIC (PZT) materials have been most commonly used as active elements in adaptive structures for various industrial and research applications. For the purpose of structural actuation, the mechanical output performance and dynamic behaviors of PZT elements have been widely investigated (Bailey and Hubbard, 1985; Crawley and de Luis, 1987; Crawley and Lazarus, 1991; Dimitriadis et al., 1989; Liang et al., 1993; Zhou et al., 1993). For space applications, system power consumption is one of the major concerns. Enhancing energy conversion efficiency results in a reduction in the cost and mass of systems, two of the major objectives of adaptive structures. Stein et al. (1993) investigated the power consumption of a PZT actuator integrated on an underwater structure that radiates sound, and considered the power requirements in the active acoustic control. Lomenzo et al. (1993) developed a technique to maximize mechanical power transfer from the stacked PZT actuators to the host structures. Zhou et al.

(1994) performed a coupled electromechanical impedance analysis for two-dimensional PZT actuator-driven systems and discussed the influence of different dissipators on the system power factor and the system power requirement.

The system dissipative power is eventually transformed into internal heat energy in PZT elements. An increase in the temperature of the actuators is thus inevitable. The phenomenon of temperature rise of PZT actuators has often been noticed in experiments. When PZT elements operate at a certain temperature, piezoelectric properties, such as the dielectric constant and the piezoelectric constant, change because of the strong temperature dependency. Figures 1 and 2 show the variation of piezoelectric constant d_{31} and relative dielectric constant (K) with temperature, respectively (Piezo Systems, Inc., 1993). The material of PSI-5H displays stronger temperature sensitivity than PSI-5A.

If the temperature is close to the Curie temperature of PZT materials, which represents a maximum operating temperature before suffering a permanent loss of piezoelectricity, the maximum safety stress of PZT elements is reduced and thermal damage may take place. The Curie temperature is about 350°C for PSI-5A, and about 200°C for

*Author to whom correspondence should be addressed.

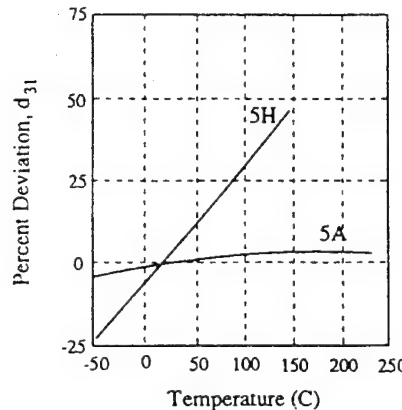


Figure 1. Influence of temperature on the piezoelectric constant, d_{31} , for typical piezoelectric materials: PSI-5A and PSI-5H (Piezo Systems, Inc.).

PSI-5H, respectively. In practice, as PZT elements are used for structural actuation at the system resonance or with a large electrical field, heat generation throughout PZT actuators may be significant. Sometimes, the tin solder points on the surface of PZT actuators even melt down. The situation becomes worse if actuated host structures are made of thermal resistant-materials, such as polymeric matrix composites or glass. In the meantime, the temperature gradient existing in PZT elements induces thermal stress, which may have an impact on the overall mechanical stress. Therefore, the heat transfer analysis of integrated PZT elements in structural actuation is of practical engineering importance. Investigation of these issues, however, has been limited.

The emphasis of this current work is on the development of a simple approach to analyze and estimate temperature rise of PZT elements because of internal heat generation. A one-dimensional heat transfer model will be applied to integrated PZT/plate structures. The temperature field of the PZT actuators will be analytically found and the corre-

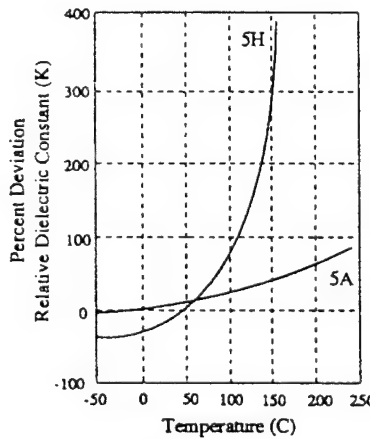


Figure 2. Influence of temperature on the relative dielectric constant, K , for typical piezoelectric materials: PSI-5A and PSI-5H (Piezo Systems, Inc.).

sponding thermal stress will be quantitatively estimated. To determine the rate of internal heat generation in PZT actuators, a coupled electro-mechanical system model developed by the authors is directly used. The system dissipative power will be predicted and treated as equivalent thermal dissipation to generate a distributed heat source throughout PZT actuators and host structures. A piezoelectric actuator-driven simply-supported plate will be used in the case studies. A comparison between the thermal stress level and the mechanical stress level is made to identify the impact of the thermal stress on the overall stress level. The effects of the actuator thickness, the magnitude of applied voltage, and material properties on the actuator temperature and the thermal stress level will be investigated.

ANALYTICAL MODEL

Figure 3 illustrates the schematic geometry of an integrated PZT/plate structure. Two PZT patches are bonded on the top and bottom surfaces of the plate. The integrated PZT/plate system is exposed to ambient room air without an external cooling source. It is assumed that the thickness of the plate and the PZT element is much smaller than the sizes in the other coordinate directions. The flow of heat through the plate and the PZT element thus depends only on the coordinate measured normal to the x - y plane, resulting in a one-dimensional heat transfer problem with no edge effects. Figure 4(a) shows such a one-dimensional model. The internal heat generation, Q_p , is assumed to be uniform throughout the PZT element and the plate, respectively. The steady state temperature distribution of the PZT element needs to be found, and thermal stress induced in the PZT element can then be estimated.

Considering the symmetrical condition of heat transfer, the problem shown in Figure 4(a) may be simplified to the equivalent situation displayed in Figure 4(b). The mid-plane

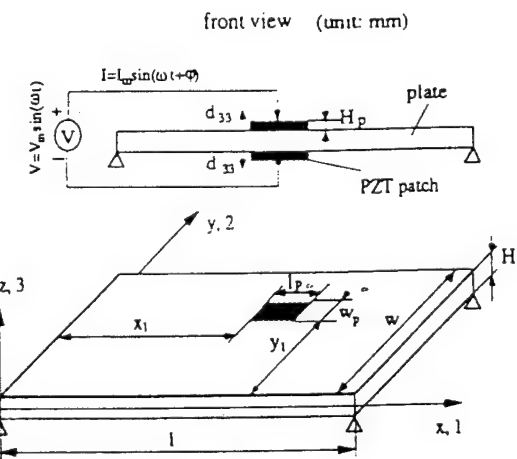


Figure 3. Schematic geometry of an integrated PZT/plate structure.

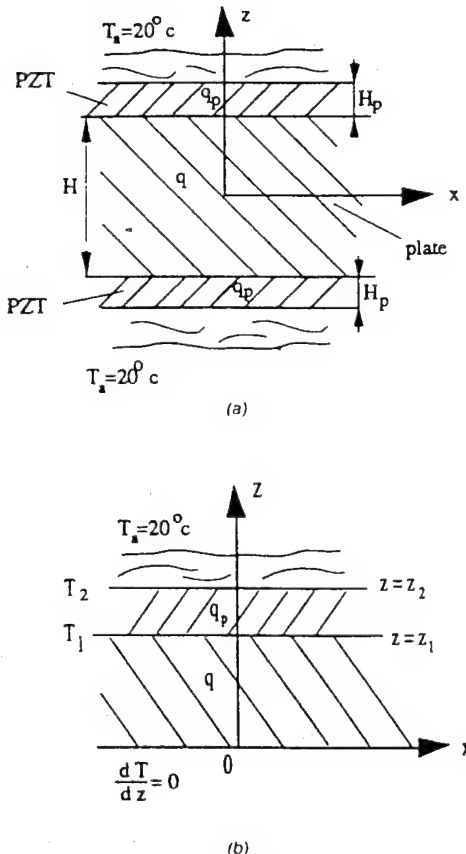


Figure 4. Schematic diagram of a heat transfer model for the analysis of temperature distribution of PZT elements integrated with a plate structure.

of the plate is isolated, that is, $dT/dz = 0$. The governing differential equation of the temperature distribution cross the PZT element is depicted by:

$$\frac{d^2T_p}{dz^2} + \frac{Q^*}{k_p} = 0 \quad (1)$$

where the subscript p denotes the parameters of the PZT element; k symbolizes the thermal conductivity; Q^* represents the rate at which heat is being internally generated in the PZT patch per unit volume (watt/m^3); $Q^* = Q/V$ and V is the volume of the element; and T is the temperature distribution in the PZT element. Twice integrating Equation (1) with respect to the coordinate z obtains:

$$T_p = a_1 + b_1 z - \frac{Q_p^*}{2k_p} z^2 \quad (2)$$

where a_1 and b_1 are the integration constants.

For the host plate, the governing differential equation of the temperature distribution and the corresponding solution are similar to Equations (1) and (2):

$$\frac{d^2T}{dz^2} + \frac{Q^*}{k} = 0 \quad (3)$$

and

$$T = a_2 + b_2 z - \frac{Q^{*2}}{2k} z^2 \quad (4)$$

where a_2 and b_2 are integration constants. To determine a_1 , b_1 , a_2 , and b_2 , one may use the boundary conditions,

$$\left\{ \begin{array}{l} \left(\frac{dT}{dz} \right)_{z=0} = 0 \\ (q_p)_{z=z_1} = h(T_2 - T_a) \end{array} \right. \quad (5)$$

and the temperature continuity and heat transfer continuity at the interface of the PZT element and the plate,

$$\left\{ \begin{array}{l} T_{z=z_1} = (T_p)_{z=z_1} \\ q_{z=z_1} = (q_p)_{z=z_1} \end{array} \right. \quad (6)$$

The constant, h , in Equation (5) refers to the convection heat transfer coefficient, or film coefficient. For free convection in air, $h = 5-25 \text{ w}/(\text{m}^2 \cdot \text{C})$ (Chapman, 1974). T_2 and T_a in Equation (6) are the surface temperature of the PZT element and the air temperature at the ventilated room, respectively. The heat flux q in Equations (5) and (6) can be found by using Fourier's law:

$$q = \frac{Q}{S} = -k \frac{dT}{dz} \quad (7)$$

in which the minus sign indicates that the heat flow is taken to be positive if dT is negative in the direction of increasing z ; S is the surface area of the plane structure. Substituting Equations (2), (4) and (7) into Equations (5) and (6) and solving for the integration constants yield:

$$\left\{ \begin{array}{l} a_1 = -\frac{Q_p^* - Q^*}{k_p} z_1 z_2 + \frac{Q_p^*}{2k_p} z_2^2 \\ \quad + \frac{1}{h} [Q^* z_1 + Q_p^*(z_2 - z_1)] + T_a \\ b_1 = \frac{z_1}{k_p} (Q_p^* - Q^*) \\ a_2 = \frac{z_1^2}{2} \left(\frac{Q^*}{k} - \frac{Q_p^*}{k_p} \right) + a_1 + b_1 z_1 \\ b_2 = 0 \end{array} \right. \quad (8)$$

where z_1 and z_2 are the coordinates of the two surfaces of the

PZT element; and the heat generation rate, Q_p^* in the PZT actuator and Q^* in the plate, can be obtained from a coupled electro-mechanical system model and will be developed later. Substituting Equation (8) into Equation (2), the surface temperature of the PZT element, T_2 , can be obtained by:

$$T_2 = \frac{1}{h} [Q^* z_1 + Q_p^*(z_2 - z_1)] + T_a \quad (9)$$

Equation (9) indicates that the temperature in a PZT element increases with the rate of the internal heat generation, Q_p^* and Q^* , respectively. In addition, the temperature is inversely proportional to the heat conductivity of host structures.

The induced thermal stress, σ_T , is estimated by:

$$\sigma_T = \gamma_p Y_p (T_1 - T_2) \quad (10)$$

where Y_p and γ_p denote the real Young's modulus and the coefficient of thermal expansion of piezoelectric materials, respectively. For PSI-5A-S3 material (Piezo System, Inc., 1993), $\gamma_p = 4 \times 10^{-6}$ (m/m·°C).

HEAT GENERATION OF THE INTEGRATED SYSTEM

To estimate the heat generation in integrated PZT/plate systems, a coupled electro-mechanical system model is needed to quantitatively predict dissipative power consumption in the system. The power supplied to the PZT actuator is actually decomposed into two components (Zhou et al., 1994): one is the dissipative power,

$$P = \frac{I_m V_m}{2} \cos \phi = \frac{V_m^2}{2} \operatorname{Re}(A^*) \quad (11)$$

and the other is the reactive power,

$$R = \frac{I_m V_m}{2} \sin \phi = \frac{V_m^2}{2} \operatorname{Im}(A^*) \quad (12)$$

where A^* is the electro-mechanical admittance of the system and the superscript * symbolizes a complex number. The subscript m denotes the magnitude of the electrical parameters: the applied voltage, $V = V_m e^{j\omega t}$ and the current in the circuit, $I = I_m e^{j(\omega t + \phi)}$; ϕ denotes the phase between the current and voltage; j symbolizes the imaginary part of a complex number; and ω is the input angular frequency; and the total electrical power, i.e., apparent power, is expressed by:

$$W = \sqrt{P^2 + R^2} \quad (13)$$

The power requirement of the system can be estimated from the maximum value of the apparent power.

It is clearly seen that the system power consumption is essentially dominated by the coupled electro-mechanical admittance of the system. The complex electro-mechanical impedance of the integrated PZT/plate system was derived by the authors. The detailed theoretical development can be found in a separate reference (Zhou et al., 1994). The relevant formulations are directly given here. When an electrical field, $E = V/H_p$, is applied cross a PZT element along the polarization direction (3), the current passing through the PZT actuator can be derived based upon the capacitor behavior for the PZT material. Then, following the definition of coupled electro-mechanical admittance gives:

$$A^* = j\omega \frac{l_p w_p}{H_p} \left[\epsilon_{33}^* - \frac{2d_{31}^2 Y_p^*}{1 - \nu_p} + \frac{d_{31}^2 Y_p^*}{1 - \nu_p} \left(\frac{S_l S_w}{l_p w_p} \right) N_{2x2}^{-1} \right] \quad (14)$$

where $S_l = \sin(\alpha_p l_p)$ and $S_w = \sin(\alpha_p w_p)$; l_p , w_p , and H_p are the length, width, and thickness of the PZT element, respectively; d_{31} is the piezoelectric constant; ν_p is the Poisson's ratio of the PZT material; $\epsilon_{33}^* = \epsilon_{33}(1 - j\delta_p)$ is the complex dielectric constant at zero stress; δ_p is the dielectric loss factor of the PZT actuator; $Y_p^* = Y_p(1 + j\eta_p)$ is the complex Young's modulus at a zero electrical field; η_p is the structural loss factor. The wave number, α_p , is defined as:

$$\alpha_p = \omega \sqrt{\frac{\rho}{Y_p^*}} \quad (15)$$

in which ρ is the mass density. The matrix N_{2x2} in Equation (14) is depicted by:

$$N_{2x2} =$$

$$\alpha_p \begin{pmatrix} C_l \left(1 - \nu_p \frac{w_p}{l_p} \frac{Z_{yx}}{Z_{pxx}} + \frac{Z_{xx}}{Z_{pxx}} \right) & C_w \left(\frac{l_p}{w_p} \frac{Z_{xy}}{Z_{pyy}} - \nu_p \frac{Z_{yy}}{Z_{pyy}} \right) \\ C_l \left(\frac{w_p}{l_p} \frac{Z_{yx}}{Z_{pxx}} - \nu_p \frac{Z_{xx}}{Z_{pxx}} \right) & C_w \left(1 - \nu_p \frac{l_p}{w_p} \frac{Z_{xy}}{Z_{pyy}} + \frac{Z_{yy}}{Z_{pyy}} \right) \end{pmatrix} \quad (16)$$

in which $C_l = \cos(\alpha_p l_p)$ and $C_w = \cos(\alpha_p w_p)$; Z_{xx} and Z_{yy} are the direct impedance, and Z_{xy} and Z_{yx} are the cross impedance of the plate at the mid-point of the edge of the PZT element, respectively. For a simply-supported plate, the analytical solutions of the mechanical impedance of the system have been derived by the authors (Zhou et al., 1994). For complex structures, a finite element analysis or experimental approaches is helpful to determine the mechanical impedance of the system.

Our current interest is in the system dissipative power. It basically includes three parts in an integrated PZT/substrate system: (1) the power dissipated by the structural damping of the host structure, which is related to the structural loss factor in the complex Young's modulus; (2) the power consumed by the material damping of the PZT actuator; (3) the power consumption caused by the dielectric loss of the PZT actuator. The dissipative power is assumed to be totally converted into thermal energy to heat the system. The heat generation rate in the PZT element may be obtained by setting a zero structural loss factor for the plate in Equations (11) and (14):

$$Q_p^* = \frac{P_{\eta=0}}{l_p w_p H_p} \quad (17)$$

Similarly, assuming a zero mechanical loss and dielectric loss of the PZT element in Equations (11) and (14) gives the heat generation rate in the plate:

$$Q^* = \frac{P_{\eta_p=\delta_p=0}}{lwH} \quad (18)$$

where l , w , and H are the length, width, and thickness of the plate, respectively.

NUMERICAL CASES AND DISCUSSION

A simply-supported aluminum thin plate integrated with PZT patch elements is used in the current case studies. The geometric configuration of the integrated PZT/plate system is shown in Figure 3. The PZT elements are located on the plate at $x_1 = 158.8$ mm (6.25") and $y_1 = 82.6$ mm (3.25"). The sizes of the plate and the PZT patch are $228.6 \times 127 \times 1$ mm (9" \times 5" \times 0.04") and 38.1×25.4 mm (1.5" \times 1"), respectively. Table 1 lists the basic material properties of the PZT (PSI-5A-S3) and the plate.

The effect of the applied electrical field on the surface temperature of the PZT element is first examined. The thickness of the PZT actuator is selected as $H_p = 0.1$, 0.2, and 0.4 (mm). The free convection heat-transfer coefficient h in air at the ventilated room temperature, $T_e = 20^\circ\text{C}$, is chosen as 7 (w/m²·°C). The integrated system is assumed to be excited with a harmonic input at the 5th mode that is at a frequency of about 800 Hz. The surface temperature of

the PZT actuator is calculated using Equation (9). Figure 5 shows the numerical results. The temperature rapidly increases with the applied voltage because the internal heat generation rises with the order of the square of the applied voltage. At a constant voltage, decreasing the actuator thickness produces a stronger electrical field, resulting in an increment of the surface temperature.

When a voltage of 120 volts is applied to the PZT actuator with the thickness of 0.2 mm to excite the 5th mode, the temperature is up to 216°C which exceeds the melting point of the tin solder. A simple experiment was conducted to actuate an aluminum plate of the size $203 \times 101.6 \times 1$ mm (8" \times 4" \times 0.04") using the PZT patches ($H_p = 0.19$ mm). The phenomenon of melting of the tin solder was observed.

To identify the impact of the thermal stress on the overall stress level of the PZT actuator, the mechanical stress needs to be determined. The induced mechanical stress in the PZT element, σ_x and σ_y , can be calculated as follows (Zhou et al., 1994):

$$\begin{pmatrix} \sigma_x \\ \sigma_y \end{pmatrix} = \frac{Y_p^* V_m}{H_p (1 - \nu_p^2)} \begin{pmatrix} 1 & \nu_p \\ \nu_p & 1 \end{pmatrix} \cdot \left[\alpha_p \begin{pmatrix} \cos(\alpha_p x_p) & 0 \\ 0 & \cos(\alpha_p y_p) \end{pmatrix} N_{2 \times 2}^{-1} - I_{2 \times 2} \right] \begin{pmatrix} d_{31} \\ d_{32} \end{pmatrix} e^{j\omega t} \quad (19)$$

where $I_{2 \times 2}$ is an identical matrix; and x_p and y_p are the location coordinates of the stress point on the PZT actuator. The mechanical stress is a function of excitation frequency and the mechanical impedance of the system. It is assumed that the stress is measured at $x_p = 3$ mm and $y_p = 19$ mm. The size of the plate is again $228.6 \times 127 \times 1$ mm (9" \times 5" \times 0.04"). The size of the PZT element is $38.1 \times 25.4 \times 0.2$ mm (1.5" \times 1" \times 0.04"). Figure 6 illustrates the mechanical stress characteristics. The induced dynamic stress is a complex stress. At the resonant frequencies of the integrated system, the induced stress levels are very high because of the minimum structural impedance. While at off-resonance the induced dynamic stress approaches the static stress that is calculated using the static model developed by Dimitriadis et al. (1989).

If a $228.6 \times 127 \times 4$ mm (9" \times 5" \times 0.16") plate is excited at the 5th mode and the applied electrical field is main-

Table 1. Material properties of the PZT element* and the aluminum plate.

Young's Modulus (N/m ²)	Mass Density (kg/m ³)	Poisson's Ratio	Dielectric Constant (m/volt)	Loss Factor	Thermal Conductivity (w/m.c)
PZT	5.7×10^{10}	7700	0.3	-1.8×10^{-10}	0.005
Aluminum	6.9×10^{10}	2700	0.33	N/A	0.005

*Piezo Systems, Inc.

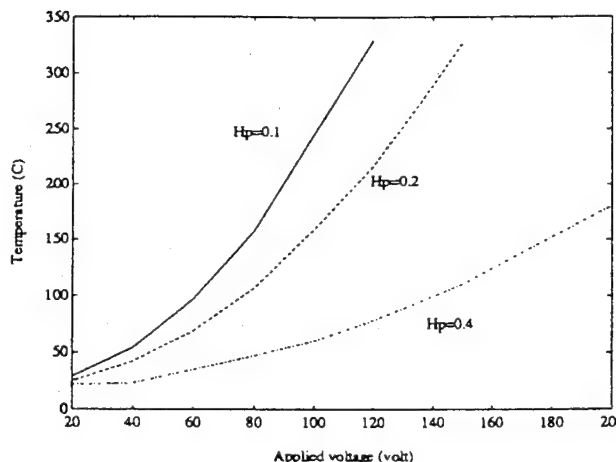


Figure 5. Effect of the applied electrical field on the surface temperature of PZT elements.

tained at 250 (volt/mm), Equations (10) and (19) can be used to obtain the thermal stress and mechanical stress of the PZT element, respectively. Figures 7 and 8 show the numerical results. The thermal stress induced in the PZT element increases when the element becomes thicker and thicker, as displayed in Figure 7. The mechanical stress, however, significantly declines when the thickness of the PZT element goes up, as displayed in Figure 8. It can be explained that the thicker PZT element has a larger cross sectional area that relieves the mechanical stress. On the other hand, the thicker element produces a larger temperature difference, leading to a higher thermal stress. This observation implies that the thermal stress in a stack PZT actuator (or a multilayer actuator) may become a major factor to influence the overall stress levels. It is also noted that the stress doesn't linearly change with the actuator thickness because the structural mechanical impedance is not simply linear function of the actuator thickness.

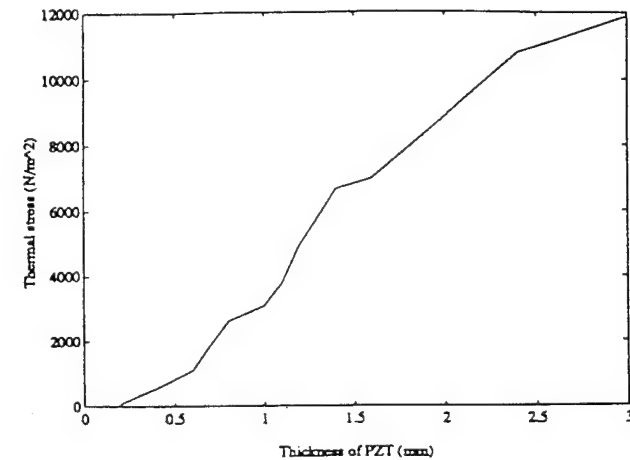


Figure 7. The thermal stress goes up as the thickness of the integrated PZT element increases ($E = 250$ volt/mm; $H = 4$ mm).

From a design point of view, one way to reduce the induced stress level in PZT elements is to limit the active voltage, leading to a decline in both the mechanical and thermal stress. In this case, the actuation force also decreases. The other way is to increase the cross-sectional area of PZT elements as the voltage increases so that the electrical field is maintained at a relatively low level to avoid possible thermal damage and mechanical degradation in the PZT elements. In general, when a thin PZT patch is used for the structural actuation, the induced mechanical stress is of major concern and the surface temperature of the actuator should also be considered. While a multilayer actuator or a stack actuator is applied for the actuation, the thermal stress may become an important factor in the actuator design and application.

To examine the influence of the thermal conductivity of the host plate on the surface temperature of PZT elements, three types of materials with different thermal conductivity are selected: aluminum, nickel steel, and glass. Table 2 lists

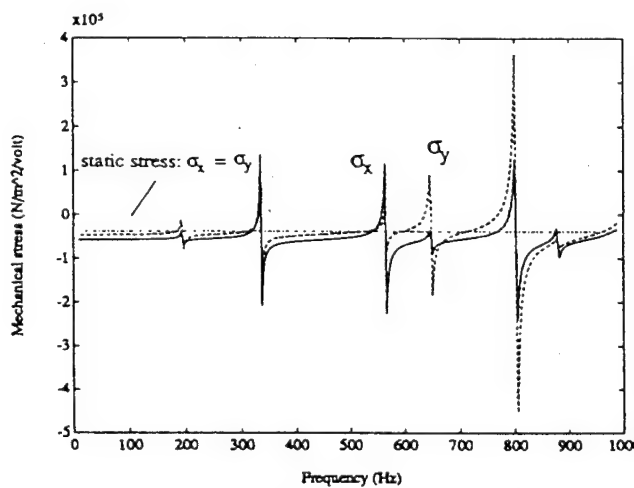


Figure 6. The mechanical stress characteristics of the integrated PZT elements.

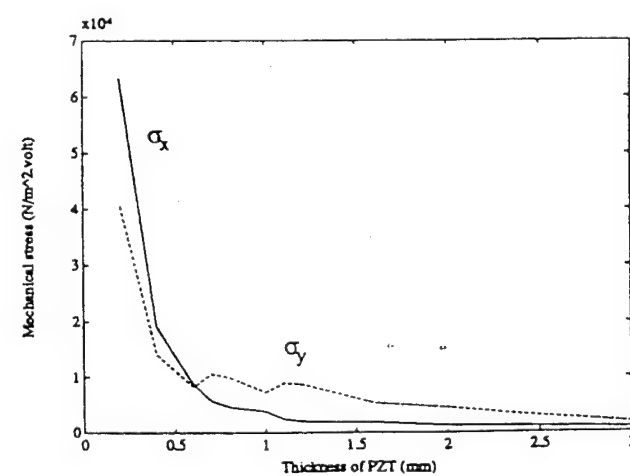


Figure 8. The mechanical stress decreases as the thickness of the integrated PZT element increases ($E = 250$ volt/mm; $H = 4$ mm).

Table 2. Material properties of the different plates and the PZT actuators.

	Young's Modulus (N/m ²)	Mass Density (kg/m ³)	Thermal Conductivity (w/m·°C)
Nickel steel	21×10^{10}	8800	18.6
Glass plate	6.4×10^{10}	2300	0.76
Aluminum	6.9×10^{10}	2700	112.5

the basic properties of the materials. For simplification, it is assumed that three investigated plates have the same geometric size and the structural damping. Figure 9 shows the numerical results. As PZT actuators are used to excite thermal-resistant material, such as glass and nickel steel, the temperature rises quickly. Under the condition of a constant magnitude of applied voltage, host structures with a good conductivity can slow down the temperature hike of PZT actuators as shown in Figure 9. The possible thermal degradation can be then relieved.

CONCLUSIONS

- A simple one-dimensional heat transfer model for piezoelectric elements for structural actuation has been suggested. The analytical model has been developed to quantitatively estimate the temperature rise and the induced thermal stress of the PZT elements.
- The heat generation of the integrated PZT/plate system has been determined from the dissipative power consumption using the electro-mechanical system model.
- Case studies have demonstrated that when the PZT actuator operates at system resonance, or with a relatively high

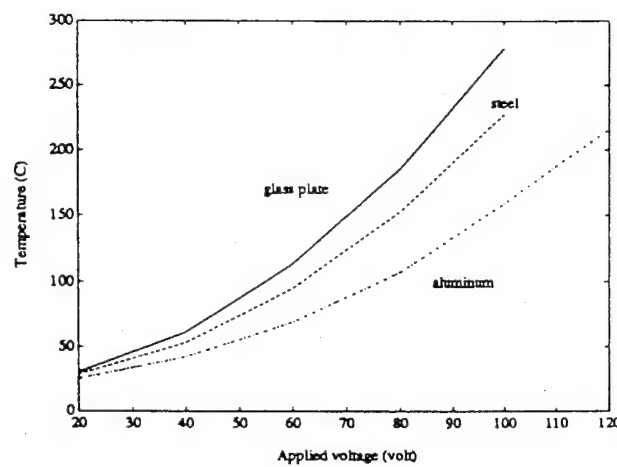


Figure 9. Influence of the thermal conductivity of the host structures on the surface temperature of the integrated PZT element ($E = 250$ volt/mm; $H = 4$ mm; and $H_p = 0.2$ mm).

electrical field, the heat generation and temperature rise of PZT actuators is significant and may cause the thermal degradation, even damages of PZT elements. The temperature of PZT actuators increases with the applied voltage because the heat dissipation is proportional to the square of the applied voltage. Under the excitation with a constant voltage, a thinner PZT actuator gains higher temperature rise due to the higher electrical field.

- The thermal stress increases with the thickness of PZT actuators. When a thicker PZT patch or a multilayer or a stacked PZT actuator is used for structural actuation, the thermal stress may become a significant factor influencing the strength design of the PZT actuator.
- When the thermal resistant materials are used for host structures, the temperature in PZT elements increases quickly, and cooling measures may be needed to avoid the possible thermal damages.

NOMENCLATURE

- A Electro-mechanical admittance
 d Piezoelectric constant
 E Electric field
 h Convection heat transfer coefficient
 H Thickness of a structure
 j Imaginary part of a complex number
 k Thermal conductivity
 l Length of a structure
 P Dissipative power
 q Heat flux
 Q Heat generation
 S Surface area of a structure
 T Temperature
 V Voltage
 w Width of a structure
 Y Young's modulus
 Z Mechanical impedance

Greek

- α Wave number
 γ Coefficient of thermal expansion
 σ Stress
 η Structural loss factor
 ν Poisson's ratio
 ϱ Mass density
 ω Angular frequency

Subscripts

- m Amplitude
 p Piezoelectric element
 x x -direction
 y y -direction

ACKNOWLEDGEMENT

The authors gratefully acknowledge the support of the Air Force Office of Scientific Research under AFOSR Grant No. F49620-93-1-0166; Dr. Jim Chang, Program Manager.

REFERENCES

- Bailey, T. and J. E. Hubbard. 1985. "Distributed Piezoelectric-Polymer Active Vibration Control of a Cantilever Beam", *AIAA Journal of Guidance and Control*, 6(5):605-611.
- Chapman, A. J. 1974. *Heat Transfer*. New York: Macmillan Publishing Co.
- Crawley, E. F. and J. de Luis. 1987. "Use of Piezoelectric Actuators as Elements of Intelligent Structures", *AIAA Journal*, 29(6):1373-1385.
- Crawley, E. F. and K. B. Lazarus. 1991. "Induced Strain Actuation of Isotropic and Anisotropic Plates", *AIAA Journal*, 29(6):945-951.
- Dimitriadis, E. K., C. R. Fuller and C. A. Rogers. 1989. "Piezoelectric Actuators for Distributed Noise and Vibration Excitation of Thin Plates", *ASME Failure Prevention and Reliability*, DE-Vol. 16:223-233.
- Liang, C., F. P. Sun and C. A. Rogers. 1993. "Coupled Electro-Mechanical Analysis of Piezoelectric Ceramic Actuator-Driven Systems-Determination of the Actuator Power Consumption and System Energy Transfer", *Proceedings of Smart Structures and Materials '93*, SPIE, Albuquerque, NM, Vol. 1917, pp. 286-298.
- Lomenzo, R. A., H. Sumali and H. H. Cudney. 1993. "Maximizing Mechanical Power Transfer from Piezoelectric Stacked Actuators to Structures", *Proceedings of Adaptive Structures and Material Systems*, ASME, AD-Vol. 35, New Orleans, LA, pp. 229-235.
- Piezo Systems, Inc. 1993. *Piezoelectric Product Catalog*.
- Stein, S. C., C. Liang and C. A. Rogers. 1993. "Power Consumption of Piezoelectric Actuators in Underwater Active Structural Acoustic Control", *Proceedings of the Second Conference on Recent Advances in Active Control of Sound and Vibration*, Blacksburg, VA, pp. 189-203.
- Zhou, S. W., C. Liang and C. A. Rogers. 1993. "Impedance Modeling of Two-Dimensional Piezoelectric Actuators Bonded on a Cylinder", *Proceedings of Adaptive Structures and Material Systems*, ASME, AD-Vol. 35, New Orleans, LA, pp. 245-253.
- Zhou, S. W., C. Liang and C. A. Rogers. 1994. "Coupled Electro-Mechanical Impedance Modeling to Predict Power Requirement and Energy Efficiency of Piezoelectric Actuators Integrated with Plate-Like Structures", *Proceedings of Adaptive Structures, the 35th AIAA/ASME/ASCE/AHS/ASC SDM Conference*, Hilton Head, SC, pp. 259-269.

62

Integration and design of piezoelectric actuators

Zhou, S.W., Liang, C., and Rogers, C.A., "Integration and Design of Piezoceramic Elements in Intelligent Structures," *Journal of Intelligent Material Systems and Structures*, Vol. 6, November 1995, pp. 733-743.

Integration and Design of Piezoceramic Elements in Intelligent Structures

S. ZHOU, C. LIANG AND C. A. ROGERS*

Center for Intelligent Material Systems and Structures, Virginia Polytechnic Institute and State University, Blacksburg, VA 24061-0261

ABSTRACT: The design of induced strain elements (actuators) is a comprehensive issue, involving not only the materials and geometry of the elements, but also the behaviors of the coupled host structures. In particular, the design of the active elements is essentially related to the prediction of induced strain or stress in the elements. A high stress or strain level in the actuators is useful to excite host structures; however, degradation or fatigue damage of the actuators may take place at the same time. This paper presents a dynamic analytical approach for the design and integration of active piezoceramic (PZT) patch elements locally coupled with host structures. Several critical design issues are addressed. These issues include the determination of the actuator dynamic outputs, the prediction of energy conversion efficiency, the estimation of system power requirement, and the limitation of induced alternate peak stress. A coupled electro-mechanical analytical model was developed to reveal the inherent connections among these issues. Both the mechanical stress behavior and the thermal stress characteristics of the PZT patch elements were investigated. A system power consumption-based model was developed to estimate the temperature and thermal stress distribution of the elements. The attention in parametric design was directed to the thickness and location of the elements. A simply-supported thin plate with surface-bonded PZT patches was built and tested to directly measure the induced dynamic strain of the PZT element so that the prediction accuracy and ability of the design model has been validated.

INTRODUCTION

DISTRIBUTED piezoceramic (PZT) elements have been widely used in various research and applications, since PZT elements have demonstrated competitive characteristics, such as light weight, small size, and good dynamic output performance. When PZT elements, as actuators, are integrated with conventional engineering structures and used in scientific research and industrial processes, several basic and important issues are raised.

First, the actuation ability of the active elements must be primarily considered. The question is whether host structures can be sufficiently excited using these elements. This issue involves the quantitative prediction of output performance of PZT actuators, such as displacement output, forces, or moments. As a matter of fact, the issue was noticed in the early development and implementation of PZT actuators. Several static-based modeling techniques were developed to determine static forces or moments (Bailey and Hubbard, 1985; Crawley and Louis, 1987; Crawley and Lazarus, 1991; Dimitriadis et al., 1989; Wang and Rogers, 1990). The static approaches, however, are limited to analyzing the static mechanical behavior of the actuators. An approximate dynamic analysis using the static models is not accurate because active forces provided by PZT actuators are usually alternate forces. The dynamic in-

teraction between the host structures and the active elements always exists and affects the performance of both the structures and the actuators. Recently, an impedance-based analytical model developed by the authors (Liang et al., 1993a; Zhou et al., 1993, 1994a) provides a better understanding of the dynamic essence of PZT element-driven systems. The frequency-dependent force output behavior is accurately predicted in the impedance model.

Second, designers of engineering and space structures are concerned with how efficiently a PZT actuator, as a transducer, transforms electrical energy into mechanical energy. The reason is that minimizing power consumption and enhancing energy conversion efficiency result in a reduction in the cost and mass of systems, two of the major objectives of adaptive structures (Rogers, 1993). Recently, research regarding actuator energy conversion and system power requirement has been active. Liang et al. (1993a) suggested an actuator power factor, defined as the ratio of the dissipative mechanical power in the system to the total electrical power supplied to the actuator. This concept was used to optimize the location of the actuator (Liang et al., 1993b). Stein et al. (1993) investigated the power consumption of a PZT actuator integrated on an underwater structure that radiates sound, and considered the power requirements in the active acoustic control. Lomeno et al. (1994) developed a technique to maximize mechanical power transfer from the stacked PZT actuators to the host structures. Zhou et al. (1994b) performed a coupled electro-mechanical impedance

*Author to whom correspondence should be addressed.

analysis for two-dimensional PZT actuator-driven systems and discussed the influence of different dissipators on the system power factor and the system power requirement. The analysis of system power consumption will provide a powerful tool to design energy-efficient smart structures.

Third, PZT elements are most often placed under a certain amount of alternate stress. The question is how to quantitatively predict the alternate stress so that a safety design can be effectively conducted. However, investigations done to date on this issue have fairly been limited. Intensive strain or stress is expected for the actuation, but brittle piezoceramic materials may be degraded in such a stress level. In addition, the stress signs are of concern in the design because the tensile strength of piezoceramic materials is much lower than the compressive strength. Another important issue, which has been ignored in the design of PZT actuators, is the estimation of the thermal stress levels and the temperature distribution of the actuators.

In this paper, the generic principle in the design of active PZT elements will describe using a coupled electro-mechanical analytical approach. The discussion will focus on the issues mentioned above and their inherent connections. The mechanical stress and thermal stress characteristics of the PZT patch elements will be specifically investigated. An analytical model for estimation of the temperature distribution and the induced thermal stress will be developed. The important design parameters, such as the location and thickness of the PZT elements will be addressed. A piezoceramic element-drive thin plate will be used in the parametric study. An experiment will be conducted on a simply-supported aluminum plate to prove the accuracy and utility of the theoretical model. A comparison will be made to demonstrate the significant difference between conventional static approaches and the developed dynamic integration method in physical concept and numerical results.

INTEGRATION AND MODELING

In this section, an impedance-based analytical approach will be presented to integrate PZT elements in host structures. Theoretical formulations will be derived for generic two-dimensional PZT elements. The design-related performance prediction, such as the actuator dynamic output, the system energy conversion efficiency, and the actuator stress behaviors will be quantitatively obtained.

Mathematical Model

Figure 1 illustrates a generic model of a two-dimensional PZT element integrated with a structure. x_p and y_p represent a coordinate system of the PZT element, corresponding to the 1 and 2 directions of the PZT material. The dynamic performance of the host structure is represented by the direct impedance Z_{xx} and Z_{yy} , as well as the cross impedance Z_{xy} and Z_{yx} , respectively.

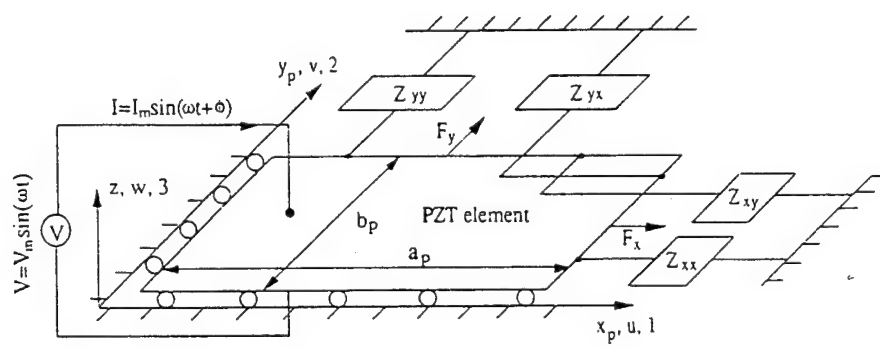
Using the dynamic force equilibrium between the PZT element and the host structure, the force output of the PZT element may be expressed by

$$\begin{Bmatrix} F_x \\ F_y \end{Bmatrix} = - \begin{bmatrix} Z_{xx} & Z_{xy} \\ Z_{yx} & Z_{yy} \end{bmatrix} \begin{Bmatrix} \dot{u} \\ \dot{v} \end{Bmatrix} \quad (1)$$

The minus sign in the equation indicates that F_x and F_y are equal and opposite to the structural reaction. \dot{u} and \dot{v} are the in-plane velocity responses of the PZT element and are related to the input impedance of the element itself, Z_{pxx} and Z_{pyy} defined as:

$$Z_{pxx} = \frac{F_x}{\dot{u}} = -j \frac{h_p Y_p^E}{\omega} \frac{k_p b_p}{\tan(k_{p11} a_p)} \quad (2a)$$

$$Z_{pyy} = \frac{F_y}{\dot{v}} = -j \frac{h_p Y_p^E}{\omega} \frac{k_p a_p}{\tan(k_{p22} b_p)} \quad (2b)$$



Z_{xx}, Z_{yy} — direct impedance of a 2-D host structure
 Z_{xy}, Z_{yx} — cross impedance of a 2-D host structure

Figure 1. A coupled electro-mechanical model of integrating a two-dimensional piezoceramic element with a host structure.

65

where the subscript p refers to the parameters of the PZT element. a_p , b_p , and h_p are the length, the width, and the thickness, respectively. $k_{p11(22)}$ is the wave number, ω is the input angular frequency, and j symbolizes the complex number. The complex Young's modulus at a constant electrical field, Y_p^E is expressed by:

$$Y_p^E = Y_p(1 + j\eta_p) \quad (3)$$

where η_p is the structural loss factor.

To quantitatively evaluate the force output, the displacement (or velocity) response of the PZT element should be solved from its constitutive equation and the geometric boundary condition. It is noted that when an AC voltage is applied cross a PZT element along the polarization direction (3), an in-plane thermal expansion (or contraction) is induced in both 1(x_p) and 2(y_p) axes of the patch. The displacement response of the PZT actuator may be described by:

$$u = [A \sin(k_{p11}x_p) + B \cos(k_{p11}x_p)]e^{j\omega t} \quad (4a)$$

$$v = [C \sin(k_{p22}y_p) + D \cos(k_{p22}y_p)]e^{j\omega t} \quad (4b)$$

where the wave numbers k_{p11} and k_{p22} are identical for isotropic piezoceramic materials:

$$k_p^2 = k_{p11}^2 = k_{p22}^2 = \omega^2 \frac{\rho_p}{Y_p^E} \quad (5)$$

ρ in the equation denotes the mass density. To solve for A , B , C , and D in Equation (4), the displacement boundary condition, $u_{xp=0} = 0$ and $v_{yp=0} = 0$ is applied to Equation (4), resulting in $B = D = 0$. A and C may be evaluated from the constitutive equation of the PZT patch at $x_p = a_p$ and $y_p = b_p$:

$$\begin{Bmatrix} \epsilon_x \\ \epsilon_y \end{Bmatrix} = \begin{Bmatrix} \frac{\partial u}{\partial x_p} \\ \frac{\partial v}{\partial y_p} \end{Bmatrix} = \begin{Bmatrix} \frac{1}{Y_p^E b_p h_p} & -\frac{v_p}{Y_p^E a_p h_p} \\ -\frac{v_p}{Y_p^E b_p h_p} & \frac{1}{Y_p^E a_p h_p} \end{Bmatrix} \begin{Bmatrix} F_x \\ F_y \end{Bmatrix} + \begin{Bmatrix} d_{31} \\ d_{32} \end{Bmatrix} E \quad (6)$$

where $E = v/h_p$ is the electrical field and $V = V_m e^{j\omega t}$ is the applied voltage. Substituting Equations (1) and (4) into Equation (6) is performing some algebraic operations yields:

$$\begin{Bmatrix} A \\ C \end{Bmatrix} = \frac{V_m}{h_p} \begin{Bmatrix} k_p \cos(k_p a_p) \left\{ 1 - v_p \frac{b_p Z_{xy}}{a_p Z_{pxx}} + \frac{Z_{xx}}{Z_{pxx}} \right\} \\ k_p \cos(k_p a_p) \left\{ \frac{b_p Z_{xy}}{a_p Z_{pxx}} - v_p \frac{Z_{xx}}{Z_{pxx}} \right\} \end{Bmatrix} \quad (7)$$

$$\left. \begin{aligned} & k_p \cos(k_p b_p) \left(\frac{a_p Z_{yx}}{b_p Z_{pyy}} - v_p \frac{Z_{yy}}{Z_{pyy}} \right) \\ & k_p \cos(k_p b_p) \left(1 - v_p \frac{a_p Z_{yx}}{b_p Z_{pyy}} + \frac{Z_{yy}}{Z_{pyy}} \right) \end{aligned} \right]^{-1} \begin{Bmatrix} d_{31} \\ d_{32} \end{Bmatrix} = \frac{V_m}{h_p} N^{-1} \begin{Bmatrix} d_{31} \\ d_{32} \end{Bmatrix}$$

in which d_{31} and d_{32} are the piezoelectric constants. v_p is the Poisson's ratio of the PZT material. Once the coefficients, A and C , are determined, the dynamic force output and the induced strain of the PZT actuator can be predicted using Equation (1) and Equation (6), respectively.

To estimate the energy conversion and power requirement of the system, the mechanical impedance model can be expanded to include the electrical parameters of the PZT actuator. The constitutive equation of the PZT actuator is again revoked for the electric displacement field, D_3 , in the axis direction:

$$D_3 = \epsilon_{33}^* E + d_{31} \sigma_x + d_{32} \sigma_y \quad (8)$$

where $\epsilon_{33}^* = \epsilon_{33}(1 - j\delta_p)$ is the complex dielectric constant at zero stress and δ_p is the dielectric loss factor of the PZT actuator. σ_x and σ_y in Equation (8) are the induced stresses, which can be derived from Equation (6). The current passing through the PZT actuator is thus given by:

$$I = I_m e^{j\omega t} = \int_0^{a_p} \int_0^{b_p} \dot{D}_3 dx_p dy_p \quad (9)$$

It is noted that I is a function of the applied voltage, V . The complex electro-mechanical impedance of the system, A^* is then determined from its definition (Elgerd, 1981): $A^* = I/V$. Once A^* is determined, the system power consumption and energy requirement can be quantitatively predicted.

Actuator Output Dynamics

Substituting Equations (4) and (7) into Equation (1), the dynamic force output of the PZT actuator can be determined by:

$$\begin{Bmatrix} F_x \\ F_y \end{Bmatrix} = \begin{Bmatrix} \bar{F}_x \\ \bar{F}_y \end{Bmatrix} e^{j\omega t} = -j\omega \frac{V_m}{h_p} \begin{Bmatrix} Z_{xx} & Z_{xy} \\ Z_{yx} & Z_{yy} \end{Bmatrix} \times \begin{Bmatrix} \sin(k_p a_p) & 0 \\ 0 & \sin(k_p b_p) \end{Bmatrix} N^{-1} \begin{Bmatrix} d_{31} \\ d_{32} \end{Bmatrix} e^{j\omega t} \quad (10)$$

To transform the in-plane force actuation of the PZT actuator to a pair of pure bending moments on a structure, two PZT patches are symmetrically bonded on the top and bottom surfaces of the structure and then the patches are actuated out-of-phase. The amplitude of the line moments per unit length created by a pair of PZT actuators, $\bar{M}_{x,y}$ (in

N·m/m), can be directly obtained using the basic relation, $M_{x,(y)} = (h + h_p)F_{x,(y)}$:

$$\begin{aligned} \begin{Bmatrix} \bar{M}_x \\ \bar{M}_y \end{Bmatrix} &= (h + h_p) \begin{Bmatrix} \bar{F}_x/b_p \\ \bar{F}_y/a_p \end{Bmatrix} = -j\omega \frac{(1 + h/h_p)V_m}{a_p b_p} \\ &\times \begin{Bmatrix} a_p Z_{xx} & a_p Z_{xy} \\ b_p Z_{yx} & b_p Z_{yy} \end{Bmatrix} \begin{Bmatrix} \sin(k_p a_p) & 0 \\ 0 & \sin(k_p b_p) \end{Bmatrix} N^{-1} \begin{Bmatrix} d_{31} \\ d_{32} \end{Bmatrix} \end{aligned} \quad (11)$$

The distributed line moments are thus expressed by:

$$\begin{aligned} M_x &= \bar{M}_x [\delta(x - x_1) - \delta(x - x_2)] \\ &[h(y - y_1) - h(y - y_2)] e^{j\omega t} \end{aligned} \quad (12a)$$

$$\begin{aligned} M_y &= \bar{M}_y [\delta(y - y_1) - \delta(y - y_2)] \\ &[h(x - x_1) - h(x - x_2)] e^{j\omega t} \end{aligned} \quad (12b)$$

where $\delta(x)$ and $\delta(y)$ are the Dirac delta functions. $h(x)$ and $h(y)$ are the Heaviside functions, x_1 , x_2 , y_1 , and y_2 are the location coordinates of the edge of PZT patches on the host structure.

Induced Mechanical Stress

The dynamic stress, $\sigma_{x,(y)}$, can be determined from Equation (6), using the relation of the stress and the force, $\sigma_x = F_x/(b_p h_p)$ and $\sigma_y = F_y/(a_p h_p)$:

$$\begin{aligned} \begin{Bmatrix} \sigma_x \\ \sigma_y \end{Bmatrix} &= Y_p^E \begin{bmatrix} 1 & -\nu_p \\ -\nu_p & 1 \end{bmatrix}^{-1} \left(\begin{Bmatrix} \epsilon_x \\ \epsilon_y \end{Bmatrix} - \begin{Bmatrix} d_{31} \\ d_{32} \end{Bmatrix} E \right) \\ &= \frac{Y_p^E V_m}{h_p (1 - \nu_p^2)} \begin{bmatrix} 1 & \nu_p \\ \nu_p & 1 \end{bmatrix} \\ &\times \begin{Bmatrix} \cos(k_p x_p) & 0 \\ 0 & \cos(k_p y_p) \end{Bmatrix} N^{-1} - I_{2x2} \begin{Bmatrix} d_{31} \\ d_{32} \end{Bmatrix} e^{j\omega t} \end{aligned} \quad (13)$$

where I_{2x2} is an identical matrix.

System Power Requirement and Energy Conversion

The power consumption and energy conversion efficiency are essentially dominated by the coupled electro-mechanical admittance. Substituting Equation (13) into Equation (8) and using the definition of the complex admittance yields:

$$\begin{aligned} A^* &= \frac{I}{V} = j\omega \frac{a_p b_p}{h_p} \left(\epsilon_{33} - \frac{2d_{31}^2 Y_p^E}{1 - \nu_p} + \frac{d_{31}^2 Y_p^E}{1 - \nu_p} \right. \\ &\times \left. \begin{Bmatrix} \sin(k_p a_p) & \sin(k_p b_p) \\ a_p & b_p \end{Bmatrix} N^{-1} \begin{Bmatrix} 1 \\ 1 \end{Bmatrix} \right) \end{aligned} \quad (14)$$

The power supplied to the PZT actuator is actually decomposed into two components: one is the dissipative power,

$$P = \frac{I_m V_m}{2} \cos \phi = \frac{V_m^2}{2} \operatorname{Re}(A^*) \quad (15)$$

and the other is the reactive power,

$$R = \frac{I_m V_m}{2} \sin \phi = \frac{V_m^2}{2} \operatorname{Im}(A^*) \quad (16)$$

where ϕ is the phase between the current and voltage, and I_m is the magnitude of the current in the circuit. The total electrical power, i.e., apparent power, is expressed by:

$$W = \sqrt{P^2 + R^2} \quad (17)$$

The power requirement of the system can be estimated from the maximum value of the apparent power. The power factor of the system, PF , representing the energy conversion efficiency of the system is defined as:

$$PF = \cos \phi = \frac{P}{W} = \frac{\operatorname{Re}(A^*)}{|A^*|} \quad (18)$$

In the derivation above, it is assumed that the system is linear and the host structure is a generic two-dimensional structure. The developed formulations thus represent generic solutions. Once the actuator input impedance, the structural impedance, and the coupled electro-mechanical impedance of the system are numerically computed or experimentally obtained, the formulations can be directly used to design active PZT elements integrated with host structures. For some typical two-dimensional structures, such as simply-supported plates and simply-supported cylinders, the analytical solutions of the mechanical impedance of the system have been derived by the authors (Zhou et al., 1993; 1994a). For complex structures, a finite element analysis of experimental approaches are helpful to determine the mechanical impedance of the system.

MECHANICAL STRESS CHARACTERISTICS OF PZT ELEMENTS

The mechanical stress induced in the PZT element is a function of frequency and the mechanical impedance of the system, and it varies along the location coordinate x_p and y_p . However, how significantly the location coordinate (x_p , y_p) exerts an influence on the stress distribution, as expressed in Equation (13), depends on the variation of the wavelength λ_p of the PZT element, defined as:

$$\lambda_p = \frac{2\pi}{k_p} = \frac{1}{f} \left(\frac{Y_p^E}{\rho_p} \right)^{1/2} \quad (19)$$

**Table 1. The stress strength of G1195 material
(Piezo Systems, Inc.)**

Compressive Strength (N/m ²)	Tensile Strength (N/m ²)	
	Static	Dynamic
5.2 × 10 ⁸	7.6 × 10 ⁷	2.1 × 10 ⁷

where f is the input frequency. Usually, commercial segmented PZT actuators have a small size, for example, 38.1 × 63.5 mm (1.5" × 2.5"). Assuming the excitation frequency, 2,000 Hz gives the ratio of the wavelength to the maximum length of the PZT patch:

$$\beta = \frac{\lambda_p}{a_p} = 46 \gg 1 \quad (20)$$

In this case, the wavelength is much longer than the maximum size of the PZT element. The coordinate (x_p, y_p) does not significantly influence the dynamic stress distribution on the PZT element. The PZT actuator, thus, can be treated as a "point" stress source. At very high frequency, or in the case of a relatively large size of PZT patch elements, the ratio coefficient, β , approaches 1. The dynamic strain or stress may significantly change along the coordinate location (x_p, y_p) . The PZT patch then becomes a "line" or a "plane" stress source.

For the purpose of designing PZT actuators, the dynamic stress should be required to satisfy the basic stress criteria:

$$\max \sigma_{x,(y)} \leq \sigma, \quad (21)$$

where σ is the stress strength of the piezoelectric material and $\max \sigma_{x,(y)}$ is the maximum stress allowed in the design. It should be noticed that the dynamic tensile strength of the piezoelectric materials is much lower than the compressive stress. For example, for G1195 piezoceramic material, the tensile strength is only about one-twentieth of the compressive strength, as listed in Table 1. The peak tensile stress, σ_p , should be limited to a value less than the dynamic tensile strength. Otherwise, there is a danger of degrading the performance and even a crack may take place. The safety factor, SF , should be considered by:

$$\max \sigma_{x,(y)} = \frac{\sigma_{ps}}{SF} \quad (22)$$

THERMAL STRESS ANALYSIS OF PZT ELEMENTS

When other stress factors degrading the performance of PZT elements are considered in the design procedure, the thermal stress should be included. The electrical energy, supplied by PZT actuators in driving host structures, is eventually transformed into internal heat in the PZT ele-

ments and structures. The dissipators in the system include structural damping loss and dielectric loss, which create a distributed heat generation throughout the PZT element and the host structure. The temperature increase in the system results in thermal stress in the PZT elements.

We consider a case in which both a PZT element and a host structure are plane structures. The top surface temperature of the PZT actuator is specified at room temperature, $T = 20^\circ\text{C}$. The heat generation rate per unit volume, Q , is assumed to be uniform throughout the body. The steady state temperature needs to be found in order to estimate the thermal stress induced in the PZT actuator.

For simplification, a one-dimensional heat conduction model (Chapman, 1974) is applied in this case. Figure 2(a) illustrates the schematic geometry of the integrated PZT/plate structure. Two PZT patches are bonded on the top and bottom surfaces of the plate. Considering the symmetrical geometry and boundary temperature, the problem may be simplified to the equivalent situation shown in Figure 2(b). The mid-plane of the plate is isolated at $z = 0$, that is, $dT/dz = 0$. The governing differential equation of the temperature distribution throughout the PZT element is depicted by:

$$\frac{d^2T}{dz^2} + \frac{Q_p}{\alpha_p} = 0 \quad (23)$$

with the boundary condition, $T = T_1$ at $z = z_1$ and $T_2 = 20^\circ\text{C}$ at $z = z_2$. The subscript p in Equation (23)

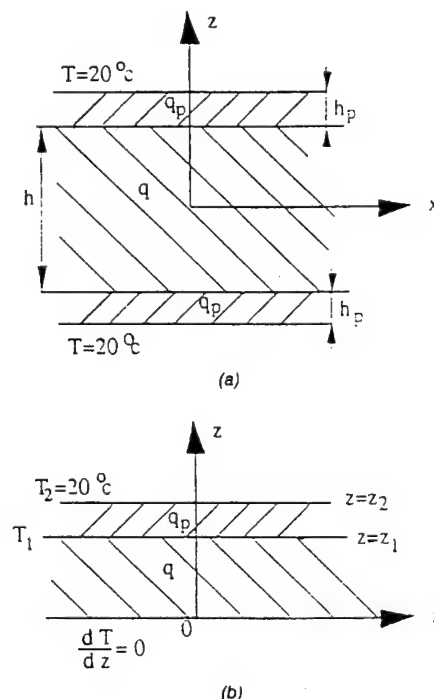


Figure 2. A heat conduction model for thermal stress analysis of a PZT element-driven plate-like structure.

again denotes the parameters of the PZT element. α symbolizes the thermal conductivity. Q represents the rate at which heat is being internally generated in the PZT patch per unit volume (watt/m³). Solving for T from Equation (23), the temperature distribution in the PZT element is determined by:

$$T = T_1 + (T_2 - T_1) \frac{z - z_1}{(z_2 - z_1)} + \frac{Q_p(z_2 - z_1)^2}{2\alpha_p} \times \left[\frac{z - z_1}{z_2 - z_1} - \left(\frac{z - z_1}{z_2 - z_1} \right)^2 \right] \quad (24)$$

The highest temperature in the patch element can be found by:

$$T_{max} = T_1 + \left[\frac{1}{2} + \frac{\alpha_p}{Q_p} \frac{T_2 - T_1}{(z_2 - z_1)^2} \right] \times \left[\frac{1}{2}(T_2 - T_1) + \frac{Q_p(z_2 - z_1)^2}{4\alpha_p} \right] \quad (25)$$

at

$$z_{T_{max}} = \frac{1}{2}(z_1 + z_2) + \frac{\alpha_p T_2 - T_1}{Q_p z_2 - z_1} \quad (26)$$

where Q_p can be estimated from the dissipative power consumption of the PZT element: $Q_p = P_p / (a_p b_p h_p)$. P_p here is calculated from Equation (15), by setting zero structural damping of the plate. The only unknown in Equations (24) and (25) is T_1 , which can be determined using the additional boundary condition at the interface of the PZT patch and the plate: $H_p = H$ at $z = z_1$. H is the ratio of the rate of heat flow, q , to the surface area of the structure, s , i.e., $H = q/s$, and q is expressed by:

$$q = -\alpha s \frac{dT}{dz} \quad (27)$$

The temperature distribution of the plate, T , is solved from the same form of governing equation as Equation (23) with the different boundary condition, $(dT/dz) = 0$ at $z = 0$ and $T = T_1$ at $z = z_1$. q is equivalent from Equation (27) and H is obtained by:

$$\left(H = -\alpha \frac{\partial T}{\partial z} \right)_{z=z_1} = (T_0 - T_1) \frac{\alpha}{z_1} + \frac{z_1}{2} Q \quad (28a)$$

$$\left(H = \alpha \frac{\partial T}{\partial z} \right)_{z=0} = (T_0 - T_1) \frac{\alpha}{z_1} - \frac{z_1}{2} Q = 0 \quad (28b)$$

Equation (28) can be reduced to:

$$H_{z=z_1} = Qz_1 \quad (29)$$

Substituting Equation (24) into Equation (27) gives H_p of the PZT element:

$$(H_p)_{z=z_1} = (T_1 - T_2) \frac{\alpha_p}{z_2 - z_1} - \frac{(z_2 - z_1)}{2} Q_p \quad (30a)$$

$$(H_p)_{z=z_2} = (T_1 - T_2) \frac{\alpha_p}{z_2 - z_1} + \frac{(z_2 - z_1)}{2} Q_p \quad (30b)$$

Letting Equation (29) equate Equation (30a) yields:

$$T_1 = T_2 + \frac{z_2 - z_1}{\alpha_p} [Qz_1 + Q_p(z_2 - z_1)] \quad (31)$$

The maximum temperature difference in the PZT patch is then obtained from Equation (25), resulting in the thermal stress, σ_T ,

$$\sigma_T = \gamma Y_p^E (T_{max} - T_1) \quad (32)$$

where γ is the coefficient of thermal expansion of piezoceramic materials. For G1195 material, $\gamma = 6 \times 10^{-6}$ (m/m°C). The thermal stress increases with the thickness of the PZT actuator and with the rate of the internal heat generation, Q_p , respectively. For a very thin PZT patch, such as $h_p = 0.19$ mm, the thermal stress may be ignored in the overall stress analysis. In case of stacked actuators or high voltage actuation, however, the thermal stress may be significant. In this case, a principal stress, σ_1 , or equivalent Von Mises stress, σ_v , should be used in the safety design of the actuator:

$$\max \sigma_{x,(y)} = \frac{\sigma_{1,(v)}}{SF} \quad (33)$$

PARAMETRIC DESIGN AND DISCUSSION

When a piezoceramic element, as an actuator, is considered in a design process, its geometric configuration integrated with a host structure should be first determined. The sandwich-type of PZT/substrate structures are widely used in intelligent material systems. This type of the configuration is also used in our case study. Once the geometry of an integrated PZT/substrate structure is selected, the formulations derived earlier can be directly utilized to qualitatively predict the performance of the PZT actuator.

In current case study, a simply-supported aluminum thin plate is used. The size of the plate is 381 × 228.6 × 1.5 mm (15" × 12" × 0.06"). Two PZT patches are bonded on the top and the bottom surface of the plate and located on the center of the plate. The size of the PZT patch (G1195) is 63.5 × 38.1 × 0.19 mm (2.5" × 1.5" × 0.0075"). Figure 3 shows the geometric configuration of the integrated PZT/plate system. Table 2 lists the basic material properties

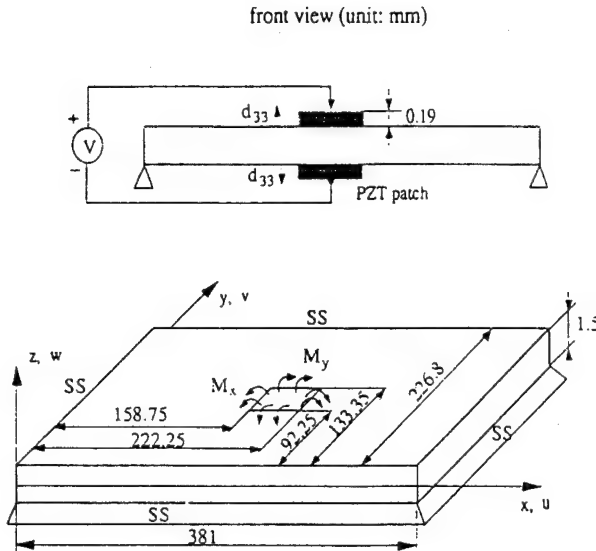


Figure 3. Geometry of a simply-supported (ss) aluminum plate with surface-bonded PZT patch elements.

of the PZT and the plate. When the PZT patch is actuated out-of-phase, a pair of bending moments, M_x and M_y , is generated along the edge of the patch. The analytical solutions of direct impedance, Z_{xx} and Z_{yy} , and the cross impedance, Z_{xy} and Z_{yx} , along the edge of the PZT patch were derived by the authors. The formulations can be found in a separate reference (Zhou et al., 1994a). The numerical results are directly given in this parametric study.

Figure 4 demonstrates the moment outputs of the PZT actuator, calculated from Equation (11). The amplitude of the dynamic moments varies significantly near the resonant frequencies of the system because of the dynamic interaction between the actuator and the plate. It is clearly demonstrated that the amplitude of the moment is a function of frequency and $M_x \neq M_y$. A static model developed by Dimitriadi et al. (1989) is used here in comparison with the dynamic model. At low frequencies, which can be regarded as a static zone, the static moment has a good approximation of the dynamic moments M_x and M_y , as shown in Figure 4.

The dynamic stress induced in PZT patch actuators is a complex stress, predicted using Equation (13). The real part can reflect both stress signs and stress levels. A positive stress sign represents a tensile stress while a negative sign indicates a compressive stress. It is assumed that the stress is measured at the location: $x_p = 3$ mm and $y_p = 19$ mm.

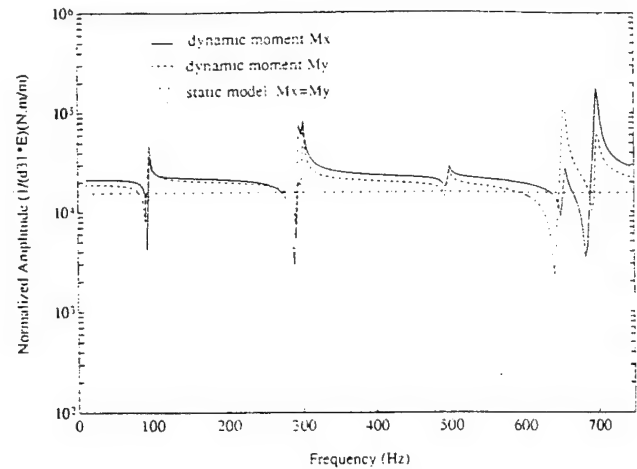


Figure 4. The dynamic moment outputs of the PZT patch actuator, predicted by the static model and the dynamic model, respectively.

Figure 5 shows that the tensile stress is up to 2×10^5 (N/M²/volt) at some resonant frequencies, while at anti-resonance and off-resonance, the induced stress is a compressive stress. The potential degradation or damage of the PZT actuator is most likely caused by the tensile stress because of the low tensile strength of the PZT material, as listed in Table 1. It is assumed that the plate is excited at the 2nd mode and a driving voltage of 100 volt is applied across each PZT patch, the mechanical stress level will exceed the tensile strength of the PZT material. A crack or degrading performance of the PZT actuator may take place.

The thermal stress is estimated using Equation (32). The rate of heat generation is calculated from Equation (15): $q_p = P_p$. It is assumed that the plate is actuated by the PZT actuator at the frequency of 400 Hz and the active voltage of 50 volt for each PZT actuator is applied. The heat conductivity of the PZT material is assumed to be 23 watt/m·°C. The temperature increase in the PZT actuator is less than 1°C because of the very thin thickness of the PZT patch, $h_f = 0.19$ mm. In this situation, the induced thermal stress can be ignored in the safety design of the actuator. If stacked PZT patch actuators are considered in the design procedure, the thermal stress may become an important factor to influence the overall stress levels.

One way to reduce the induced stress level in the active element is to limit the active voltage. Declination of the actuation force then results. The other way is to increase

Table 2. Material properties of the PZT element and the aluminum plate*

Young's Modulus (N/m ²)	Mass Density (kg/m ³)	Poisson's Ratio	Dielectric Constant (m/volt)	Loss Factor
PZT	6.3×10^{10}	0.3	1.66×10^{-10}	0.005
Aluminum	6.9×10^{10}	0.33	N/A	0.005

*Piezo Systems, Inc.

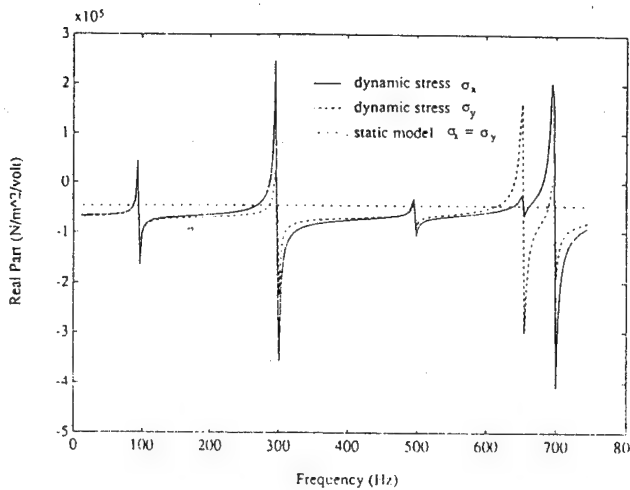


Figure 5. The induced mechanical stress characteristics of the PZT element, predicted by the static model and dynamic model, respectively.

the cross-sectional area of a PZT element as the voltage increases. Figure 6 displays that when the thickness of the PZT patch doubles from 0.19 mm to 2×0.19 mm, the overall moment output increases in the whole frequency range (0–750 Hz). While Figure 7 shows that the stress peak, however, is almost kept unchanged at the resonant frequencies. At off-resonance, the stress increment is not a big concern because of the relatively low compressive. Increasing the thickness of PZT patch elements is thus recommended to amplify the actuation and to relieve the peak stress level in the PZT elements.

In addition to the thickness, another important design parameter is the location of the PZT actuator. When the PZT actuator is placed in different locations on a host structure, as shown in Figure 8, the mechanical impedance at the edge of the actuator changes, and so does the dynamic out-

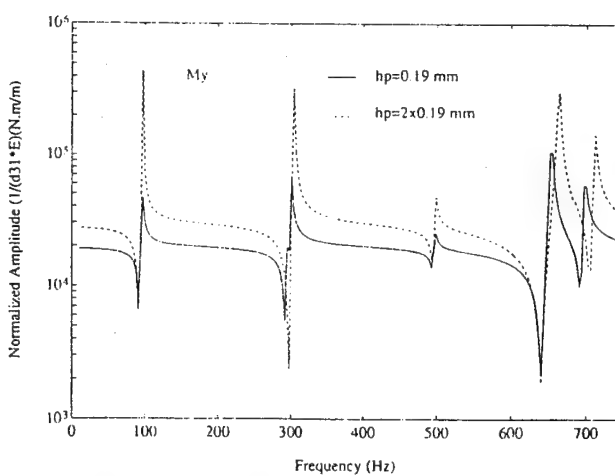


Figure 6. The influence of the thickness of the PZT element on the moment output (M_y).

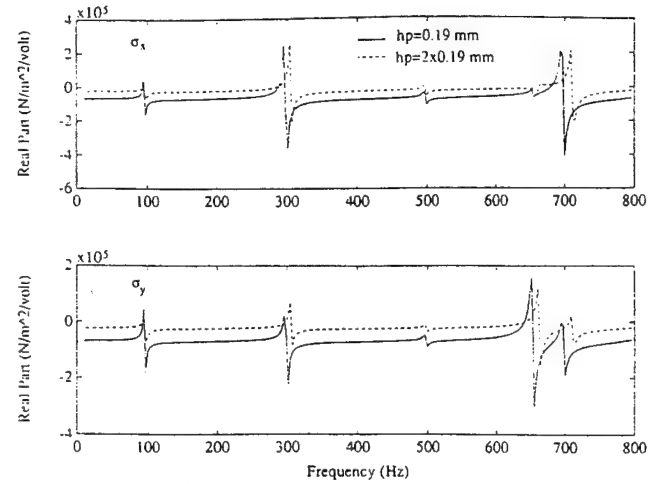


Figure 7. The influence of the thickness of the PZT element on the dynamic stress.

put performance of the actuator. Figure 9 clearly shows that the moment actuation is strongly related to the location of the PZT patch. When the center of the PZT patch is placed on the nodal lines of the host structure, the maximum moment output corresponding this mode cannot be achieved. For instance, when the center of the PZT patch is on location #1, which is the center of the plate, the moment actuation on the 2nd mode (2,1) is limited, as illustrated in Figure 9. This mode may be missed in the frequency response function. To actuate modes at a broad frequency band, the PZT element should be intentionally placed to be off the nodal lines of any interesting modes; otherwise, some of them may be lost in the response. The influence is similar for the dynamic stress, as shown in Figure 10.

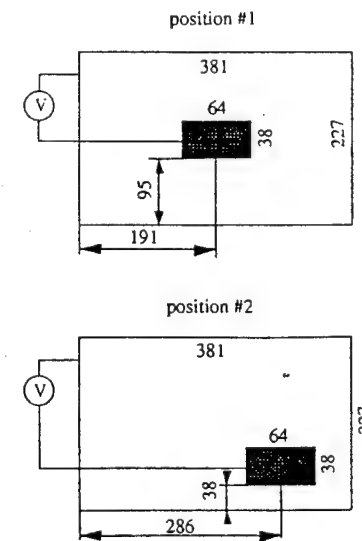


Figure 8. The geometric location of the PZT element on the plate (unit:mm).

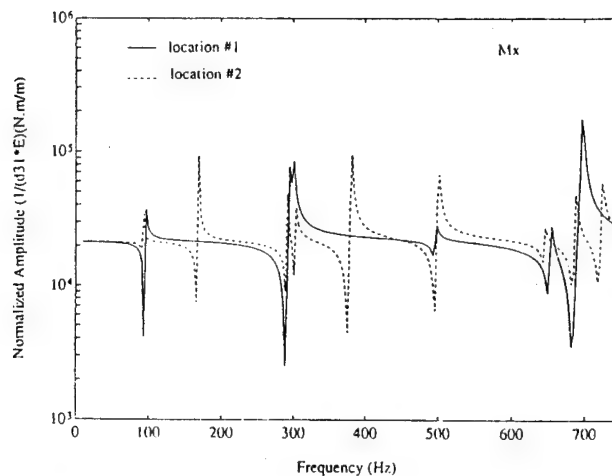


Figure 9. The influence of the location of the PZT element on the moment output (M_x).

The system power factor calculated from Equation (18) is displayed in Figure 11. A small power factor implies that little electrical energy is converted into mechanical energy in actuating host structures. A large power factor at a certain resonant frequency indicates that the actuator has a higher authority to excite this mode of the structure than the same actuator to vibrate other modes. This implies that the energy conversion efficiency of the system is related to specific modes.

EXPERIMENTAL VERIFICATION

A simply-supported thin plate was built and tested to verify the design model. The experimental set-up to excite the plate is illustrated in Figure 12. The thin plate in the experiment is made of aluminum and the PZT material is

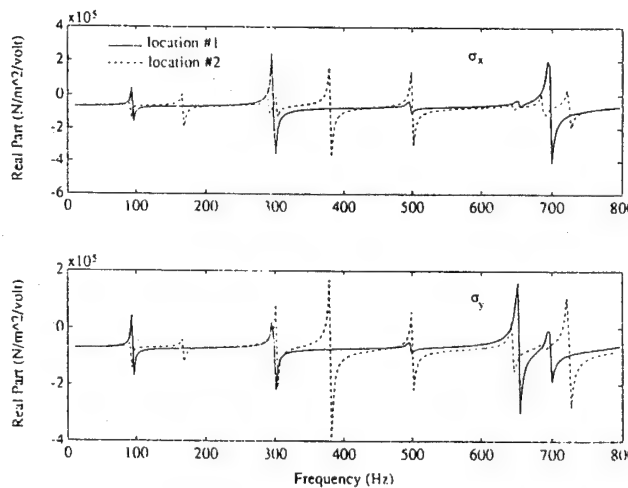


Figure 10. The effect of the location of the PZT element on the dynamic stress.

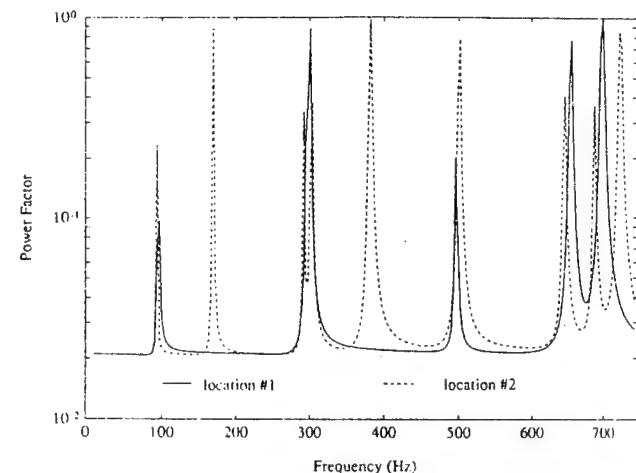


Figure 11. The effect of the location of the PZT element on the system power factor.

G195. The basic material properties are listed in Table 2. The geometric size of the PZT patch is $50.8 \times 50.8 \times 0.19$ mm ($2'' \times 2'' \times 0.0075''$), and the size of the plate is $305 \times 203 \times 1.5$ mm ($12'' \times 8'' \times 0.06''$).

A pseudo-random signal was used in a burst mode to activate the plate. The dynamic strain of the PZT actuator was directly measured using the strain gages. Two strain gages were placed on each surface of the PZT patches at right angles to measure the induced strain in the x and y directions, respectively, as shown in Figure 12. A half-bridge configuration was used to improve the ratio of the signal to the noise in the measurement. The coherence of the active voltage signal and the response voltage signal obtained from the strain gage was used to examine the accuracy of all of the excited modes.

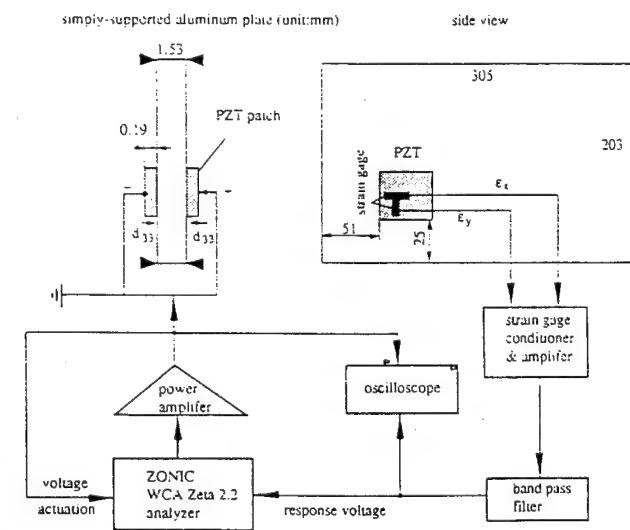


Figure 12. The experimental set-up for measuring the dynamic strain of the PZT patch element.

72

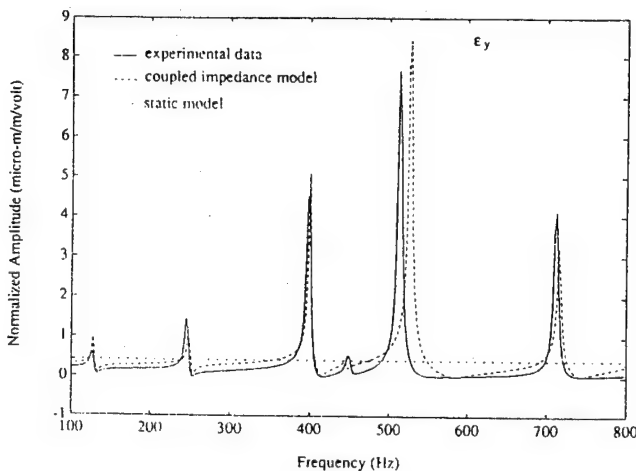


Figure 13. The predicted and measured dynamic strain of the PZT patch element in the *y* direction.

Figures 13 and 14 illustrate the measured and predicted strain in the *x* direction and *y* direction, respectively. The theoretical prediction based upon the impedance analysis (dashed line) agrees well with the experimental data (solid line). Compared with the static model, the developed dynamic model provides an accurate prediction of dynamic output behaviors of the active PZT elements.

CONCLUSION

- A dynamic design model has been developed for the integration and the performance prediction of the two-dimensional PZT elements. The model can be used to quantitatively predict the dynamic outputs, the induced strain (or stress) and its signs, the system power requirement, and the system energy conversion efficiency.
- A system dissipative power consumption-based heat con-

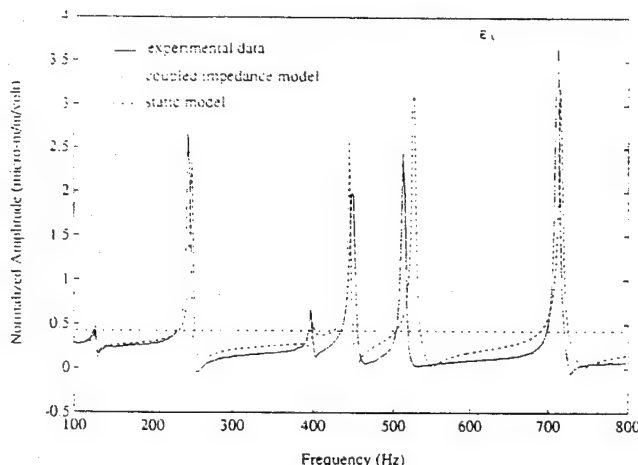


Figure 14. The predicted and measured dynamic strain of the PZT patch element in the *x* direction.

duction model has been suggested for the thermal stress estimation of the PZT elements. The thermal stress may become a significant factor influencing the strength design of the PZT actuator when a high voltage actuation or stacked PZT actuators is considered in the design procedure.

- The parametric study shows that increasing the thickness of the PZT actuator not only intensifies the actuation, but also relieves the induced stress. The actuation of the vibrational modes of the integrated system is strongly related to the location of the PZT element on the host structure.
- The excitation experiment of the integrated PZT/plate system has verified the ability and utility of the theoretical model to integrate and design PZT elements in intelligent structures.

NOMENCLATURE

<i>a</i>	length of a structure
<i>b</i>	width of a structure
<i>d</i>	piezoelectric constant
<i>E</i>	electric field
<i>F</i>	force output
<i>h</i>	thickness of a structure
<i>H</i>	the ratio of the rate of heat flow to the surface area of a structure
<i>j</i>	complex number
<i>k</i>	wave number
<i>M</i>	moment output
<i>q</i>	the rate of heat flow
<i>Q</i>	heat generation rate per unit volume
<i>T</i>	temperature
<i>u</i>	displacement in <i>x</i> direction
<i>v</i>	displacement in <i>y</i> direction
<i>V</i>	voltage
<i>w</i>	displacement in <i>z</i> direction
<i>Y</i>	Young's modulus
<i>Z</i>	mechanical impedance

Greek

α	thermal conductivity
ϵ	strain
σ	stress
η	structural loss factor
ν	Poisson's ratio
ρ	mass density
ω	angular frequency
λ	wave length

Subscripts

<i>m</i>	amplitude
<i>p</i>	piezoceramic actuator
<i>x</i>	<i>x</i> -direction
<i>y</i>	<i>y</i> -direction

- 1 1 direction of piezoceramic materials
- 2 2 direction of piezoceramic materials
- 3 3 direction of piezoceramic materials

Superscript

- E complex Young's modulus
 $*$ complex electro-mechanical admittance

ACKNOWLEDGEMENT

The authors gratefully acknowledge the support of the Air Force Office of Scientific Research under AFOSR Grant No. F49620-93-1-0166; Dr. Jim Chang, Program Manager.

REFERENCES

- Bailey, T. and J. E. Hubbard. 1985. "Distributed Piezoelectric-Polymer Active Vibrational Control of a Cantilever Beam", *AIAA Journal of Guidance of Control*, 6(5):605-611.
- Chapman, A. J. 1974. *Heat Transfer*, Macmillan Publishing Co., New York.
- Crawley, E. F. and J. de Louis. 1987. "Use of Piezoelectric Actuators as Elements of Intelligent Structures", *AIAA Journal*, 29(6):1373-1385.
- Crawley, E. F. and K. B. Lazarus. 1991. "Induced Strain Actuation of Isotropic and Anisotropic Plates", *AIAA Journal*, 29(6):945-951.
- Dimitriadis, E. K., C. R. Fuller and C. A. Rogers. 1989. "Piezoelectric Actuators for Distributed Noise and Vibration Excitation of Thin Plates", *ASME Failure Prevention and Reliability*, DE, 16:223-233.
- Elgerd, O. I. 1981. *Electric Energy Systems Theory*, McGraw-Hill Inc., New York.
- Ikeda, T. 1990. *Fundamentals of Piezoelectricity*, Oxford University Press, New York.
- Liang, C., F. P. Sun and C. A. Rogers. 1993a. "Coupled Electro-Mechanical Analysis of Piezoelectric Ceramic Actuator-Driven Systems-Determination of the Actuator Power Consumption and System Energy Transfer", *Proceedings of Smart Structures and Materials 93*, SPIE, Albuquerque, NM, 1917:286-298.
- Liang, C., F. P. Sun and C. A. Rogers. 1993b. "Design of Optimal Actuator Location and Configuration Based on Actuator Power Factor", *Proceedings of the Fourth International Conference on Adaptive Structure*, Cologne, Germany, pp. 657-673.
- Lomenzo, R. A., H. Sumali and H. H. Cudney. 1993. "Maximizing Mechanical Power Transfer from Piezoelectric Stacked Actuators to Structures", *Proceedings of Adaptive Structures and Material Systems*, ASME, AD, New Orleans, LA, 35:229-235.
- Piezo Systems, Inc. 1992. *Piezoelectric Motor/Actuator Kit Manual*.
- Rogers, C. A. 1993. "Intelligent Material Systems: The Dawn of a New Material Age", *Journal of Intelligent Material Systems and Structures*, 4(1):4-14.
- Stein, S. C., C. Liang and C. A. Rogers. 1993. "Power Consumption of Piezoelectric Actuators in Underwater Active Structural Acoustic Control", *Proceedings of the Second Conference on Recent Advances in Active Control of Sound and Vibration*, Blacksburg, VA, pp. 189-203.
- Wang, B. T. and C. A. Rogers. 1990. "Laminate Plate Theory for Spatially Distributed Induced Strain Actuators", *Proceedings of the Fifth Japan-U.S. Conference on Composite Materials*, Tama City, Japan.
- Zhou, S. W., C. Liang and C. A. Rogers. 1993. "Impedance Modeling of Two-Dimensional Piezoelectric Actuators Bonded on a Cylinder", *Proceedings of Adaptive Structures and Material Systems*, ASME, AD, New Orleans, LA, 35:245-253.
- Zhou, S. W., C. Liang and C. A. Rogers. 1994a. "A Dynamic Model of a Piezoelectric Actuator-Driven Thin Plates", *Proceedings of Smart Structures and Materials*, SPIE, Orlando, FL, pp. 550-562.
- Zhou, S. W., C. Liang and C. A. Rogers. 1994b. "Coupled Electro-Mechanical Impedance Modeling to Predict Power Requirement and Energy Efficiency of Piezoelectric Actuators Integrated with Plate-Like Structures", *Proceedings of Adaptive Structures*, AIAA/ASME/ASCE/AHS/ASC, the 35th SDM, Hilton Head, SC, pp. 259-269.

74

Analysis of other types of actuators

Ackerman, A.E., Liang, C., and Rogers, C.A., "Dynamic Transduction Characterization of Magnetostrictive Actuators," *Proceedings, Second International Conference on Intelligent Materials*, Williamsburg, VA, 5-8 June 1994, Technomic Publishing, Lancaster, PA, pp. 73-84.

Flint, E.M., Liang, C., and Rogers, C.A., "Electro-Dynamic Transduction Equations for Piezoelectric Stack Actuators," *Proceedings, ASME International Mechanical Engineering Congress and Exposition*, Chicago, IL, 6-11 November 1994, ASME Technical Publishing, New-York, NY, AD-Vol. 45, pp. 201-210.

Flint, E.M., Liang, C., and Rogers, C.A., "Dynamic Output and Structural Response Prediction for Stack Active Members Integrated in Complex Structures," *Proceedings, AIAA/ASME/ASCE/AHS/ASC 36th Structures, Structural Dynamics, and Materials Conference, Adaptive Structures Forum*, New Orleans, LA, April 1995, pp. 3554-3564.

Dynamic Transduction Characterization of Magnetostrictive Actuators

A. E. ACKERMAN, C. LIANG AND C. A. ROGERS

ABSTRACT

The development of an analysis approach for formulation of transduction or input/output representations for magnetostrictive actuators is presented. The transduction model is developed through application of an impedance modeling approach which includes the mechanical dynamics and the electro-magneto-mechanical interaction of the actuator device. Experimental behavior correlation has also been presented. The transduction model allows for in-depth investigation of the frequency-dependent behaviors of the magnetostrictive actuator such as energy conversion factor, output stroke, and force.

INTRODUCTION

Magnetostriction is the ability of a material to strain in the presence of a magnetic field. Until recently "giant" magnetostrictions were available only at cryogenic temperatures for certain materials. The alloying of rare-earth elements with iron produced a magnetostrictive material known as Terfenol-D which is capable of strains on the order of 1000 micron at room temperature and higher (Clark, 1992). The biased linearized constitutive equations for Terfenol-D (Butler, 1988) which define the mechanical strain and magnetic flux behaviors are known as:

$$S = \bar{s}^H T + dH \quad (1)$$

$$B = dT + \bar{\mu}^T H \quad (2)$$

In the constitutive equations shown above, S is the strain, \bar{s}^H is the complex material compliance with constant magnetic field, T is the stress, d is the biased material constant relating applied magnetic field to induced strain, H is the applied magnetic field, B is the magnetic flux density, and $\bar{\mu}^T$ is the complex permeability at a constant stress.

Magnetostrictive materials like Terfenol-D that strain in the presence of an applied magnetic field show great promise in industry applications because of improved stroke and force capabilities in comparison to piezoelectric ceramics. However, obtaining these behavior characteristics from magnetostrictive materials is more complex than with the piezoelectric counterparts and requires the construction of an actuator device.

The typical actuator consists of a rod of Terfenol-D surrounded by a wire coil or solenoid that applies a magnetic field to the material when a current is passed through the windings as shown in Fig. 1. Magnetic biasing is performed either with permanent magnets or a dc coil current. Also included inside the actuator is a prestress fixture usually consisting of a spring or other mechanism and an output shaft. The entire assembly is surrounded by a casing which serves as a portion of the prestress fixture, and provides magnetic shielding.

Vibration attenuation and base isolation experiments conducted with Terfenol-D actuators have shown the need for adaptive or ANN (artificial neural network) controllers as a result of actuator model inadequacies and material non-linearities. Previous modeling efforts consist of two main concentrations: static-based models (Haynes, Geng, and Teter, 1993; Hiller, Bryant, and Umegaki, 1989) and block diagram realizations (Bryant and Wang, 1992; Reed, 1988). The static models assume a frequency-independent relationship between the applied electrical signal and the induced mechanical output of the actuator. The block diagram models represent the electrical and mechanical behaviors of the actuator as lower order transfer functions with experimentally determined feedforward and feedback gains representing the electro-magneto-mechanical interaction of the device.

ACTUATOR LAYOUT AND MECHANICAL MODEL

The modeled Terfenol-D actuator is shown in Fig. 1 with the mechanical and electrical subsystems separated and identified. The modeling approach involves developing impedance relationships for the magnetostrictive element and fixture inside the actuator and to combine those expressions in order to correctly simulate the behavior of the actuator. Figure 2 shows the developed mechanical impedance diagram including Terfenol-D rod impedance Z_T , prestress fixture impedance Z_F , output shaft impedance Z_R , external impedance Z_s , output force \bar{F}_4 , and velocity \bar{x}_4 .

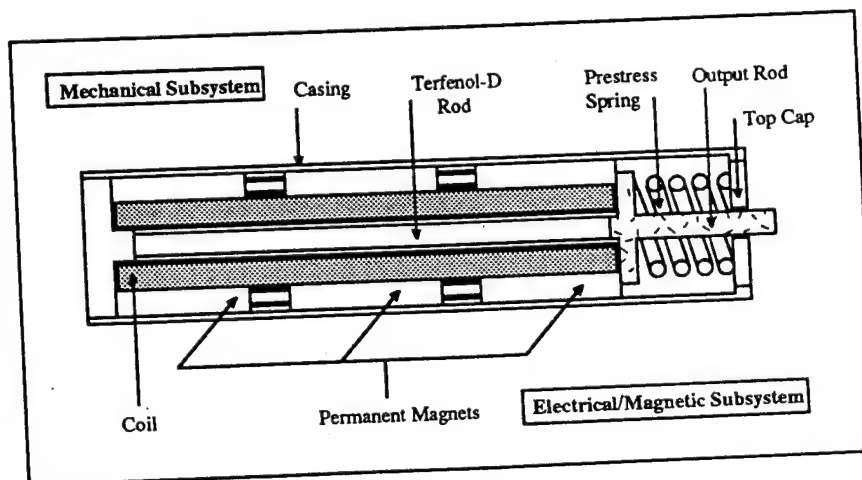


Figure 1: Terfenol-D Actuator Configuration Showing Mechanical and Electrical Subsystems

The equation of motion for longitudinal vibration in the Terfenol-D rod shown in Fig. 1 may be expressed as:

$$\frac{\partial^2 v_T}{\partial t^2} = (C^H)^2 \frac{\partial^2 v_T}{\partial y^2} \quad (3)$$

where v_T is the displacement of the rod as a function of axial position y and time t , C^H is the wave speed given as $\sqrt{1/\rho s^H}$ or $\sqrt{\bar{Y}^H/\rho}$ where \bar{Y}^H is the complex modulus of Terfenol at a constant field and ρ is the density.

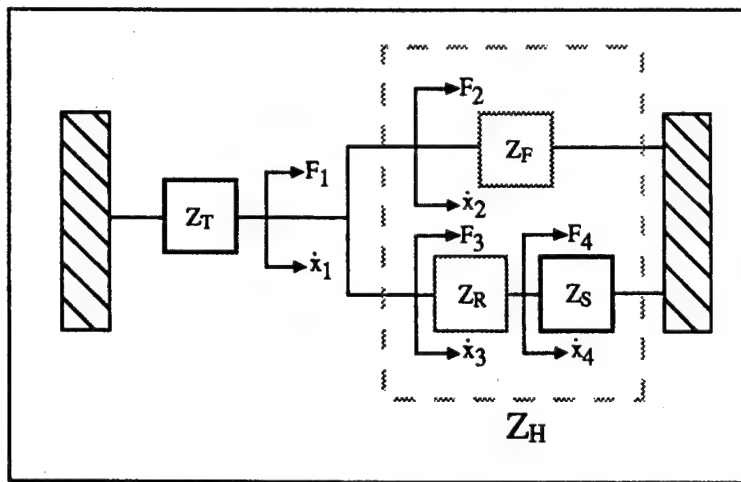


Figure 2: Generic impedance representation of induced strain actuator device with pre-stress fixtures

Vibration transverse to the axis of the rod is assumed negligible. The solution to the equation of motion is:

$$v_T = \bar{v}_T e^{j\omega t} = [A \sin(\kappa_T y) + B \cos(\kappa_T y)] e^{j\omega t} \quad (4)$$

where κ_T is the Terfenol-D wave number given by $\kappa_T = \omega/C^H$. Applying the fixed boundary condition at the left end of the Terfenol-D rod simplifies the displacement solution to:

$$v_T(y) = [A \sin(\kappa_T y)] e^{j\omega t} \quad (5)$$

For an arbitrary applied force $F e^{j\omega t}$ at $y = l_T$, the corresponding rod strain is:

$$S(l_T) = \left. \frac{dv_T(y)}{dy} \right|_{y=l_T} = [A\kappa_T \cos(\kappa_T l_T)] e^{j\omega t} \quad (6)$$

The stress T at $y = l_T$ is related to both the rod strain S and applied force F as:

$$T(l_T) = S(l_T) \bar{Y}^H = \frac{F(l_T)}{A_T} \quad (7)$$

where A_T is the cross-sectional area of the Terfenol-D rod. Plugging Eq. (7) into Eq. (6) and solving for the A constant in terms of the applied force yields:

$$A = \frac{F(l_T)}{\bar{Y}^H A_T \kappa_T \cos(\kappa_T l_T) e^{j\omega t}} \quad (8)$$

To produce the impedance expression relating applied force to resulting velocity, the Terfenol-D rod velocity at $y = l_T$ is found in terms of the applied force. The time derivative of the rod displacement Eq. (5) is:

$$\dot{v}_T(l_T) = j\omega [A \sin(\kappa_T l_T)] e^{j\omega t} \quad (9)$$

Substituting the A constant, Eq. (8), into Eq. (9), simplification and rearrangement yields the Terfenol-D rod short-circuit mechanical impedance as:

$$Z_T = \frac{F(l_T)}{\dot{v}_T(l_T)} = \frac{K_T}{j\omega} \left[\frac{\kappa_T l_T}{\tan(\kappa_T l_T)} \right] \quad (10)$$

where $K_T = \frac{A_T \bar{Y}^H}{l_T}$ is the Terfenol-D static stiffness, including the loss factor.

When the Terfenol-D rod is placed in the actuator configuration, as shown in Figs. 1 and 2, the boundary conditions at the $y = l_T$ change. Shown in Fig. 3 is the condensed mechanical impedance diagram for the actuator with Z_H representing the fixture, rod, and external impedances. The A constant for the solution to the equation of motion shown in Eq. (5) must be found for the new boundary conditions.

In the configuration shown in Fig. 3, the stress at the right end of the Terfenol-D rod is calculated as:

$$T(l_T) = \frac{F(l_T)}{A_T} = \frac{-Z_H \dot{v}(l_T)}{A_T} = \frac{-Z_H v(l_T)}{A_T} j\omega \quad (11)$$

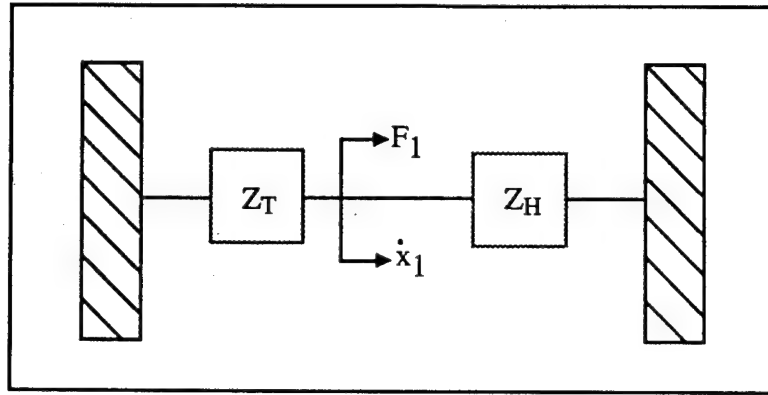


Figure 3: Condensed Actuator Impedance Model

Plugging the Terfenol-D stress, Eq. (11), into the first constitutive equation, Eq. (1), produces the first rod strain equation. Taking the spatial derivative of Eq. (5) produces the second rod strain equation. Setting these equations equal allows for solution of the A constant as:

$$A = \frac{dHZ_T}{\kappa_T \cos(\kappa_T l_T) [Z_T + Z_H]} \quad (12)$$

Plugging the A constant Eq. (12) into the solution for the equation of motion Eq. (5) gives the Terfenol-D tip displacement as:

$$\bar{x}_1 = \bar{v}(l_T) = dHl_T \left[\frac{Z_T}{Z_T + Z_H} \right] \left[\frac{\tan(\kappa_T l_T)}{\kappa_T l_T} \right] \quad (13)$$

Using one of the strain equations multiplied by the Terfenol-D elastic modulus \bar{Y}^H and cross-sectional area gives the output force as:

$$\bar{F}_1 = \bar{F}(l_T) = -A_T \bar{Y}^H dH \left[\frac{Z_H}{Z_T + Z_H} \right] \quad (14)$$

The impedance of the actuator fixture is that of a spring k and mass m in parallel and is shown as:

$$Z_F = j\omega m - \frac{jk}{\omega} \quad (15)$$

A continuous impedance expression (Snowdon, 1968; Harris, 1988) as a function of

the output rod characteristic impedance Z_o and actuator external impedance Z_s is used for the actuator output rod and is shown as:

$$Z_R = Z_o \left[\frac{Z_s + jZ_o \tan(\kappa_R l)}{Z_o + jZ_s \tan(\kappa_R l)} \right] \quad (16)$$

where $Z_o = A_R \sqrt{Y_R \rho_R}$ and κ_R is the output rod wave number given by $\kappa_R = \omega/C^R$. A_R is the cross-sectional area of the output rod, Y_R is the modulus of the rod, C^R is the wave speed for the rod material, and ρ_R is the rod density. The output force and velocity of the actuator as a function of the Terfenol-D velocity, external impedance, and output rod characteristic impedance are shown as:

$$\dot{\bar{x}}_4 = \frac{Z_o \dot{\bar{x}}_1}{Z_o \cos(\kappa_R l_R) + jZ_s \sin(\kappa_R l_R)} \quad (17)$$

$$\bar{F}_4 = \frac{Z_o Z_s \dot{\bar{x}}_1}{Z_o \cos(\kappa_R l_R) + jZ_s \sin(\kappa_R l_R)} \quad (18)$$

ELECTRICAL MODEL

The total flux Φ of the Terfenol-D rod and coil combination is defined as the flux density times the cross-sectional area of the Terfenol-D rod assuming that the only net magnetic flux passes through the ends of the rod and that the area contribution of the windings is negligible. The total flux is found to be:

$$\Phi = BA_T \quad (19)$$

Plugging the second constitutive equation, Eq. (2), including the Terfenol-D stress, into Eq. (19) yields:

$$\Phi(y) = \left\{ d^2 \bar{Y}^H \left[\frac{Z_T}{Z_T + Z_H} \right] \left[\frac{\cos(\kappa_T y)}{\cos(\kappa_T l_T)} \right] - d^2 \bar{Y}^H + \bar{\mu}^T \right\} A_T H \quad (20)$$

The voltage drop across the actuator leads, found from the integration of $\Phi(y)$ along the rod is:

$$V_{\text{out}} = j\omega N A_T H \left\{ d^2 \bar{Y}^H \left[\frac{Z_T}{Z_T + Z_H} \right] \left[\frac{\tan(\kappa_T l_T)}{\kappa_T l_T} \right] + (\bar{\mu}^T - d^2 \bar{Y}^H) \right\} \quad (21)$$

The relationship between the applied magnetic field H and current I (Butler, 1988) is:

$$H = nI = \frac{NI}{l_T} \quad (22)$$

where N is the total number of turns in the actuator coil and n is the number of turns per unit coil length ratio given as $n = N/l_T$. Substituting Eq. (22) into Eq. (21) and rearrangement provides the electrical impedance of the coil with the mechanical interaction included as:

$$Z_E = \frac{V_{\text{out}}}{I} = \frac{j\omega N^2 A_T}{l_T} \left\{ d^2 \bar{Y}^H \left[\frac{Z_T}{Z_T + Z_H} \right] \left[\frac{\tan(\kappa_T l_T)}{\kappa_T l_T} \right] + (\bar{\mu}^T - d^2 \bar{Y}^H) \right\} \quad (23)$$

TRANSDUCTION REPRESENTATIONS

A two-port network representation of a transducer relates the electrical parameters to the mechanical ones (Kinsler et al., 1982). The canonical transduction equations are:

$$V = Z_{EB} I + T_{em} u \quad (24)$$

$$F = T_{me} I + Z_{mo} u \quad (25)$$

In the above relationships, T_{em} and T_{me} are the transduction coefficients, Z_{EB} is the blocked electrical impedance, and Z_{mo} is the open circuit mechanical impedance. V and I are the voltage and current respectively. F and u are the output force and velocity respectively.

Generally, the ability of a transducer to provide a usable electric signal in response to an applied mechanical quantity, and vice versa, is defined as electro-mechanical coupling. The coupling coefficient, designated as k , may be derived from the energy ratio of a transducer defined as:

$$k^2 = \frac{T_{em} T_{me}}{Z_{EB} Z_{mo}} \quad (26)$$

The device energy ratio defined above is for a transducer device, it is an index representing the capability of the transducers to convert electrical energy to mechanical energy or vice versa. It differs from the energy ratio defined for a transducer material. In the case of Terfenol-D or any other magnetostrictive material, the coefficients of the constitutive equation and material-based coupling coefficient are material properties. This coupling coefficient for Terfenol-D is then:

$$k^2 = \frac{d^2}{\bar{s}^H \bar{\mu}^T} \quad (27)$$

82

The device energy ratio defined by Eq. (26) is frequency dependent, while the ratio defined for a material is more or less a constant. A representative value of a Terfenol-D coupling coefficient is in the range of 0.7-0.75 (Butler, 1988). However, because of the material property dependence on stress levels, driving field magnitude, and temperature, the coupling coefficient can vary out of this range significantly. In comparison, lead zirconate titanate (PZT) has a coupling coefficient in the range of 0.35-0.7.

A rearrangement of the canonical equations, known as the mechanical dual form, is shown below:

$$V = IZ_{EF} + \phi F \quad (28)$$

$$u = I\phi + \frac{F}{Z_{mo}} \quad (29)$$

For this form of the transduction equations, a reciprocal transducer shows $T_{em} = T_{me} = \phi_M$ and $\phi = \phi_M/Z_{mo}$. An antireciprocal transducer shows $\phi_M = T_{em} = -T_{me}$.

The mechanical dual form shown in Eqs. (28),(29) will be developed for the Terfenol-D actuator. The transduction coefficient ϕ is first found from Eq. (29) by setting the applied force to zero and plugging in the free actuator velocity. The transduction coefficient is found to be:

$$\phi = j\omega dN \left[\frac{Z_T}{Z_T + Z_F + Z_R} \right] \left[\frac{\tan(\kappa_T l_T)}{\kappa_T l_T} \right] \quad (30)$$

The other way of determining the transduction coefficient is by setting the applied electrical current and, therefore, magnetic field to be zero in Eq. (28), yielding:

$$V|_{INDUCED} = \phi F \quad (31)$$

$V|_{INDUCED}$ is the voltage that develops across the open-circuit actuator coil leads when an external force F is applied to the actuator output rod. In this case ($H = 0$) the Terfenol-D constitutive equations Eqs. (1),(2) are changed to:

$$S = \bar{s}^H T \quad (32)$$

$$B = dT \quad (33)$$

The force applied to the Terfenol-D rod, F_A , in terms of the force applied to the actuator output rod, F , is:

$$F_A = \left[\frac{Z_T}{Z_F + Z_T + Z_R} \right] F \quad (34)$$

The A constant for the solution to the equation of motion is found again in the same manner as described previously for Eqs. (11),(12). The voltage induced across the leads of the actuator coil as a function of the force applied to the Terfenol-D rod is found to be:

$$V_{INDUCED} = j\omega dN \left[\frac{\tan(\kappa_T l_T)}{\kappa_T l_T} \right] F_A \quad (35)$$

Substituting the force experienced by the Terfenol-D rod Eq. (34) into Eq. (35) yields the induced voltage as a result of an externally-applied force shown as:

$$V_{INDUCED} = j\omega dN \left[\frac{Z_T}{Z_T + Z_F + Z_R} \right] \left[\frac{\tan(\kappa_T l_T)}{\kappa_T l_T} \right] F \quad (36)$$

Factoring Eq. (36) shows that:

$$V_{INDUCED} = \phi F \quad (37)$$

Therefore, the Terfenol-D actuator is a reciprocal transducer according to this formulation. The transduction equations showing the electro-magneto-mechanical interaction are:

$$u = j\omega dN \left[\frac{Z_T}{Z_T + Z_H} \right] \left[\frac{\tan(\kappa_T l_T)}{\kappa_T l_T} \right] I + \frac{F}{Z_T + Z_H} \quad (38)$$

$$V = \frac{j\omega N^2 A_T}{l_T} \left\{ d^2 \bar{Y}_H \left[\frac{Z_T}{Z_T + Z_H} \right] \left[\frac{\tan(\kappa_T l_T)}{\kappa_T l_T} \right] + \bar{\mu}^T - d^2 \bar{Y}_H \right\} I + j\omega dN \left[\frac{Z_T}{Z_T + Z_H} \right] \left[\frac{\tan(\kappa_T l_T)}{\kappa_T l_T} \right] F \quad (39)$$

The actuator blocking force ($u = 0$) in terms of applied current is found to be:

$$\bar{F}_4|_{blocked} = j\omega dN Z_T \left[\frac{\tan(\kappa_T l_T)}{\kappa_T l_T} \right] I \quad (40)$$

The actuator free stroke ($F = 0$) is found to be:

$$\bar{x}_4|_{free} = dN \left[\frac{Z_T}{Z_T + Z_H} \right] \left[\frac{\tan(\kappa_T l_T)}{\kappa_T l_T} \right] I \quad (41)$$

EXPERIMENTAL VERIFICATION

Shown on the following section is the correlated actuator free-stroke to voltage transfer function and the real and imaginary electrical impedances. This correlation includes implementation of a system identification procedure used to determine the actual fixture stiffness based upon the dynamic characteristics of the actuator. The first actuator resonance is at 3100 Hz as seen in Fig. 4. At this frequency an impedance match occurs where the imaginary portions of the Terfenol-D impedance, Eq. (10), and the fixture impedance, Eq. (15), have imaginary portions opposite in sign.

The correlations of the real and imaginary free electrical impedances seen in Figs. 5 and 6 respectively show the effect of the actuator electro-magneto-mechanical interaction. The slight mismatch in resonant peak prediction and curve shape is a result of coil electrical non-linearity and variation of the "d" constant near actuator resonance. Baseline adjustment of the electrical model using the dc resistance, effective free permeability, and inductive loss factor of the actuator coil improved the correlation. A detailed discussion of this correlation is presented by Ackerman (1993).

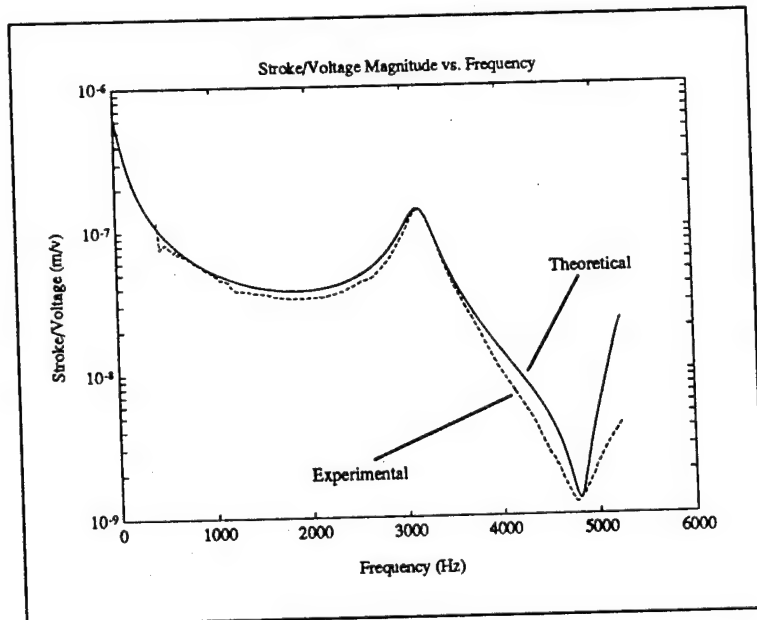


Figure 4: Correlated Terfenol-D Actuator Free-Stroke to Voltage Transfer Function

SUMMARY

This paper has presented an analysis approach for developing the transduction representations for a magnetostrictive actuator in terms of measurable electrical and mechanical properties. This model quantifies the mechanical dynamics and the complexity of the electro-magneto-mechanical interaction in the device.

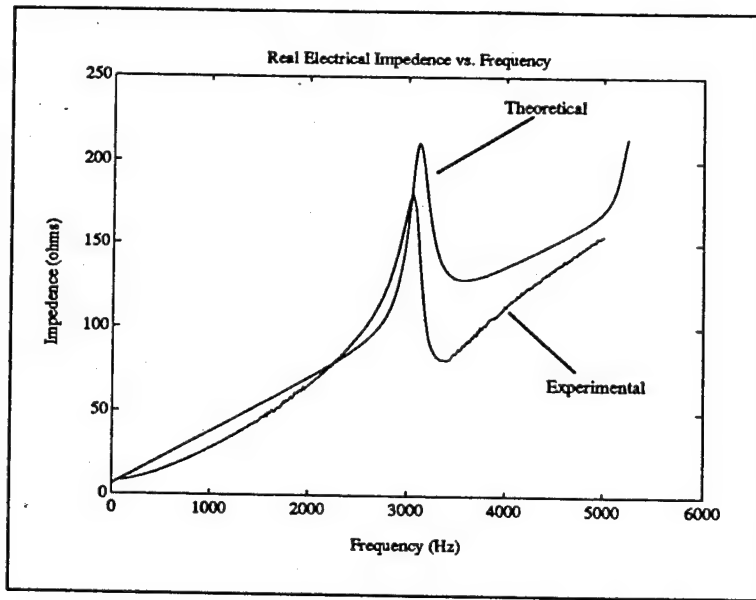


Figure 5 Correlated Real Electrical Impedance of the Terfenol-D Actuator

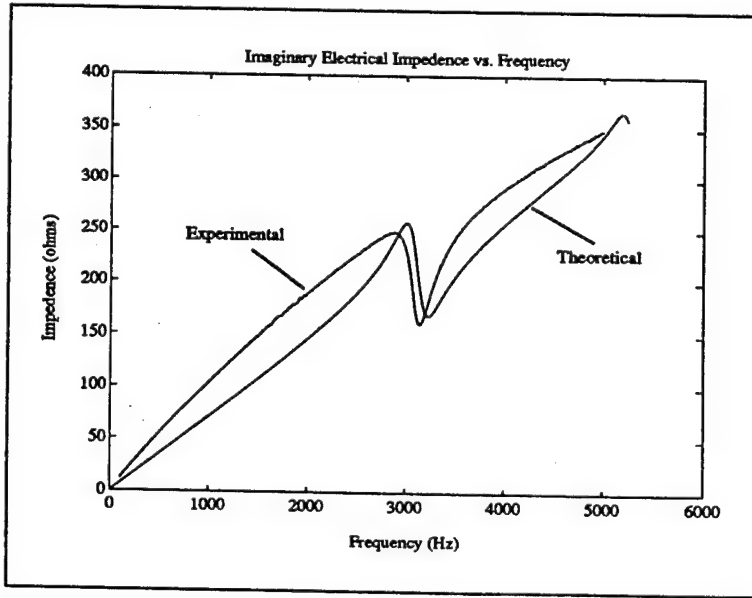


Figure 6: Correlated Imaginary Electrical Impedance of the Terfenol-D Actuator

The developed transduction model allows for analysis of the frequency and boundary condition dependent actuator behaviors including power consumption, output stroke and force, and efficiency as a transducer. The model also provides a better understanding of the relationship between the physical actuator parameters and the behavior characteristics.

Use of the Terfenol-D actuator as a collocated actuator/sensor is also realizable with

the mechanical dual form transduction representation. Two easily measured electrical quantities, voltage and current, allow for simultaneous actuation and sensing by the actuator.

ACKNOWLEDGEMENTS

The authors would like to thank Intelligent Automation, Inc., Dr. Zheng Geng, for supplying the Terfenol-D actuator and acknowledge the support of the Air Force Office of Scientific Research, Grant No. F49620-93-1-0166, and Dr. Walter F. Jones and Dr. Jim Chang.

REFERENCES

- Ackerman, A. E. 1993. "Dynamic Transduction of Magnetostrictive Actuators", Masters of Science Thesis.
- Bryant, M. D., N. Wang. 1992. "Audio Range Dynamic Models and Controllability of Linear Motion Terfenol Actuators", Proceedings of the Conference on Recent Advances in Adaptive and Sensory Materials and Their Applications, 27-29 April, 398-408.
- Butler, J. L. 1988. "Application Manual For the Design of EtremaTM Terfenol-D Magnetostrictive Transducers", Edge Technologies, Inc., EtremaTM Division, Ames, Iowa.
- Clark, A.E. 1992. "High Power Rare Earth Magnetostrictive Materials", Proceedings of the Conference on Recent Advances in Adaptive and Sensory Materials and Their Applications, 27-29 April, 387-397.
- Haynes, L., Geng, Z. and J. Teter. 1993. "A New Terfenol-D Actuator Design With Application to Multiple DOF Active Vibration Control", Proceedings of SPIE Smart Structures and Materials 1993, Albuquerque, New Mexico, 1-4 February.
- Harris, C. M. 1988. Shock and Vibration Handbook, 3rd Ed., MacGraw-Hill, 10.1-10.46.
- Hiller, M. W., Bryant, M. D. and J. Umegaki. 1989. "Attenuation and Transformation of Vibration Through Active Control of Magnetostrictive Terfenol", Journal of Sound and Vibration, 134:507-519.
- Ikeda, T. 1990. Fundamentals of Piezoelectricity, Oxford Science Publications, 5-30.
- Kinsler, L. E., Frey, A. R., Coppens, A. B. and J. V. Sanders. 1982. Fundamentals of Acoustics, 3rd Ed., Wiley, 344-349.
- Reed, R. S. 1988. "Model of a Magnetostrictive Actuator With Application To Simple Systems," Modeling and Simulation: Proceedings of the Annual Pittsburgh Conference, 19:2105-2109.
- Snowdon, J. C. 1968. Vibration and Shock In Damped Mechanical Systems, Wiley, 134-135.

ELECTRO-DYNAMIC TRANSDUCTION EQUATIONS FOR PIEZOELECTRIC STACK ACTUATORS

Eric M. Flint and Craig A. Rogers

Department of Mechanical Engineering
Virginia Polytechnic Institute and State University
Blacksburg, Virginia

Chen Liang

Department of Mechanical Engineering
San Diego State University
San Diego, California

ABSTRACT

In this paper the transduction equations needed to predict the electro-dynamic behavior of piezoelectric stack actuators are derived. An impedance approach is used to develop the parameters; free electrical impedance, transduction coefficient, and short circuited mechanical impedance, needed to fully characterize the transduction equations. Methods to experimentally determine the electro-dynamic transduction parameters are discussed and the developed theory is shown to match experimental data quite well for a PZT stack actuator active member. Potential applications of this work are wide ranging. Some possibilities include optimization of actuator placement in dynamic systems, prediction of power consumption (of particular concern on spacecraft), system ID, and accurate models for design of structural vibration reduction and isolation control algorithms.

INTRODUCTION

Since the commercial development of piezoceramic materials, stack actuators have found applications in many fields. A limited list of examples include micro-positioning, vibration isolation, fast acting valves and nozzles, sonic transducers, and gas ignitors. Stack actuators have been extensively used in experimental studies of truss structure control (Fanson et al., 1989, Preumont et al., 1990, Blackwood, et al. 1991, Rahman, et al., 1993). They have also been studied for use in luxury car shocks (Tsuka et al., 1990), spacecraft jitter reduction (Glaser et al., 1993) and active engine mounts (Sumali and Cudney, 1994).

The common feature of all the above stack actuators is that many thin layers of piezoelectric material, typically PZT, are glued or cofired together with an electrode between each layer. This arrange-

ment allows the mechanical displacement to sum in series while the electrical properties remain in parallel. This leads to large displacements, 0.1% strain, for lower voltage levels than would be achievable with a monolithic element of the same length.

In this paper, a method of predicting the steady state dynamic behavior of a stack actuator is developed. It is an extension of the impedance analysis method and is based on a transduction equation approach. First, a brief overview of typical stack actuator configurations and the design constraints which typically force a stack actuator to be implemented as an active member is given. A variety of analysis methods are reviewed with the goal of highlighting the advantages of the impedance approach which is discussed in some detail.

Next, the appropriate transduction equations are established and the three major parameters of the transduction equation (free electrical impedance, transduction coefficient and short circuited mechanical impedance) are theoretically derived. It is shown that the same set of equations can also be used to describe an active member after accounting for the impedance of the output rod and pre-stress spring.

Each of the three parameters are experimentally measured and compared to theoretical predictions for an piezoelectric active member. The agreement is shown to be quite good. The methods used to measure the parameters are discussed in detail along with other possible alternative measurement techniques.

The transduction equations provide a means to study the coupled electro-dyanamic behavior of the stack actuators. This work can be extended to the consideration of power requirements and amplifier sizing, dynamic operation self induced heat rise, transmitted force and structural response, control algorithm development and coupled optimization of structure, control and power subsystems in a truly integrated smart structure.

BACKGROUND

In Fig. 1, the typical configuration of a stack actuator is shown. Multiple layers of electroceramic material are placed together with alternating positive and negative electrodes in between. Since the mechanical displacements add in series, the more layers used the larger the total output displacement. This displacement is limited by the fact that as number of layers increases the stiffness of the actuator decreases along with resonant frequencies. Stiffness degradation is primarily driven by the compliance of the glue layers needed to assemble the actuator. Another effect of this glue layer is that stack actuators are easily damaged by tensile loads. This weakness is further compounded by the fact that PZT is ceramic and therefore brittle and weak under tension.

The coordinate system of a stack actuator is typically defined from the poling direction which is referred to as the 3 or z direction. As shown in Fig. 1, the plane orthogonal to the 3 direction holds the 1 and 2 (x and y) directions. Corresponding with the coordinate directions are 3 displacement coordinates, u, v and w for the 1, 2 and 3 directions. For stack actuators one is typically only interested in displacement in the z direction or w.

To help prevent damage from tensile loads, stack actuators are typically pre-stressed such that even for worst case external loading the actuator material always remains under compression. This can be achieved with a large mass in a machine positioning applications or with pre-stress springs. The latter approach is referred to as an active member in this paper.

A representative active member is shown in Fig. 2. The use of a prestress spring, typically belleville washers, also creates a requirement for an output rod to transmit the displacement of the actuator to the host structure. Similarly, to provide the initial compression of the spring and to keep boundary conditions rigid, compared to the actuator and spring, an actuator housing is required.

Another important feature in most active members is a means of isolating the stack from bending moments. Such moments can damage stacks because they put the actuator in alternating compression and tension despite the prestress springs. This leads not only to the possibility of total failure but increased fatigue as well. Solid hinges

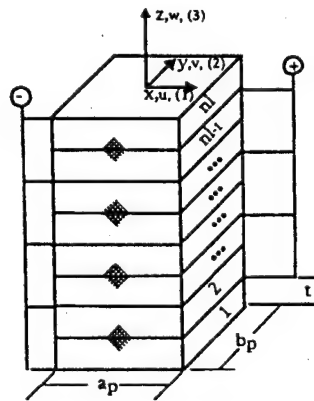


FIG. 1 TYPICAL STACK ACTUATOR

Showing reference direction conventions, alternating poling directions and electrode leads. The stack is arranged in this manner so that mechanical properties sum in series while electrical properties remain in parallel.

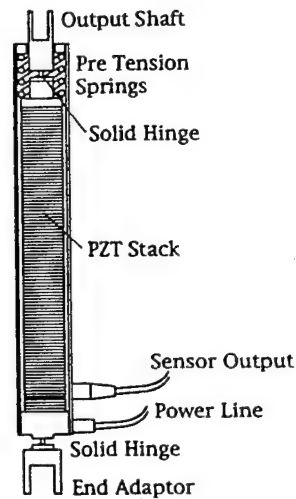


FIG. 2 REPRESENTATIVE ACTIVE MEMBER

Shows the major components of an active member including the actuator stack, pretension springs, output shaft and moment isolation mechanisms.

as shown in Fig. 2 or cross blade flexures are typically used to isolate the stack actuator.

To analyze the behavior of stack actuators many methods have been developed. The first are basically static and primarily useful in micro-positioning and other quasi-static applications. Finite element approaches now available on standard commercial software are very accurate. The stiffness approach of Umland et al. (1993) provides one method of analysis that is closed form and takes into account the pre-stress and flexure dynamic stiffness. Marlow (1993) developed a closed form analysis of the dynamics of actively controlled optical surfaces starting from Maxwell's equations.

IMPEDANCE APPROACH

The methods discussed above have some disadvantages. Static methods do not work satisfactorily in dynamic cases. FEM, while accurate, is time consuming, computationally expensive and cumbersome to use at conceptual design levels. The stiffness method does not explicitly account for the host structure enforced boundary conditions. Equations of motion do not provide information on power consumption. The impedance approach can correct all this. First applied by Liang et al. (1992) to simple one degree of freedom mass spring damper systems, the approach has since been expanded to cover beams, rings, cylinders, and thin plates for both structural and acoustic control. A summary and details of some of this work can be found in Liang et al. (1993).

In this paper, the impedance approach is extended to the coupled electro-mechanical analysis of stack actuators and active members. Some initial work on mechanical power transfer (Lomenzo et al., 1993) and actuator authority (Sumali and Cudney, 1994) has already been done in this field. The latter adapted a 3 port transduction approach presented by Kino (1987) for high frequency acoustics work.

Power consumption of stack actuators using the impedance method has also been investigated (Flint et al., 1994). In fact, this paper extends and refines that earlier work by creating a coupled analysis framework for both the mechanical and electrical properties of stack actuators and active members.

To start, some basics of impedance analysis must be provided (Harris, 1988). In a mechanical sense, impedance, Z_{mech} , is the ratio of force over velocity at a given point and direction in a structure:

$$Z_{mech} = \frac{\text{Force}}{\text{Vel}}. \quad (1)$$

The electrical impedance, Z_{elec} , of a device is the ratio of voltage, V , over current, I :

$$Z_{elec} = \frac{V}{I}. \quad (2)$$

It is easily shown that a standard lumped approximation mechanical mass-spring-damper system can be represented in impedance terms as:

$$Z = -\frac{k}{\omega} i + c + m i \omega, \quad (3)$$

where k , c , m are the stiffness, damping and mass of the mass-spring-damper system, i is $\sqrt{-1}$ and ω is the frequency in rad/sec.

Equation (3) is strictly valid only for lumped parameter systems. If a component of a system transmits force from one end to another then a lumped parameter model is rarely accurate enough. In order to correctly model such an element, a transmission line formulation must be used. One particular form of this relation (Harris, 1988) is:

$$Z_{rod} = Z_{radj} Z_{or} \left[\frac{Z_{HS} + i Z_{or} \tan(k_r l_r)}{Z_{or} + i Z_{HS} \tan(k_r l_r)} \right], \quad (4a)$$

which can be extended to relate the velocity of the output, \dot{w}_4 , to the input velocity, \dot{w}_2 :

$$\dot{w}_4 = \frac{Z_{or} \dot{w}_2}{Z_{or} \cos(k_r l_r) + i Z_{HS} \sin(k_r l_r)}, \quad (4b)$$

where:

$$Z_{or} = a_r \sqrt{Y_r \rho_r}, \quad (5)$$

$$k_r = \omega \sqrt{\frac{\rho_r}{Y_r}}, \quad (6)$$

Z_{or} , the rod characteristic impedance, and k_r , the rod wave speed, are composed of a_r , the rod cross sectional area, Y_r , the rod Young's modulus and ρ_r , the rod density. l_r , the rod length. Z_{HS} is the external single point impedance of the host structure seen by the transmitting rod. Z_{radj} comes from a need to fit data as the transmission line equation is sensitive to initial conditions.

Using Eq. (3) and (4) it is possible to model most components of a system. The individual components are then combined using the fact that the impedance of components in parallel (Z_{p1} , Z_{p2}) sum and when in series the inverse of the component impedances (Z_{s1} , Z_{s2}) sum:

$$Z_{p1+p2} = Z_{p1} + Z_{p2}, \quad (7)$$

$$\frac{1}{Z_{s1+s2}} = \frac{1}{Z_{s1}} + \frac{1}{Z_{s2}}. \quad (8)$$

TRANSDUCTION EQUATIONS

Transduction equations are a standard means of representing the coupling of two systems that are normally analyzed separately. In the case of stack actuators, the two subsystems are the mechanical and electrical. The analysis is coupled because applied electrical fields produce mechanical strain and applied strain generates electrical fields. While a wide variety of formats of the transduction equations exist, the most convenient is the following reciprocal format:

$$\dot{w} = \frac{F}{Z_{ms}} + \phi V, \quad (9)$$

$$I = \phi F + \frac{V}{Z_{EF}}, \quad (10)$$

where \dot{w} and I , the output velocity and generated current respectively, are independent variables and F and V , the force and voltage, are dependent. Z_{ms} , the short circuited mechanical impedance, ϕ , the transduction coefficient, and Z_{EF} , the free electrical impedance are parameters set by the actuator design and operating conditions.

To fully characterize the behavior of an actuator described by Eq. (9) and (10), one needs to measure any two of the four variables and know the parameters Z_{EF} , ϕ , and Z_{ms} . Perhaps the easiest way to obtain these parameters is to measure them experimentally. Methods to do this will be described latter. However, such measurements are only valid for the exact conditions at which they were taken and are not useful for parametric design studies. As is shown in the following sections, it is possible to derive closed form equations in terms of actuator material parameters that fully describe Z_{EF} , ϕ , and Z_{ms} .

Free Electrical Impedance

The starting point in the derivation of Z_{EF} is the equation of

motion of PZT material in the z direction, w :

$$\frac{\partial^2 w}{\partial x^2} = \frac{1}{c^2} \frac{\partial^2 w}{\partial t^2}. \quad (11)$$

where c is the wave speed. By using Eq. (11) the stack has been modeled continuously. As a consequence of this, the effect of the glue and electrode layers are assumed to be negligible.

It can be shown that the displacement of a PZT wafer in the z direction, w :

$$w = [A \sin(k_z z) + B \cos(k_z z)] e^{i\omega t}, \quad (12)$$

satisfies Eq. (17); where k_z , the material wave number and Y_z^{*E} , the complex Young's modulus are:

$$k_z = \omega \sqrt{\frac{\rho}{Y_z^{*E}}}, \quad (13)$$

$$Y_z^{*E} = Y_z^E (1 + \eta_m i). \quad (14)$$

for ρ , the PZT density, and η_m the PZT mechanical loss factor. The superscripts E, T, and D that are seen throughout this paper indicate that the property is defined for a constant electrical field (short circuited), stress, or open circuited condition respectively. The superscript * refers to complex variables with associated real terms and imaginary loss factor components.

Due to the assumption that one end of the actuator is fixed $w|_{z=0} = 0$ and B, a solution constant, is seen to be zero, leaving:

$$w = A \sin(k_z z) e^{i\omega t}. \quad (14)$$

A can be solved for using the fact that the stress, T_z , of a PZT with cross sectional area, a , is:

$$T_z = -\frac{1}{a} Z_{ext} \dot{w} \quad (15)$$

and a constitutive equation in strain (S) and electric field (E) format:

$$S_z = \frac{\partial w}{\partial z} = \frac{1}{Y_z^{*E}} T_z + d_{33} E. \quad (16)$$

with d_{33} being the PZT dielectric constant. At $z = tn_l$, where t is the thickness of each of the n_l PZT layers, after substituting Eq. (15) and the appropriate time and displacement derivatives of w (from Eq. (14)) into Eq. (16):

$$A = \frac{d_{33} \bar{E}}{k_z \cos(k_z tn_l) [1 + \frac{Z_{ext}}{Z_z}]}. \quad (17)$$

where Z_z , the input stack impedance, is:

$$Z_z = -\frac{K_z k_z tn_l}{\omega \tan(k_z tn_l)} i. \quad (18)$$

and K_z , the static extension stiffness, is:

$$K_z = Y_z^{*E} \frac{a}{tn_l}. \quad (19)$$

Until this point, the PZT stack was treated as a monolithic element for the consideration of strictly mechanical functions. However, the parallel electrical properties must be treated layer by layer. It can be shown that the current, I, in the PZT patch is:

$$I = i\omega \iint_{area} D_3 da \quad (20)$$

where D_3 , the electric flux density, can be represented as:

$$D_3 = \sum_{n=1}^{n_l} (\epsilon_z^{*T} E + d_{33} T_z^n). \quad (21)$$

The summation in D_3 accounts for the parallel electric flux density in each of the n_l layers. The components of D_3 are:

$$\epsilon_z^{*T} = \epsilon_z^T (1 + \eta_e i), \quad (22)$$

$$T_z^n = Y_z^{*E} (S_z^n - d_{33} E), \quad (23)$$

for ϵ_z^{*T} , the dielectric constant with ϵ_z^T being the real part and η_e the electrical loss factor. It can be seen that Eq. (23) is just another form of Eq. (16) that takes into account the individual electrical properties of each layer. Equation (16) is rewritten again to calculate the average strain of the nth layer:

$$S_z^n = \partial w / \partial z = A k_z \cos(k_z t(n - 0.5)) e^{i\omega t}. \quad (24)$$

Noting that D_3 is independent of x and y, the substitution of Eqs. (21) - (24) into Eq. (20) yields, after integration:

$$I = i\omega A [(\epsilon_z^{*T} - d_{33}^2 Y_z^{*E}) \frac{\bar{V}}{t} n_l + d_{33} k_z Y_z^{*E} A \sum_{n=1}^{n_l} \cos(k_z t(n - 0.5))] e^{i\omega t} \quad (25)$$

It can be shown that the summation term in Eq. (25) can be replaced by an integral term equivalent to $\sin(k_z tn_l) / k_z t$.

Recognizing that the admittance, $Y = I / V$, Y is, after substitu-

tion for A:

$$Y = i\omega a[(\epsilon_z^{*T} - d_{33}^2 Y_z^{*E}) \frac{n_l}{t} + d_{33}^2 Y_z^{*E} \frac{\tan(k_z t n_l)}{k_z t^2 [1 + \frac{Z_{ext}}{Z_z}]}] \quad (26)$$

Electrical impedance, Z_E , is just the inverse of the admittance Y. Therefore Z_{EF} is:

$$Z_{EF} = \frac{1}{i\omega a[(\epsilon_z^{*T} - d_{33}^2 Y_z^{*E}) \frac{n_l}{t} + \frac{d_{33}^2 Y_z^{*E} \tan(k_z t n_l)}{k_z t^2 [1 + \frac{Z_{ext}|_{Zhs=0}}{Z_z}]}} \quad (27)$$

where Z_{ext} is analyzed at $Z_{hs} = 0$. This satisfies Eq. (10) because for force to be zero the actuator must be free to displace and there can be no host structure restricting the actuator displacement.

Transduction Coefficient

To solve for the transduction coefficient the easiest method is to set the force to zero in Eq. (9) and solve for:

$$\phi = \frac{\dot{w}}{V}. \quad (28)$$

Taking the time derivative of Eq. (14) yields an expression for the velocity at the top of the stack:

$$\dot{w}_1 = i\omega A \sin(k_z t n_l). \quad (29)$$

where the reference system from Fig. 3 is being followed. Substituting for A (Eq. 27) and bringing the voltage term in A over to the other side one gets:

$$\frac{\dot{w}_1}{V} = \frac{i\omega d_{33} \tan(k_z z)}{k_z t [1 + \frac{Z_{ext}|_{Zhs=0}}{Z_z}]} \quad (30)$$

A similar approach can be taken starting with Eq. (10), shorting out the voltage, V, and solving for $\phi = I / F$. This approach gives the same result as Eq. (30) (after much manipulation) and verifies the fact that the active member does indeed follow a reciprocal transduction equation format.

Short Circuit Mechanical Impedance

As the name implies and inspection of Eq. (9) reveals, the short circuit mechanical impedance, Z_{ms} , is for operating conditions when there is no voltage applied. Since electrical properties no longer apply the active member can be treated as a solely mechanical system and:

$$Z_{ms} = Z_Z \quad (31)$$

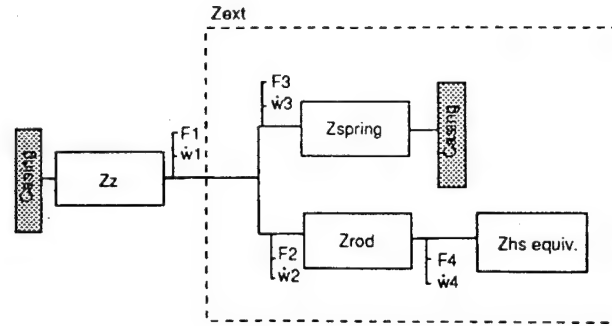


FIG. 3 ACTIVE MEMBER IMPEDANCE FLOW
Force and velocity conventions are shown for each intersection. If just an stack by it self then Z_{ext} is the same as Z_{hs} . Otherwise the dynamic mechanical characteristics of the pre-stress spring and output rod must be accounted for.

Extension to Active Members

As shown earlier, large systems are analyzed by considering the impedances of components separately. The analysis of a stack actuator can be separated into two parts. The first is that of the stack itself, with the second being the impedance, Z_{ext} , of all the components external to it. For a stack this is simply:

$$Z_{ext} = Z_{HS} \quad (32)$$

Analysis of active members can be approached the same way except that it is important to consider the behavior of the pre-stress spring and output rod individually. It is possible to represent the spring as a mass-spring-damper system following Eq. (3). The output rod is analyzed using the transmission line method of Eq. (4) - (6). The transmission line representation of Eq. (4) automatically takes the host structure impedance into account. The external impedance seen by the stack actuator is the parallel combination of the spring, Z_{Spring} , and rod, Z_{Rod} , impedance:

$$Z_{ext} = Z_{Spring} + Z_{Rod} \quad (33)$$

Incorporating this change is sufficient to allow accurate calculation of Z_{EF} for active members. However, further modification is necessary for ϕ and Z_{ms} . Using Eq. (1.4b), it is possible to relate the ratio of the velocity on either side of the output transmission line modelled rod when the host structure loading is zero to:

$$\frac{\dot{w}_4}{\dot{w}_1} = \frac{1}{\cos(k_R l_R)} \quad (34)$$

Using Eq. (34) with Eq. (30) yields:

$$\phi = \frac{\dot{w}_4}{V} = \frac{i\omega d_{33} \tan(k_z t n_l)}{k_z l \left(1 + \frac{Z_{ext}|_{Z_{hs}=0}}{Z_z}\right) \cos(k_R l_R)} \quad (35)$$

Similarly, the derivation of the short circuited mechanical impedance is amended to include the effect of having a stack within an active member. When short circuited, the stack and spring are in parallel with each other because they have the same boundary condition. Because of the transmission line modeling of the rod impedance, the rod impedance is in series with the spring and stack both resulting in:

$$Z_{ms} = \frac{Z_{Rod}(Z_{Spring} + Z_z)}{(Z_z + Z_{Spring} + Z_{Rod})} \quad (36)$$

where Z_{spring} , Z_{rod} and Z_z are determined exactly as before in Eq. (3,4 and 18).

EXPERIMENTAL VERIFICATION

The derivations of the transduction equation parameters, Eq. (27), (35), and (36), were used to predict the behavior of an active member produced by Physik Instrumente. From information provided by the manufacturer it was possible to fully characterize almost all of the important constants which are shown in Table 1.

The actuator itself consists of 182, 10 mm diameter PZT wafers, each 0.5 mm thick held together by glue and prestress. The reported PZT properties in Table 1 are within 5% of the manufacturers supplied data. One exception to this is the Young's modulus which was reduced 25% from the manufacturer claim of 50 GPa. It is believed that the reported value is for the material itself while the behavior of the actuator is influenced and made less stiff by the presence of the glue layers.

As it was not possible to disassemble the actuator, it was assumed to have 16 belleville springs which corresponded to the supplied weight total. This allowed calculation of a stiffness given the known prestress displacement. The damping ratio was experimentally determined.

The output rod parameters proved to be the most difficult to establish. It was assumed to be steel matching the rest of the actuator casing material. Its length was calculated from the known showing distance and the assumed internal length available from plans and the amount of space 182 layers of PZT, electrodes and glue had to occupy. Finally, the known rod cross sectional area was reduced by a factor of ten to account the moment isolation devices.

The process of establishing the unknown actuator parameters was an iterative one in which assumed values were used to generate theoretical predictions that were then compared to experimental results. While the given parameters agree with all known physical characteristics of the active member, in the future it is desired to test an actuator that can be disassembled. This would allow estimates of the stack actuator, spring and output rod characteristics to be experimentally developed prior to active member integration.

Table 1 Experimental Active Member Parameters

PZT	Symbol	Value	Units
cross-sectional area	a	7.85e-5	m ²
wafer thickness	t	0.5e-3	m
number of layers	n _l	182	---
density	p _p	7800	kg/m ³
Young's Modulus	Y _Z	36.0e9	Pa
mechanical loss factor	η _s	8.33e-3	---
dielectric loss	ε _Z	1.95e-8	
electric field constant	d ₃₃	427e-12	m/V
dielectric loss factor	η _e	0.015	---
Spring (bellvue)			
stiffness	K _s	9.66e6	N/m
damping	ζ _s	0.03	---
mass	m _s	7.3e-3	kg
Rod (steel)			
cross-sectional area	A _r	5.02e-6	m ²
Young's Modulus	Y _r	190e9	Pa
density	p _r	7689	kg/m ³
length	l _r	22.0e-3	m
Adjustment Factor	Z _{radi}	0.44	---

Electrical Impedance

From Eq. (10) it is easily seen that if the force, F, is zero, i.e. the actuator is free to displace because there are no constraints, Z_{EF} is easily determined from the ratio of the voltage over the current. This measurement is a fairly common one in the field of electrical engineering. In the experimental results shown below a HP 4194A impedance gain analyzer was used. It operates by measuring the current necessary to maintain a constant 2 volt AC signal in the measured circuit, which in this case is an active member.

Experimentally, the active member was left unconstrained on both

Impedance Analyzer

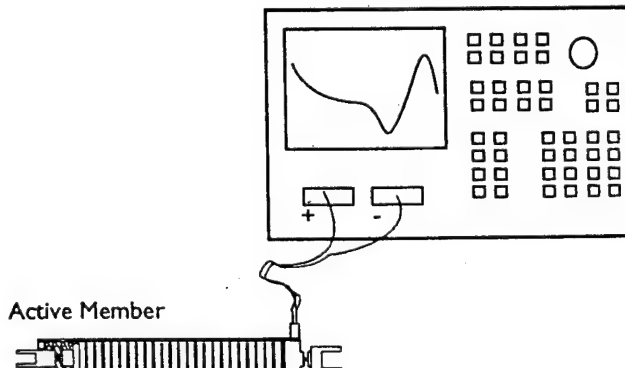


FIG. 4 Zef EXPERIMENTAL SET UP

The active member is attached to the impedance analyzer which measures the current needed to maintain ± 2 V AC. If there is no host structure loading this measurement is then Zef.

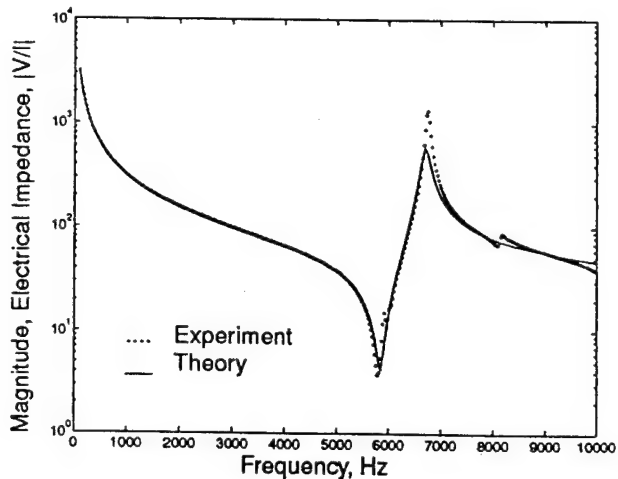


FIG. 5a MAGNITUDE OF Z_{ef}

Theoretical predictions (solid) agree very well with experimental data (dots) over a very wide frequency range. Note the capacitive behavior at lower frequencies and the resonance around 5800 Hz which is caused by an electrical resonance of the active material.

and attached to the impedance analyzer (Fig. 4). Because of the high impedance of the casing compared to the spring and stack, this is effectively a fixed free boundary condition. Frequency was swept from 100 to 10,000 Hz in 20 Hz steps and averaged 8 times for each step. Experimental magnitude and phase results (dotted line) are compared in Fig. 5(a&b) with theoretical predictions (solid) generated from Eq. (27) and the parameters of Table 1.

The agreement between theory and experiment is quite good in the low frequency range (0 to 2000 Hz). This agreement starts to drift slightly as the influence of the PZT stack resonance becomes stronger. It should be noted that when considering impedance, a valley in the frequency response denotes a resonance. This makes sense, because at a resonance, the structure vibrates more for a given force, therefore the velocity is higher and the impedance (F/V) decreases.

As can be seen in Fig. 5a, the theoretical resonance occurs slightly after the measured experimental value of about 5800 Hz. The location of the theoretical resonance is driven by the stiffness of the PZT stack (i.e. its Young's modulus) and to some degree the electric field constant, d_{33} . The steepness of the transition from resonance to the anti resonance was underpredicted as well. This behavior is primarily driven by ϵ_i^7 . The lack of perfect agreement in the magnitude plot also shows in the phase where the theoretical phase shift is narrower than the experimental data.

The sources of the unpredicted spikes in the experimental response are not exactly known but are most likely caused by unmodeled higher order dynamics in the spring. Other possibilities could be non extensional mode shapes (bending, torsion, etc.) that are coupling into extension or the effects of nonuniformities in glue layers. In fact, the possibilities are endless and until each element of the active member can be characterized separately it is impossible to

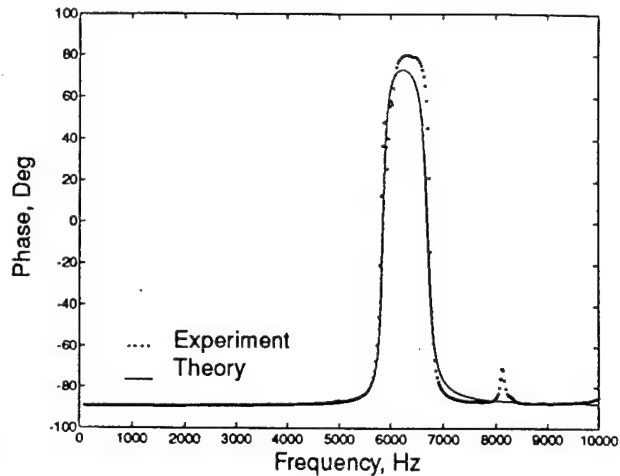


FIG. 5b PHASE OF Z_{ef}

The large phase shift corresponds to the electrical resonance. The smaller shifts are most likely due to unmodelled higher order behavior of the prestress spring. As before, solid lines are theoretical and dotted lines signify experimental data.

attribute a particular unpredicted resonance to any one cause.

Transduction Coefficient

There are two experimental ways to measure the transduction coefficient. The first comes from Eq. (9) and the fact that when there is no force (i.e. free displacement), ϕ is just the ratio of the output velocity over the applied voltage. The second is based on Eq. (10) and involves the ratio of current over force when the actuator is short circuited so that the voltage is zero. The first proves more

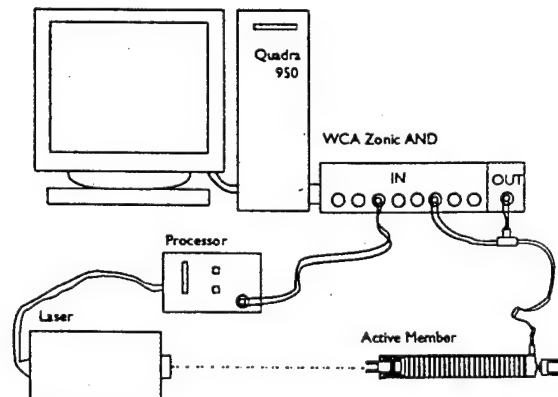


FIG. 6 PHI EXPERIMENTAL SET UP

The active member is excited with random noise generated by an internal function generator of the WCA. Applied voltage and resulting output velocity (measured with a velocimeter) is recorded and turned into a FRF on the WCA.

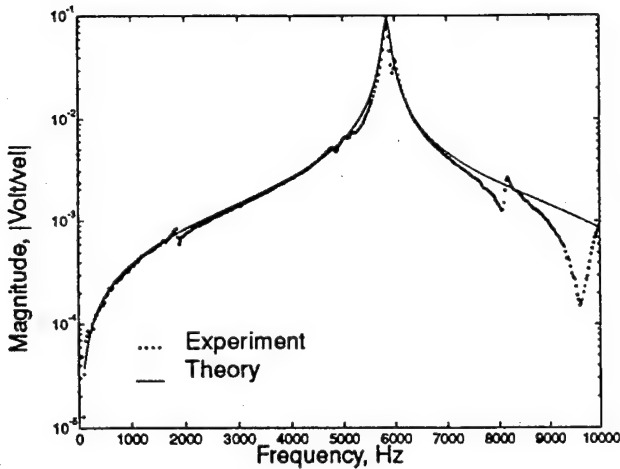


FIG. 7a MAGNITUDE OF PHI

Experimental and theoretical results agree well. The large peak corresponds to the electrical resonance of the stack. Other resonances are due to unmodeled system dynamics. As before, they are above the electrical resonance and therefore above the typical use range anyway.

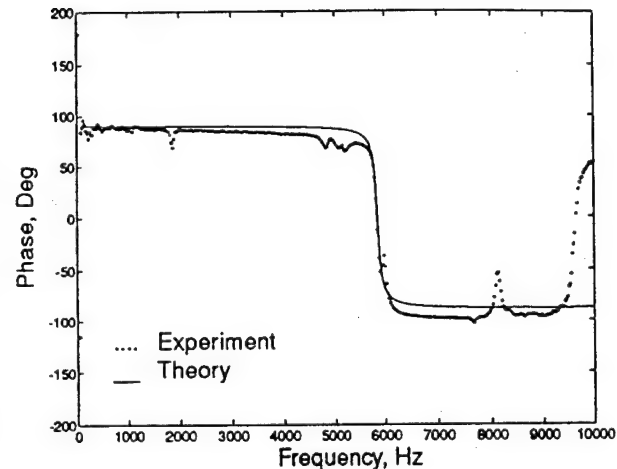


FIG. 7b PHASE OF PHI

Experimental and theoretical results agree well except for the phase shift drift of 10 to 15 degrees seen in the experimental data. The phase shift at 9500 Hz corresponds to the unmodelled resonance seen in Fig. 7a.

desirable in that the velocity can be measured non contactively and voltage is the standard output of most function generators. If the second set up is used then a force transducer must be attached with its corresponding degradation of the free boundary condition.

Experimentally the transduction coefficient was measured from the frequency response function of velocity over applied voltage. Velocity was measured using a Polytec Vibrometer system with a OFV 2500 Controller and OFV 350 Optical Single Point Head. The laser light path was aimed at the tip of the active member output rod such that the laser light hit the output rod as close to straight on as possible. The angle was adjusted until coherent return scatter was indicated by the laser control system.

The actuator itself was excited by a 0.5 volt amplitude shaped random noise from 0 to 10,000 Hz. Data was gathered on a Quadra 950 based WCA Zonic AND data acquisition system. 1024 data points were averaged 1000 times with a Hanning window to create the frequency response function. Once again the actuator was left unconstrained on both ends and rested on foam.

As seen in Fig. 7(a&b) the agreement between theoretical predictions (solid line) from Eq. (38) and the parameters of Table 1 and experimental results (dotted line) are good. Agreement is quite good until the electrical resonance is reached. After this point there is strong coupling with unidentified modes around 8000 and 9500 Hz.

In the phase plane (Fig. 7b) agreement is good as to the general shape. The predicted 180 degree phase shift occurs exactly at the experimental electrical resonance. One discrepancy is a downward drift of the experimental phase by about 10 to 15 degrees over the 0 to 5000 Hz range. This downward drift might account for the fact that after the resonance induced phase shift, theoretical predictions are 10 to 15 degrees higher than the experiment in the upper

frequency range. The unpredicted phase shift at 9500 Hz corresponds to resonance in the magnitude.

Short Circuit Mechanical Impedance

This parameter proved to be the hardest to measure experimentally. The most obvious method comes from Eq. (9). When the voltage is forced to be zero (i.e. short circuited) then Z_{ms} is just

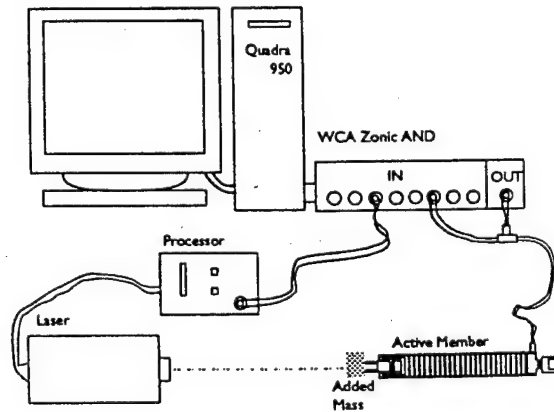


FIG. 8 Z_{ms} EXPERIMENTAL SET UP
The set up is exactly the same as Fig. 6 except that a mass is added to the tip of the active member output rod so a known force /impedance relationship can be calculated.

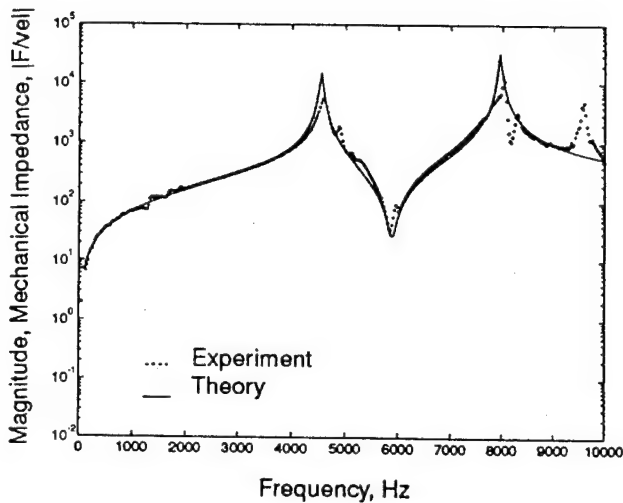


FIG. 9a MAGNITUDE OF Z_{ms}

The resonance at 5750 Hz corresponds to the electrical resonance. The magnitude and frequency of the two major anti-resonances are determined by the output rod impedance.

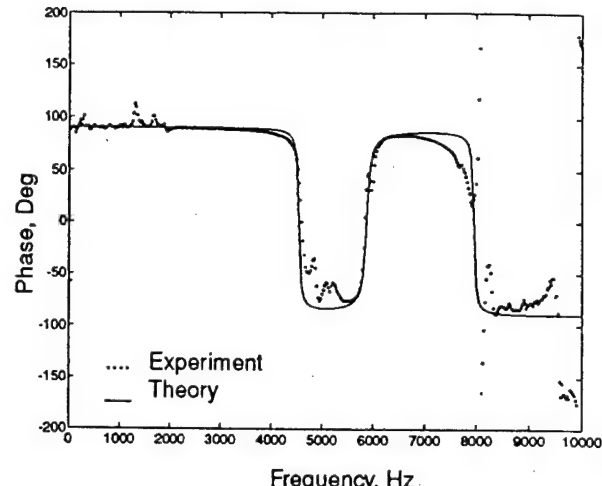


FIG. 9b PHASE OF Z_{ms}

Agreement between theory and experiments is quite good. The relatively greater amount of discrepancies comes from the fact that the experimental values for Z_{ms} were determined from two measurements; Φ and \dot{w}/V .

the ratio of force over velocity. Another more practical possibility is to rearrange Eq. (9) into:

$$Z_{ms} = \frac{F}{\dot{w} - \phi V} = \frac{F/V}{\dot{w}/V - \phi} \quad (37)$$

However the experimental set up can be simplified further by realizing that if a known impedance is applied, say that provided by a fixed mass, the force and velocity can be related by the standard mechanical impedance relationship, Eq. (1), repeated here in a modified format:

$$F = Z_{mass} \dot{w} \quad (38)$$

This allows further simplification of the experiment because only one measurement, \dot{w}/V , is now required to satisfy the modified Eq. (40):

$$Z_{ms} = Z_{mass} \frac{\dot{w}/V}{\dot{w}/V - \phi} \quad (39)$$

As shown in Fig. 8, the experimental set up is almost exactly the same as that used for measuring the transduction coefficient, Φ . The only change is the addition of a mass to the actuator output rod which weighed 24 grams. The applied voltage was measured on the WCA Quadra along with the resulting laser signal. A shaped random noise AC voltage from 0 to 10,000 Hz was applied to the actuator. As before, the WCA Zonic AND system was used to collect the data and form the transfer function. Data from 0 to 10,000 Hz

was taken in blocks of size 2048, averaged 5,000 times.

After acquisition, the data was used in Eq. (39) along with the experimental transduction coefficient, ϕ , and the weight of the mass to generate the experimental results shown in Fig. 9a&b. As before, the agreement is quite good. Electrical resonance at 5750 Hz dominated behavior as in the other two parameters but is modified by the presence of two anti resonances. The relatively large amount of discrepancies can be attributed to the fact that two sets of experimental measurements were combined to generate this data set. This is especially clear with regards to phase (Fig. 9b). As always agreement above the electrical resonance is the least acceptable.

In order to achieve the fit of magnitude and frequency shown for the antiresonances of Fig. 9a, the adjustment factor, Z_{radj} was introduced and iteratively tuned until agreement was reached. Introduction of this factor, included in Eq. (4) had minimal effect on the predictions off Z_{ef} and Φ and thus this approach is deemed acceptable until a more detailed understanding of the physics of the rod impedance can be developed.

CONCLUSIONS

In this paper, theoretical predictions of the transduction equations necessary to describe the behavior of stack actuators by themselves or as active members in host structures were developed. These results were experimentally verified with good agreements up to the first natural resonance of the active member system. Agreement after the first resonance was acceptable but was disturbed by unmodeled higher order system dynamics.

The impedance modeling approach taken, along with the use of the transduction equations, offers a great amount of useful information within two coupled equations. The mechanical output and elec-

trical behavior of any piezoelectric stack actuator can now be theoretically predicted. This information along with that of the power consumption can be used to develop optimized design at a conceptual level.

The methodology shown here can be inverted and used to solve for the point host structure dynamics and used as a form of system ID and damage detection. The knowledge of the system electrical behavior can be used to size amplifiers to prevent saturation and non linear effects. Also, knowledge of dissipative power allows predictions of resistive heating induced temperature changes within the active material. In control applications where the accuracy of the model is critical, higher fidelity stack actuator models are now available.

When using the results of this paper it is important to remember that they depend on several assumptions. First, the theory was based on steady state dynamic excitation and linear behavior. Thus, the hysteretic and drift behavior of the actuator material is not considered. The effect of the glue layer was taken into account by reducing the PZT Young's modulus. Material properties are assumed to be constant with frequency, temperature and applied voltage. The single degree of freedom spring assumption limits modeling after the first actuator resonance. This, however, is not typically of concern as in most applications stack actuators are used well below electrical resonance.

ACKNOWLEDGMENTS

The authors would like to thank the Virginia Space Grant Consortium and the Air Force Office of Scientific Research, Grant # F-49620-93-1-0166, technical monitors Dr. Walter F. Jones and Dr. Jim Chang, for the funding that enabled this work.

REFERENCES

- Anderson, E., Moore, D., J. Fanson, 1990, "Development of an Active Member Using Piezoelectric and Electrostrictive Actuation for Control of Precision Structures", AIAA-90-1085-CP, *Proceedings 31st SDM Conference*, pp. 2221-2233.
- Blackwood, G., Jacques, R., Miller, D., 1991, "The MIT Multipoint Alignment Test Bed: Technology Development for Optical Interferometry", *Active and Adaptive Optical Systems, SPIE Vol. 1542*, pp. 371-391.
- Ealey, M., 1991, "Actuators: Design Fundamentals, Key Performance Specifications, and Parametric Trades", *Active and Adaptive Optical Components, SPIE Vol. 1543*, pp. 346-362.
- Fanson, J., Blackwood, G., Chu, C., 1989, "Active-Member Control of Precision Structures", AIAA-89-1329-CP, *Proceedings, 30th SDM Conference*, pp. 1480-1494.
- Flint, E., Liang, C., Rogers, C., 1994, "Electro-mechanical Analysis of Piezoelectric Stack Active Member Power Consumption", *Proceedings, International Conference on Intelligent Material*, pp. 534-545.
- Glaser, R., Kuo, C., Garba, J., 1993, "Application of Smart Structure Concepts to Vibration Suppression of Cryocooler Coldfinger", *Smart Structures and Intelligent Systems, SPIE Vol. 1917*, pp. 555-563.
- Harris, C., 1988, *Shock & Vibration Handbook*, McGraw Hill, New York, pp. 10.1-10.46.
- Kino, G.S., 1987, *Acoustic Waves*, Prentice-Hall, Englewood Cliffs, N.J., Chpt. 1.
- Liang, C., F. P. Sun, C. A. Rogers, 1992, "Investigation of the Energy Transfer and Consumption of Adaptive Structures", IEEE Tuscon Conference, Dec. 16-18.
- Liang, C., F. P. Sun, C. A. Rogers, 1994, "Electro-mechanical Modeling of Active Material Systems," *Smart Structures and Materials, 94*, ASME, Orlando, Florida, Feb. 1994, in press.
- Lomenzo, R., H. Sumali, H. Cudney, "Maximizing Mechanical Power Transfer from Piezoceramic Stacked Actuators to Structures", *AD-VOL. 35, Adaptive Structures and Material Systems*, ASME 1993, pp. 229-235.
- Marlow, W., 1993, "On the Dynamics of Deformable Mirror Actuators", *SPIE Vol. 1917, Smart Structures and Intelligent Systems*.
- Physik Instruments, 1990, *Products for Micro-positioning*, pp. 5.1-5.27.
- Preumont, A., Sparavier, M., Dufour, J., 1990, "Application of Piezoelectric Actuators to the Active Damping of a Truss Structure", AIAA-90-0950-CP, *Proceedings of the 31st SDM Conference*, pp. 1907-1913.
- Rahman, Z., Spanos, J., O'Brien, J., Chu, C., 1993, "Optical Path Length Control Experiment On a Precision Truss Structure", *SPIE Vol. 1917, Smart Structures and Intelligent Systems*. pp. 848-855.
- Sumali, H., Cudney, H., 1994, "An Active Engine Mount with a Piezoelectric Stacked Actuator", AIAA-94-1466-CP, *Proceedings of the 35th SDM Conference, Hilton Head, SC*, pp. 1233-1241.
- Tsuka, H., Nakomo, J., Yokoya, Y., 1990, "Toyota Electronic Modulated Suspension", *IEEE Workshop on Electronic Applications in Transportation*.
- Umland, J.W., M. Webster, B. Johnson, Active Member Design, Modeling and Verification, 1993, ", *Adaptive Structures and Material Systems*, ASME 1993, AD-Vol. 35., pp. 217-227.

DYNAMIC OUTPUT AND STRUCTURAL RESPONSE PREDICTION FOR STACK ACTIVE MEMBERS INTEGRATED IN COMPLEX STRUCTURES

Eric M. Flint *

Institute For Structural Mechanics, DLR, Braunschweig, Germany

Chen Liang †

San Diego State University, San Diego CA

Craig A. Rogers ‡

Center For Intelligent Material Systems and Structures, Virginia Tech, Blacksburg, VA

Abstract

A closed form method of predicting the dynamic force and velocity output of stack active members integrated within complex truss structures is presented. By active member it is meant an actuator that is an integral part of the host structure providing both a structural load path and an ability to control. If such an active member is modeled in terms of transduction equations based on force, output, voltage and current, along with a boundary condition imposed by the host structure it is possible to predict the force transmitted by the active member into the host structure. A method of converting the host structure mobility at each end of the active member into an equivalent host structure impedance is provided as most transduction equations are derived with an assumption of single point equivalent impedance. The theoretical predictions are experimentally tested with a PZT stack active member integrated in a complex truss structure representative of a small satellite. This work can be used to provide accurate predictions of the actuator output applied to the structure it is integrated within for use in active control law development or structural dynamic analysis.

1.0 Introduction

Integrated strain actuators (ISA) are devices that take input energy and convert it into a mechanical displacement output while being part of the structure they impart the mechanical energy into. Because the ISAs are within a structure, the displacement is restricted by frequency varying boundary conditions. Hence, this displacement is better thought of as a strain input and thus the

name, ISA. Some common examples are voice coils and hydraulic actuators. Smart materials, such as piezoelectrics, electrostrictives, shape memory alloys and magnetostrictives have also been used as ISAs.

In this paper, a subclass of ISA's known as piezoelectric stack active members will be concentrated on. These devices are put in a host truss structure in order to provide some sort of shape, vibration control or sensing capability to an otherwise passive truss structure. They are called members because they replace passive structural members but remain an integral part of the structural load paths. The "active" part of the name comes from the fact that they are most often placed within a structure as actuators to provide control authority. "Active" also indicates that the so called "smart materials" are used rather than the more traditional hydraulic, electromagnetic or compressed air actuators.

It is important to make clear the distinction between stack actuators and an active member. Piezoelectric stack active members use stacks but also have pre-stress springs and output shafts that make them useful in structural applications. Thus, an active member is the whole device while the stack is just the motor.

Within this paper some of the truss structures for which active members were considered are reviewed. This is followed by discussion of piezoelectric stack active members. A specific formulation of the transduction equations for piezoelectric stack active members is reviewed and previous analytical approaches are discussed. These equations are then used in conjunction with an expression for the boundary conditions imposed by the host structure to develop a set of equations for the current requirements and force output of the integrated stack.

Most active members are implemented within a structure with two boundary conditions. A method of accounting for this is and finding the equivalent host structure impedance is provided based on

* Wissenschaftler Mitarbeiter, Student Member

† Assistant Professor, Associate Member

‡ Professor, Member

mobility. The models of the admittance signature and force output predictions are then experimentally verified with a PZT stack active member integrated within a complex truss structure representative of a small satellite.

With theoretical predictions of the force output available it is possible to perform detailed design studies prior to prototyping or production. These results also allow coupled optimization of the structural control output authority especially with regards to output saturation and non constant force output vs. frequency. With this knowledge, better simulation of the response of the host structure to active control is possible.

2.0 Background

Interest in the implementation of active members within truss structures has been high. Some notable examples include the NASA Langley Control Structure Interaction Evolutionary Model (CEM) Phases 1-3, the MIT Multipoint Alignment Test Bed (Blackwood et al., 1991) and the various JPL test beds (Kuo et al., 1991, Umland & Chen, 1992, to mention just a few).

2.1 Previous Analytical Methods

Ealey (1991) gives a good overview of most available active member materials and implementations. Umland et al. (1993) specifically reviews the actuator types studied at JPL (PZT, PMN and Terfenol) and gives an analytical method to predict the output force and displacement based on a stiffness analysis. This allows inclusion of the dynamic nature of pre-stress springs and moment isolation devices but neglects the coupling with the host structure boundaries with regards to force output, electrical and mechanical actuator properties.

Most past research has concentrated on modeling the behavior of the actuators by themselves. Others studies have been interested in force output but mostly in how it affected control algorithm behavior. In some cases, static models have been used which is not applicable to dynamic situations. As finite element modeling routines become more sophisticated modeling by computer analysis is possible but computationally expensive and time consuming. This is especially true if one wishes to perform optimization iterations.

The already discussed work of Umland (1993) is a good step in that it allows consideration of the dynamic properties of the active member but does not include host structure imposed boundary conditions. Lomenzo et al. (1994) provides an initial analysis based on an impedance approach

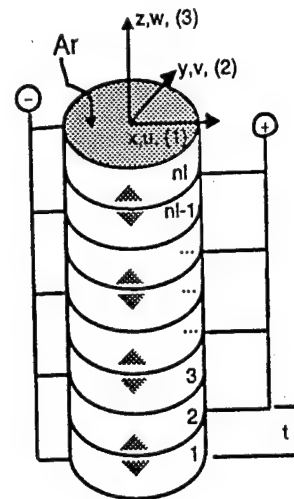


Fig. 2.1 Typical stack actuator architecture

that does consider the interactions between just a PZT stack actuator and host structure.

2.2 Stack Actuators

Piezoelectric and electrostrictive active members are usually constructed in the same manner as shown in Fig. 2.1. Thin layers of the active material are electrode and layered, or alternatively cofired, together on top of each other. This is done so that the mechanical properties are in series while electrical properties are in parallel. This arrangement leads to relatively large displacements for reasonable voltages. This happens because the applied electric field (which is what causes the expansions) is directly related to the applied voltage over the thickness. Thus for a constant voltage, the thinner the layer the larger the applied electric field.

Due to the glue used during assembly, not to mention the characteristic of the ceramic active material itself, stack actuators are weak under tension loads typically found in dynamic applications. This led to the development of active members which include a pre-stress spring to protect the stack from tension during operation. Typically, an active member also provides isolation from moments by solid hinges or flexures in order to prevent excessive cyclic loading (leading to fatigue) and alternating tension in the stack. Also, active members are typically instrumented with strain gage or eddy current sensors. Another possibility is to use the active material as a sensor in addition to actuator. Anderson, et al. (1992) has studied this specifically with regards to PZT active members in truss structures. A generic schematic of a typical active member is shown in Fig. 2.2

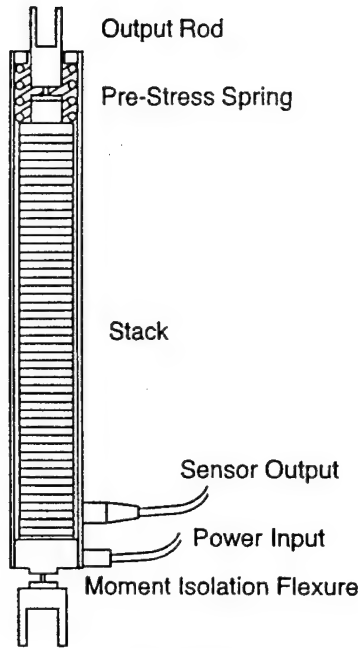


Fig. 2.2
Typical active member architecture

2.3 Mechanical Impedance

This paper depends heavily on an understanding of mechanical impedance and its dual, mobility. Therefore the necessary basic principals are reviewed here. Mechanical impedance and mobility, which are simply the inverse of each other, are the ratios of force and velocity at a given point and direction in a structure (Harris, 1988):

$$Z_M = \frac{Force}{Vel}, \quad (2.1)$$

$$M = \frac{Vel}{Force}. \quad (2.2)$$

Starting from first principals of mechanical systems represented by second order differential equations it can be shown that for steady state excitation a standard mechanical mass-spring-damper system can be represented in terms of impedance as:

$$Z_M = -\frac{k}{\omega} i + c + m i \omega. \quad (2.3)$$

Alternatively, it is sometimes necessary when the element to be modeled transmits force from one end to another to use a transmission line modeling approach. This results in a final expression for the impedance of the element as (Harris, 1988):

$$Z_M = Z_{Mod} Z_{or} \left[\frac{Z_{HS} + i Z_{or} \tan(k_r l_r)}{Z_{or} + i Z_{HS} \tan(k_r l_r)} \right], \quad (2.4)$$

where Z_{or} and k_r are:

$$Z_{or} = a_r \sqrt{Y_r \rho_r}, \quad (2.5)$$

$$k_r = \omega \sqrt{\frac{\rho_r}{Y_r}}. \quad (2.6)$$

Using the above two methods, it is possible to model most components of a system. The individual components are then combined using the fact that the impedance of components in parallel (Z_{p1}, Z_{p2}) sum and when in series the inverse of the component impedances (Z_{s1}, Z_{s2}) sum:

$$Z_{p1+p2} = Z_{p1} + Z_{p2} \quad (2.7)$$

$$\frac{1}{Z_{s1+s2}} = \frac{1}{Z_{s1}} + \frac{1}{Z_{s2}} \quad (2.8)$$

As an example of how to use these equations that will also be useful latter, a model of an stack active member is now shown. In Fig. 2.3 one can see the active member shown in Fig. 2.2 in a schematic component form. The stack imparts force and displacement to a pre-stress spring and output rod. The rod in turn delivers the actuator output to the attached host system which is assumed to load the active member from one side only. As the spring is fixed by the rigid (compared to the rest of the components) active member casing a mass-spring-damper approximation of its behavior using Eq. (2.3) is acceptable. However, since the output rod transfers forces from one end to another, a transmission line model as provided by Eq. (2.4) is more appropriate.

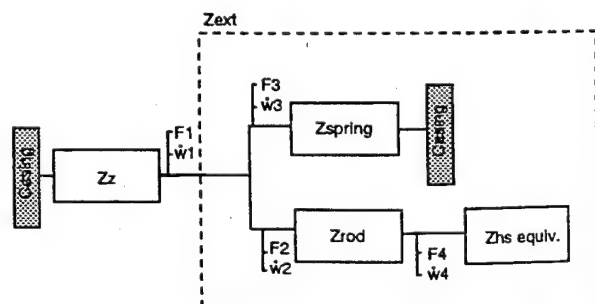


Fig. 2.3 Impedance diagram of typical active member architecture

Examination of Eq. (2.4) reveals that the host structure impedance is already included in the transmission line impedance model of the output rod. Thus, the final expression for the impedance external to the stack actuator, Z_{ext} , is simply :

$$Z_{ext} = Z_{spring} + Z_{rod}, \quad (2.9)$$

because the spring and output rod (including the effects of the host structure) are in parallel with each other and hence Eq. (2.7) applies.

3.0 Transduction Equations.

In this section the transduction equations critical to determining the force output are presented. This work is provided in summary form as the details are available in Flint et al., 1994b.

3.1 Transduction

The transduction equations that most accurately depicts the behavior of piezoelectric stack actuators take the form:

$$\dot{w} = \frac{F}{Z_{ms}} + \phi V, \quad (3.1)$$

$$I = \phi F + \frac{V}{Z_{EF}}. \quad (3.2)$$

The particular representation used here is typically called the dual form. These equations relate the velocity and current to the applied force and voltage through the three transduction parameters, Z_{EF} , Φ and Z_{ms} .

3.2 Z_{EF}

The electrical admittance of a PZT stack actuator can be written as:

$$Y = \frac{I}{V_{ac}} = i\omega a \frac{n_l}{t} (\epsilon_z^{*T}) + \quad (3.3)$$

$$i\omega a \frac{n_l}{t} \left(-d_{33}^2 Y_z^{*E} + d_{33}^2 Y_z^{*E} \frac{\tan(k_z t n_l)}{k_z t n_l \left[1 + \frac{Z_{ext}}{Z_z} \right]} \right)$$

with:

$$k_z = \omega \sqrt{\frac{\rho}{Y_z^{*E}}}, \quad (3.4)$$

$$Y_z^{*E} = Y_z^E (1 + \eta_m i), \quad (3.5)$$

$$Z_z = -\frac{K_z k_z t n_l}{\omega \tan(k_z t n_l)} i, \quad (3.6)$$

$$K_z = Y_z^{*E} \frac{a}{t n_l}, \quad (3.7)$$

$$\epsilon_z^{*T} = \epsilon_z^T (1 + \eta_e i). \quad (3.8)$$

If Z_{ext} is calculated using Eq. (2.9) with the host structure impedance set to zero then Eq. (3.3) results in an expression for the free electrical admittance which can be inverted to yield the free electrical impedance, Z_{EF} . If the effects of the boundary conditions are retained one has a measure of the coupled electrical impedance. In either case the impedance is gained by inverting the admittance of Eq. (3.3) using:

$$Z_E = \frac{1}{Y}. \quad (3.9)$$

3.3 Phi

The transduction coefficient, Φ , is:

$$\Phi = \frac{i a d_{33} \tan(k_z t n_l)}{k_z t (1 + \frac{Z_{ext}|_{Z_{hs}=0}}{Z_z})} \frac{1}{\cos(k_R l_R)} \quad (3.10)$$

where the cosine term in the denominator incorporates the influence of the output rod impedance.

3.4 Z_{ms}

The short circuited mechanical impedance represents the behavior of the active member when the member is not capable of behaving as an active member. The exact form of the short circuited mechanical impedance is given by:

$$Z_{ms} = \frac{Z_{Rod}|_{Z_{hs}=0} (Z_{Spring} + Z_z)}{(Z_z + Z_{Spring} + Z_{Rod}|_{Z_{hs}=0})} \quad (3.11)$$

Z_z is described by Eq. (3.6) and is used in this equation because when the stack is short circuited it behaves purely mechanically. As for all of the transduction equation parameters, Z_{Rod} is calculated for the case of no host structure loading.

4.0 Structural Coupling

Because the host structure loading was not directly included in the transduction equations

they are strictly valid only when the active member is free or blocked. However, when integrated in a structure a force and output equilibrium must exist at the connection between the output rod and the host structure. This equilibrium can be expressed as:

$$F = -Z_{HS} \dot{w} \quad (4.1)$$

With this expression it is now possible to solve for the any three of the transduction equation variables in terms of the fourth. If voltage is chosen as the dependent variable, the current, force and velocity can be determined. First, Eq. (4.1) is substituted into Eq. (3.2) resulting in

$$I = \phi(-Z_{HS} \dot{w}) + V / Z_{EF} \quad (4.2)$$

which is then rearranged to solve for the velocity and then set equal to Eq. (3.1) which is another expression for the velocity:

$$\dot{w} = \frac{I - V / Z_{EF}}{-\phi Z_{HS}} = \frac{F}{Z_{ms}} + \phi V. \quad (4.3)$$

The resulting expression is then rearranged in terms of the force:

$$F = (\frac{I - V / Z_{EF}}{-\phi Z_{HS}} - \phi V) Z_{ms} \quad (4.4)$$

which is then substituted into Eq. (3.2) resulting in an expression that is in terms of the current and voltage variables only:

$$I = \phi(\frac{I - V / Z_{EF}}{-\phi Z_{HS}} - \phi V) Z_{ms} + \frac{V}{Z_{EF}}. \quad (4.5)$$

Solving for the current in terms of voltage yields:

$$I = \frac{(Z_{ms} / Z_{EF} - \phi^2 Z_{HS} Z_{ms} + Z_{HS} / Z_{EF})}{(Z_{HS} + Z_{ms})} V. \quad (4.6)$$

This expression can then be substituted back into Eq. (4.4) and the first half of Eq. (4.3) and the force and velocity output of the active member are known for a given input steady state harmonic voltage.

5.0 Determining Equivalent Host Structure Impedance

While not explicitly shown, the development of

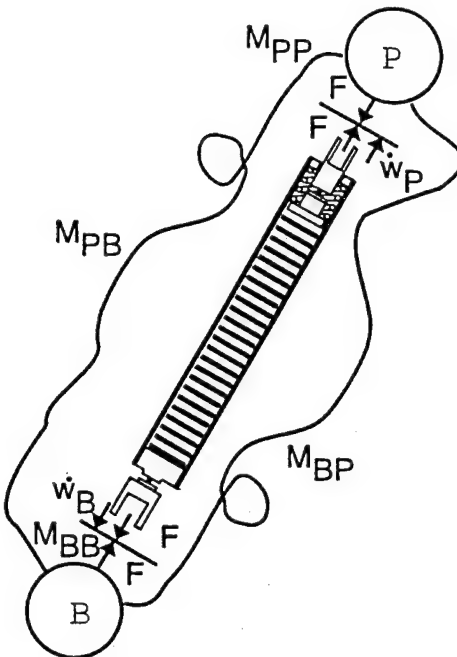


Fig. 5.1 Direct mobility points and cross mobility paths of a host structure that a active member is integrated within.

the transduction equation parameters assumes that the actuator has output only at one end as shown in Fig. 2.3. During implementation in dynamic structures this will rarely be the case. Thus a method of accounting for the boundary conditions imposed on the actuator at both ends must be developed. In Fig. 5.1 the reference directions and possible structural paths for force transmission between each end of the actuator are shown. Using the mechanical mobility relationship:

$$M_{ij} = \frac{\dot{w}_j}{Force_i} \quad (5.1)$$

where i indicates the location of excitation and j the location of response, it is possible to determine the displacement at each actuator end:

$$\dot{w}_B = M_{BB} F_B + M_{PB} F_P \quad (5.2)$$

$$\dot{w}_P = M_{BP} F_B + M_{PP} F_P \quad (5.3)$$

From this, the equivalent host structure impedance seen by the active member can be determined by taking the ratio of applied force over the difference in velocity:

$$Z_{eqHS} = \frac{Force}{\Delta \dot{w}} = \frac{1}{M_{BB} - M_{PP}} \quad (5.4)$$

In the derivation an assumption of structural linearity was made allowing the cancellation of the cross mobilities, M_{BP} and M_{PB} . It is important to ensure this assumption is valid when the active member is integrated in a host structure before these results can be used with confidence.

Equivalent host structure impedance and response mobilities can be determined by any means desired. If the truss structure is simple enough, closed form analytical predictions are possible. The host structure can be broken down into a series of components represented as mass-spring-dampers whose combined behavior can then be approximated using standard mechanical engineering principals discussed in Section 2.3.

If accurate knowledge of the final structural configuration is available, a finite element model can be developed to allow predictions. This approach is also useful during preliminary and conceptual design stages. Finally, if the host structure is available the various mobilities and impedances can be measured directly which is the approach taken in this paper.

6.0 Experimental Verification

In this section the results of a series of experiments performed to verify the predictions of the previous sections are described and presented.

6.1 Set Up

In testing the theoretical derivations given above, a piezoelectric stack active member produced by Physik Instrumente was used. The basic parameters needed to describe the stack, pre-stress spring and output rod behavior in terms of the transduction equation parameters are given in Table 6.1. These parameters were either provided by the manufacturer or determined from the measurements. The required damping of the pre-stress spring can be determined from the given data by using the fact that $c = 2\pi m \zeta n f_{rad}$ and $n f_{rad} = \sqrt{k/m}$.

The active member was integrated in a truss structure representative of a small spacecraft with deployed solar array. This test structure is shown in Fig. 6.1 in a passive state with the location of integration and the node reference systems indicated. One can also see that the test structure was secured so that it was effectively cantilevered. Such a boundary condition was beneficial for initial testing as it forced several main structure bending modes down out of the high modal density region that exists above 300 Hz. Additionally it eliminated potential confusion between rigid body modes

Table 6.1
PZT stack active member parameters

Symbol	Definition	Value
t	layer thickness	500e-6 m
n_l	number of layers	184
a_r	cross sectional area	78.54e-6 m^2
ρ	density	7800 kg/m^3
Y^E	Youngs modulus	36e9 Pascals
η_m	mechanical loss	0.0083
ϵ^T	electrical permitivity	1.947e-8
η_e	electrical loss	0.015
d	piezoelectric constant	3.65-14 m/V
Spring		
k	stiffness	9.66e6 N/m
m	mass	7.3e-3 kg
ζ	damping	0.03
Output Rod		
Y_r	Youngs modulus	190e9 Pa
ρ_r	density	7689 kg/m^3
a_r	cross sectional area	5.02e-6 m^2
l_r	length	22.0e-3 m
Z_{Madj}	adjustment factor	0.44

and the solar array dynamics. The test structure itself consists of anodized aluminum longerons, battens and diagonals attached between node balls. These node balls are arranged in a cube pattern and there is 10" along the edge of the cube between nodes. The joints were designed so that individual members could easily be removed and rearranged.

6.2 Host Structure Boundaries

All the derivations presented earlier depend on accurate knowledge of the host structure boundary conditions. In this section the method used to measure the required direct and cross mobilities are described.

As shown in Fig. 6.2 a shaker was suspended so that it acted along the same axis that the active member would use when integrated in the structure. The shaker was excited by a 1 V ac, 0 to 600 Hz shaped random signal provided by the WCA built in signal generator. This signal was routed through a Trek amplifier before being delivered to the shaker. The exact force input of the shaker through its attachment stinger and the resulting host structure acceleration was measured by a PCP impedance head. Response at the cross point was measured with a PCP 336 Flexcel

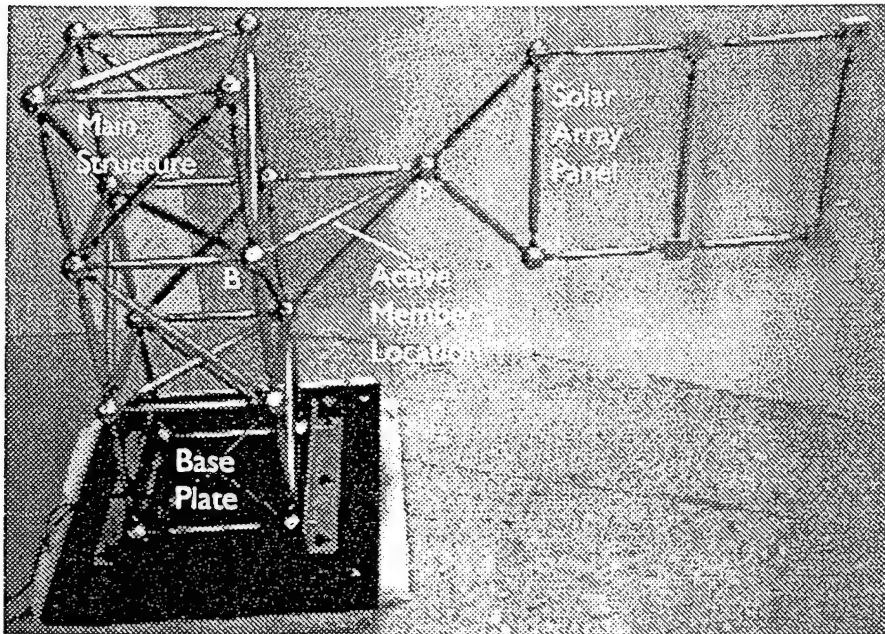


Fig. 6.1 Host structure in its passive state showing the desired active member integration point, node reference notation and the cantilevered boundary condition.

accelerometer. The data was collected from 0 to 500 Hz with a 1024 divisions per sample as modified by a Hanning window using a WCA Zonix AND measurement system running off of a Quadra 950 platform. 150 linear averages were taken for each measurement. The set up was then reversed to measure the response in to excitation at the panel location

The generated frequency response functions(FRFs) were then integrated in the frequency domain to yield the desired mobility functions from the measured acceleration over force. A total of four FRFs were measured corresponding to the direct mobilities at and the cross mobilities.

In Fig. 6.3 one can see the magnitude of the measured mobilities. The most important fact is that the two cross mobilities (dotted lines) are very similar below 300 Hz thus giving confidence that the structure does indeed behave linearly below the region of high modal density. In the individual mobilities one sees a strong resonance near 180 Hz. This corresponds to one of the global bending modes of the main structure. The effect of this mode is especially strong in the direct mobility measured at the base point. Similarly, the effects of several solar array modes are seen mainly in the measurement of the direct mobility at the panel point.

While not shown, the coherence of the measured FRFs was especially good for the point mobilities

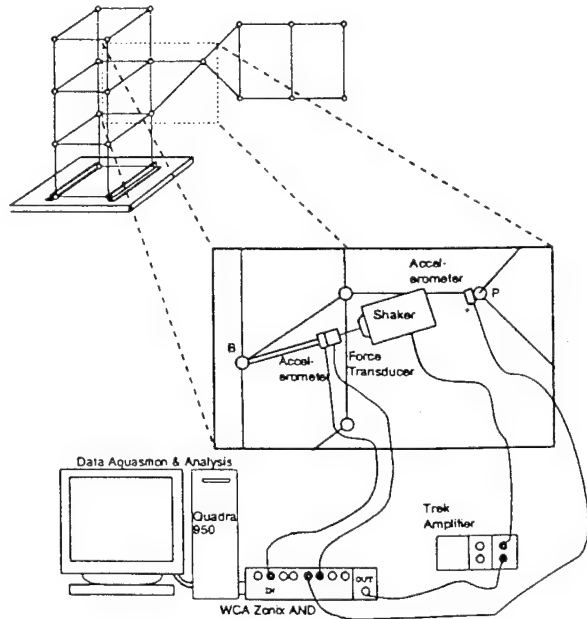


Fig. 6.2 Experimental set up for measuring the direct and cross mobilities necessary to predict ZeqHS

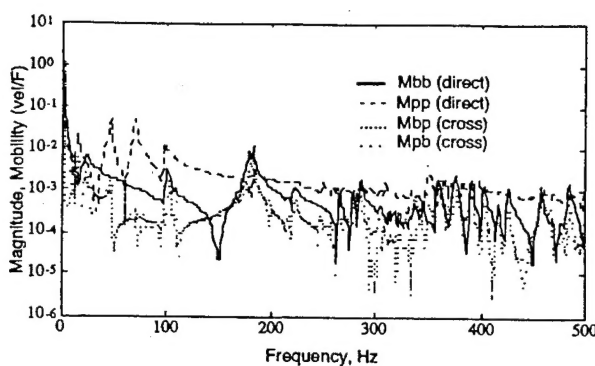


Fig. 6.3 Magnitude of the measured direct and cross mobilities at the desired integration point.

and acceptable for transfer mobility measurements being above 0.8 above 50 Hz. Below that frequency noise from the sensors and laboratory environment corrupted the results.

6.3 Admittance Signature

Shown in Fig. 6.4 is the experimental set up for measuring the electrical admittance of the integrated actuator. In this test, the actuator was integrated into the desired location and a HP 4194a impedance gain analyzer was used to measure the current required to maintain a 1 Volt rms signal. Results are not presented for below 100 Hz as the impedance analyzer cuts off at that frequency.

Figure 6.5 shows the results of this test as well as the theoretical predictions prepared using Eq. (3.3) where the direct mobility of the base point (M_{bb}) has been inverted to provide the host structure impedance. The panel mobility was neglected as it mostly contains information about the solar array dynamics which occur at frequencies below the 100 Hz cut off. As one can see, the agreement, while not perfect, is good in regards to the magnitude and frequency of the predicted coupling.

There are many possible sources for the discrepancies. First, when the actuator is installed it is possible that it adds some extra stiffness to the overall structure and removes some slack that could have caused damping. This is especially true about the attachment shaft which could not be tightly secured in the tests for the mobilities. Additionally, some discrepancies might be driven by unmeasured structural dynamics that the coupled impedance measurement is sensitive to.

6.4 Mechanical Force Response

The final test of the developed theory was its ability to predict the force output of an integrated

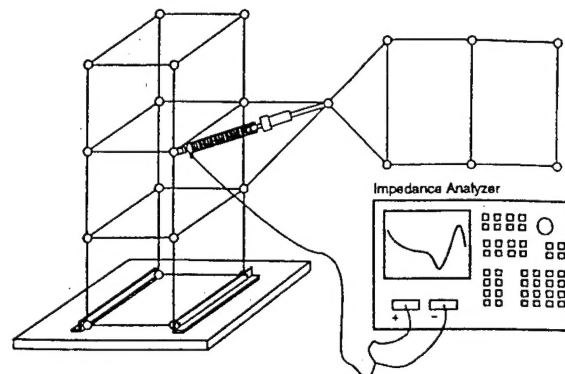


Fig. 6.4 Experimental set up for measuring the electrical impedance of the integrated active member

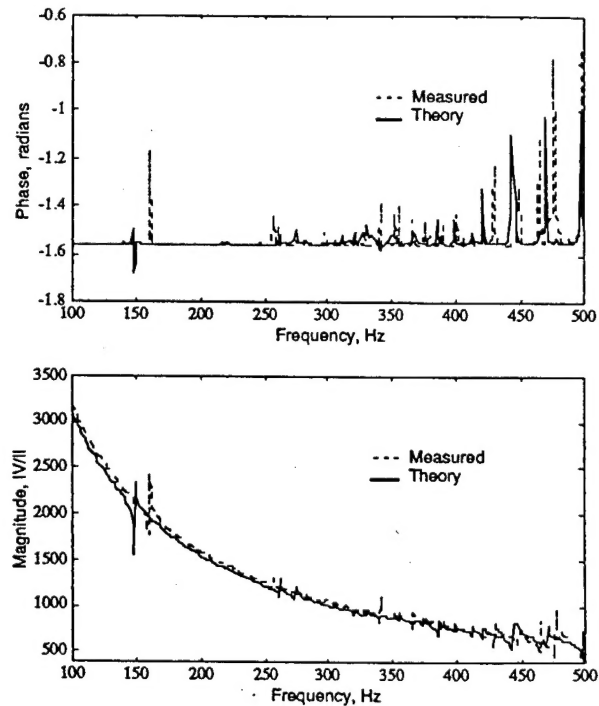


Fig. 6.5 A comparison of the experimental and theoretical electrical impedance signature for the active member integrated in the host structure

stack actuator. Figure 6.6 shows the experimental set up used. In order to generate a measurable force, it was necessary to operate the actuator at high voltages. This was achieved by supplying a negative DC bias from a HP 6200B DC power source and a shaped random noise signal from 0 to 600 Hz from the internal WCA signal generator. These signals were combined with a power transformer and then sent to a TREK 50/750 power amplifier.

After the amplification stage the resulting -250 V DC bias combined with a narrow band ± 100 V p2p noise was applied to the integrated actuator. The WCA signal analysis program was used to measure the resulting force and applied voltage levels (after it was stepped down with a 10⁴ reduction cable). Two hundred and fifty samples were linear averaged from 0 to 500 Hz with a frame size of 1024 (1 Hz resolution and 1 second sample time) as modified by a Hanning window.

The resulting frequency response of output force over the voltage is shown in Fig. 6.7 along with the theoretical predictions generated using Eq. (4.4) with Eq. (4.6) substituted in place of the current. The required Z_{EF}, Phi and Z_{ms} were calculated using the active member parameters of Table 6.1 in Eqn.'s (3.3), (3.10) and (3.11) respectively. Z_{eqHS} was calculated, as in the previous section, using solely the inverse of the measured base mobility.

As can be seen the results agree in regards to the general trends but lack a precise fit. Closer inspection reveals that the theoretical predictions appear to be frequency shifted from the experimental results in most cases. As for the impedance signature, one possible explanation for this is that the equivalent host structure impedance was measured without the pre-stress in the attachment shaft that comes from incorporating the active member in the truss structure. Thus the attachment shaft had less stiffness when the mobilities were measured as compared to when the integrated force was measured.

7.0 Summary

In this paper a generic formulation to predict the dynamic output of piezoelectric stack active members integrated within structures is derived and experimentally verified for a PZT active member. This was accomplished through transduction equation approach. The important feature of these equations is that they, in a simple way, allow the inclusion of the effects of integrating the active member within structures. As shown experimentally with the PZT stack active member, knowledge of the host structure boundary conditions can be used to predict the admittance signature. Additionally, as also shown with the PZT active member, the free electrical impedance, (Z_{EF}) along with Φ , and Z_{ms} can be used to predict the force output of the stack actuator. As long as the boundary conditions seen by the active element are only at two ends, this method can be extended to actuators within any piece of complicated machinery or structures.

With theoretical predictions of the force and velocity output available it is possible to perform

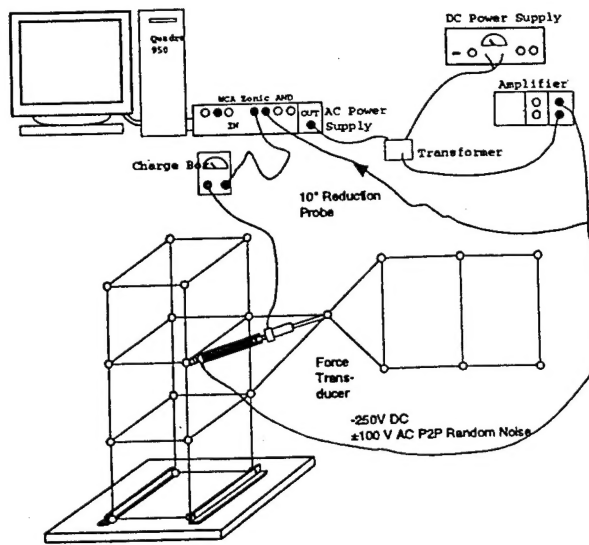


Fig. 6.6
Experimental set up for measuring the integrated active member force output

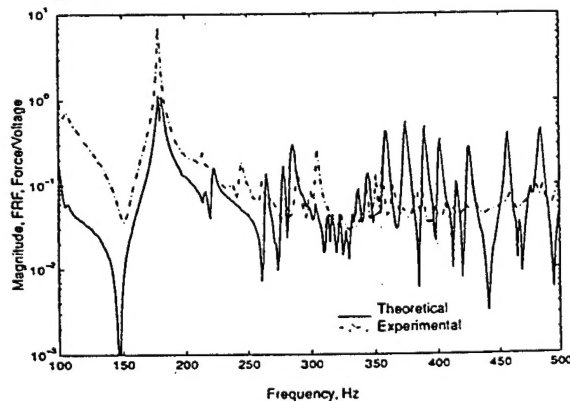


Fig. 6.7
A comparison of the experimental and theoretical force output for the active member integrated in the host structure

detailed design studies prior to prototyping or production. These results also allow coupled optimization of the structural control output authority especially with regards to output saturation and non-constant force output vs. frequency. With this knowledge, better simulation of the response of the host structure to active control is possible. Finally, as discussed in Flint, et al. (1994a and 1995), the methods presented here on how to account for the structural coupling between the host structure and the electrical admittance signature can be used to predict resonances in the power supply system needs and self induced temperature rise due to dynamic operation.

8.0 Acknowledgments

The authors would like to thank the Virginia Space Grant Consortium and the Air Force Office of Scientific Research, Grant # F-49620-93-1-0166, technical monitors Dr. Walter F. Jones and Dr. Jim Chang, for the funding that enabled this work. The authors would also like to thank Dr. Ray Kvaternik of NASA Langley for providing the experimental test structure.

9.0 Nomenclature

D	electric displacement
E	applied electric field
F	actuator force output
F_B	force output at base
F_P	force output at panel
I, I_e	current, rms voltage
K_z	actuator static stiffness
M	mobility
M_{BB}	direct mobility at base
M_{PP}	direct mobility at panel
M_{PB}	cross mobility at base excited at panel
M_{BP}	cross mobility at panel excited at base
V, V_e	voltage, rms voltage
Y	admittance (electrical)
Y^E	Youngs modulus for a constant electric field
Y^{*E}	complex Y^E
Y_r	output rod Youngs modulus
Z_{eqHS}	equivalent host structure impedance
Z_{ext}	mechanical impedance external to stack
Z_{EF}	free electrical impedance
Z_{HS}	host structure point impedance
Z_{ms}	short circuited mechanical impedance
Z_M	mechanical impedance
Z_{Madj}	transmission line adjustment factor
Z_{or}	output rod static impedance
Z_{p1}, Z_{p2}	parallel mechanical impedance components
Z_{rod}	mechanical impedance of output rod
Z_{s1}, Z_{s2}	serial mechanical impedance components
Z_{spring}	mechanical impedance of pre-stress spring
Z_z	stack stiffness
a	active material cross sectional area

a_r	output rod cross sectional area
c	damping of mass-spring-damper
d	piezoelectric constant
i	imaginary, $\sqrt{-1}$
k_r	output rod wave value
k_z	material wave value
k	stiffness of mass-spring-damper
l_r	output rod length
m	mass of mass-spring-damper
$n f_{rad}$	mass-spring-damper natural frequency (in rad.)
t	wafer thickness
v	rms voltage amplitude
w_B	velocity at the base attachment point
w_p	velocity at the panel attachment point
ϵ^T	permittivity at constant stress
ϵ_z^{*T}	complex permittivity at constant stress
η_e	capacitive electrical loss
n_l	number of active layers in a stack
η_m	actuator mechanical loss factor
ϕ	transduction coefficient
ρ	active material density
ρ_r	output rod density
ω	frequency in rad/sec
ζ_i	damping

10.0 References

- Anderson, E., Hagood, N., Goodliffe, J., " Self-Sensing Piezoelectric Actuation: Analysis and Application to Controlled Structures", AIAA-92-2465-CP, Proceedings of the 33rd SDM Conference, pp. 2141-2155.
- Blackwood, G., Jacques, R., Miller, D., 1991, "The MIT Multipoint Alignment Test Bed: Technology Development for Optical Interferometry", Active and Adaptive Optical Systems, SPIE Vol. 1542, pp. 371-391.
- Ealey, M., 1991, "Actuators: Design Fundamentals, Key Performance Specifications , and Parametric Trades", SPIE Vol. 1543 Active and Adaptive Optical Components, pp. 346-362.
- Fanson, J., Blackwood, G., Chu. C., 1989, "Active-Member Control of Precision Structures", AIAA-89-1329-CP, Proceedings, 30th SDM Conference, pp. 1480-1494.
- Flint, E., Liang, C., Rogers, C., 1994a, " Electro-Mechanical Analysis of Piezoelectric Stack Active Member Power Consumption", Proceedings, 2nd

International Conference on Intelligent Material,
Williamsburg, June 5-8, Pp. 534-545.

Flint, E., Liang, C., Rogers, C., 1994b, "Theoretical and Experimental Investigation of Coupled Electro-Dynamic Transduction Equations for Piezoelectric Stack Actuators", Proceedings, ASME Winter Annual Meeting, Chicago, November 6-11, Pp. 201-210.

Flint, E., Liang, C., Rogers, C., 1995, "Self induced temperature rise of stack actuators due to dynamic excitation" Proceedings of the 1995 North American Conference on Adaptive Systems, SPIE # 2443-46, in press.

Harris, C., 1988, Shock and Vibration Handbook, McGraw Hill, NY, Pp. 10.1-10.46.

Kino, G., 1987, Acoustic Waves, Prentice -Hall, Englewood Cliffs, N.J.

Kuo, C., Chen, G., Pham, P., Wada, B., 1990, "On Orbit System Identification Using Active Members", AIAA-90-1129-CP, Proceedings of the 31st SDM Conference., pp. 2306-2316.

Lomenzo, R., Sumali, H., Cudney, H., 1993, "Maximizing Mechanical Power Transfer form Piezoceramic Stack Actuators to Structures", ASME WAM, Adaptive Structures and Material Systems Forum, AD-Vol. 35, pp. 229-235.

Physik Instruments, 1990, Products for Micro-positioning, pp. 5.1-5.27.

Rahman, Z., Spanos, J., O'Brien, J., Chu, C., 1993, "Optical Path Length Control Experiment On a Precision Truss Structure", SPIE Vol. 1917, Smart Structures and Intelligent Systems. pp. 848-855.

Umland, J., Chen, G., 1992, "Active Member Vibration Control for a 4 Meter Primary Reflector Support Structure", AIAA-92-2341-CP, Proceedings of the 33rd SDM Conference., pp. 393-401.

Umland, J.W., M. Webster, B. Johnson, 1993, "Active Member Design, Modeling and Verification", Adaptive Structures and Material Systems, ASME 1993, AD-Vol. 35., pp. 217-227.